SOLID SOLUTION $GaSe_{1-x}S_x$ SINGLE CRYSTALS FOR THz GENERATION

by

John F Molloy

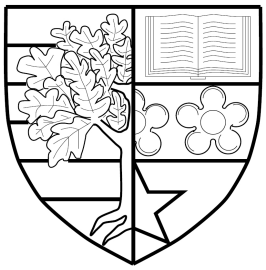

Submitted for the degree of
Doctor of Engineering

Department of Physics
School of Engineering and Physical Sciences
Heriot-Watt University

April 2016

Abstract

A table top source of coherent Terahertz (30-1000 μm) radiation, which is high power, narrow bandwidth, and broadly tunable, is high desired for applications in imaging, non-destructive testing (NDT), quantum, security and biomedical technologies. In spite of intensive research over many decades such a device remains elusive.

Sulpher doped Gallium Selenide ($GaSe_{x-1}S_x$) solid solution ε-polytype crystals are an outstanding candidate for the efficient generation of radiation and tunability throughout the majority of the Terahertz (THz) regime; thanks to the prodigious linear and nonlinear optical properties of the Gallium Selenide (GaSe) parent crystal.

Close control of doping and the crystal growth process enable the manufacture of superior quality nonlinear crystals, where the optical properties may be engineered and the mechanical properties vastly improved. Thus overcoming many of the physical issues that, despite its exceptional optical properties, have frustrated the widespread adoption of GaSe for laser frequency down conversion to the THz regime. In order to fully exploit the potential of $GaSe_{x-1}S_x$ crystals and successfully design efficient sources for THz generation the optical properties of these crystals must be accurately determined and their transformation with doping well understood. The work in this thesis aims to accurately determine the optical properties of GaSe, Gallium Sulphide (GaS) and $GaSe_{x-1}S_x$ crystals in the Far-Infrared and THz regimes to enable this exploitation.

In the first phase of investigation we determine the linear refractive index (n) and absorption (α) coefficient for both the o and e waves in the THz regime (0.1-4.5 THz) using Terahertz - Time Domain Spectroscopy (THz-TDS) for GaSe, and a dense set of $GaSe_{x-1}S_x$ crystals (x = 0.05 0.11 0.22 0.29 0.44). Measurements of THz dispersion and absorption properties of GaS crystals are performed for the first time. The transformation of the optical properties of the crystals and their phonon structure is studied. We examine the sources of inaccuracy in the THz-TDs measurements of high refractive index birefringent crystals and propose a set of criteria for the selection of adequate data. The nonlinear Figure of Merit (FOM) of available high quality $GaSe_{x-1}S_x$ crystals is found to be an order of magnitude less than that predicted in the literature, with FOM = 19.8 for GaSe, FOM = 17 for $GaSe_{x-1}S_x$, on the other hand estimates for double doping with Sulphur and Aluminium predict significant enhanced of these FOM values, up to 5-10 times.

In the second phase of investigation we examine the phonon band of the GaSe, GaS and $GaSe_{x-1}S_x$ by FTIR and Raman spectroscopy. For the first time we determine the absorption coefficients of the main phonon peak in the set of $GaSe_{x-1}S_x$ crystals. The transformation of the phonon band with doping is studied.

In the third phase of investigation we attempt to determine the nonlinear optical properties d_{eff} and n_2 of GaSe and $GaSe_{x-1}S_x$ in the Far Infra-Red (FIR) and THz regimes using the Maker fringe and Z-scan methods on the FELIX free electron laser.

Acknowledgements

I am grateful to my supervisors, Professor Ajoy Kar, whose help and advice was always available, and guided me though many challenges; and Dr Mira Naftaly, whose rigour and attention to detail taught me many valuable lessons, improving both my work and writing.

I would like to thank my colleagues and friends at NPL, who have assisted me in many ways these past years. In particular I'd like to thank: Dr Andrew Smith for facilitating my studies and many escapades at NPL; Mr Robert Ferguson, for his positive attitude, good humour and patience in processing my various mystery materials; Dr Maud Seraffon, Dr Achilleas Sesis and Miss Maria Lodeiro for their help and assistance with my Raman Spectroscopy measurements; and Dr Richard Dudley, Dr David Humpherys and Dr Irshaad Fatadin for their many helpful discussions and advice.

I wish to thank my many friends and fellow students at NPL and Heriot-Watt CDT; their friendship, chats and devilment were a welcome and often much need diversion and did much to make my experience as positive an experience as it was.

Thank you to my friends and colleagues at the Felix facility, Radboud University, Nijmegen, and at the University of Surrey for their help in facilitating and performing my nonlinear measurements, especially Dr Konstantin Litvenko, Dr Nikolas Stavrias, Dr Kamyar Saeedi Ilkhchy, Prof Ben Murdin and Dr Britta Redlich.

I am indebted to my colleagues and good friends Prof Yury Andreev and Dr Grigory Lanskii of IMCES SB RAS, Tomsk whose yarns, anecdotes and insights sped many the long dark hour in the lab. Though their generosity with their time, knowledge and experience they have greatly contributed to my development and the work presented here. My thanks to my friends and colleagues in Tomsk State University, who kindly provide materials, measurements, and helpful discussions, especially Dr Valery Svetlichnyi, Dr Konstantin Kokh, Dr Ivan Lapin and Dr Anastasia Shabalina whose warmth and hospitality made my visit there so memorable.

Thank you Maria, your advice, patience, confidence and love have help me though so many deadlines, set backs and difficulties, I am truly lucky to have you by my side and look forward to out next adventure together.

Finally, I wish to thank my family, especially my parents Helen & Shaun, and my brother Kieran for their constant support and encouragement through-out my studies. They have in so many ways enabled me to pursue and successfully complete this Eng.D.

ACADEMIC REGISTRY
Research Thesis Submission

Name*:*	John F Molloy		
School:	School of Engineering & Physical Sciences		
Version: *(i.e. First, Resubmission, Final)*	Final	Degree Sought:	Doctor of Engineering

Declaration

In accordance with the appropriate regulations I hereby submit my thesis and I declare that:

1) the thesis embodies the results of my own work and has been composed by myself
2) where appropriate, I have made acknowledgement of the work of others and have made reference to work carried out in collaboration with other persons
3) the thesis is the correct version of the thesis for submission and is the same version as any electronic versions submitted*.
4) my thesis for the award referred to, deposited in the Heriot-Watt University Library, should be made available for loan or photocopying and be available via the Institutional Repository, subject to such conditions as the Librarian may require
5) I understand that as a student of the University I am required to abide by the Regulations of the University and to conform to its discipline.
6) I confirm that the thesis has been verified against plagiarism via an approved plagiarism detection application e.g. Turnitin.

* *Please note that it is the responsibility of the candidate to ensure that the correct version of the thesis is submitted.*

Signature of Candidate*:*		Date:	

Submission

Submitted By *(name in capitals):*	John F Molloy
Signature of Individual Submitting:	
Date Submitted:	

For Completion in the Student Service Centre (SSC)

Received in the SSC by *(name in capitals):*			
Method of Submission *(Handed in to SSC; posted through internal/external mail):*			
*E-thesis Submitted (**mandatory for final theses)***			
Signature:		Date:	

Please note this form should be bound into the submitted thesis.

Contents

List of Tables

List of Figures

List of Publications by the Candidate

Refereed Journal Publications

1. J. F. Molloy, M. Naftaly, and R. A. Dudley, "Charaterisation of Terahertz Beam Profile and Propagation," IEEE Journal of Selected Topics in Quantum Electronics, vol. 19, p. 8401508, 2013.

2. M. Naftaly, J. Molloy, G.V. Lansky, and Y. M. Andreev,"Terahertz time-domain spectroscopy for textile identification," Applied Optics vol. 52, no. 19, p. 4433-4437, 2013

3. John Molloy and Mira Naftaly, "Wool textile identification by terahertz spectroscopy," Journal of the Textile Institute, vol. 105, no. 8, p. 794-798, 2014

4. J. F. Molloy, M. Naftaly, Y. M. Andreev, G. V. Lanskii, I. N. Lapin, A. I. Potekaev, K. A. Kokh, A. V. Shabalina, A. V. Shaiduko, and V. A. Svetlichnyi, "Dispersion properties of GaS studied by THz-TDS," Crystal Engineering Communications, vol. 16, no. 10, p. 1995, 2014.

5. J. F. Molloy, M. Naftaly, Y. M. Andreev, K. A. Kokh, G. V. Lanskii, and V. A. Svetlichnyi, "Absorption anisotropy in sulfur doped gallium selenide crystals studied by THz-TDS," Optical Materials Express, vol. 4, no. 11, pp. 2451-2459, 2014.

6. K. Kokh, J. Molloy, M. Naftaly, Y. Andreev, V. Svetlichnyi, G. Lanskii, I. Lapin, T. Izaak, and A. Kokh, "Growth and optical properties of solid solution

crystals GaSe1xSx," Materials Chemistry and Physics, vol. 154, pp. 152-157, 2015.

7. Yu. M. Andreev, M. Naftaly, J. F. Molloy, A. E. Kokh, G. V. Lanskii, V. A. Svetlichnyi, V. F. Losev, N. G. Kononova and K. A. Kokh, "LBO: optical properties and potential for THz application," Laser Phys. Lett. vol. 12, 115402, 2015.

8. M. Naftaly, J. F. Molloy, Y. M. Andreev, K. A. Kokh, G. V. Lanskii, and V. A. Svetlichnyi, "Dispersion properties of sulfur doped gallium selenide crystals studied by THz TDS," Optics Express, vol. 23, no. 25, p. 32820, 2015.

9. M. Naftaly, J. F. Molloy, Magnusson, Y. M. Andreev and G. V. Lanskii, "Silicon carbide a high-transparency nonlinear material for THz applications," Optics Express vol. 24, no. 3, pp. 2590-2595, 2016.

10. V.A. Svetlichnyi, M. Naftaly, J.F. Molloy, Yu.M. Andreev, K.A. Kokhd, G.V. Lanskii, N.G. Kononova, A.E. Kokh, "Comments on 'Optical properties of borate crystals in the terahertz domain'," , Optics Communications vol. 365, pp. 14-15, 2016

Invited Conference Publications

1. J. F. Molloy and M. Naftaly, "Metrology for terahertz time-domain spectrometers," Proceedings of SPIE, vol. 9810, International Conference on Atomic and Molecular Pulsed Lasers XII, pp. 98101H-98101H-7, Tomsk, Russia 2015. DOI: 10.1117/12.2225622

2. Z. Huang, J. Huang, Y. Gao, Q. Yang, Yu. Andreev, K. Kokh, G. Lanskii2, V. Svetlichnyi, and J. Molloy, "Down-conversion in doped GaSe for spectroscopic applications," Advanced Laser Technologies 2016, Galway, Ireland 2016

Conference Publications

1. J. Molloy, M. Naftaly, G. Lanskii, K.A. Kokh, Yu. Andreev, "Investigation of modified GaSe crystal compositions for nonlinear THz applications", Infrared, Millimeter, and Terahertz waves (IRMMW-THz), 2013 38th International Conference on,

2. J.F. Molloy, M. Naftaly, Yu.M. Andreev, T.I. Izaak, G.V. Lanskii, and V.A. Svetlichnyi, "IDENTIFICATION OF TEXTILE FIBER BY IR AND RAMAN SPECTROSCOPY," Infrared, Millimeter, and Terahertz waves (IRMMW-THz), 2014 39th International Conference on,
   DOI: 10.1109/IRMMW-THz.2014.6956443

3. D.A. Humphreys, M. Naftaly, J.F. Molloy, "Effect of time-delay errors on THz spectroscopy dynamic range," Infrared, Millimeter, and Terahertz waves (IRMMW-THz), 2014 39th International Conference on,
   DOI: 10.1109/IRMMW-THz.2014.6956138

4. J.F. Molloy, M. Naftaly, Yu. M. Andreev, K.A. Kokh, G.V. Lanskii, V.A. Svetlichnyi, "Solid solution GaSe1xSx crystals for THz applications Infrared, Millimeter, and Terahertz waves (IRMMW-THz), 2014 39th International Conference on,
   DOI: 10.1109/UCMMT.2013.6641542

5. M. Janek, D. Zich, J. Molloy, M. Naftaly, "THz spectroscopy of amines and aminoacids intercalated in clays," Infrared, Millimeter, and Terahertz waves (IRMMW-THz), 2014 39th International Conference on,
   DOI: 10.1109/IRMMW-THz.2014.6956053

6. J.F. Molloy, M. Naftaly, Yu. M. Andreev, K.A. Kokh, G.V. Lanskii, V.A. Svetlichnyi, "Dispersion equations for the entire transparency range of GaSe," Infrared, Millimeter, and Terahertz waves (IRMMW-THz), 2015 40th International Conference on,
   DOI: 10.1109/IRMMW-THz.2015.7327751

7. J.F. Molloy, M. Naftaly, Yu. M. Andreev, K.A. Kokh, G.V. Lanskii, V.A. Svetlichnyi, "Evolution of GaSe1xSx phonon absorption peaks with S-doping studied by THz-TDS," Infrared, Millimeter, and Terahertz waves (IRMMW-THz), 2015 40th International Conference on,
DOI: 10.1109/IRMMW-THz.2015.7327728

8. J.F. Molloy, N. Stavrios, K. Litvienenko, M. Naftaly, "Non-linear coefficients of crystals measured at THz frequencies," Infrared, Millimeter, and Terahertz waves (IRMMW-THz), 2016 41th International Conference on,
DOI: 10.1109/IRMMW-THz.2016.7759006

Chapter 1

Introduction

THz has always been and remains a difficult regime to work in; where a lack of practical sources and detectors has continually hampered advances [1, 2], leaving it a somewhat arcane field that was principally the domain of astronomers. Since the late 1990's the development of new sources, of ultrafast solid state laser pump sources, and the discovery of new optical materials have made the generation and detection of Terahertz radiation substantially easier [2].

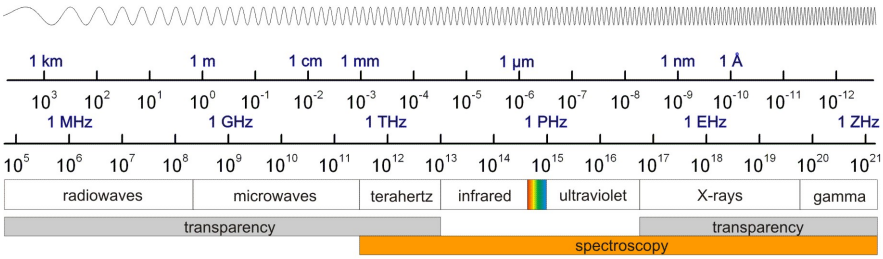

Figure 1.1: Representation of the electromagnetic spectrum showing the location of THz radiation (http://www.physik.uni-kl.de/)

Together with the advances in technology making this regime more accessible, there has been an increased demand from other sectors for capabilities that Terahertz radiation can provide [2, 3, 4], which has lead to a sustained period of intense interest in Terahertz radiation and its applications. This is evident from the almost exponential growth in publications featuring the word THz in the title in the past 20 years, across a wide range of disciplines [4].

Many optically opaque materials are transparent in the THz regime, and this has

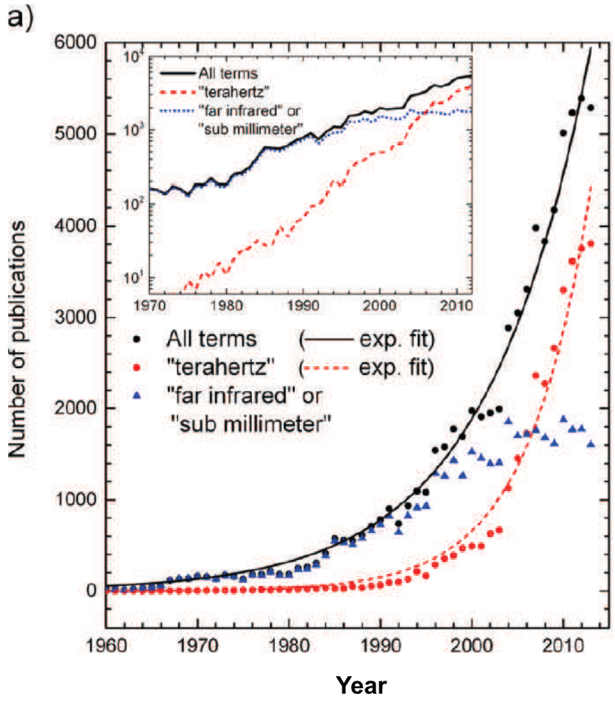

Figure 1.2: Exponential fit to the growth in Terahertz publications between 1960-2013 [4]

been widely exploited in security and imaging applications. It is employed in the detection of concealed weapons, explosives and contraband among airline passengers [2, 3, 5], as well as being used in a number of medical imaging devices due to its nonionising nature [2, 3, 6, 7]. In the military and defence sectors applications exist for Terahertz in remote sensing, from the identification of enemy targets to explosive devices [2, 3, 5, 4].

Numerous chemical compounds, in particular organic compounds, as well as biological samples have been found to possess molecular resonances within the Terahertz regime [2, 3, 8, 9]. These resonances, and THz radiation in general, are of great interest to manufacturing in particular for polymers [4] and pharmaceutical industries, not only for the non-destructive testing of their products by THz imaging, but also because of the precise determination of chemical composition of those products through THz-TDS.

Interest in THz applications in the semiconductor industry is also growing once again. THz devices enable the rapid characterisation of new materials and inspection of devices, as semiconductors are often transparent to THz throughout a large

portion of the regime; the electronic structure of the semiconductors can be inferred [10]; time-resolved studies of carrier lifetimes are possible [11]; carrier mobility and conductance mapping may be undertaken [12, 13] and hence the quality of new materials determined.

Solid-state quantum devices show great potential in that they are integrable with currently industrial scale silicon wafer processes and existing microelectronic devices. The operation of implanted silicon devices such as phosphorous in silicon (Si:P), calls for a source of intense narrowband and tunable THz frequency pulses. The control of spin orbitals that is essential for entangling neighbouring P atoms and developing quantum memory and read out is currently only available through Free Electron Laser facilities. Development of novel compact THz sources is necessary to bring these devices to fruition.

1.1 Historical Background of THz Science

1.1.0.1 Early Work

The first of what might be considered Infra-Red (IR) experiments were conducted by Italian Renaissance polymath Giambattista della Porta of Naples (1535-1615)[14]. In his book, Magiae Naturalis, published in 1589, della Porta describes the focusing of heat with a concave mirror. The only detectors available to him were his 'natural senses' [14]. Indeed Infra-Red radiation is well known to us all, we emit and can detect it in the heat of our bodies and the familiar warmth of the sun. Work proceeded slowly over the centuries aided by technological advances. Another Italian Renaissance scholar Santrio Santorio (1561-1636), often referred to as Sanctorius of Padua, known for his studies in medicine and biology and as a famous experimentalist, Sanctorius used the recently invented thermometer to observe the heating due to the sun's radiation [14]. In an early use of spectroscopy, famed Hanoverian Astronomer William Herschel (1738-1822), performed the first quantitative measurements of visible and Infra-Red radiation, using a glass prism and a set of thermometers. Herschel presented his results to the Royal Society in 1800

[15, 14].

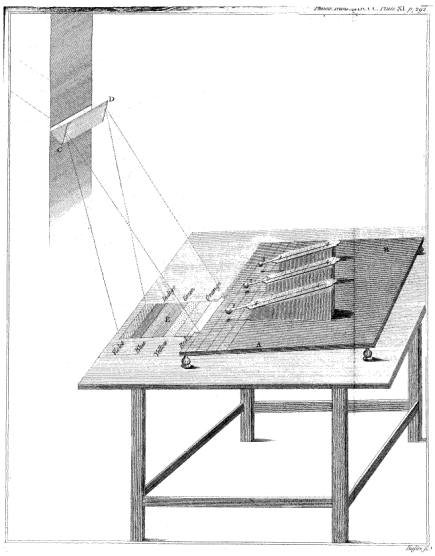

Figure 1.3: Sketch of Herschel's Experiment from his paper of 1800 [15]

1.1.0.2 The 1890's

Work in what we now know as the THz or the FIR regime began with a series of experiments in Berlin by Henrich Rubens and colleagues. They had been working with prismatic spectrometers to extend the range of understanding in the infrared spectrum, using the ionic crystals rock salt (NaCl), sylvine (KCl) and fluorite (CaF_2) [16, 14]. Rubins was later joined by American scientist Ernest Fox Nichols, professor of physics at Colgate University. Nichols found an anomalous change in reflectivity of quartz crystal, where over a narrow band (7-9 μm) where it increased, approaching the reflectivity of "burnished silver" [17]. We now know that this reflection is due to the Restrahlen Effect, the anomalous change in refractive index around the phonon band, leading to strong Fresnel reflections. Finding Restrahlen bands in other crystals, Rubens and Nichols quickly exploited the effect to build a plate spectrometer producing almost monochromatic light out to 50 μm [14, 18]. The previous limit of definite knowledge had been at about 9 μm [19]. Having opened up a new area of the electromagnetic spectrum, they set to work exploring the optical properties of a variety of materials in this range, documented in a series of

publications in 1897 [20, 21, 22]. Famously in "Heat Rays of Great wavelength" they first identified the existence of the "Terahertz Gap" [20, 18]. As the electromagnetic spectrum is continuous, the Terahertz Gap existed first as a gap in knowledge, a *terra incognita*, and later as a Ruben and Nichols pointed out a technological gap, that continues to the present day.

1.1.0.3 1910's - 1930's

Technological progress of THz devices remained slow prior to WWII, and only one significant source was developed in this period: the mercury arc lamp [23]. Mercury lamps proved boon to spectroscopy and became the work horse for the IR regime; a position it maintains to the present day. In 1911 Rubens and Beayer showed the utility of the new device as a FIR source [24, 14]. Used in conjunction with blazed gratings produced by Woods at John Hopkins University in 1910 [25], the mercury lamp was principally applied towards the study of absorption bands in gases [26, 27]. The development of new detectors however remained stalled, with Langley's room temperature Bolometer from 1800 [28] dominating.

Rubens was a major figure in the development of FIR science; of the 150 papers on the subject published in the 30 years from 1892 to his death in 1922, he was an author on all but 13 of them [14]. His work and its accuracy played a significant part in the developement of Planck's Radiation Law [14, 18]. Following Rubens' death Planck wrote: *"Without the intervention of Rubens the formulation of the radiation law, and consequently the formulation of quantum theory, would have taken place in a totally different manner, and perhaps even not at all in Germany"* [29].

In 1923, Nichols and colleagues succeed in closing the gap between the lower extent of the Mercury lamp 420 μm and "electric-waves," using Hertzian Oscillators to generate 220 μm light [30]. The following year overlap was further increased to 90 μm by Russian physicist Glagolewa Arkadiewa, who used brass filings as dipole sources [31].

1.1.0.4 1940's - 1950's

Over the course of the second World War huge amounts of energy was directed into the advancement of microwave technology and atmospherics studies to enable radar applications. Shortly after the war, Marcel Golay invented his famous "pneumatic infrared detector," [32] the Golay Cell, still in use today. From this point on, there was steady progress in developing sources and detectors [33, 34]. The lower end of the THz regime was more accessible through advances in high frequency mm-wave sources e.g. klystrons [35, 36, 37], magnetrons [37] and BWO's [38, 39], mixers and multipliers [40, 41, 42, 43], built upon the war time radar work. The war time development of computing also had a major impact on the field. In 1951 at Cambridge University, Fellgett described in his thesis the use a computed Fourier transform spectrometer [44], this was soon extended into the FIR [45] and by 1957 commercial Fourier Transform Infra-Red Spectroscopy (FTIR) instruments were available [46, 47].

As the post-war period drew to a close, 1959 saw the development of first convenient cooled bolometer, the Carbon Bolometer [48] and a photoconductive detector for the FIR [49]. Modern Spectroscopy had arrived.

1.1.0.5 1960's - 1970's

The 60's and 70's was an era of massive growth for THz science, with more than 10,000 papers published. A range of THz / mm-wave sources sources and detectors that we are familiar with today were developed: electronic devices including Gunn [50], IMPATT [51, 52] and tunnelling diodes [53], high power electron beam devices [54] and the Free Electron Laser [55], bolometric detectors including n-InSb electron bolometer [56], Ge bolometer [57], Si composite bolometer, pyroelectric detector [58], and new photoconductive FIR detectors [59]. In large part, the growth was driven by the semiconductor industry and its need to understand the impurities and electronic structure of its materials. Applications in other areas included: Cosmic Microwave Background (CMB) studies in astronomy [60, 61, 62], investigations of condensed-matter physics, and early biological work [18, 14].

However what really opened up the THz field was the invention of the laser; arguably the most significant invention of the period, directly contributing to 11 Noble prizes. While Maiman succeeded in demonstrating the first and in the process inventing a new type of laser [63], it would be incorrect to ascribe the laser's invention to a single individual. Beginning with Einstein's work on the photoelectric effect [64] and later on the quantum theory of light, predicting the stimulate emission of light [65, 66], numerous individuals and groups were involved in the development of the laser [67, 68, 69, 70, 71, 72], often from spectroscopy backgrounds and in particular spectroscopy in the mm-wave and FIR [73, 74]. It is telling of this origin that in the early years the laser was alternatively known as the "Optical MASER" [75], Townes stated that part of the motivation for his work was to develop a molecular generator for the THz band [76] and in 1958 Prokhorov suggested a laser for generation of Far Infra-Red waves [71]. Following Maiman's demonstration, laser development and invention came thick and fast: 1960, the Helium Neon (HeNe) laser [77]; 1961, 1st commercial lasers [78], Nd^{+3} lasers [79, 80], diode lasers [81, 82, 83, 84]; 1962, Q-Switching [85]; 1963, mode-locking [86]; 1964, Neodymium:Yttrium Aluminium Garnet Nd:$Y_3Al_5O_12$ (Nd:YAG) Lasers [87], Ar^+lasers [88], Carbon Dioxide (CO_2) lasers [89].

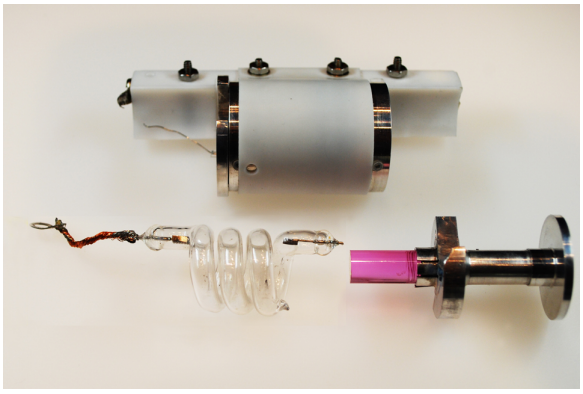

Figure 1.4: Components of Maiman's original Ruby Laser(en.wikipedia.org).

Laser based optical generation has resulted the widest variety of THz sources including: quantum cascade lasers, quantum dot devices and optically pumped THz lasers, p-doped germanium lasers and a further range through the use of optical non-

linearities such as photoconductive dipole antennae, optical rectification, difference frequency generation and the optical parametric generation [2, 90]. This thesis is concerned with the last.

1.2 Thesis Outline

A table top, high power, narrow bandwidth, broadly tunable, coherent source of Terahertz (30-1000 μm) radiation is highly desired for novel applications in quantum, security and biomedical technologies; in addition to the traditional areas of spectroscopy, imaging and non-destructive testing (NDT). In spite of intensive research over many decades such a device remains elusive. The clear demand for such a source is the driving force of this D.Eng project, which aims to identify, characterise and test a material that enables the construction of a widely tunable multi-terahertz optical frequency conversion source and, ultimately an Optical Parametric Oscillator, allowing ready access to higher frequencies. Current table top source technologies in this area of THz applications, i.e. Photoconductive Dipole antennae and Lithium Niobate ($LiNbO_3$) Optical Parametric Oscillator (OPO)'s, are limited to 3-4 THz [3, 90] and air-plasma devices are often prohibitively expensive due to the pump laser requirements [91, 92].

Sulphur-doped solid solution ε-polytype Gallium Selenide ($GaSe_{x-1}S_x$) crystals have the potential for efficient generation of THz radiation and broadband tunability throughout the majority of this regime; as a result of the prodigious linear and nonlinear optical properties of the Gallium Selenide parent crystal. Close control of doping and the crystal growth process has enabled the manufacture of high quality nonlinear crystals, where the optical properties may be engineered and the mechanical properties vastly improved, thus overcoming many of the physical issues that have frustrated the widespread adoption of GaSe despite being *"the best nonlinear optical material ever used"* (Shi 2004) [93] for laser frequency down conversion to the THz regime.

In order to fully exploit the potential of $GaSe_{x-1}S_x$ crystals and successfully design efficient sources for THz generation the optical properties of these crystals

must be accurately determined and their transformation with doping well understood. The work in this thesis aims to accurately determine the optical properties of GaSe, GaS and $GaSe_{x-1}S_x$ crystals in the THz regime to enable this exploitation. The literature relating to $GaSe_{x-1}S_x$ is highly scattered and often contradictory. Details relating to the e-wave properties of GaSe and $GaSe_{x-1}S_x$ are extremely limited, we were unable to find the THz absorption and dispersion spectra of GaS in the literature. Though a number of Sellmier equations for the crystals exist, these are again often in contradiction, particularly so for the THz regime, seriously hindering the utilisation of these crystals.

Chapter 2 examines the early development of nonlinear optics from Franken's observation of Second Harmonic Generation (SHG) [94] and the basic theory of nonlinear optics in the early 1960's through to the first era of THz and FIR source development using nonlinear optics in the late 1960's and 70's. The requirements for a successful, efficient OPO are outlined through a review of their theory of operation. Optical materials for nonlinear optical frequency conversion in the mid to far-IR and THz regimes are reviewed with the requirements for an OPO in mind.

Chapter 3 determines the linear refractive index (n) and absorption coefficient (α) for both the o and e waves in the THz regime (0.1- 4.5 THz) by direct measurement using Terahertz - Time Domain Spectroscopy for GaSe, and a dense set of $GaSe_{x-1}S_x$ crystals (x = 0.05, 0.11, 0.22, 0.29, 0.44) fabricated with facets perpendicular to the c axis. Measurements of THz dispersion and absorption properties of THz crystals are performed for the first time. We determine the birefringence for GaSe, GaS and $GaSe_{x-1}S_x$ crystals, and recommend from existing Sellmeier equations those that best fit the experimental data. The transformation of the optical properties of the crystals and their phonon structure with respect to doping content is studied. We examine the sources of inaccuracy in the THz-TDS measurements of high refractive index birefringent crystals and propose a set of criteria for the selection of adequate data.

Chapter 4 investigates the possibility of engineering the transparency windows in $GaSe_{x-1}S_x$ crystals by means of doping. The phonon bands of the GaSe, GaS

and $GaSe_{x-1}S_x$ crystals are examined by FTIR and Raman spectroscopy and their transformation with respect to doping is studied. For the first time we determine the absorption coefficients of the main phonon peak in the set of $GaSe_{x-1}S_x$ crystals using thin (10s of μm) exfoliated samples.

Chapter 5 reports on attempts to determine the key nonlinear optical properties d_{eff} and n_2 in the FIR and THz regimes for GaSe and $GaSe_{x-1}S_x$ crystals by the classic Maker fringe and z-scan methods. Measurements of these properties, which are crucial for efficient nonlinear optical frequency conversion, have to date been largely confined to around 1.064 μm. Measurements are made using the Felix free electron laser facility in Nijmegen as a source.

Chapter 6 reports on the conclusions reached for the work of this thesis. We describe ongoing and future work to generate THz radiation in $GaSe_{x-1}S_x$ crystals using both difference frequency generation and the development of an optical parametric oscillator that will exploit these new results.

1.3 Summary

The aim of the work presented in this thesis was to develop a robust understanding of the linear and nonlinear optical properties of $GaSe_{x-1}S_x$ crystals to enable their successful exploitation in Difference Frequency Generation (DFG) and OPO devices at THz frequencies, and where possible, clarify discrepancies in the literature. The work includes studies of GaSe, GaS & $GaSe_{x-1}S_x$ crystals at THz and FIR frequencies by means of THz-TDS, FTIR and Raman spectroscopy. The absorption and dispersion spectra for the crystals are presented and the effect of dopant concentration is examined, enabling the identification of optimal doping and best existing Sellmeier equations. Furthermore the development of improved Sellmeier equations and phase matching curves is facilitated. The possibility of engineering optical properties of the crystals though doping is examined. The nonlinear optical properties of the crystal are studied in the THz and FIR regimes, by the classic z-scan and Maker fringe techniques, to understand further the possibilities of pumping GaSe devices at long wavelengths.

Chapter 2

THz OPO Technology

"The study of non-linear physics is like the study of non-elephant biology."

— Stanislaw Ulam, mathematician

2.1 Introduction to Nonlinear Optics

In this chapter we will examine the early development of nonlinear optics from Franken's observation of SHG [94] through to the early nonlinear optical sources of THz. A brief introduction to the theory of nonlinear optics is given and the key parameters for efficient DFG and OPO devices are outlined through a review of their theory of operation. Optical materials for nonlinear optical frequency conversion in the mid to far-IR and THz regimes are reviewed with the requirements of DFG and OPO operation in mind.

Since the laser's, invention the development of a broadly tunable, coherent source of radiation has been highly sought after. However, the laser for all its positive features, is not well-suited to broad tuning. Conventionally, lasers oscillate at single discrete frequencies, these frequencies are dependent upon the energy transitions in the gain media, and in general, they are neither widely nor continuously tunable. However, the high intensity of the optical frequency electric fields generated by lasers, through Non Linear Optics (NLO), have enabled the development of OPOs that can provide broadband, continuously tunable, efficient, high power, sources of coherent radiation. Intense DC E-fields, available to 19^{th} Century experimenters,

allowed some nonlinear optical phenomena, e.g. Kerr Effect, to be observed [95]; however, it was the advent of the laser that really brought the field to life [96]. In

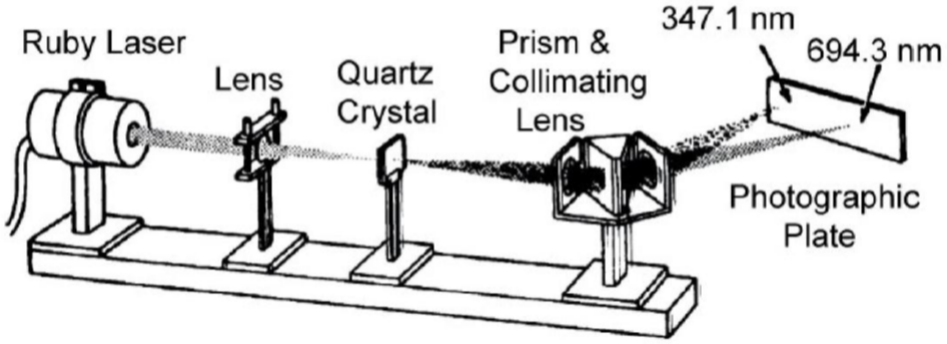

Figure 2.1: Schematic of the setup for Franken's experiment [94].

1961, shortly after Maiman's demonstration of the laser, Franken *et al* passed the 694 nm beam of a red ruby laser through a quartz crystal, into a monochromator and projected the output on to a photographic plate. Examination of this photograph revealed a remarkable thing: there were two spots. One spot corresponded to the frequency of the laser ω_1 and the other occurred at twice the laser frequency, $\omega_2 = 2\omega_1$, or half the wavelength at 347 nm in the ultraviolet [94]. Thus, nonlinear optics was born with a demonstration of what we call SHG.

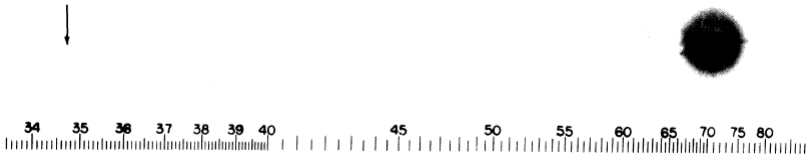

Figure 2.2: Original figure from Franken's experiment with the Second Harmonic Generation spot missing [94, 96].

To explain this phenomenon, let us consider an electro-magnetic wave, in this case a laser beam, propagating through a dielectric material. As the wave propagates, it produces variations in the distribution of electric charges within the material, both spatially and temporally. This is most easily observed as the generation of electric dipoles, leading to the polarisation of the material. Generally, these dipoles

respond in a linear fashion to the E-fields oscillation and the wavelength propagating through the material remains unchanged [97, 98, 99]. From Maxwells equations, the electric displacement D is described by Eqn 2.1.

$$D = \varepsilon_0 E + P \tag{2.1}$$

Where ε_0 is the permittivity of free space, E is the electric field strength and P is the polarisation. The polarisation P experienced by a material is dependent upon the incident E-field and can be described by Eqn 2.2 [100].

$$P = \varepsilon_0 \chi E \tag{2.2}$$

where χ is the linear susceptibility. As the E-field flux, i.e. the intensity of the incident light, increases, this representation as a simple linear relationship breaks down. The effect is normally quite small and, for all intents and purposes, it is negligible in everyday life. To illustrate this let us consider the atomic field strength on an electron is of the order of E = 10^9 V/cm^2, so in order for an effect to be noticeable the applied E-field has to have a large magnitude, say E = 10^5 V/cm^2. This is equivalent to a light beam with an intensity on order of $10^1$0 W/cm^2. In a 10 cm kettle this would boil a litre of water in approximately 10$^-$6 of a second. Intensity I is related to the E-field by Eqn 2.3

$$I = x|E|^2 \tag{2.3}$$

where x is a constant dependent upon the units chosen in the definition. However, if a high intensity optical source such as a focused laser beam is projected on to the material, the required variation in the E-field is approached and deviations from the linear model begins to become apparent. At high intensities the linear representation is no longer valid, but may be expanded out into a power series in E, to model the dipole response as in Eqn 2.4 [100].

$$P = \varepsilon_0(\chi^{(1)}\mathbf{E} + \chi^{(2)}\mathbf{E}^2 + \chi^{(3)}\mathbf{E}^3...) \tag{2.4}$$

where $\chi^{(2)}$ and $\chi^{(3)}$ are the second and third order nonlinear susceptibility tensors respectively. If the oscillating E-field is defined by Eqn 2.5

$$\mathbf{E}(t) = \mathbf{E}_\omega cos(\omega t) \tag{2.5}$$

where ω is the frequency of oscillation and t is time, restricting ourselves to the first two terms only, then Eqn 2.4 can be rewritten as Eqn 2.6 [100]

$$P = \varepsilon_0(\chi^{(1)}\mathbf{E}_\omega cos(\omega t) + \chi^{(2)}\mathbf{E}_\omega^2 cos^2(\omega t) + ...) \tag{2.6}$$

Using the trigonometric identity

$$cos^2(\theta) = \frac{1}{2}(1 + cos(2\theta)) \tag{2.7}$$

this can be recast as :

$$P = \frac{1}{2}\varepsilon_0\chi^{(2)}\mathbf{E}_\omega^2 + \varepsilon_0\chi^{(1)}\mathbf{E}_\omega cos(\omega t) + \frac{1}{2}\varepsilon_0\chi^{(2)}\mathbf{E}_\omega^2 cos(2\omega t) + ... \tag{2.8}$$

The first term in Eqn 2.8 is a DC term; the second term describes a wave oscillating at ω i.e. linear propagation; and the third term describes a wave oscillating at 2ω, i.e. nonlinear second harmonic generation [100]. The generation is nonlinear in that the amplitude of 2ω wave is proportional to E^2.

$\frac{1}{2}\varepsilon_0\chi^{(2)}\mathbf{E}_\omega^2$	DC term
$\varepsilon_0\chi^{(1)}\mathbf{E}_\omega cos(\omega t)$	Linear propagation term
$\frac{1}{2}\varepsilon_0\chi^{(2)}\mathbf{E}_\omega^2 cos(2\omega t)$	SHG term

$\chi^{(2)}$, the second order nonlinear susceptibility, is responsible for many nonlinear effects including: second harmonic generation, shown above, sum and difference frequency generation, and parametric amplification, which is discussed below. $\chi^{(2)}_{ijk}$ is a rank 3 tensor with 27 coefficients [100]; this can be reduced to a 3 x 6 tensor,

known as the d-tensor, by a series of symmetry arguments where the material is lossless. In many nonlinear materials the majority of the d-tensor coefficients are equal to zero thus reducing the complexity of calculations and if the frequency of the interaction is less than the lowest resonant frequency of the material system, $\chi^{(2)}$ can be assumed to be a constant [101].

The d-tensor is related to $\chi^{(2)}$ by the below relations, where the $\frac{1}{2}$ factor is a legacy of convention.

$$d_{ijk} = \frac{1}{2}\chi^{(2)}_{ijk} \tag{2.9}$$

It is then possible to write the nonlinear polarisation for SHG as a sum over the components of the d-tensor where

$$P_i(\omega_n + \omega_m) = \varepsilon_0 \sum_{jk} \sum_{(nm)} 2 d_{ijk} E_j(\omega_n) E_k(\omega_m) \tag{2.10}$$

Table 2.1: Reducing d_{ijk} to contracted d_{il} notation

jk	11	22	33	23,32	31,13	12,21
l	1	2	3	4	5	6

The d-tensor is presented below in its full form in Eqn 2.11. By Kleinman symmetry arguments, where the medium is lossless and the frequencies of the incident beams are less than the lowest resonance of the material system, it can be further reduced to 10 independent elements as given below and the notation contracted to

the d_{il} form as given in Table 2.1 [101].

$$d_{ijk} = \begin{pmatrix} d_{111} & d_{112} & d_{113} \\ d_{121} & d_{122} & d_{123} \\ d_{131} & d_{132} & d_{133} \\ d_{211} & d_{212} & d_{213} \\ d_{221} & d_{222} & d_{223} \\ d_{311} & d_{312} & d_{313} \\ d_{321} & d_{322} & d_{323} \\ d_{331} & d_{332} & d_{333} \end{pmatrix} \equiv d_{il} = \begin{pmatrix} d_{11} & d_{12} & d_{13} & d_{14} & d_{15} & d_{16} \\ d_{21} & d_{22} & d_{23} & d_{24} & d_{25} & d_{26} \\ d_{31} & d_{32} & d_{33} & d_{34} & d_{35} & d_{36} \end{pmatrix} \tag{2.11}$$

$$d_{il} = \begin{pmatrix} d_{11} & d_{12} & d_{13} & d_{14} & d_{15} & d_{16} \\ d_{21} & d_{22} & d_{23} & d_{24} & d_{25} & d_{26} \\ d_{31} & d_{32} & d_{33} & d_{34} & d_{35} & d_{36} \end{pmatrix} = \begin{pmatrix} d_{11} & d_{12} & d_{13} & d_{14} & d_{15} & d_{16} \\ d_{16} & d_{22} & d_{23} & d_{24} & d_{14} & d_{12} \\ d_{15} & d_{24} & d_{33} & d_{23} & d_{13} & d_{14} \end{pmatrix} \tag{2.12}$$

The nonlinear polarisation from Eqn 2.10 can be rewritten as a matrix equation in d_{il} for SHG in the form

$$\begin{pmatrix} P_x(2\omega) \\ P_y(2\omega) \\ P_z(2\omega) \end{pmatrix} = 2\varepsilon_0 \begin{pmatrix} d_{11} & d_{12} & d_{13} & d_{14} & d_{15} & d_{16} \\ d_{21} & d_{22} & d_{23} & d_{24} & d_{25} & d_{26} \\ d_{31} & d_{32} & d_{33} & d_{34} & d_{35} & d_{36} \end{pmatrix} \times \begin{pmatrix} E_x(\omega)^2 \\ E_y(\omega)^2 \\ E_z(\omega)^2 \\ 2E_y(\omega)E_z(\omega) \\ 2E_x(\omega)E_z(\omega) \\ 2E_x(\omega)E_y(\omega) \end{pmatrix} \tag{2.13}$$

For fixed polarization and propagation directions it is possible to express the nonlinear polarization through a scalar relationship and in the case of SHG it is given by Eqn 2.14.

$$P(2\omega) = 2\varepsilon_0 d_{eff} E(\omega)^2 \tag{2.14}$$

The crystal structure and symmetry further reduce the number of independent and non-vanishing components in d_{il} and in the case of ε-GaSe, which is a hexagonal

crystal of the $\bar{6}m2$ / D^1_{3h} symmetry [102], d_{il} is reduced further to

$$d_{il} = \begin{pmatrix} - & - & - & - & - & -d_{22} \\ -d_{22} & d_{22} & - & - & - & - \\ - & - & - & - & - & - \end{pmatrix} \tag{2.15}$$

where there is only one independent component d_{22} and $d_{16} = -d_{22}$. Hence, the effective nonlinear coefficient for the interaction depends on the polarisation of the beam and the on the θ and ϕ angles as given by [103, 104]

$$\text{Type I (e-oo)} \quad d_{eff} = d_{22}cos(\theta)sin(3\phi) \tag{2.16}$$

$$\text{Type II (e-oe)} \quad d_{eff} = d_{22}cos^2(\theta)sin(3\phi) \tag{2.17}$$

where $0 \leq \theta \geq \pi$ is the polar angle relative to the crystal c-axis, and $0 \leq \phi \geq 2\pi$ is the azimuthal about the crystal c-axis.

In centro-symmetric or isotropic material, such as glass and the β-polytype of GaSe which has , the $\chi^{(2)}$ tensor is equal to zero and therefore second order effects are not possible [100].

The conversion efficiency of the interaction in Franken's experiment was extremely low 1:10^{-9} [105], and so the latter spot was extremely faint. Bloembergen relates the anecdote, *"The editorial office of Physical Review Letters removed these spots [sic] as undesirable smudges, evidence was thus erased from the original publication. The markable fact is that an erratum never appeared"* [96].

The reason for this poor efficiency was the material dispersion, i.e. frequency dependent refractive index, of the nonlinear crystal. The fundamental frequency ω_1 of the ruby laser and the second harmonic ω_2 propagate through the nonlinear crystals at different velocities, moving in and out of phase with each other. So the amplitude of the second harmonic signal grows and decays in sinusoidal fashion, see Figure 2.3, resulting in only a tiny fraction of the length of the crystals being responsible for the generation of the observed second harmonic radiation. We will address these points and phase matching mathematically for the three wave case

below.

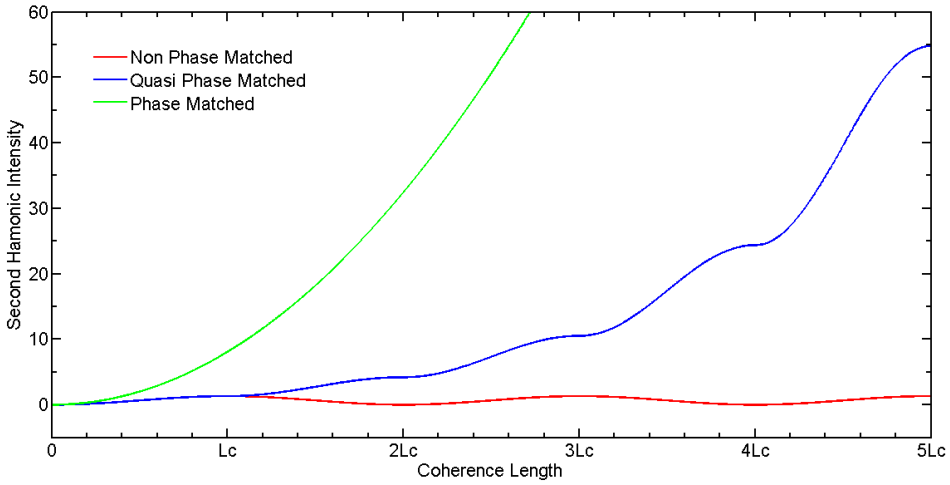

Figure 2.3: Comparative growth of the optical power generated through nonlinear means for Phase Matched (green), Quasi-Phase-Matched (blue) and Non Phase Matched (red) set ups as they propagated through the nonlinear crystal.

This was soon overcome by Giordmaine [106] and Maker *et al* [107], who exploited the birefringence of anisotropic crystals. In birefringent crystals the refractive index is dependent upon the polarisation of the light, varying between the refractive indices of the orthogonally polarised ordinary and extraordinary rays, i.e. ordinary refractive index ordinary refractive index (n_o) and extraordinary refractive index n_e respectively. In these crystals the refractive index of the extraordinary ray n_e is also a function of the angle of propagation, which can be described by an ellipsoid. If the ellipsoid for both $n_o(\omega_1)$ and $n_e(\omega_2)$ are overlaid on one another, then some direction(s) could be found where they intersect, i.e. the refractive indices are equal in magnitude as shown in Figure 2.4 . When propagating along this direction the beams are said to be phase matched.

This phase matching condition is, in general, unique for each particular set of ω_1 and ω_2 and thus is sometimes referred to as critical, or more generally, Birefringent Phase Matching (BFM). Both ω_1 and ω_2 will now propagate together in phase, and the intensity of ω_2 will grow with the square of the distance travelled. Both Giordmaine and Maker demonstrated phase matching in Potassium Dihydrogen Phosphate KH_2PO_4 (KDP), showing that nonlinear optics could become a prac-

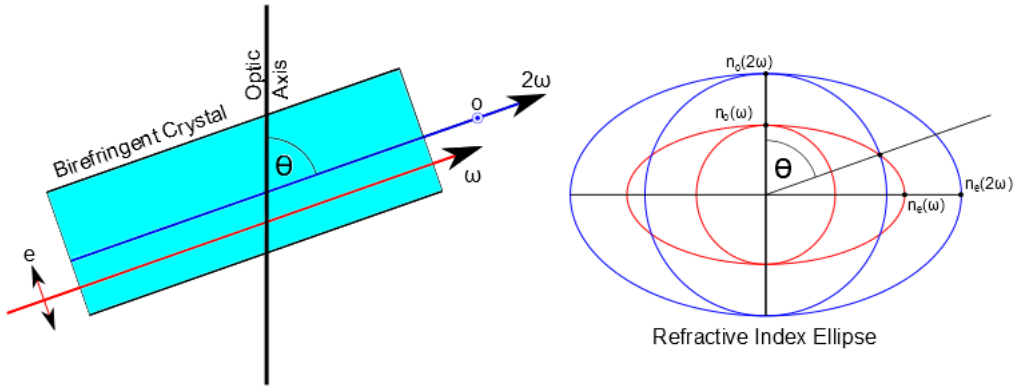

Figure 2.4: Schematic of Type I phase matching for SHG in a positive uniaxial birefringent crystal.

tical source of coherent radiation rather than an interesting, if impractical, physical curiosity.

Subsequently, Bass *et al* demonstrated Sum Frequency Generation (SFG) in Triglycine Sulfate, using two Ruby Lasers one of which was liquid nitrogen cooled shifting the frequency of oscillation by 1 nm [108]. DFG had been initially suggested by Laine in 1961 [109], but it was some time before it could be realised.

Following these initial reports by Franken [94] and Bass [108] working at University of Michigan Ann Arbour, significant effort was expended and rapid development achieved in both the theoretical underpinning of nonlinear optical generation and experimental advances. While there were workers in various groups on both sides of the Atlantic, much of this early development was driven by those at Bell Labs, New Jersey and Moscow State University.

In their seminal 1962 paper, Armstrong, Bloembergen, Ducuing and Pershan [110] introduced, amongst other things, an alternative scheme to achieve phase-matching. Quasi Phase Matching (QPM) as it is now known, was intended as a means to circumvent problems relating phase matching in cases of too much or too little birefringence. We can see in the non-phase-matched case (Figure 2.3) that as the ω_1 beam propagates through the crystal the amplitude of $\mathbf{E}_{\omega_2}$ grows until $\Delta k = \frac{\pi}{2}$ and then decreases again until $\Delta k = \pi$ and so on and so forth every $\Delta k = \frac{m}{2}\pi$. The energy moving back and forth between the $\boldsymbol{E}_{\omega}$ and $\boldsymbol{E}_{\omega_2}$ waves. If however we could divide the crystal into $\frac{\pi}{2}$ long domains and alternatively rotate each by π

then the amplitude of $\boldsymbol{E}_{\omega_2}$ would continuously grow. Bloembergen went on to patent the idea, however the engineering was extremely intricate, practical orientation of micron thin layers required new growth techniques, so by the time it was realised 25 years later in 1988 using $LiNbO_3$ [111, 112, 113], the 20 year patent had expired [105].

The idea of parametric amplification and generation of tunable light arose and was analysed independently by several authors in 1962; by Kingston [114], Armstrong et al. [110] and by Akhmanov & Khokhlov [115]; and Kroll proposed a tunable OPO [116]. These devices took some time to realise.

The importance of phase-matching for efficient nonlinear generation was further emphasised by Boyd *et al* [117], and demonstrated in $LiNbO_3$ crystal, which had begun to receive much attention as the preferred crystal for nonlinear generation due to its large negative birefringence ($\Delta n = 0.085$), and nonlinear coefficient $d_{31} \approx$ -4.5 pm/V , which was the greatest of any phase-matchable material studied up to that point. [117].

In 1965, Wang and Racette observed parametric amplification in a 3-wave mixing experiment, i.e. an Optical Parametric Amplifier (OPA). The same year Giordmaine and Miller demonstrated the first OPO, three years after its initial proposal. The tunable IR (0.97 - 1.15 μm) OPO was implemented in a $LiNbO_3$ crystal, pumped at 0.529 μm by a frequency doubled Q-switched Nd:CaWO laser. Akhmanov *et al*, in Moscow State University, soon followed with another tunable IR (0.958 - 1.178 μm) OPO in KDP [118]. Boyd and Askin further extended the theoretical understanding on oscillation threshold and the effects of temperature, electric field and pump frequency variation, and proposed that it would be possible to develop Continuous Wave (CW) OPOs with low thresholds $\backsim$ 10s mW [119].

Further development of the theoretical understanding followed, conducted by: Yariv (1966), on parametric oscillation, frequency conversion and laser modulation [120]; Yariv and Louisell (1966), on oscillation threshold, Manley-Rowe conditions, power output and index matching; and others [121]. Boyd and Kleinman (1968) developed a complete theory of parametric generation for focused Gaussian laser

beams, providing examples for Tellurium (Te), and $LiNbO_3$ [122].

The development of OPO's devices was equally rapid. Using a set-up similar to Akhmanov's [118], Miller and Nordland in 1967 demonstrated an OPO using $LiNbO_3$ [123]. The same year, Kreuzer demonstrated for the first time an OPO pumped without SHG, using the fundamental of a ruby laser at 694.3 nm [124]. Tuning was achieved by means of the electro-optic effect in $LiNbO_3$ [124]. The first singly resonant OPO was demonstrated by Bjorkholm in 1968 [125]. The same year, and two years after its proposal, Smith *et al* first demonstrated a CW OPO in Barium Sodium Niobate ($Ba_2NaNb_5O_{15}$), operating in the Near Infra-Red (NIR) (0.98 - 1.06 μm) pumped at 0.532 μm by a frequency doubled Nd:YAG [126], and were quickly followed by Byer *et al*, who demonstrated the first visible (0.680-0.705 μm) OPO, in $LiNbO_3$ pumped at 0.514 μm by an Ar^+:Laser [127].

2.1.1 Early THz / FIR Generation by Nonlinear Optics

Optical Parametric Amplifiers were first reported by Patel (1966), where a 17.888 μm signal from a neon laser was amplified in a Tellurium, crystal pumped by a CO_2 laser at 10.6 μm [128]. The first report of tunable Terahertz radiation generated from a parametric source with a Near Infra-Red pump was by Yarborough et al (1969) [129]. They observed parametric radiation from a $LiNbO_3$ crystal, having no mirrors and only polished facets, tunable from 2-6 THz, using a nanosecond Q-switched ruby pump laser. Non-collinear Phase Matching conditions were employed. A corner was cut from the crystal perpendicular to the direction of propagation of the THz beam to reduce the optical path within the crystal, as $LiNbO_3$ is strongly absorbing in the THz regime, and to improve coupling to free space, reducing losses associated with the large refractive index mismatch between the crystal and air [129].

Fixed frequency DFG was first observed by Zernike & Berman (1965) [130] using two NIR lines, 1060 nm and 1071.5 nm from a neodymium glass laser, in quartz crystal, resulting in radiation at 3 THz. Yajima and Inoue (1968) [131] demonstrated DFG at 0.87 THz by means of the R1 and R2 lines from a single ruby laser in Zinc Telluride (ZnTe) crystal [131]. Coffinet and De Martini (1968) [132] described for

the first time the observation of DFG in Gallium Phosphide (GaP) crystal at 11 THz, using a ruby laser [132]. Tunable Terahertz DFG between 0.03-0.24 THz was first demonstrated by Faries et al (1969) [133] using temperature-tuned ruby lasers. Both Quartz and $LiNbO_3$ were used as the nonlinear medium, with frequency tuning achievable through the rotation of the crystals [133]. Zernike (1969) [134] described temperature dependent phase matching at 3 THz, for DFG between the 1047 and 946 cm^{-1} lines of a CO_2 laser, in an Indium Antimonide (InSb) crystal. While DFG is a viable means of producing THz radiation, it suffers from a number of drawbacks: first, the system is more complicated and often more expensive due to the requirement for two pump sources; and second, it is less efficient than Optical Parametric Generation (OPG), which can be readily used in an intra-cavity set-up. DFG experiments however, provide useful data about the optical properties of various crystals, phase matching and their tunable ranges, which may be used to inform choices for potential OPO's.

Piestrup, Fleming & Pantell (1975) [135], following on from Yarborough *et al*'s work [129], though using a resonator in this instance, reported on an extended continuously tunable range of 0.3-3 THz in a $LiNbO_3$ crystal pumped by a ruby laser.

Bianchi, Ferrario & Musci (1978) [136], described tunable optical down conversion between 4-12 μm of the output from a $LiNbO_3$ OPO in a GaSe crystal. Oudar, Kupecek & Chemla (1979) [137] described tunable DFG between a Nd:YAG and an IR dye laser in a GaSe crystal between 9-19 μm. After this initial rush of growth, the further development of optical nonlinear THz sources through DFG and OPOs [90, 138] stalled. There are a range of reasons why: the difficulty in acquiring new crystals, the emergence of tunable Dye Lasers, early over-optimism on the part of various authors leading to a general scepticism [138], which would return to haunt THz in the late 2000's [139], and the availability of molecular gas lasers in the submillimetre regime [90].

2.2 Operation of OPOs

2.2.1 Sum and Difference Frequency Generation

We will briefly describe the operation of an efficient OPO following the analysis of Boyd[101] and Keochner [100]. If two electromagnetic waves of similar intensities, but differing frequencies ω_1 and ω_2, are incident upon a second order optical nonlinear material, a third wave with a frequency ω_3 will be created, where $\omega_3 = \omega_1 + \omega_2$, in the case of sum frequency generation, or similarly, $\omega_3 = \omega_1 - \omega_2$ in the case of difference frequency generation. We can describe this mathematically as below, first examining the E-field [100]:

$$\mathbf{E} = \mathbf{E}_1 + \mathbf{E}_2 = \mathbf{E}_1 cos(\omega_1 t) + \mathbf{E}_2 cos(\omega_2 t) \tag{2.18}$$

and

$$P_{\chi^{(2)}} = b\chi^{(2)}\mathbf{E}^2 = b\chi^{(2)}[\mathbf{E}_1 cos(\omega_1 t) + \mathbf{E}_2 cos(\omega_2 t)]^2 \tag{2.19}$$

where b is a constant. This can be written as:

$$P_{\chi^{(2)}} = b\chi^{(2)}\left\{\mathbf{E}_1^2 cos^2(\omega_1 t) + \mathbf{E}_2^2 cos^2(\omega_2 t) + \mathbf{E}_1\mathbf{E}_2[cos(\omega_1 t + \omega_2 t) + cos(\omega_1 t - \omega_2 t)]\right\} \tag{2.20}$$

Resulting in 3 terms in, using trigonometric identity $cos^2\theta = \frac{1}{2}(1 + cos\,2\theta)$ as before, $\mathbf{E}$, the first two terms describe the DC and second harmonic component for both ω_1 and ω_2, while the last term describes two new oscillating waves, one $\omega_1 + \omega_2$ at the sum frequency and the other $\omega_1 - \omega_2$ at the difference frequency [97, 100], such that

$$\mathbf{E}_3 = \mathbf{E}_1\mathbf{E}_2 cos(\omega_1 t - \omega_2 t) \tag{2.21}$$

2.2.2 Difference Frequency Generation

A plane wave oscillating at ω_3 and propagating in the +z through a nonlinear medium can be describe as

$$\mathbf{E}_3(z,t) = A_3 e^{i(k_3 z - \omega_3 t)} + ... \tag{2.22}$$

where A the amplitude of the wave is constant and $k_3 = \dfrac{n_3\omega_3}{c}$ and for convenience (and as is convention) using the scalar approximation, n_3 is the linear refractive index of the medium appropriate for polarization state of ω_3.

$$\mathbf{P}_3(z,t) = P_3 e^{i(k_3 z - \omega_3 t)} + ... \tag{2.23}$$

$$\begin{aligned} P_3 &= b\chi^{(2)}\mathbf{E}_1\mathbf{E}_2 \\ &= 4\varepsilon_0 d_{eff}\mathbf{E}_1\mathbf{E}_2 \\ &= 4\varepsilon_0 d_{eff} A_1 A_2 e^{i(k_1 - k_2)z} \end{aligned} \tag{2.24}$$

These Eqns 2.22, 2.23 & 2.24, can be substituted into the wave equation for a lossless medium

$$\nabla^2\mathbf{E}_n - \frac{\varepsilon^1(\omega_n)}{c^2}\frac{\partial^2\mathbf{E}_n}{\partial t^2} = \frac{1}{\varepsilon_0 c^2}\frac{\partial^2\mathbf{P}_n^{NL}}{\partial t^2} \tag{2.25}$$

As the field varies only in the z direction ∇^2 can be reduced to $\dfrac{d^2}{dz^2}$.

$$\frac{d^2A_3}{dz^2} - 2ik_3\frac{dA_3}{dz} = \frac{-4d_{eff}\omega_3^2}{c^2}A_1A_2e^{i(k_1-k_2-k_3)z} \tag{2.26}$$

In the slowly varying amplitude approximation, where $\left|\ \frac{d^2A_3}{dz^2} \ll k_3\frac{dA_3}{dz^2}\ \right|$, Eqn 2.26 becomes

$$\frac{dA_3}{dz} = \frac{2id_{eff}\omega_3^2}{k_3c^2}A_1A_2e^{i\Delta kz} \tag{2.27}$$

Where $\Delta k = k_1 - k_2 - k_3$, the wavevector mismatch. Eqn 2.27 is a coupled amplitude equation which describes the variation in the amplitude of ω_3 with respect to ω_1 &

ω_2 as it propagates. Similar coupled amplitude equations can be derived for ω_1 & ω_2 describing their spatial variation.

$$\frac{dA_2}{dz} = \frac{2id_{eff}\omega_2^2}{k_2c^3}A_3A_1^*e^{i\Delta kz} \tag{2.28}$$

$$\frac{dA_1}{dz} = \frac{2id_{eff}\omega_1^2}{k_1c^3}A_3A_2^*e^{i\Delta kz} \tag{2.29}$$

To examine the behaviour of Eqn 2.27 we differentiate it with respect to z such that it becomes

$$\frac{d^2A_3}{dz^2} = \frac{4id_{eff}\omega_3^2\omega_2^2}{k_3k_2c^2}A_1A_1^*A_3 \equiv \kappa^2A_3 \tag{2.30}$$

where κ^2 is the real coupling constant. The solution to Eqn 2.30 has the form

$$A_3 = P\,sinh\,\kappa z + Q\,cosh\,\kappa z \tag{2.31}$$

where P and Q are integration constants. If we assume the boundary conditions $A_3(0) = 0$ and $A_2(0)$ has an arbitrary value, then a solution can be found that satisfies the boundary conditions where

$$A_2(z) = A_2(0)cosh\,\kappa z \tag{2.32}$$

$$A_3(z) = i\left(\frac{n_2\omega_3}{n_3\omega_2}\right)^{\frac{1}{2}}\frac{A_1}{\mid A_1 \mid}A_2^*(0)sinh\,\kappa z \tag{2.33}$$

Thus A_3 and A_2 both grow monotonically as they propagate in the +z direction and

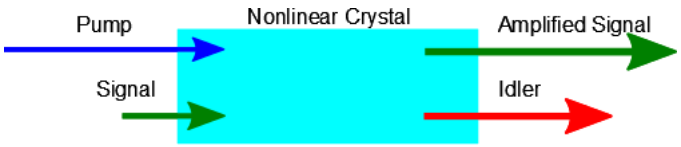

Figure 2.5: Schematic of optical parametric amplification.

hence, optical amplification can be achieved through a series of difference frequency generation interactions.

If we consider, as above, two electromagnetic waves at frequencies ω_1 and ω_2, which are referred to as the pump and signal waves respectively, both are incident on

a nonlinear crystal. Furthermore, the intensities of these to waves are not equal, i.e. $|E_1|^2 \gg |E_2|^2$. These to waves will interact, through difference frequency generation, to generate a third wave at $\omega_3 = \omega_1 - \omega_2$, (Figure 2.5), which is referred to as the idler. For $\kappa z \gg 1$ the idler wave grows rapidly ($\propto e^{\kappa z}$) due to the high intensity of the pump, and goes on to interact with the pump in the same fashion, i.e. DFG, to create more radiation at the signal frequency $\omega_2 = \omega_1 - \omega_3$. Thus, through this two-stage nonlinear process it is possible to amplify the weak signal wave and create a new idler wave; this process is referred to as optical parametric amplification [97, 99, 100].

2.2.3 Manely-Rowe Relations

If we take the coupled amplitude equations Eqns 2.28, 2.28 & 2.29 and substitute intensity I_i for amplitude A_i using the relation $I_i = 2n_i\varepsilon_0 c A_i A_i^*$ (where i = 1, 2, 3), it can be show that the spatial variation of the intensity of the waves is given by:

$$\frac{dI_3}{dz} = -8\varepsilon_0 d_{eff}\omega_1 Im\left(A_1 A_3^* A_2^* e^{-i\Delta kz}\right) \tag{2.34}$$

$$\frac{dI_2}{dz} = -8\varepsilon_0 d_{eff}\omega_1 Im\left(A_1 A_3^* A_2^* e^{-i\Delta kz}\right) \tag{2.35}$$

$$\frac{dI_1}{dz} = -8\varepsilon_0 d_{eff}\omega_1 Im\left(A_1^* A_3 A_2 e^{-i\Delta kz}\right) \tag{2.36}$$

$$= 8\varepsilon_0 d_{eff}\omega_1 Im\left(A_1 A_3^* A_2^* e^{-i\Delta kz}\right) \tag{2.37}$$

Form these equations it can be seen that the $\frac{dI_3}{dz} = \frac{dI_2}{dz} = -\frac{dI_1}{dz}$ and that the movement of energy between the 3 waves is dependent upon their relative phases. If we define the total intensity $I = I_3 + I_2 + I_1$, then we can show that the total intensity is invariant as the waves propagate.

$$\frac{dI}{dz} = \frac{dI_3}{dz} + \frac{dI_2}{dz} + \frac{dI_1}{dz} = -8\varepsilon_0 d_{eff}(\omega_3 + \omega_2 - \omega_1) Im\left(A_3^* A_2^* A_1 e^{-i\Delta kz}\right) = 0 \tag{2.38}$$

It can also be shown that:

$$\frac{d}{dz}\left(\frac{I_3}{\omega_3}\right) = \frac{d}{dz}\left(\frac{I_2}{\omega_2}\right) = -\frac{d}{dz}\left(\frac{I_1}{\omega_1}\right) \tag{2.39}$$

The relations in Eqn 2.38, known as the Manley-Rowe relations, demonstrated that the rate of creation of photons at ω_3 is equal to the rate of creation of photon at ω_2 and the rate of destruction of photons at ω_1. Furthermore, we can see that in the absence of loss, the distribution of power between the waves is also governed by these relations such that [140]:

$$\frac{\Delta P_3}{\omega_3} = \frac{\Delta P_2}{\omega_2} = -\frac{\Delta P_1}{\omega_1} \tag{2.40}$$

And hence, the limit of the power conversion efficiency from the pump ω_1 to ω_3 is defined as

$$\eta_3^{max} = \frac{\omega_3}{\omega_1} \tag{2.41}$$

So, for THz generation the use of long wavelength pump sources confers a significant advantage.

2.2.4 Parametric Oscillation

Parametric fluorescence is a spontaneous two-photon emission within a nonlinear crystal at the level of optical noise. An Optical Parametric Oscillator is a laser cavity resonator, which amplifies this fluorescence in the crystal, from within the noise floor to an oscillating coherent signal, provided that the length of the cavity corresponds to an integer number of half wavelengths of the fluorescent frequency [97, 98]. Parametric fluorescence, which only occurs in the direction that satisfies phase matching, is a quantum phenomenon, where two photons of frequencies ω_2 and ω_3, the signal and idler frequencies, are spontaneously emitted within a nonlinear crystal, which has a high-intensity coherent light beam of frequency ω_1, the pump frequency, incident upon it. From the conservation of energy [100]:

$$\omega_1 = \omega_2 + \omega_3 \tag{2.42}$$

Byer and Herbst [98], note that *"This prompted one chemist to call a parametric generator a 'photon cutter'."* In OPOs the assignation of signal and idler labels is

quite arbitrary.

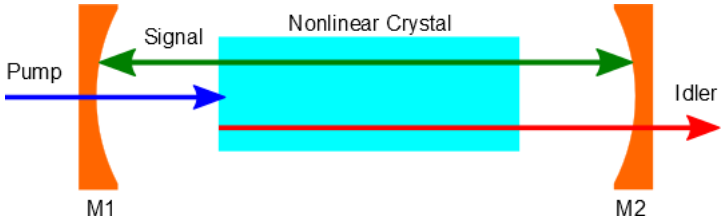

Figure 2.6: Schematic of an Optical Parametric Oscillator

Parametric fluorescence can be explained in terms of scattering of laser light from polaritons. Polaritons are quasi-particles that behave as photon-phonon mixed states. They occur when photon and transverse optical (TO) phonon wave fields become coupled, due to intense laser light incident on an optical nonlinear material. Near the resonant frequency of the TO phonon ω_{TO}, polaritons behave as if they were phonons, away from ω_{TO} they behave like photons, creating both a signal and idler photons parametrically from the pump photon [90, 99]. The split in energies or frequencies between the signal and idler beams is tunable so long as the conservation of momentum is observed, i.e. $k_1 = k_2 + k_3$ where k is a vector; this is commonly referred to as phase matching [100].

2.2.5 Performance

As stated above, OPOs are optical amplifiers, within a low loss optical cavity in order to build up the initial spontaneous fluorescence into a coherent signal. Thus, its performance is of particular interest. Below follows a brief treatment of a Doubly Resonant Oscillator. The coupled amplitude equations Eqn 2.27 & 2.27, describing the variation in amplitude of the waves as they propagate, have solutions in the from

$$A_3(z) = \left[A_3(0)\left(cosh\, gz - \frac{i\Delta k}{2g} sinh\, gz\right) + \frac{\kappa_3}{g} A_2^* sinh\, gz\right] e^{\frac{i\Delta kz}{2}} \tag{2.43}$$

$$A_2(z) = \left[A_2(0)\left(cosh\, gz - \frac{i\Delta k}{2g} sinh\, gz\right) + \frac{\kappa_2}{g} A_3^* sinh\, gz\right] e^{\frac{i\Delta kz}{2}} \tag{2.44}$$

$$g = \sqrt{\kappa_3 \kappa_2^* - (\frac{\Delta k}{2})^2} \tag{2.45}$$

$$\kappa_i = \frac{2i\omega_i^2 d_{eff} A_1}{k_i c^2} \tag{2.46}$$

Where g is the gain [99]. In the special case where $\Delta k = 0$ Eqn 2.43 reduces to:

$$A_3(z) = \frac{1}{2} A_1(0) e^{gz} \tag{2.47}$$

$$A_2(z) \propto A_3^*(0) e^{gz} \tag{2.48}$$

The parametric gain Eqn 2.45 can alternatively be defined in terms of intensity as [99, 141]:

$$g = \sqrt{\Gamma^2 - (\frac{\Delta k}{2})^2} \tag{2.49}$$

where Γ is the damping or coupling constant, which is defined as [99]:

$$\Gamma^2 = \frac{\omega_3 \omega_2 |d_{eff}|^2 |\mathbf{E}_1|^2}{n_3 n_2 c^2} = \frac{\omega_3 \omega_2 |d_{eff}|^2 I_1}{n_1 n_2 n_3 \varepsilon_0 c^2} \tag{2.50}$$

The wave at ω_3 experiences in a single pass a power gain defined as [99, 141]:

$$G_s(l) = \frac{I_3(0)}{I_3(0)} - 1 = \Gamma^2 L^2 \frac{sinh^2 gL}{(gL)^2} \tag{2.51}$$

where L is the length of the crystal. Assuming that there is no loss and that depletion of the pump is negligible this can be approximated as [99, 100]:

$$G_3(L) = \frac{1}{4} exp(2\Gamma L) \tag{2.52}$$

in the high gain limit, provided that the phase mismatch $\Delta k < g$.

The threshold of oscillation in a Doubly Resonant Oscillator (DRO) cavity, where the amplitude of the generated fields at least matches their initial state after one

round trip, overcoming the cavity losses, can more generally be described as

$$A_3(z) = \left[A_3(0)\left(cosh\, gd - \frac{i\Delta k}{2g} sinh\, gd\right) + \frac{\kappa_3}{g} A_2^* sinh\, gd\right](1 - l_3) \tag{2.53}$$

$$A_2(z) = \left[A_2(0)\left(cosh\, gd - \frac{i\Delta k}{2g} sinh\, gd\right) + \frac{\kappa_2}{g} A_3^* sinh\, gd\right](1 - l_2) \tag{2.54}$$

where d is the length of the cavity and l_i is the round trip loss in the cavity, taking into account the crystal absorption(α_i), Fresnel losses (R_f), and the mirror reflectivity (R_m).

$$l_i = 1 - R_m R_f e^{\alpha_i d} \tag{2.55}$$

For a DRO cavity to oscillate Eqn2.53 must be satisfied simultaneously such that

$$cosh\, gd = 1 + \frac{l_3 l_2}{2 - l_3 - l_2} \tag{2.56}$$

or in the low loss case $l_3, l_2 \ll 1$

$$g^2 d^2 = l_3 l_2 \tag{2.57}$$

In the case of a single resonant cavity, i.e. where there is no feedback on the idler $l_2 = 1$ and low loss on the signal ($l_3 \ll 1$), then the threshold condition increase to $g^2 d^2 = 2l_3$. In the case of low loss the threshold condition for a singly resonant cavity is considerably higher than a doubly resonant cavity, though singly resonant cavities are often preferred for their higher stability.

To reach the oscillation threshold, the OPO must amplify the spontaneous parametric fluorescence approximately 10^{16} times from the level of noise [98], overcoming the losses in the cavity. Above the threshold, the OPO oscillates, efficiently producing, coherent, continuously tunable signal and idler radiation.

2.2.6 Phase Matching

Phase matching is critical for the efficient generation of radiation in the majority of second order nonlinear processes. While the frequencies are matched automatically,

this does not imply phase matching. k, the wave vector, is described as below: [100]

$$k_i = \frac{2\pi n_i}{\lambda_i} \quad (\text{i} = 1,2,3) \tag{2.58}$$

where n is the refractive index of the material at the wavelength λ; as before we use the scalar approximation for convenience. As the majority of materials are dispersive, the refractive index which is a function of wavelength $n(\lambda)$ varies in magnitude for different values of λ; thus, the phase matching condition is [100]:

$$\frac{2\pi n_1}{\lambda_1} = \frac{2\pi n_2}{\lambda_2} + \frac{2\pi n_3}{\lambda_3} \tag{2.59}$$

Physically, this implies that if these waves were to propagate collinearly, with the same polarisation state, they would not be phase-matched (Figure 2.7).

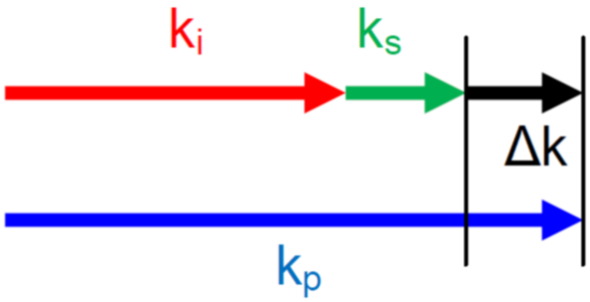

Figure 2.7: Schematic of phase mismatch between pump signal and idler wave vectors

If the wave vectors were phase-matched the signal and idler beam contributions from each radiating dipole would add constructively along the entire length of the crystal and the amplitude of the wave will grow with L^2. If we consider the case of Eqn 2.30, where the condition $\Delta k = 0$ is not satisfied, the amplitude of the wave emitted from the crystal is reduced. The phase mismatch is described as [100]:

$$\Delta k = \left(\frac{2\pi n_1}{\lambda_1} - \frac{2\pi n_2}{\lambda_2} - \frac{2\pi n_3}{\lambda_3} \right) \tag{2.60}$$

The magnitude of A_3, the emitted wave, can be found by integrating Eqn 2.27 from

z = 0 to z = L, where L is the length of the nonlinear medium and is given by.

$$A_3(L) = \frac{2id_{eff}\omega_3^2}{k_3c^2}A_1A_2^*\int_0^L e^{i\Delta kz} = \frac{2id_{eff}\omega_3^2}{k_3c^2}A_1A_2^*\left(\frac{e^{i\Delta kL}-1}{i\Delta k}\right) \tag{2.61}$$

Defining the intensity of the ω_i wave as I_1, the time average Poynting vector:

$$I_i = 2n_i\varepsilon_0 c|A_i|^2, \quad (i = 1,2,3) \tag{2.62}$$

The intensity of the ω_3 wave at the exit face of the crystal is describe by:

$$I_3 = \frac{8n_3\varepsilon_0 d_{eff}^2\omega_3^4\left|A_1\right|^2\left|A_2^*\right|^2}{k_3^2c^3}\left|\frac{e^{i\Delta kL}-1}{\Delta k}\right|^2 \tag{2.63}$$

Where the exponential term can be recast as:

$$\left|\frac{e^{i\Delta kL}-1}{\Delta k}\right|^2 = L^2\frac{sin^2(\frac{\Delta kL}{2})}{(\frac{\Delta kL}{2})^2} \equiv L^2sinc^2\frac{\Delta kL}{2} \tag{2.64}$$

So, intensity of the ω_3 wave can be related to the intensity of the other two and where the $sinc^2$ term fully considers the effect of wave vector mismatch, such that I_3 is at a maximum when $\Delta k = 0$

$$I_3 = \frac{8n_3\varepsilon_0 d_{eff}^2\omega_3^4 I_1I_2}{k_3^2c^3}L^2sinc^2\frac{\Delta kL}{2} \tag{2.65}$$

If the beams are not phase-matched, the generated signal and idler will continually change phase with respect to each other and the pump. As they change their relative phases the energy moves between the generated frequencies ω_3 & ω_2 and the pump ω_1 or vice versa (Eqn 2.34), varying in a sinusoidal manner (Figure 2.3). As such, the signal will not build up efficiently over the propagation length of the crystal [100]. The period of this variation between the pump and the signal and idler is defined as [100]:

$$\frac{\Delta kl}{2} = \pi \tag{2.66}$$

where half of this period, l_c, is the coherence length of the system.

By increasing the coherence length of the beams within the crystal, through the

reduction or elimination of the phase mismatch, the efficiency of generation can be improved by several orders of magnitude [100], so is highly desirable. If we rewrite the phase matching conditions in term of frequency for DFG, it becomes

$$\frac{n_1\omega_1}{c} = \frac{n_3\omega_3}{c} + \frac{n_2\omega_2}{c} \tag{2.67}$$

Consider the case, where $n(\omega)$ increases with ω (i.e. $n_1 > n_2 > n_3$); we can show that phase matching is not possible. First let us we write Eqn 2.67 to define n_1 in relation to the other terms for phase matching.

$$n_1 = \frac{n_3\omega_3 + n_2\omega_2}{\omega_1} \tag{2.68}$$

And use it do examine the refractive index mismatch $n_1 - n_2$

$$n_1 - n_2 = \frac{n_3\omega_3 + n_2\omega_2 - n_2\omega_1}{\omega_1} \tag{2.69}$$

$$= (n_3 - n_2)\frac{\omega_3}{\omega_1} \tag{2.70}$$

In the case described, the left hand side of the equation $n_1 - n_2$ must be positive, while the right hand side $n_3 - n_2$ must be negative, so there is no solution which will satisfy this case. In real systems, a caveat exists where phase matching can be achieved due to the anomalous dispersion around absorption functions, though this is rather limiting. A more satisfactory and common solution it to make use of birefringence as pioneered by Giordmaine [106], and Maker *et al* [107]. In birefringent crystals, where different polarisations of light experience different refractive indices can be exploited to counteract the material dispersion. A variety of cases exist dependent upon the crystal structure, we will restrict ourselves to the case relevant for ε-GaSe, which is a negative uniaxial crystal, where $n_o > n_e$.

In negative uniaxial crystals the ordinary refractive index is experienced by beams propagating parallel to the direction of the optic axis, regardless of polarisation. The extraordinary refractive index is experienced by beams propagating perpendicular to the optic axis (c or z-axis) whose polarisation parallel in the plain

containing the propagation vector **k** and the optic axis referred to as the extraordinary polarisation. The magnitude of the extraordinary refractive index, $n_e(\theta)$, experienced by light with the extraordinary polarisation depends on its direction of propagation relative to the optic axis

$$\frac{1}{n_e(\theta)} = \frac{sin^2\,\theta}{n_e^2} + \frac{cos^2\,\theta}{n_o^2} \tag{2.71}$$

The ordinary polarisation is perpendicular to the plane containing the propagation vector **k** and the optic axis. In exploiting birefringence for phase matching, the highest frequency wave ω_1, which typically has the largest refractive index, is given the polarisation that has the lowest refractive index, narrowing the refractive index mismatch. In the case of uniaxial crystals this is the extraordinary polarisation. The remaining two waves ω_2 & ω_3 can be assigned either polarisation. If both polarisations are the same and orthogonal to ω_1, with ordinary polarisations, it is referred to as Type-I phase matching. If ω_2 & ω_3 are orthogonal, then it is referred two as Type-II phase matching. This example does not always hold, in the case of many crystals, e.g. GaSe the THz frequencies have higher refractive indices and would thus be assigned the extraordinary polarisation. Other factors can be accounted for in the assignment of polarisations, such as reducing loss or limiting the the size of the angles.

We can now rewrite the phase matching condition as:

$$n_e(\omega_3, \theta) = n_o(\omega_1) - n_o(\omega_2) \tag{2.72}$$

As described above, critical phase matching, or referred to more generally as Birefringent Phase Matching (BFM), can be achieved for a given combination of signal and idler frequencies, at the angle where their refractive index ellipsoids intersect [100]. We can find this angle, θ, by rewriting Eqn 2.72 in terms of Eqn 2.71

for the case of Type-II phase matching.

$$\frac{sin^2\,\theta}{n_e(\omega_3)^2} + \frac{cos^2\,\theta}{n_o(\omega_3)^2} = \frac{1}{n_o(\omega_1)^2} - \frac{1}{n_o(\omega_2)^2} \tag{2.73}$$

$$sin^2\,\theta = \frac{\frac{1}{n_o(\omega_1)^2} - \frac{1}{n_o(\omega_2)^2} - \frac{1}{n_o(\omega_3)^2}}{\frac{1}{n_e(\omega_3)^2} - \frac{1}{n_o(\omega_3)^2}} \tag{2.74}$$

The solution to this equation may not exist or be physically realisable, other exotic phase matching types exist such as Type-0, where all wave have ordinary polarisations, or Type-IV where all waves have extraordinary polarisations. As the refractive index is dependent not only on the direction of propagation in the crystal but also on its temperature, it is possible through the rotation of the crystal and or the variation of its temperature to tune what particular signal and idler pair is phase-matched, and hence the frequency of the OPO output [100]. Some crystals possess electro-optic susceptibility, which can also be used as a tuning method, as described by Kreuzer [124].

A major drawback of this method is that many of the nonlinear crystals employed for THz OPO's, e.g. $LiNbO_3$, are strongly absorbing at THz frequencies, and hence it would be desirable to couple the signal beam out of the crystal in as short a distance as possible. This can be achieved through non-collinear phase matching [98] (Figure 2.8). In this technique, each of the beams propagates at an angle with respect to the

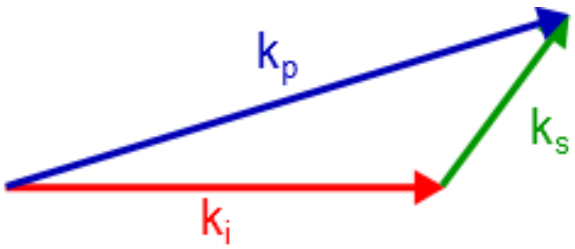

Figure 2.8: Schematic of non-collinear phase matching between pump, signal and idler wave vectors.

other, and phase matching is achieved through simple vector addition. In general, for THz generation the pump and idler wavelengths are of a similar magnitude and thus the angular difference in the propagation is quite small, ($\sim 5°$). As a result,

the angle of propagation of the signal beam is quite high ($\sim$ 65°) with respect to the other two, and the optical path-length within the absorbing crystal is minimised as it is coupled out from a side facet. These devices are often aligned such that the pump and idler beams propagate close to the crystals surface, to maximise the effect of this method. The signal and idler frequencies are tuned by adjusting the angle between the pump and idler beams, and by extension so is the signal beam [98, 100]. On the downside, noncollinear phase-matching reduce the interaction length of the 3 waves.

2.2.6.1 Quasi Phase Matching

Phase matching can be achieved by another means where an additional k-vector is introduced through the creation of a periodic structure or domain grating within the nonlinear material. Referred to as Quasi Phase Matching, it was first proposed in 1962 by Armstrong et al [110]; the first practical demonstration of quasi-phase-matching through electrical means was by Yamada et al (1993) [142] who used it to achieve SHG in a periodically poled $LiNbO_3$ crystal. Periodic Polling is the inversion of the domain structure in the crystal at regularly spaced intervals. This is achieved through the one-time application of a high voltage (24 kV/mm) pulse (100 μs) through a set of lithographically patterned electrodes [142]. The period of the electrodes and thus the period of the polling is determined by the phase matching condition [100]:

$$\Delta k = k_1 - k_2 - k_3 - k_\Lambda \tag{2.75}$$

where k_Λ is the wave vector associated with the grating. k is defined as [100]:

$$k_\Lambda = \frac{2\pi}{\Lambda} \tag{2.76}$$

where Λ is the grating period, which is the coherence length of the system in a non-phase-matched case, l_c [100]. The first OPO using quasi phase matching was reported by Meyers et al [143] who demonstrated tunable generation in the mid-infrared using Periodically Poled Lithium Niobate (PPLN). This technique allows

the phase matching to be achieved with the 3 waves travelling collinearly; however, as the THz signal is absorbed within the crystal in many instances, this is not always a desirable situation. Slant Strip Periodic Polling, as reported on by Sasaki *et al* [144], allows the pump and idler beams to remain collinear, maximising the interaction between waves, with the THz signal beam propagating orthogonally to the other two, the angled grating wave-vector compensation allowing for phase matching (Figure 2.9). Thus the THz beam can be quickly coupled out from the

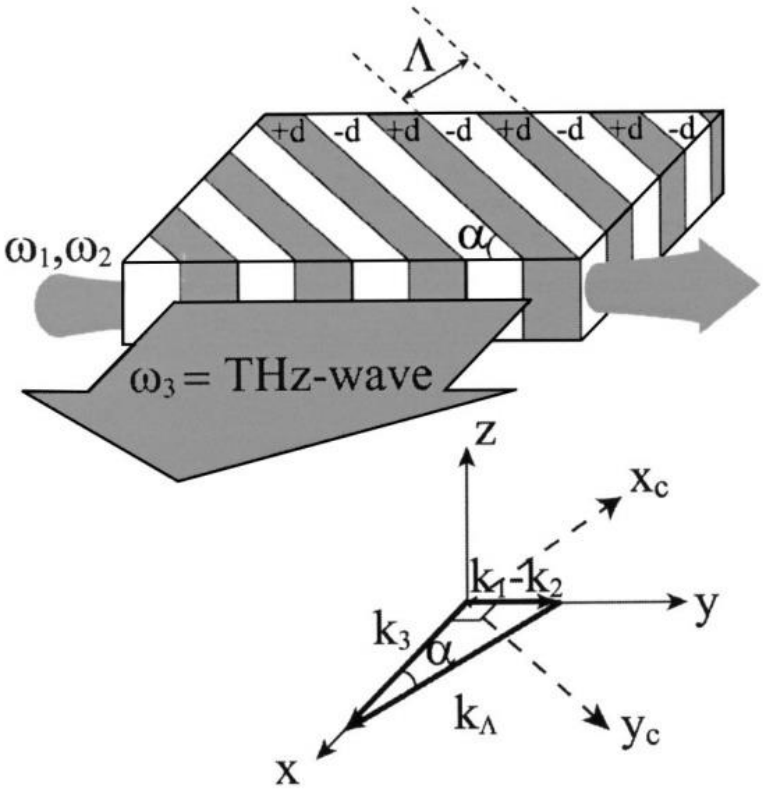

Figure 2.9: Schematic of Slant Strip Quasi-Phase Matching and vector diagram [144].

side of the crystal, minimising absorption. As before, the required grating period Λ and also the grating angle, α, can be calculated from the phase matching conditions [144]:

$$k_\Lambda sin(\alpha) = k_1 - k_2 \tag{2.77}$$

and

$$k_\Lambda cos(\alpha) = k_3 \tag{2.78}$$

where k is a wave-vector in the usual form (Eqn 2.58 & 2.76). From these two equations (Eqn 2.77 & 2.78) the solutions for α and λ can be shown to be [144]:

$$\alpha = tan^{-1}\left(\frac{k_1 - k_2}{k_3}\right) \tag{2.79}$$

and

$$\Lambda = \frac{2\pi}{k_1 - k_2} sin\left[tan^{-1}\left(\frac{k_1 - k_2}{k_3}\right)\right] \tag{2.80}$$

This particular technique, periodic poling by the application of high voltage across electrodes, is only available for use with ferroelectric crystals. For other crystals additional options exist such as diffusion bonded stacks and orientation patterning [145, 146, 147, 148, 149, 150]. Quasi-Phase-Matching provides additional advantages over birefringent phase matching, in that the crystal orientation can be selected to optimise the nonlinear interaction, e.g. the d_{33} coefficient in $LiNbO_3$, which can only be accessed by QPM, is seven times larger than the d_{31} coefficient, accessible by birefringence [105].

2.2.7 OPO Resonator Design

Optical parametric oscillator resonators come in a variety of different designs, depending on the pumping scheme and whether they are singly or doubly resonant. The most common type of OPO is a sequentially pumped Singly Resonant Oscillator (SRO) [97] (Figure 2.10 A). In this scheme, the nonlinear crystal is placed within an optical cavity whose length corresponds to an integer number of half wavelengths of the frequency that has been chosen to oscillate, generally the idler. The cavity is pumped from one end, through a dichroic input coupler that is transparent at the pump frequency and highly reflecting at the idler frequency. At the other end of the cavity is the output coupler, which is transparent at the signal frequency and highly reflecting at the idler; though in some case a portion of the idler may also be coupled out [97]. In a pulsed system, this can be further refined such that the round trip time of the OPOs cavity is matched with that of the mode-locked pump laser, allowing the pump and idler pulses to overlap continuously while propagating

in the OPO resonator (Figure 2.10 B). This design is referred to as synchronously pumped. The benefits of this design are higher peak powers, greater conversion efficiency and improved beam quality [151]. It is common in this sort of scheme for purposes stability to slave one cavity to the other through piezoelectric servos or other similar devices. The second form of sequentially pumped OPOs is the Doubly Resonant Oscillator (DRO) (Figure 2.10 C); in this cavity both the signal and idler frequencies oscillate, with the input coupler being highly reflective for both, and as required, transparent to the pump frequency. The output coupler may allow a portion of one, or both, of the signal and idler to be ported out of the system. DROs are more complex to construct, as two wavelength conditions must be satisfied. This can be achieved by several different configurations: a signal cavity satisfying both frequencies, two cavities intersecting each other, or alternatively, both the beams travel collinearly through the nonlinear crystal and share one common mirror in the output coupler, and then by means of a dichroic mirror placed within the cavity each has separate highly reflective mirrors at the opposite ends of the resonator. Despite the complexity of the DRO resonator, they possess an attractive advantage over SROs, in that the threshold of oscillation is approximately two orders of magnitude lower [105] as shown above (Eqn 2.57). As both the signal and idler experience gain together, the threshold for oscillation is reduced by the reciprocal of the round trip loss per resonance frequency, approximately 1% [97]. Where the DRO is pumped by a tunable laser, variation in the pump frequency can effectively be used to tune the output of the OPO [97] (Figure 2.10D). DRO cavities do suffer from some serious drawbacks besides complexity; there are difficulties in achieving continuous tuning and they often lack of stability.

A solution available to SROs, in order to overcome their disadvantage in relation to the threshold of oscillation, is to place the nonlinear crystal intracavity with the pump laser (Figure 2.10 F). This exposes the nonlinear crystal to a circulating optical field that is approximately two orders of magnitude greater than that which would typically be available from the output coupler of the laser. Increased conversion efficiency and terahertz pulses with energies 25 times greater than that of otherwise

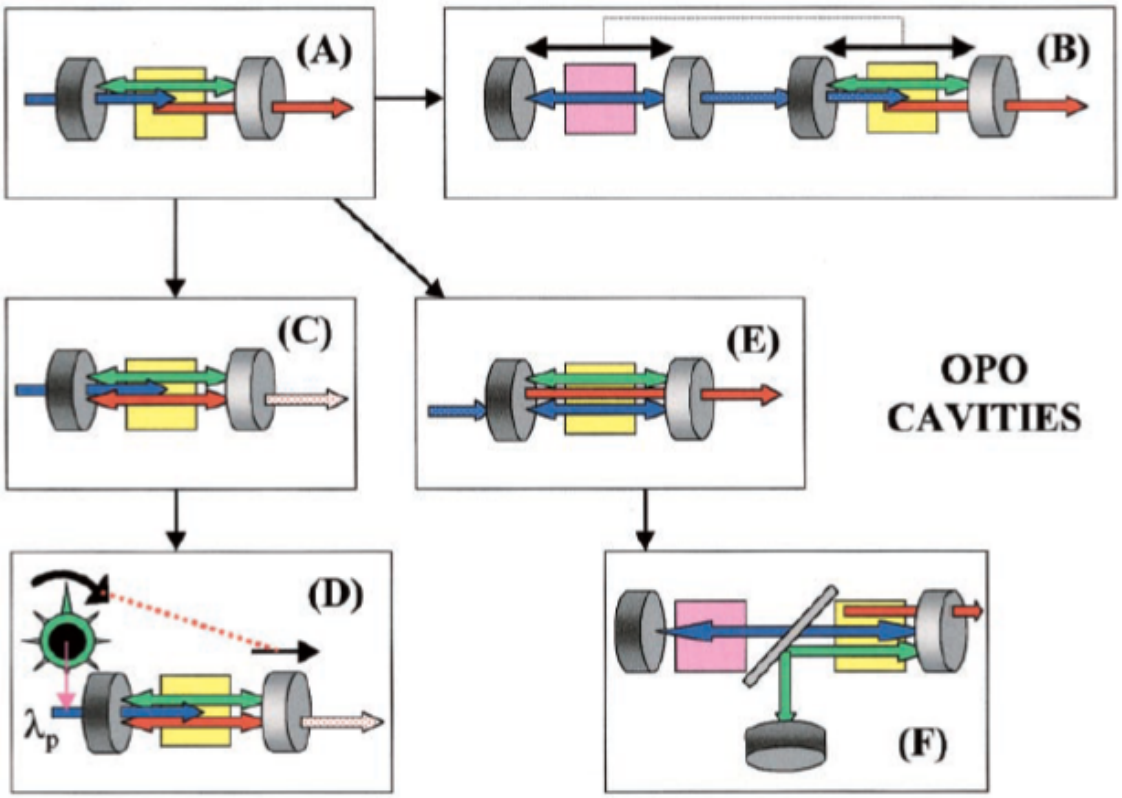

Figure 2.10: Optic Parametric Oscillator Cavities: (A) Singly Resonant Oscillator (SRO), (B) Synchronously Pumped SRO, (C) Doubly Resonant Oscillator (DRO), (D) Pump-tuned DRO, (E) Pump-enhanced SRO, (F) Intracavity-pumped SRO [97].

similar SRO configurations have been reported by workers using this method [152].

Various other schemes exist such as: ring cavities [153], which provide compactness and improved stability for synchronously pumped or travelling wave systems, and pump recycling schemes which have been reported to increase efficiency up to four times as compared with other designs [154].

2.2.8 Output Coupling

Coupling of the THz beam from the nonlinear crystals is problematic due to their high refractive indices. This leads to two forms of loss: the first is total internal reflection at the crystal/air interface; the second is high Fresnel reflections. As an example: $LiNbO_3$ has a refractive index $n_(THz) = 5.2$ [152], at an air interface this leads to the critical angle for total internal reflection c = 11.09° and a Fresnel

reflectivity R = 45.89 %. While non-collinear phase matching does produce a large angle for the THz component, it is not sufficiently large to avoid TIR.

Several methods have been developed to overcome these drawbacks and couple the THz radiation from the crystal into free space. In the first attempt to overcome this [129], a corner was cut from the $LiNbO_3$ crystal approximately normal to the direction of propagation of the THz beam. While effective in overcoming TIR, this did not address the Fresnel reflection and was limited to a small area, allowing only a fraction of the THz to be coupled out (Figure 2.11).

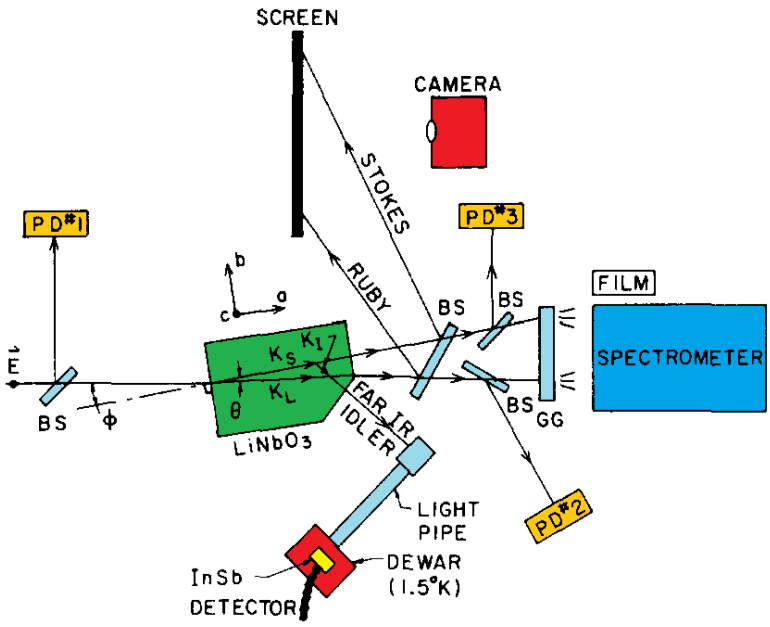

Figure 2.11: Schematic Yarborough's experimental set-up, showing the cleaved crystal corner for THz output coupling [129].

Later, monolithic $LiNbO_3$ crystals were produced with a grating cut in the side facet [155], with a reported improvement in the output coupling of 250 times. However the propagation direction of the coupled output beam is wavelength sensitive, with a variation in direction of $0.65°/\mu m$ was reported [156]. Again, the area covered by these gratings is generally small, limiting the amount of THz radiation extracted.

Further improvements in output coupling efficiency were achieved through the development of an array of right-angle Silicon (Si) prisms [156, 152], which is placed

on the facet of the nonlinear crystal that the THz radiation is to exit from. The angles of the prisms are cut so that the THz radiation will strike the face at near normal incidence. Si has a refractive index n = 3.4; at the surface with the $LiNbO_3$ this results in a critical angle c = 40.8°, and reduces the Fresnel reflectivity to R = 4.38% and at the Si/air interface to R = 29.75%. The prism array is manufactured to cover the complete surface of the exit facet of the nonlinear crystal and increases the output coupling by a further 6 times; this could be improved with the addition of Anti-Reflection (AR) coatings [1].

2.3 Nonlinear Optical Materials for THz Generation

A vast multitude of crystalline structures are known to the physical sciences, very few of them are suitable for use in optical parametric generation. Byer tells us that by 1969 22,000 crystals had been surveyed for their potential use in nonlinear optics, of which only 100 had sufficient birefringence to be capable of phase matching, and fewer again could be grown effectively or to a usable optical quality [105]. While Byer's comments refer to the time before the possibility of quasi-phase-matching, through the advent of periodic polling and other techniques, it gives a handle on the scale of the work and the difficulty involved in finding new optical crystals. Indeed this difficulty was one of the drivers in the development of QPM technologies [105].

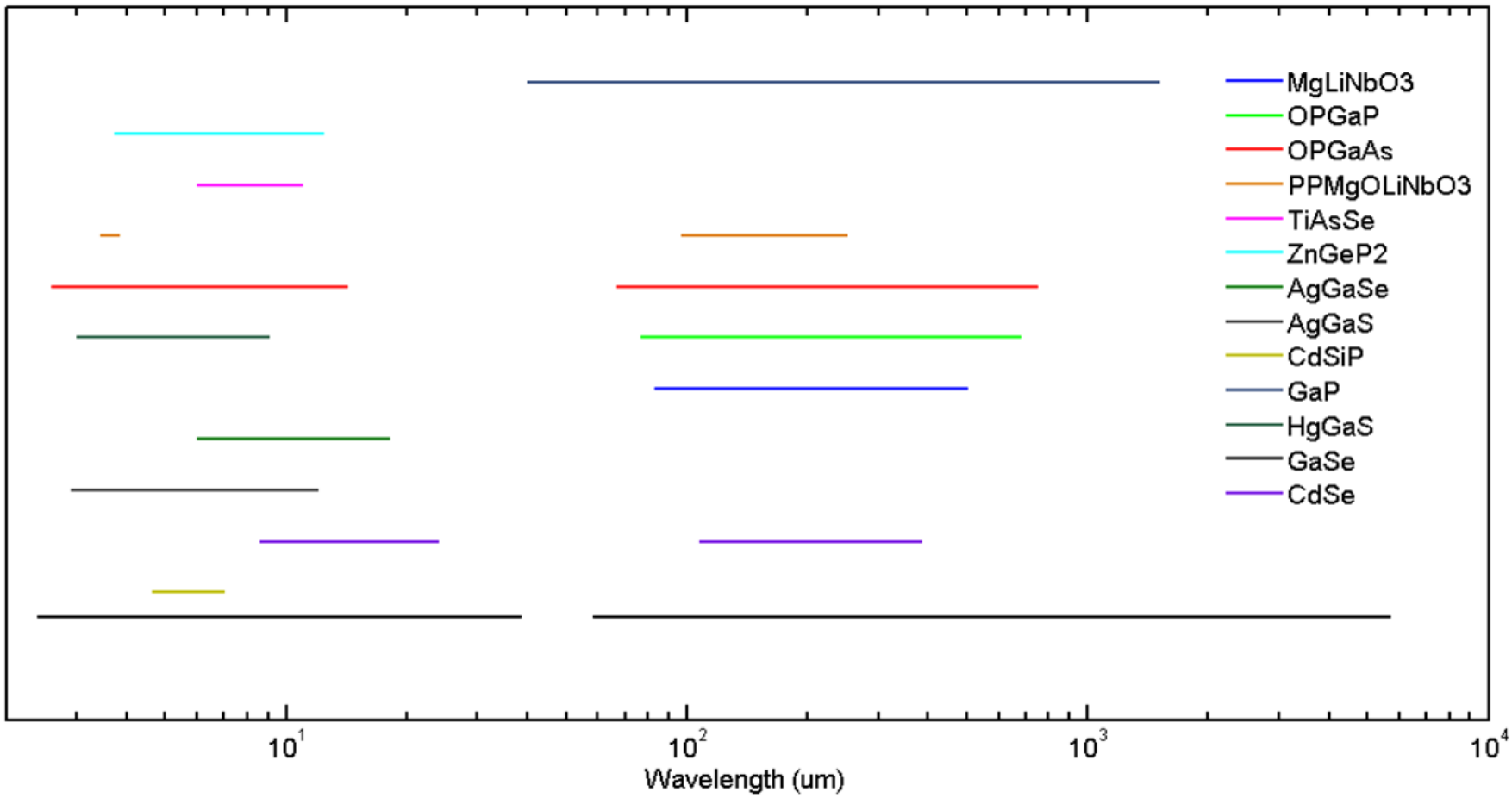

Figure 2.12: The reported tunable ranges for DFG and OPO in a number of common nonlinear optical crystals including: $MgOLiNbO_3$ [157, 1, 158, 159], GaP [160, 161], OPGaAs [147, 162, 163], OPGaP [164, 165], GaSe [166, 167, 168, 161] CdSe [169, 167, 170, 171] and $GaSe_{x-1}S_x$[172]

Of these crystals, fewer still are suitable for use in the THz regime. The growth and development of new nonlinear optical crystals is a tedious, time consuming and expensive pursuit often ending in frustration. Once a crystal can be grown it is not sufficient to simply catalogue its properties and move on to the next. A survey of the reported tuning ranges for OPO and DFG in common nonlinear materials is presented in Figure 2.12.

There are a number of necessary properties for crystals to be useful in nonlinear applications and in particular for use as OPOs, and considerable time must be expended in meeting these requirements, though improvements of the growth technology, the doping procedure and the growth processes. From the theory of operation above, we can identify some of the requirements for good nonlinear conversion efficiency. Examining the equation for parametric gain (Eqn 2.50) we can see that the crystal should possess a large magnitude of second order susceptibility and a high damage threshold to allow intense pumping. Large values of refractive index are undesirable as they are an inverse cube factor severely reducing the gain. The nonlinear Figure of Merit (FOM) is derived from the parametric gain as is describe as

$$FoM = \frac{d_{eff}^2}{n_1 n_2 n_3 \alpha^2} \tag{2.81}$$

where we use the figure of merit given by Shi [166, 93], which includes the absorption coefficient. It is also worth noting that from Eqn 2.50 we can see that the gain is proportional to $\omega_3\omega_2$ and, as consequence, the gain in THz OPOs will be considerable less than that for Near and Mid-IR devices. Examining the description of intensity from Eqn 2.65 and Figure 2.3, the need for phase matching is clear, which necessitates some birefringence. However, it should not be too strong, as collinear interactions are highly desirable and the intensity of the generated wave increases with the square of the crystal length [100, 173]. The advent of QPM has reduced the need of birefringence from an absolute requirement. A low absorption coefficient at both the pump frequency and within the proposed operational range are required as gain is typically $\ll 1$. To facilitate this the phonon band should lie well away from the desired frequency of generation and the bandgap edge should be

more than twice the pump frequency to exclude two phonon absorption. From the Manley-Rowe relations (Eqn 2.41) it is clear that pumping at longer wavelengths can have advantages in the efficiency of frequency conversion, but necessitated low absorption in the Mid-IR.

Table 2.2: Nonlinear Figure of Merit (FOM) for a range of commonly used nonlinear materials in the THz regime

Crystal	Absorption cm^{-1}	n_{THz}	n_{IR}	d_{eff} pm/V	FOM
$LiNbO_3$	10	5.2	2.2	25	2.5E-3
$LiTaO_3$	500	5.2	2.2	13	0.3E-3
GaAs	5	3.35	3.35	61	3.7
GaP	2.2	3.2	3.1	37	9.2
$ZnGeP_2$	3.4	3.1	3.1	75	10.8
AgGaSe	50	2.6	2.6	33	25E-3
GaSe	0.2	3.24	2.63	55	3375
GaSe:Er	5	3.2	2.56	75	10
$GaSe_{x-1}S_x$	0.2	3.2	2.59	30	1050

2.3.1 LiNbO3

The potential of $LiNbO_3$ having been identified [117, 174, 119], significant effort was devoted by Feigelson's team at Stanford team to its growth, development and improvement as a nonlinear optical material.

$LiNbO_3$ and Lithium Tantalate ($LiTaO_3$), are among the most commonly used crystals for nonlinear generation. They have a trigonal crystal structure and possess large nonlinear susceptibilities d_{eff}=25 pm/V for $LiNbO_3$ and approximately half of this for $LiTaO_3$ [173]. $LiNbO_3$ was the crystal used for both the first OPO [174], and the first THz OPO [129]; it is the material that has been adopted for commercial generation of THz through DFG and OPO [175]. Typically pumped in by Nd:YAG laser, $LiNbO_3$ is a mature optical material with good transparency in the range 0.4 – 5.5 μm and low two-photon absorption at the pump wavelength [90, 157]. In spite of this, both have prohibitively large absorption coefficients in the THz regime, where we propose to operate i.e. 3-10 THz, which is reflected by their low FoM. $LiNbO_3$ has an absorption coefficient of approximately 10 cm^{-1} at 2 THz and 500 cm^{-1} in the case of $LiTaO_3$ [173]. Absorption growth is near exponential at frequencies

after this point due to strong broadly absorbing phonons with peak frequencies at 7-8 THz and the location of Reststrahlen band [176], leaving the effective upper limit for THz generation in $LiNbO_3$ and $LiTaO_3$ at approximately 3 THz. Both crystals are very strongly birefringent, so collinear propagation of pump and signal is not possible [173]. The development of MgO:$LiNbO_3$[90, 177, 1, 178, 179, 180] and periodically poled $LiNbO_3$ has improved efficiency through the possibility of collinear propagation of the pump and idler waves in SRO cavities and has become widely adopted [143, 181, 182, 183, 184, 158]. However, due to the high absorption coefficient, coupling of the THz signal from the side of the crystal is still necessary.

2.3.2 GaAs and GaP

The III-V semiconductor family is another potential source of nonlinear crystals, suitable for THz optical parametric generation. GaAs, and GaP, are both zincblende crystals, having large $\chi^{(2)}$ nonlinear susceptibility, d_{eff} 61 pm/V & 37 pm/V [173] respectively, low absorption 4.5 cm^{-1} at 3 THz [185] and broad transparency ranges (0.9-17 μm) [186], resulting in a good FoM and making them very attractive for nonlinear applications. However due to their cubic structure, their birefringence is too small for effective phase matching [173]. In order to overcome this and access their nonlinearity, wafers of the crystals can be stacked in alternating rotation, so as to effectively quasi-phase match the pump and idler [173, 147], in a similar fashion to periodically poled $LiNbO_3$. First proposed by Gordon et al [145] these stacks are then diffusion-bonded to create a solid mass [173, 147]. The thickness of the wafers may be any integer multiple of the coherence length of the two beams [173]. Schaar et al [147] and Zheng et al [148] have reported on this technique being used to generate THz radiation through DFG at 2.8 THz and 18.75 THz respectively. This approach has a number of drawbacks: first, there is a limit to the number of wafers that can be stacked [173], thus limiting the interaction length and efficiency of conversion; second, at each of the wafer interfaces there is some unavoidable scattering loss [173]. At 2 THz both GaAs and GaP have an absorption coefficient of 5 cm^{-1} [173], and strong phonon absorption in the range 7-8 THz

[187]. Another approach is Orientation Patterning [146] where the crystal is grown epitaxially; after a sufficiently thick layer has been deposited, the crystal is rotated and another layer grown on top and so forth. THz generation by means of DFG in OP-GaAs has been reported in the range 0.5-4.5 THz [148, 147, 162, 164, 165]. Pumping of GaAs by means of fibre lasers has been demonstrated by various workers [148, 147, 188, 163, 189]. Ready access to these materials is hindered by various international agreements.

2.3.3 ZnGeP2

Zinc Germanium Phosphide ($ZnGeP_2$) is the workhorse material of the Mid-IR with a transparency range of 2-12 μm [190, 191, 192], high nonlinearity $\chi^{(2)} = 75\,pm/V$ [193, 192] and good thermal conductivity [140]. Widely used in military applications, it is commonly employed in countermeasure systems. Pumping for $ZnGeP_2$ is typically 2.09 μm Ho:YAG, with two phonon absorption being a major concern [192, 191]. Growth and fabrication of high quality single crystals is challenging [192, 191]. DFG in $ZnGeP_2$ has been demonstrated in the range 0.21–3.74 THz [194] and it has a good FoM for the THz region. However, access to higher frequencies is limited by phonon absorption [194] with modes at 3.6, 4.26 & 6.06 THz [195, 196].

2.3.4 Chalcogenides

The Chalcogenide family of compounds also provides some materials of interest. Silver Gallium Selenide (AgGaSe), is a tetragonal nonlinear crystal with strong birefringence permitting collinear phase matching. It has a large nonlinear coefficient $d_{eff} = 33$ pm/V [197]. Silver Gallium Selenide (AgGaSe) has been used for nonlinear SHG in the near and mid-IR, at 4-18 μm by Bianchi and Garbi (1979) [198]. However in the proposed range of operation of this project there are a number of phonon absorption peaks, 10 THz, 7.5 THz, 4.5 THz and 1 THz [199]. As a consequence AgGaSe crystals have a low FoM and are effectively ruled out for purposes of this project.

Indium Telluride, (InTe) is an anisotropic crystal, displaying relatively strong second order non-linear susceptibility; while not specified, it has been compared to that of AgGaSe. Using Second Harmonic Generation (SHG), it was found to produce approximately 50% of the intensity for a given pump [200]. The intensity of the SHG was also reported to increase with an increase in crystal size, indicating Type-I birefringent phase matching [200].

2.3.4.1 GaSe

We will focus on another chalcogenide crystal, Gallium Selenide (GaSe). Described by Shi as "the best nonlinear optical material ever used" [93], ε-GaSe is a negative uniaxial crystal with hexagonal structure, a large $\chi^{(2)}$ nonlinear susceptibility ($d_{eff} \geq 54\, pm/V$) [201, 173, 168], broad transmission band (0.6–20μm) and prodigious birefringence ($\beta = 0.39\, at\, 1\, \mu m$).

GaSe has the lowest intrinsic absorption co-efficient in the THz range of any organice nonlinear crystal [168, 161] (0.2 cm^{-1} at 2 THz) [173] the crystal experiences strong phonon absorption in the range $30 - -50\ \mu m$ corresponding to 10–6 THz [202, 203, 204]; outside of this region it is available as a source for THz, and is significantly more efficient than the other commonly used crystals above, conversion efficiencies greater than 50% and pulse energies up to 40 J have been obtained using GaSe in the FIR [167]. As a consequence of these outstanding physical properties, it is clear that for THz generation GaSe has the greatest figure of merit of the commonly used crystals, several orders of magnitude higher than $LiNbO_3$ [93], see Table 2.3.

Almost the entire Mid-IR, THz and mm-wave range has been covered by DFG in GaSe [161], generation of THz GaSe has been successfully demonstrated in the ranges 0.18-5.27 THz [166], 15.78–33.31 THz [120] and 24.98-74.95 THz [129] via DFG.

Two drawbacks exist for GaSe, the first of which is that when pumped in the near IR around 1 μm two and multiphoton absorption can be a cause for concern at high intensities, on the other hand GaSe's wide transparency band allows for pumping

at long wavelengths, e.g. CO_2, which increases efficiency for THz generation from the Manley-Rowe relations (Eqn 2.41).

The second and more serious drawback is that GaSe has poor mechanical properties [90] being extremely soft, 0 on the Mohs' scale [205, 172], and due to its layered structure with weak Van der Vals bonding it is inclined to cleavage [206, 161, 204, 205]. Despite the clear optical advantages over other materials such as $ZnGeP_2$, CdSe etc. being known since the 1970's [104], the poor mechanical properties of GaSe have continually hindered its widespread adoption.

Ordinarily this would also be a significant obstacle to wide frequency tuning as the crystals can't be processed at arbitrary angles; but it is compensated somewhat by large birefringence and small phase matching angles for THz generation by type-I interactions [104]. The small angles increase the interaction length for large aperture beams, enabling the use of long crystals, 47 mm has been reported [161], increasing the efficiency of generation [207].

2.3.4.2 Doped GaSe crystals

However, it is fortunate for us that GaSe crystals provides a flexible matrix for doping with a wide variety of elements, including Aluminium (Al) [208, 209, 210], Erbium (Er) [211, 212], Indium (In) [208, 213] Tellurium (Te) [208, 214] Sulphur (S) and others[213, 205, 206, 204]. Doping of GaSe crystals with impurities can be used to improve its mechanical properties. It also appears to be an efficient method of engineering the crystal's optical properties through close control of the doping concentration.

An effective doping method for GaSe, allowing the incorporation of large quantities of the dopant into large high quality single crystals, is growth of solid solution crystals. Solid solution crystals are grown from the melt of isostructural binary compounds e.g. GaSe:GaS. To use this technique successfully there are several requirements, the dopant should be an isovalent element e.g. S, In and Te which forms isostructural compounds e.g. GaS, InSe and GaTe [215]. GaS does not typically form an isostructural compound, being inclined to crystalise in the β-polytype; how-

ever, the ε-polytype is known to exist. Thus the grown $GaSe_{x-1}S_x$ solid solution crystals will have the ε-polytype while GaSe is the principal component, the GaS crystal adapting to the GaSe lattice structure. Al, while isovalent, does not form a binary compound e.g. AlSe, and Er forms a binary but not an isostructual compound ErSe which has a cubic lattice [215]. It remains possible to dope with these two elements but the included quantities are much reduced.

Al-doping leads to increased hardness, 2 mass % has found to be the optimal concentration, furthermore it be used to control free carriers. The increased hardness enables arbitrary cutting and polishing of the crystals. But even relatively low Al-doping reduces the optical quality of the crystals [208, 209, 210], reducing its attractiveness for use in OPOs.

Er-doping has been found to enhance the nonlinearity of the crystals, its large atoms perturb the crystal lattice structure [211, 212] . Erbium doping is also found to reduce the intensity of the phonons in the range 19–22 μm shifting the longwave edge to lower frequencies [211, 212]. On the other hand, transmission in the near IR was negatively effected, increasing losses at common pump frequencies. While an increased nonlinearity appears initially attractive, the simultaneous shifting of the phonons to longer wavelengths with Er-doping is highly undesirable. This shift will have a large negative effect the ability to generate higher frequency THz radiation efficiently and even a modest increase in absorption has a major impact on the FoM (see Table 2.3).

In-doping of GaSe has much improved mechanical properties allowing it to be cut in arbitrary crystallographic directions and optically polished [213, 204]. Feng et al (2008) [205], have reported on efficient SHG in the near and mid-IR from GaSe:In pumped with a CO_2 laser. On the other hand In doping shift the shortwave edge to longer wavelengths increasing multiphonon absorption for near-IR pumping. In-doping is found to have only a weak influence on the dispersion properties [208, 204] and the nonlinear properties remain largely the same $d_{eff} = 50$ pm/V [204].

Te doping leads to minor increases in nonlineariy for small quantities, but has little influence on the mechanical properties of the crystals [214] but in common

shifts the short wave edge to longer wavelengths increasing absorption at the pump wavelengths [208], while also reducing the damage threshold [214]

In the case of AgGaSe-doped GaSe a significant enhancement of the $\chi^{(2)}$ tensor over pure GaSe has been reported, $d_{eff} = 75$ pm/V [206], but the optical quality is severely effected. Ag-doping tends to feature scattering centres, consisting of pure silver. Attempts to eliminate these through annealing have been reported to result in cracked crystals [206]. Considering the FoM, and in common with Er-doping, the significant increase in nonlinearity achieved by AgGaSe-doping does not compensate for the related increase of absorption (see Table 2.3), and the poor quality of the crystals precludes the use ofAgGaSe crystals.

Sulphur-doping is found to improve the mechanical and optical properties of the GaSe crystals, reducing the mid-IR optical absorption coefficient by a factor of 2-3 [216, 217, 218], while increasing the optical damage threshold fivefold at the optimal mixing ratio [216, 217]. The optical properties in the THz range are also found to improve [172]. On the other hand, negative effects of S-doping on the optical damage threshold and on frequency conversion efficiency have been reported [219, 220], that reflect doping-induced degradation in optical quality.

The short wave transparency edge of $GaSe_{x-1}S_x$ crystals shifts towards shorter wavelengths, thus reducing the two-photon absorption for the near-IR pump [221, 217] and cause changes in phase matching conditions that improve frequency conversion efficiency [222]. It was also predicted and confirmed experimentally that the uncommon eee Type-IV interaction can be realised in both pure and Sulpher doped Gallium Selenide crystals [219, 209]. Composition-dependent changes in the THz phonon absorption spectrum for o-wave were reported in [223, 224] but were not confirmed by other researchers [219].

It has been reported that S-doping leads to a reduction in the nonlinearity [103], and consequenctly the FoM, though it remains large (see Table 2.3). However, the improvements in the optical quality lead to a reported increase in the nonlinear frequency conversion efficiency over GaSe of up to 15 times [215]. This improvement in efficiency, coupled with the improved mechanical properties makes $GaSe_{x-1}S_x$ a

much more attractive prospect for field applications than the pure GaSe crystals [216, 172, 217, 222, 225, 226].

2.4 THz / FIR OPO and DFG Current state of the art

Relatively few THz OPOs have been developed; a survey of the peak powers reported for OPO and DFG in a number of common nonlinear optical crystal is presented in Figure 2.13.

$LiNbO_3$ remains the leading material for the generation of THz in OPOs thanks in no small part, to the ease of pumping with a single laboratory workhorse laser like Nd:YAG [171], the maturity of the material process, and the considerable time invested in the development of these instruments. Optical to optical conversion efficiencies of 50% have been found for the THz regime in pulsed OPO's tunable 1-3 THz [1], where an upper tuning range of 3.1 THz has been reported [159]. CW OPOs generating microwatts of power in the range 1.2–2.9 THz [158], and fibre pumped systems generating at 1.48 THz have been developed [179]. Narrow linewidths are possible in $LiNbO_3$ OPO with reports of 1 MHz for CW systems [183] and ≤ 5 GHz for pulsed systems [178] making them suitable for spectroscopy. $LiNbO_3$ OPOs are the most common form commercially available OPOs and THz systems are produced by MSquared Laser, Glasgow, UK [175]. Their "Firefly" instrument is tunable 1.2-3 THz and based on the systems developed by Dunn *et al* at University of St.Andrews [175].

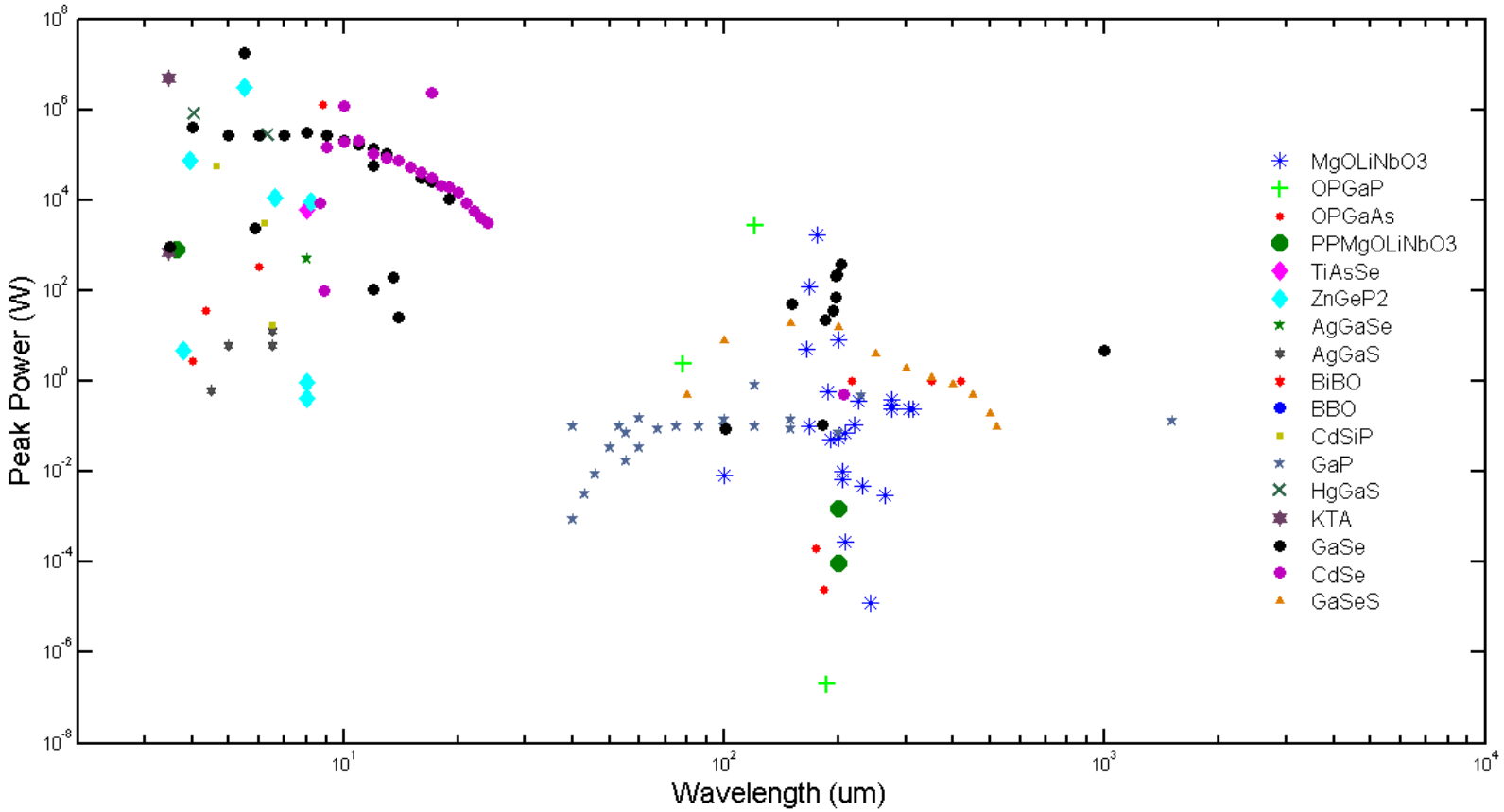

Figure 2.13: The reported peak powers for OPO and DFG in number of common nonlinear optical crystals including: $MgOLiNbO_3$ [157, 1, 158, 159], GaP [160, 161], OPGaAs [147, 162, 163], OPGaP [164, 165], GaSe [166, 167, 168, 161] CdSe [169, 167, 170, 171] and $GaSe_{x-1}S_x$[172]

$ZnGeP_2$ and CdSe are commonly used for nonlinear optical frequency conversion in the FIR normally implemented by DFG down to 22 μm [170]. $ZnGeP_2$ OPOs have been realised in the mid IR with a range 4–10 μm [104, 227, 228] and CdSe OPOs are found to have higher oscillation threshold than $ZnGeP_2$ due to the reduced magnitude of the nonlinear optical coefficient [228]. DFG in $ZnGeP_2$ has been demonstrated in the range 0.21–3.74 THz [194] and 0.8–2.45 THz [229] generating milliwatt outputs. However, phonon bands preclude its use at higher THz frequencies.

CW intracavity DFG in OP-GaAs a doubly resonant ring cavity has been developed by Keissling, with tunablity in the range 1–4.5 THz, narrow linewidth (10 MHz), and a 25 μw output [162]. Pulsed DFG systems have been developed with slightly lower tuning range 0.5-3.5 THz generating milliwatt outputs [185]. Ding has reported on pulsed DFG in the range 0.455-3.91 THz using op-GaP [165].

Organic crystals such as DAST feature, high nonlinearity 200 pm/V and low refractive index and widely tunable generation 0.7-25 THz by DFG has been reported [230]. However DAST suffers from low damage threshold and a lack of robustness. Large high quality single crystals are difficult to fabricate.

Pulsed THz generation in GaSe by DFG can produce widely tunable narrow band pulses [231, 172]. Tuneablity has been demonstrated in the range 56-5660 μm [166, 168, 161] with narrow linewidths ($<$ 50 MHz) [165] but reported result for output powers (10's of μW) [231, 207] have not met expectations with regard to output power due to poor crystal quality [231], which is strongly dependent on the growth technology and the effects of free carriers which should also be controlled. The generation of THz radiation in doped GaSe crystals is a new development with the first case of THz DFG in $GaSe_{x-1}S_x$ been reported by Huang *et al* in 2013. A tuning range of 0.57-3.57 THz with a linewidth of 100 MHz was reported, with an average output power of micro-watts [172].

2.5 Summary

In this chapter we have charted the development of the field of Nonlinear Optics, presenting a brief overview of the theory of DFG and OPO devices, and examining some of the key parameters for their efficient operation. We have also presented a survey of commonly used nonlinear crystals in the FIR and THz regions, detailing their properties with respect to the requirements of the efficient nonlinear frequency conversion by DFG or OPO via the nonlinear Figure of Merit. $GaSe_{x-1}S_x$ is identified as our preferred material for study, development and exploitation, due to its outstanding optical properties (i.e. large birefringence, low absorption & ultra-broad transparency), large Figure of Merit and improved mechanical properties compared to GaSe. A brief review of the state of the art of DFG and OPO devices for THz generation is presented.

Chapter 3

THz-TDS Spectroscopy of GaSe1-xSx

In this chapter we will briefly describe the operation of National Physical Laboratory (NPL)'s THz-TDS, and discuss the important factors in achieving accurate determination of the optical properties of GaSe crystals. We outline a rule of thumb selection criteria for measurement data, suitable for use in the formulation of Sellmeier equations and phase matching curves. We present the results of absorption and refractive index measurements of GaSe, GaS & $GaSe_{x-1}S_x$ crystals for o & e-waves in the THz regime, discuss their implications on the nonlinear Figure of Merit, and identify the most suitable dispersion equations of use in the THz regime. The transformation of the optical properties of the crystals and their phonon structure with respect to doping content is studied. The optimal doping level for $GaSe_{x-1}S_x$ crystals is estimated.

While extensive studies have been conducted into pure GaSe, the optical properties of GaSe have been published in over 1300 papers [232] and are largely concerned with the o-wave. The results within the literature are highly scattered and, it maybe assumed, dependent upon then technological state of the art for crystal growth, on the measurement facilities, and on the length of crystals studied. To a lesser extent the various doped GaSe crystals have been studied and again the data available is not consistent [219, 233, 234]. Due to difficulties in accessibility and limited processing capability, absorption spectra for e-wave (i.e. absorption anisotropy properties)

in $GaSe_{x-1}S_x$ crystals in the THz range have only been studied for 6 and 7 mass % of sulphur [209, 219]. In these studies and from measurements at fixed frequencies [194, 172] it was established that o-wave absorption (α_o) is greater than e-wave absorption (α_e) at THz frequencies in common with the results for pure GaSe. The significant absorption anisotropy suggests that e-wave generation should be the more efficient option for THz applications.

In the present work, we report, for the first time to our knowledge, detailed Terahertz - Time Domain Spectroscopy measurements of o- and e-wave absorption spectra and absorption anisotropy in the 0.3-4.0 THz range for $GaSe_{x-1}S_x$. A modified vertical Bridgman method was employed by colleagues in the Laboratory of Crystal Growth, Institute of Geology and Mineralogy SB RAS, Novosibirsk, to manufacture a dense set of high quality single solid solution crystals of $GaSe_{x-1}S_x$, (x = 0, 0.05, 0.11, 0.22, 0.29, 0.44, 1) [235, 236]. The mixing rations were selected to include key vales, x = 0.44 the maximum mixing ration possible while maintaining the ε-polytype [237, 238]; and x = 0.11-0.22 have been found to be the most efficient for THz generate [216, 217].

3.1 Introduction to THz-TDS

Of the THz techniques currently in use, Terahertz - Time Domain Spectroscopy (THz-TDS) has emerged over the past 10 years as the most popular, finding widespread usage across the natural sciences, and in many engineering and technology applications. Indeed it may now be regarded as the industry standard method in the frequency range 0.1 - 4.5 THz. This rapid proliferation is in part due to the availability of relatively reliable and inexpensive, turn-key, commercial of-the-shelf, bench top systems and data analysis software. Of course, THz-TDS has many attractive features apart from its physicist-free operation.

THz-TDS systems share the advantages common to all THz methods outlined in the introduction; briefly, many materials are transparent to THz radiation, many materials possess molecular resonances at THz frequencies, and semiconductor systems have electronic transitions resonant with THz photon energies [239]. As a

spectroscopy technique THz-TDS surpasses conventional alternatives such as FTIR in several respects [239, 240]. The sources emit single-cycle THz transients and, as such, are very broadband, and may span 5 THz [241, 239, 242]. Though the average power is low, thanks to the high spatial coherence, the source brightness exceeds that of conventional thermal sources [241, 239, 242]. The optically gated detection scheme is extremely sensitive, typical SNRs of the order of 1000-5000, and require no cooling or shielding [241, 240]. Finally, the detection is coherent i.e. both the phase and amplitude of the $\boldsymbol{E}$-field is recorded, so the complete complex dielectric constant may be readily extracted without recourse to Kramers-Konig relations [240]. Furthermore, as a short pulse, time-resolved, method THz-TDS is well suited to pump probe experiments.

3.1.1 Background

Terahertz - Time Domain Spectroscopy grew out of efforts to generate and detect ultrashort electrical pulses in transmission lines on semiconductor substrates. Several groups were involved including: Grischkowsky, at IBM Watson Research Center, Auston at Columbia University and Nuss, at Bell Labs. It was realised that, as a result of the time varying electrical currents on the transmission lines, they were acting as antenna and radiating electromagnetic pulses. In 1988, Smith, Austin and Nuss demonstrated the generation of ultrashort, sub-picosecond, pulses in these photoconductive antennae, sometimes referred to as Auston Switches. The pulses generated by the T_x antenna propagated through free space and were detected in a similar fashion by another complementary R_x antenna [243]. The frequency bandwidth of the detected pulses was $< 0.1 - > 2$ THz [243]. Fattenger and Grischkowski preformed similar experiments, integrating optical components and achieving diffraction-limited THz beams [244, 245]. From this point forward, it was possible to construct instruments. With the simple placement of the a test sample between the emitted and detection antennae Terahertz - Time Domain Spectroscopy was realised [246].

In the intervening decades and with intensive study, alternative methods of gen-

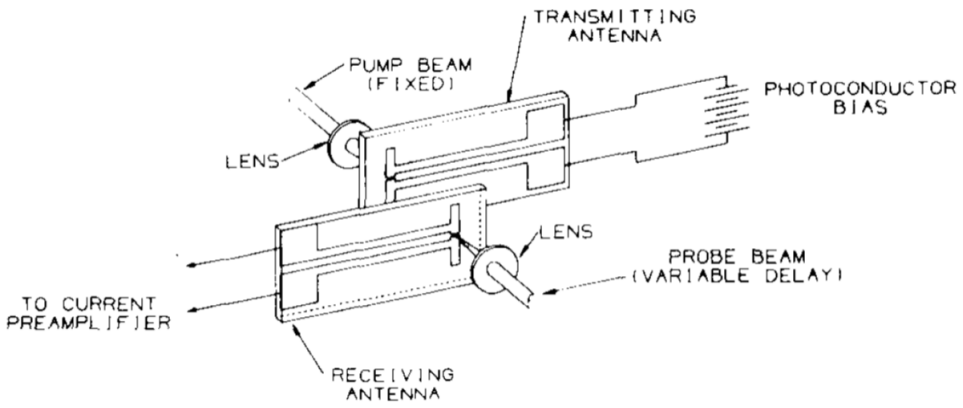

Figure 3.1: Schematic of Smith, Auston & Nuss original THz-TDS setup [243]

erating and detecting THz transients for THz-TDS applications have been developed, such as: biased photoconductive emitters, electro-optic detection [247, 248, 249, 250], optical rectification in electro-optic crystals [251], air-plasma generation [252, 253, 8, 254, 255, 92] etc. though photoconductive antennae remain the most common method employed in commercial systems.

3.1.2 NPL's THz-TDS

NPL's THz-TDS is a home-built research instrument, constructed using the standard configuration, presented in Figure 3.2. The pump laser is a mode-locked Ti:Sapphire laser (Femtosource) with a pulse length of 20 fs, a center wavelength of 800 nm, and producing an average power of 450 mW.

The terahertz radiation source is a home built biased photoconductive emitter. The electrodes are painted onto a semi-insulating GaAs substrate, using 300 μm Silver dag with a 1 mm gap between them. The GaAs substrate is mounted onto copper blocks, which facilitate cooling of the emitter and form the outer electrodes. The voltage source (Zomega) supplies a bias voltage of 205 V, across these electrodes, with unipolar modulation of 10 kHz. Producing a linearly polarised beam with an average power in the range of μw.

The THz radiation is guided through the system by a set of four off-axis 90° parabolic mirrors, as shown in Figure 3.2. All four mirrors have the diameter of 75 mm; mirrors M1 and M3 have an effective focal length of 25 mm, and 75 mm

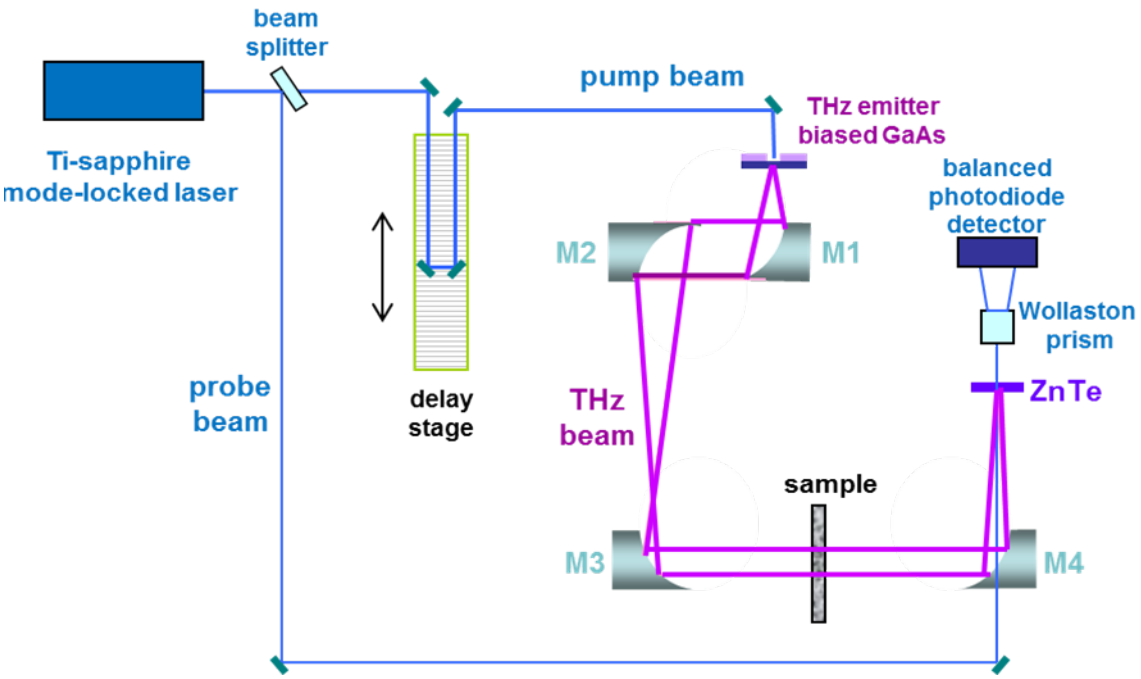

Figure 3.2: Schematic of NPL's Terahertz - Time Domain Spectroscopy system

for mirrors M2 and M4. In the collimated section of the beam between mirrors M3 and M4 the nominal beam waist is 25 mm. The short focal length and large diameter of mirror M1 allows for a sufficiently large fraction of THz radiation to be collected from the emitter, dispensing with the need for a silicon hyperhemispherical lens. The focal point between mirrors M2 and M3 is used primarily for imaging, or occasionally for spectroscopy of small objects. The collimated beam between M3 and M4 is primarily used for transmission spectroscopy measurements, which avoids errors arising from beam distortion that may be caused by placing a sample at the beam focus [8]. This nominally collimated beam section, which is 775 mm long allows of additional mirrors to implement a reflection geometry.

The THz pulses are detected electro-optically, using a 0.5 mm thick (110) ZnTe crystal, placed at the focus of M4, and balanced Si photodiodes (Nirvana).

NPL system has been calibrated for detection linearity, frequency and beam shape [256, 257, 258, 259, 260]; work is on-going with NPL's German counterpart, Physikalisch-Technische Bundesanstalt (PTB), to determine an absolute calibration of power [261]. A well calibrated instrument is particularly important for the measurement of GaSe crystals as the data is widely scattered, in particular in the THz

region. One of the origins of this scatter is the wide variation in the quality of the crystals and the technological control of their defects available in the growth process. However, an ongoing round robin intercomparison study lead by Naftaly *et al* at NPL has shown that even amongst THz-TDS specialist groups considerable variability is found in the measurement of "standard" THz materials [262, 263], the details of which are the subject of a forthcoming paper. Hence, it is likely that measurement process is another significant source of scatter in the data and we will pay particular concern to the careful performance of the measurements to reduce uncertainties.

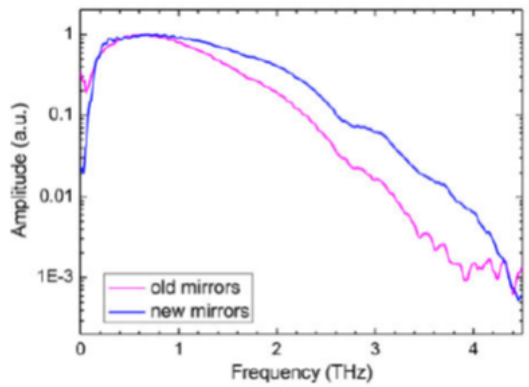

(a) THz-TDS Spectrum

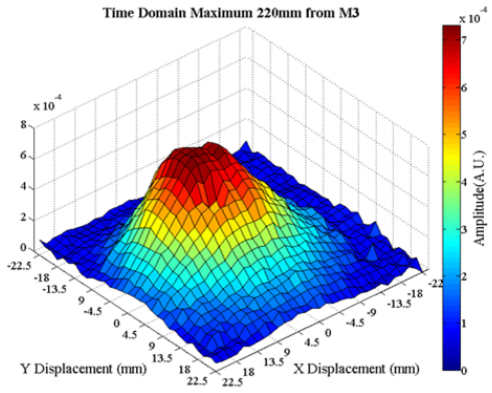

(b) Beam Shape

(c) Frequency Calibration

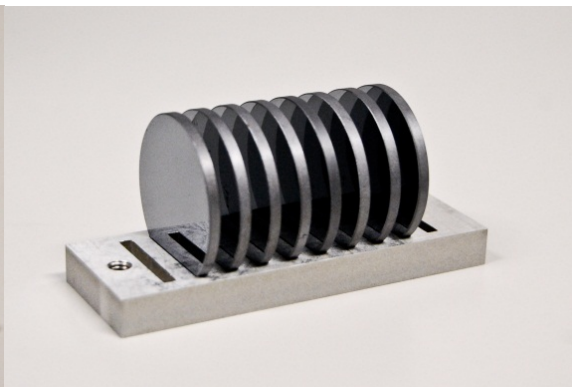

(d) Linearity Calibration

Figure 3.3: Spectrum, beamshape and artefacts for calibration of NPL's Terahertz - Time Domain Spectroscopy system

3.1.3 Operation of THz-TDS

In the case of NPL's THz-TDS, a single cycle pulse of THz radiation is generated through the excitation of a home-made Gallium Arsenide photoconductive emitter (described above), by a portion of the femtosecond laser, the pump beam. When light from the laser is focused on the gap between the electrodes it excites charged carriers into GaAs's conduction band, these carriers are then accelerated across the gap by the applied bias voltage. The acceleration leads the charged carriers to radiate, in a pulse lasting several picoseconds, at THz frequencies. The radiated field of the THz pulse E_{THz} is proportional to the time derivative of the induced photocurrent J_{pc} and given as [264]:

$$E_{THz} \propto \frac{dJ_{pc}}{dt} = q_c \frac{dN_c}{dt} v_c + q_c \frac{dv_c}{dt} n_c \tag{3.1}$$

where q_c is the carrier charge, $\frac{dN_c}{dt}$ is the change in charge density and $\frac{dv_c}{dt}$ is the charge acceleration. These THz pulses propagate through the system illuminating the object under test. The remainder of the laser beam, the probe beam, propagates along an optical delay-line and into a ZnTe electro-optic detection scheme, collinear with the transmitted THz radiation.

The fs pulses from beam probe propagate collinearly with the much longer THz pulse (ps) as they interact in the ZnTe. The THz pulse induces a change in the refractive index of the ZnTe (the electro-optic effect), which rotates the polarisation of the probe beam's fs pulse, where the phase retardation is described as [264]:

$$\Delta\phi = \frac{2\pi L}{\lambda_{probe}} n_{probe}^3 r_{eff} E_{THz} \tag{3.2}$$

where L is the length of the crystal, n is the refractive index and r_{eff} is the effective electro-optic coefficient. Using a Wollaston prism the vertical and horizontal components of the probe beam can be separated and the differential signal is detected using a pair of balanced photodiodes. The differential signal between the two beams, is proportional to the induced phase retardation of the probe beam, and hence, is proportional to the amplitude of the $\boldsymbol{E}$-field of the THz pulse. For small values of

$\Delta\phi$ a linear relationship with the detected signal can be assumed, given as [264]:

$$\frac{\Delta I}{I} = sin\,\Delta\phi \approx \Delta\phi \tag{3.3}$$

By sweeping the delay-line, phase and amplitude of the THz pulse at each point may be determined. THz-TDS systems may be used in either transmission or reflection, though in our instance all measurements will be in the preferred transmission configuration.

For each sample, a series of time-domain spectra, $f(t)$, are recorded and a simple average then taken over the series. Using the FFT algorithm we obtain the frequency-domain spectrum, $F(\omega)$, from which the absorption and refractive index spectra maybe calculated. To determine the refractive index spectra of the measured samples, it is first necessary to determine the phase-difference due to the sample's presence in the beam path with respect to frequency $\Delta\psi(\omega)$ as given by:

$$\Delta\psi(\omega) = \psi(\omega)_{ref} - \psi(\omega)_{sample} \tag{3.4}$$

where $\psi(\omega)_{ref}$ and $\psi(\omega)_{sample}$ are the phase curves of the reference spectrum, $F(\omega)_{ref}$ and the sample spectrum, $F(\omega)_{sample}$, respectively. The refractive index spectrum $n(\omega)$ may now be described by:

$$n(\omega) = 1 + \frac{c}{\omega \cdot d}\Delta\psi(\omega) \tag{3.5}$$

Where c is the speed of light, ω is the frequency and d is the sample thickness. In order to calculate the absorption spectrum of the sample $\alpha(\omega)$ it is first necessary to calculate the amplitude ratio $A(\omega)$ of the two recorded spectra:

$$A(\omega) = \frac{A(\omega)_{sample}}{A(\omega)_{ref}} \tag{3.6}$$

Where $A(\omega)_{sample}$ and $A(\omega)_{ref}$ are the amplitudes of the recorded spectra $F(\omega)_{sample}$ and $F(\omega)_{ref}$ respectively. By combining the results of Eqn 3.4, 3.5 & 3.6, the ab-

sorption coefficient for the sample $\alpha(\omega)$ maybe be described by Eqn 3.7

$$\alpha(\omega) = -\frac{2}{d} ln \left\{ \frac{A(\omega) \cdot [n(\omega) + 1]^2}{4n(\omega)} \right\} \tag{3.7}$$

These measurements and calculations were performed on the range of samples available and the results for refractive index and absorption are presented below. The resolution of THz-TDS system is dependent upon the length of the measurement by the relation $\Delta\nu = \frac{c}{2L}$, where c is the speed of light in vacuum and L is the length of the scan. In typical operating conditions NPL's THz-TDS is scanned for 40 mm (13.3 ps) leading to a resolution $\Delta\nu$ = 3.75 GHz [265]. The measurements were performed with a resolution of 3.75 GHz unless otherwise stated, at 300 K and ambient atmospheric pressure, in a dry air environment, to exclude the effects of water absorption.

3.2 Metrological Methods and Data Selection

Figure 3.4 depicts a selection of our early THz refractive index and absorption spectra for GaSe and doped GaSe samples as measured by NPL's calibrated and well aligned Terahertz - Time Domain Spectroscopy, described in detail above. The crystal samples were placed in the focus of the THz beam owing to their small size. Features of particular note are the phonon associated with the ridged layer mode $E'^{(2)}$ centred at 0.595 THz the $E''^{(2)}$ mode of $GaSe_{x-1}S_x$ crystals at 1.78 THz and the mode at 2.7 THz. The $E''^{(2)}$ mode of $GaSe_{x-1}S_x$ is due to the Sulphur doping suppressing the ridged layer mode $E'^{(2)}$.

As can be clearly seen, these early results, although reasonable care was taken in their measurement, are of a poor quality, and are in clear disagreement with various aspects of the literature, the values of refractive index for the $GaSe_{x-1}S_x$ crystals are too small and change non-linearly with sulphur content, and for Te doped GaSe (0.05%) values are wildly inaccurate below 2 THz; furthermore phase unwrapping errors can be observed at 3.4 THz in $GaSe_{x-1}S_x$ $S = 4\%$. However, as stated above, despite extensive studies of the optical properties of GaSe, the values given in the

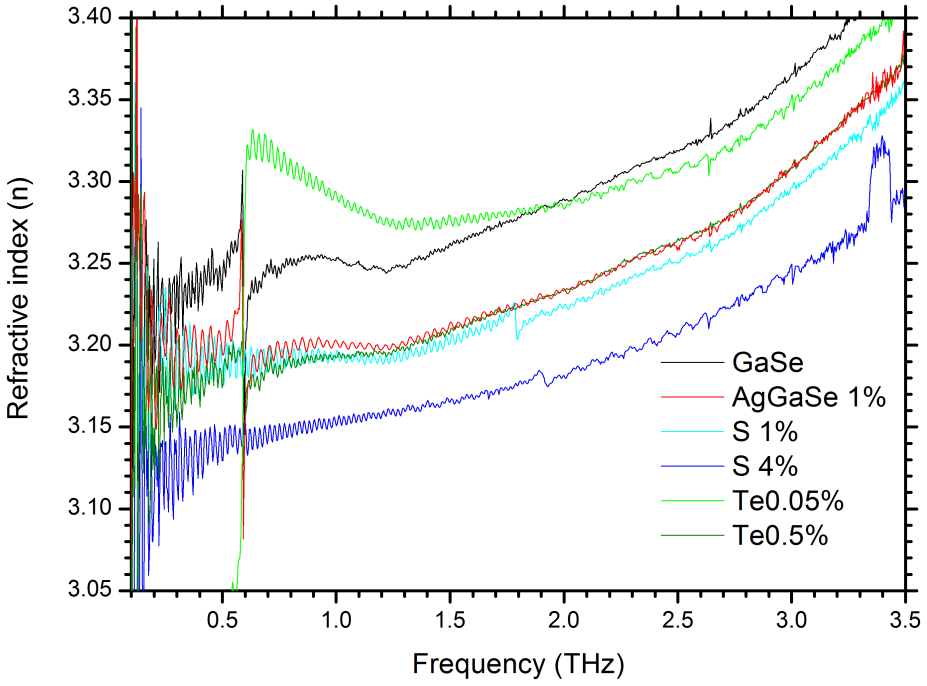

(a) Refractive Index

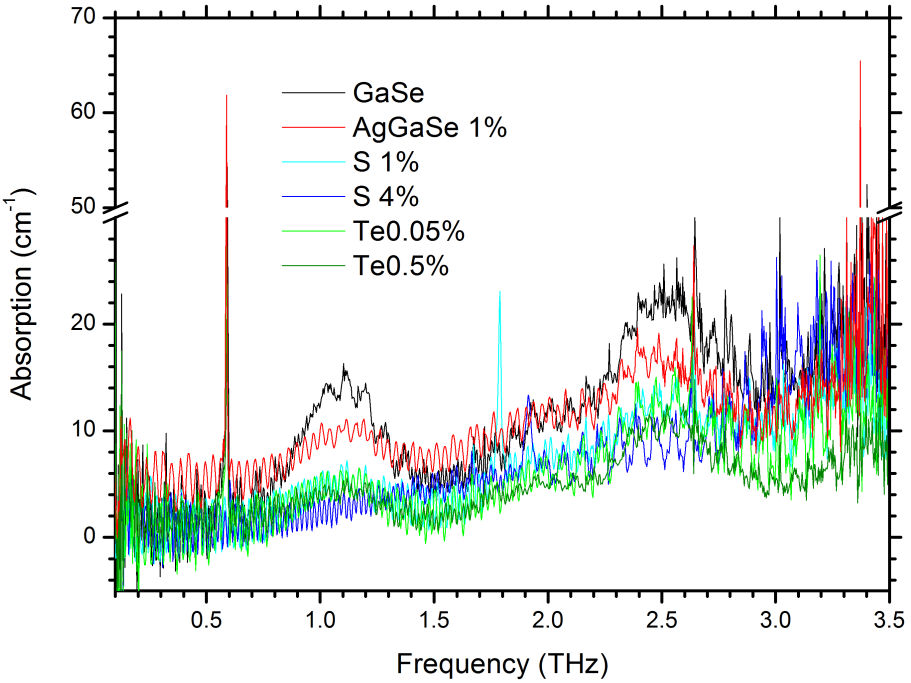

(b) Absorption

Figure 3.4: Early refractive index and absorption spectra for GaSe, AgGaSe, and GaSe doped with Sulphur (S) and Tellurium (Te)

literature as with those recorded in our early measurements, remain scattered and often contradictory, in particular for the THz regime. The consequences of this scattered data is the inability to select the best crystal for use in nonliner frequency conversion at THz frequencies, and when in use the variability of the Sellmeier equations and phase matching curves lead to difference in the generated wavelengths of 100s of μm. Moreover, it is not possible to methodically improve the doping and growth process of crystals for use at these frequencies when the fractional changes required for optimisation are lost in the measurement to measurement variation. Thus the question arises *"How can we identify valid experimental data?"* in order to bring some certainty to the optical properties of GaSe.

3.2.1 Fabrication of $GaSe_{1-x}S_x$ High Quality of Crystals

To accurately determine the optical properties of GaSe, GaS and $GaSe_{x-1}S_x$ it is imperative to have the best available quality crystals with well controlled parameters. Such crystals were specially grown by colleagues in Laboratory of Crystal Growth, Institute of Geology and Mineralogy SB RAS, Novosibirsk, using modified vertical Bridgman methods, technology and equipment they have pioneered [235, 236, 266] .

The effort to achieve crystal quality should begin with the raw material i.e. Ga 99.9997, Se 99,99 and S 99.95. These elements were further purified through remelting in a continuously evacuated ampoule. The determination of the mass of the stoichiometric charge of Ga and Se, and for $GaSe_{x-1}S_x$ nominal sulphur content x = 0, 0.01, 0.05, 0.11, 0.22, 0.29, 0.44 was performed with an accuracy of $\pm$ 0.1 mg. To minimise the quantity of rest gases and reduce the interaction between them and the melt, the ampoules were heavily loaded, in-excess of 65%. The ampoules for growth and synthesis were evacuated to a residual pressure of $\approx 10^{-4}$ Torr. Following a period of melt (crystal material in liquid form) homogenization, the temperature was decreased slowly (approx 10 K/h) to 1198 K, 40 K below the melting point of the crystal, i.e. GaSe. At this point the furnace is switched off. The resulting ampoules of synthesised large grain polycrystalline materials with various sulphur concentrations is shown in Figure 3.5

Figure 3.5: Synthesised polycrystalline material in ampoules

For the final crystals, unseeded growth was realised using a modified vertical Bridgman method with heat field rotation [266, 217]. The growth was without a seed due to the difficulty in preparing undeformed examples. The previously synthesised polycrystalline materials are loaded into cylindrical single wall quartz ampoules. The ampoule is placed into the furnace which has a temperature gradient of 15 K/cm at the estimated level of the crystallization front. After homogenization of the melt at the temperature of 30 K above the melting point, the ampoule was mechanically lowered at the speed of 10 mm/day. Further details of the synthesis and growth processes have be reported in our publications [267, 268, 269].

In order to avoid contamination, the melt should be protected from contact and interaction with the ampoule's walls. This is achieved by coating the internal surfaces with pyrolytic carbon. The carbon coating permits the easy, and without deformation, removal of the soft crystals from the the ampoule to which it might otherwise adhere.

A visual inspection of as-grown crystals indicates their high quality. Crystals showed consistent colour along their whole length. There is no or only small eutectic regions present on the top surface of the crystal as seen in Fig 3.6. This is a result of the heat field rotation which is effective in improving convection during the growth process, ensuring a good distribution of components throughout the crystal.

Figure 3.6: As grown GaSe crystal, showing consistent colour and small eutectic region to the above the red line .

3.2.2 Preparation of High quality Crystal Samples

Two types of GaSe, GaS and $GaSe_{x-1}S_x$ samples were fabricated for this study. The first type was cleaved from as-grown boules, i.e. it had faces orthogonal to the c-axis, so that a beam traversing the sample propagated parallel to the c-axis ($\| \ c$). In the cleaved GaSe, GaS and $GaSe_{x-1}S_x$ the 001 surface is atomically flat, so that the surface finish of these easily cleaved crystals is suitable for the study of optical properties [270, 210].

The second type of sample was cut so that a traversing beam propagated orthogonally to the c-axis ($\perp \ c$). These samples were prepared both at NPL and by colleagues in the Laboratory of Crystal Growth, Institute of Geology and Mineralogy SB RAS, Novosibirsk. The samples were manufactured by immersing a section of the as grown boule in methyl acrylate monomer mixed with a thermo-initiator and placing it in an oven for polymerization. Once cured, the polymer supported

the crystal structure sufficiently such that it may be cut along arbitrary crystallographic directions. For our studies the boules were cut perpendicular to the growth layers ($\perp \vec{c}$) by a thin diamond blade saw providing axis to both the o & e - wave components. The surfaces were polished with fine particles (0.8-1.2 μm), fraction separated from POLYRIT powder (ErmakChem Co., Russia) [267, 235, 268], or in the case of the locally fabricated samples by 9 μm particles.

The produced samples of both types were free of precipitates, broken layers, dislocations, micro bubbles, or other visual defects Fig 3.7. A variety of thicknesses were produced in the ranges of $<$ 1 mm to 1-2 mm.

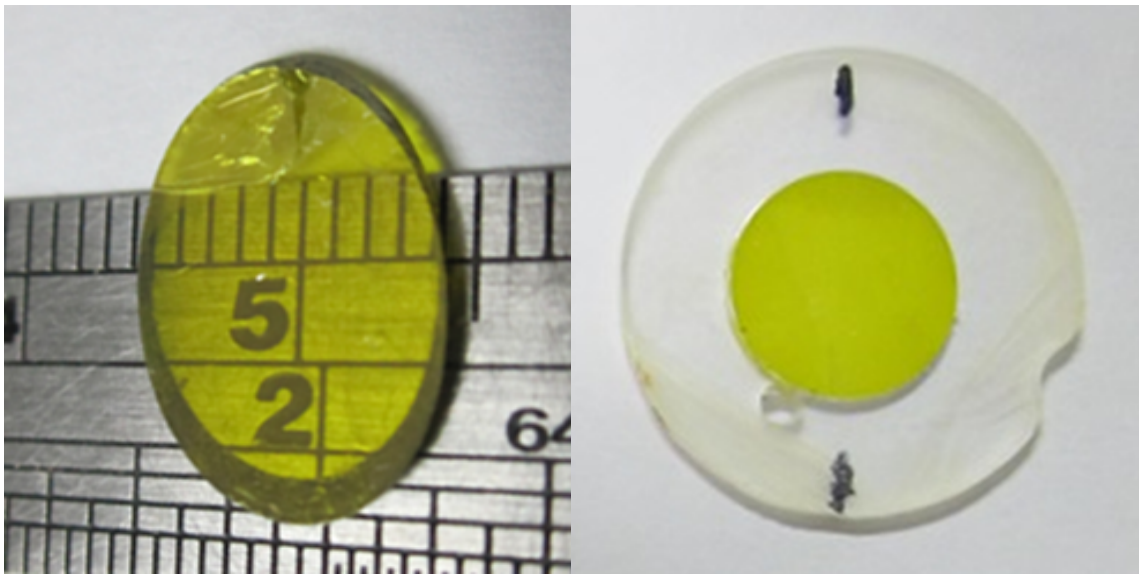

(a) Cleaved (b) Cut and Polished

Figure 3.7: Cleaved GaS, and cut and polished GaS mounted in polymer

3.2.3 Crystal Quality

In the first instance, high quality samples are required. The growth of high quality crystals is described in brief above. The samples selected for measurement should be monocrystalline and uncontaminated, of high optical quality, free from cracks, inclusions, and local deformations. For samples cut and prepared along crystallographic directions, the polish should be of good quality and care taken to ensure that the facets are plane parallel so as to exclude any scattering or wedge effects.

To insure the quality of the samples met these standards they were rigorously

studied by a variety of methods, detailed below, by colleagues at the Siberian Physical-Technical Institute of Tomsk State University, using the equipment of the Tomsk Region Common Use Centre, including the XRF, EDAX, TEM and SEM measurements. All measurements to characterise the properties of the $GaSe_{x-1}S_x$ crystal samples were conducted at 300 K.

3.2.3.1 Composition, Structure and Polytype

X-ray fluorescence analysis (XRF) was used to determine the Ga, Se and S content of the samples. Measurements were performed using a X-Ray Fluorescence Spectrometer (Shimadzu XRF 1800) with an accelerating voltage of 40 kV, a current of 95 mA, a detection limit of $\approx 10^{-6}$, a scanning step of 0.1°, and a scanning speed of 8°/min. To provide additional confidence in the results, samples with a known composition of Ga/Se/S powder were used as reference samples; the standard deviation was below 0.05 %.

The results were further verified by Energy-Dispersive X-ray Spectroscopy (EDAX) measurements of elemental composition using an EDAX ECON VI micro analyzer. An X-ray diffractometer Shimadzu XRD 6000 (Japan), and a transmission electron microscope (TEM) CM12 (Philips, Netherlands) were used in the Selected Area Electron Diffraction (SAED) method to analyse the structure. Only Ga, Se and S peaks were seen in the EDAX spectrum, indicating the high purity of the grown crystals. EDAX spectra recorded while scanning the surface confirmed the uniform distribution of the sample composition. The analysis showed that the average atomic ratio of Ga:Se:S was close agreement with to the composition of the charge placed in the boules. The diffraction patterns clearly confirm the high quality of the ε-polytype crystalline structure (point group symmetry 62m), which is similar to that of ε-GaSe widely used for THz applications. For further details please see [271].

Crystal polytype was initially determined by using a nonlinear optical method, (i.e. second harmonic generation from a CO_2 laser pump) [214]. Polymorphism is the ability of materials to exist as several different crystal structures. A special

case of polymorphism is polytypism, where the structure of the crystals varies in only one dimension, in layered crystals like GaSe we can think of this as different stacking options of the fundamental blocks. The nature of the polytype is important as the resulting structure may not always be non-centrosymmetric and hence would be unsuitable for second order nonlinear frequency conversion [237, 272]. The ε and β - polytypes are depicted in Figure 3.8.

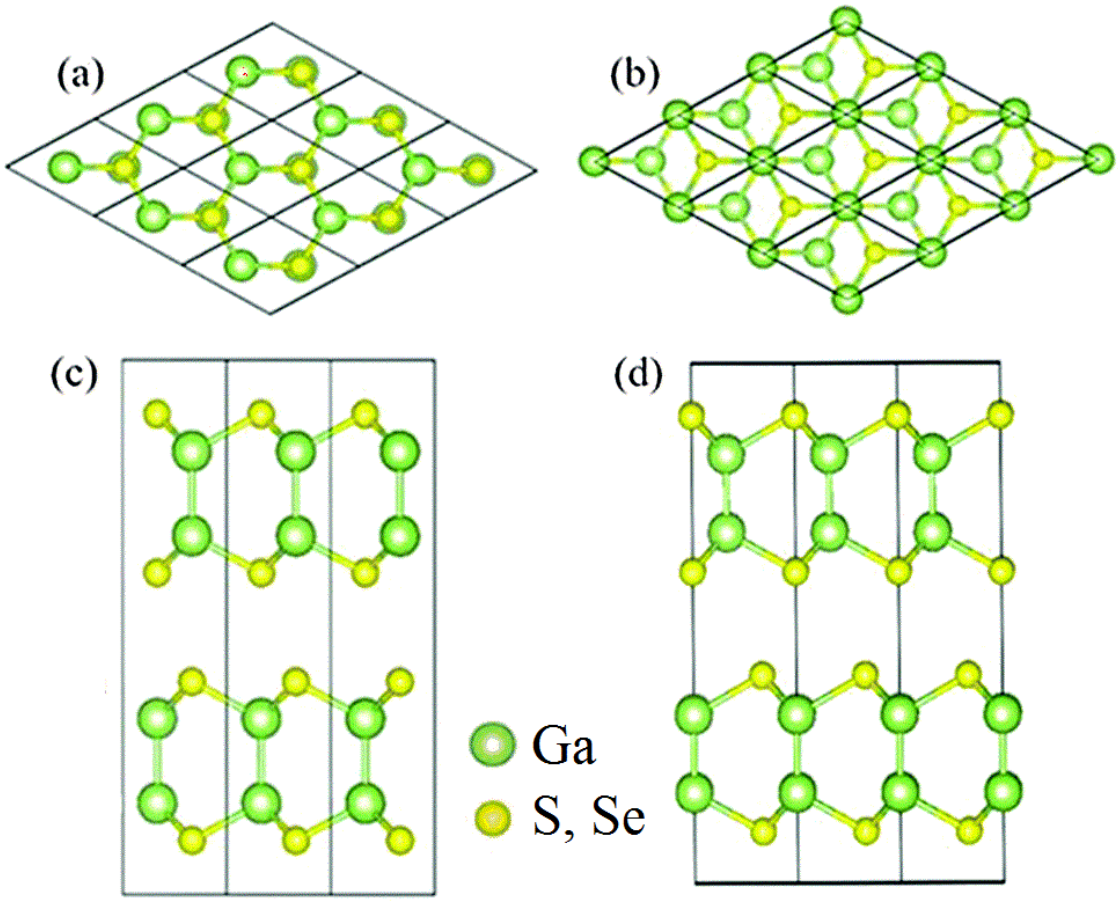

Figure 3.8: Schematic of the β - polytype (a) & (c) and ε - polytype (b) & (d) of GaSe [273]

3.2.3.2 Optical Quality

Optical absorption coefficients of GaSe grown by modified technology are three times lower than those of crystals grown by the conventional Bridgman method. It was found that in unpolarised light the absorption coefficient for both GaS and GaSe crystals does not exceed 0.05 cm^{-1} within their maximum transparency range, 0.6–

20 μm, although it is significantly narrower for GaS than for GaSe.

3.2.3.3 Surface Quality

Scanning electron microscopy (SEM) with a SEM Quanta 200 3D (FEI, Netherlands) microscope was employed to study the surface morphology of the samples. For carefully prepared samples, cleaving of the crystal along the growth layer $\langle 001 \rangle$, i.e. perpendicular to the c-axis, produces atomically flat surfaces. These high quality surfaces are suitable for studies of optical properties [270, 210]. In contrast, cut and polished samples exhibit regions of local defects, primarily scratches and fractures along growth layers. The polished surfaces of thicker $>$ 1 mm retain sufficient optical quality to facilitate THz measurements. In the thinner samples however, the density of defects is such that it prohibits their use for these measurements. Repeat handling, continued contraction of the polymer after initial curing, and differential thermal expansion may contribute to the degradation in quality of thin samples in the time following fabrication. Having considered the samples it is necessary to take into consideration several metrological issues, such that the measurement conditions are optimal and questionable results may be rejected.

3.2.4 Crystal Orientation

As $GaSe_{x-1}S_x$ is a birefringent crystal, care must be taken when measuring cut & polished samples to ensure that the crystal direction you wish to measure is well aligned with the polarisation of the THz beam. When measuring the higher refractive index o-wave, an assessment of the alignment may be made by examining the time domain trace for the e-wave component which will appear as a pre-pulse. The crystal, mounted on a stage should be rotated in the vertical plane until the pre-pulse vanishes, it is now aligned for o-wave measurements; to achieve alignment for e-wave measurements one simply rotates the crystal by 90°.

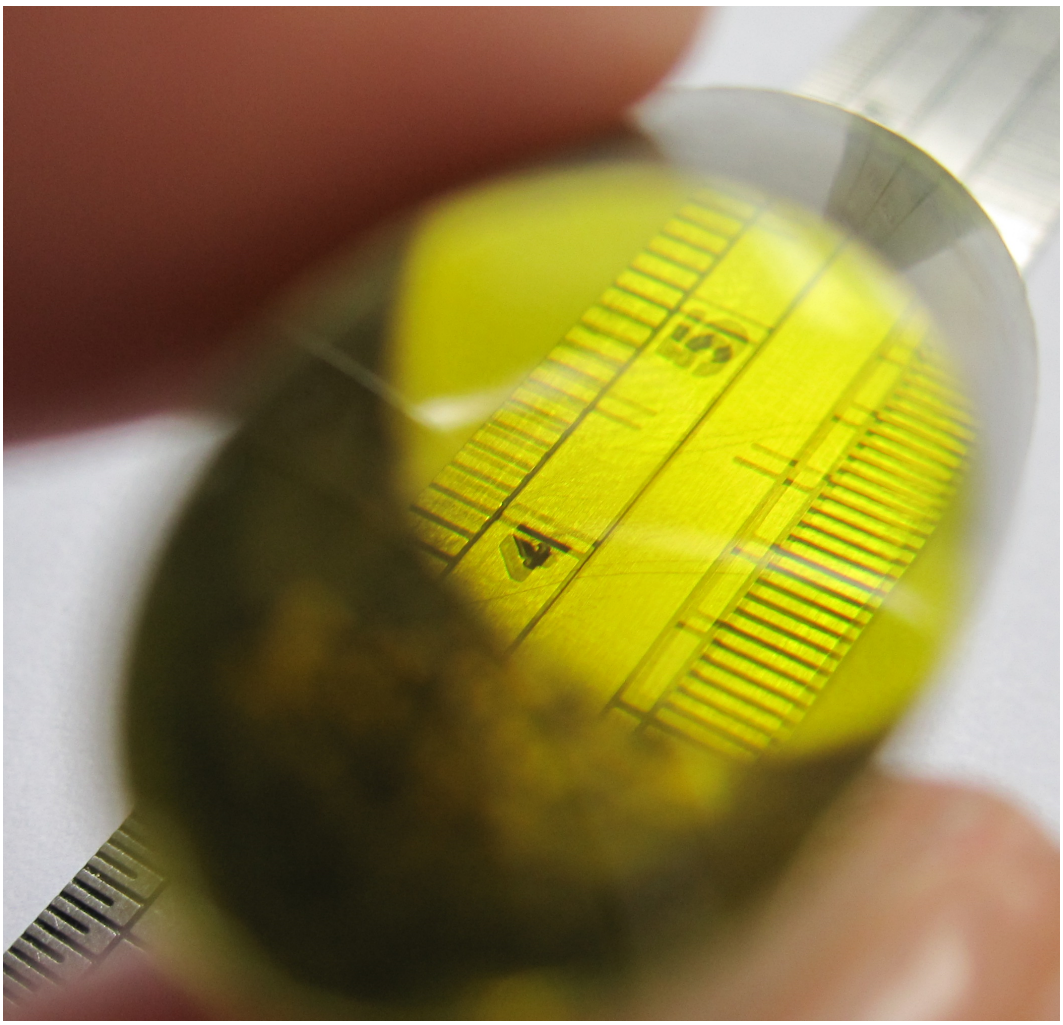

Figure 3.9: Birefringence in as grown GaS crystal.

3.2.5 Crystal Alignment

In THz-TDS systems with ZnTe electo-optic detection it is relatively straightforward to ensure that the samples are normal to the incident THz beam. One simply aligns the sample such that it is normal to the back reflection of the probe from the electro-optic crystal. For electro-optic detection of THz in ZnTe, (110) cut crystals are used and phase matching is collinear. Thus in well aligned systems, like NPL's (see above), the back reflection of the probe beam from the ZnTe surface propagates along the same axis as the incoming THz beam.

While such alignment is straight forward in NPL's THz-TDS, the benefit of the back reflection from the electro-optic crystal is not available in most commercial systems. In such cases, alignment must be approached iteratively between measure-

ment and alignment. The ordinary wave measurements n_o will be at the maximum and the extraordinary wave measurements n_e will be at a minimum when the crystal is orthogonal to the incident THz beam. We can see from Figure 3.10 that for angles greater than 5° misalignment can have a serious impact on the accuracy of both refractive index and absorption measurements.

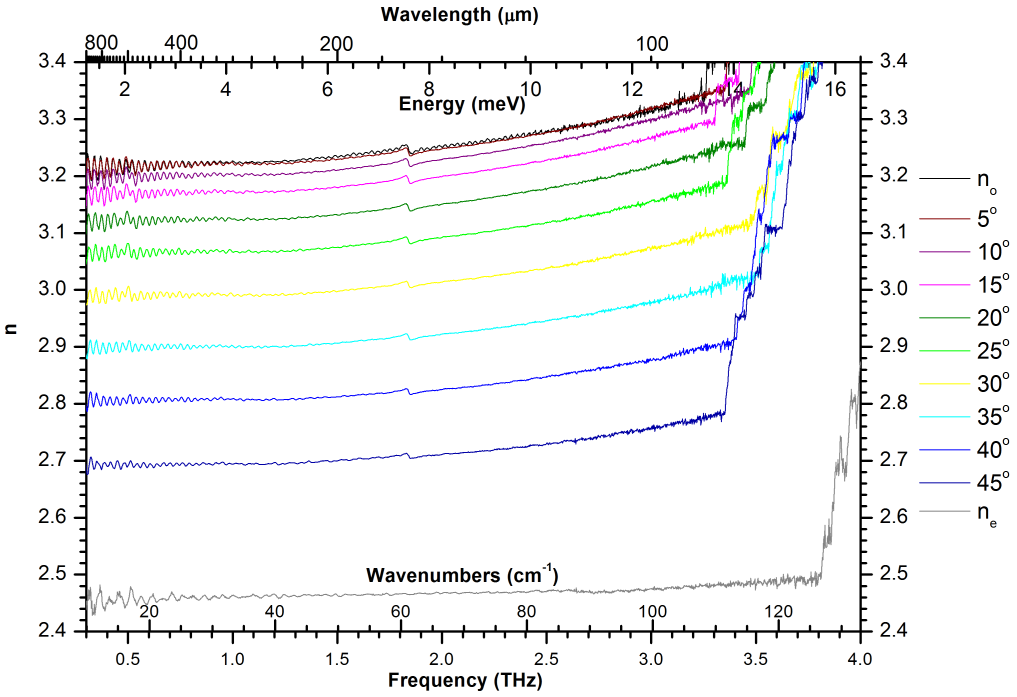

(a) Refractive Index Spectra

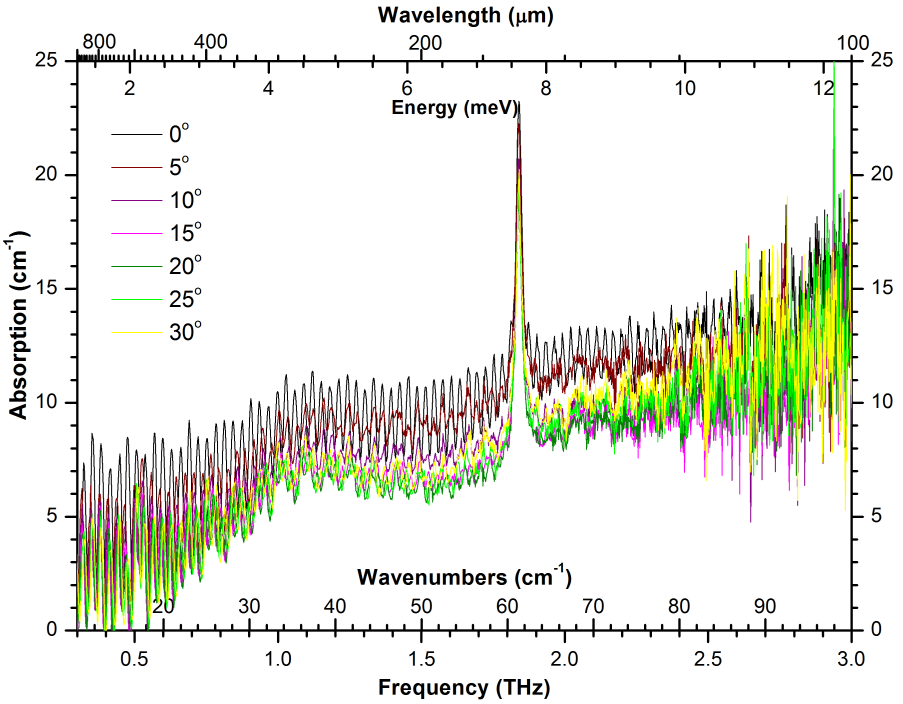

(b) Absorption Spectra

Figure 3.10: Impact of Angle Variation on the refractive index and absorption spectra.

Furthermore, in the case where processed samples are not available $n_e(\theta = 90)$ may be determined by rotating the sample. Knowing the value of n_o, the measured value of n, and the angel of inclination, n_e can be calculated using Eqn 2.71. A high quality sample of $GaSe_{x-1}S_x$ x = 0.22, was selected and mounted on a rotary stage (goniometer) between mirrors M2 and M3 and aligned normal to the path of the THz beam using the method described above. The crystal was then rotated relative to the optical axis of the system, with measurements recorded every 5 ° from normal incidence 0° to 45°. The refractive index spectra were calculated for each and are presented in Figure 3.10 (a); the absorption spectra were also calculated and are presented in Figure 3.10 (b).

The change in refractive index with rotation was calculated using Eqn 2.71 for the $GaSe_{x-1}S_x$ x = 0.22 crystal at three frequencies 1, 2 & 3 THz, this was then compared with the measure refractive indices, the results are presented in Figure 3.11. We can see from the data that the results are in reasonable agreement up to 30°, after which the result begin to underestimate the value of n_e ($\theta = 90$). This can be as a result of a number of factors, but beam distortion is likely the major factor [265].

3.2.6 Crystal Thickness

The accurate determination of refractive index is reliant on the ability to accurately measure the thickness of the samples. This is particularly important when dealing with thin high refractive index materials such as our $GaSe_{x-1}S_x$ samples. The error in the refractive index is related to the error in thickness by the relation [265]:

$$\frac{\Delta(n-1)}{n-1} = \frac{\Delta d}{d} \tag{3.8}$$

For example, our Vernier callipers (Mitutoyo) have, as is typical, an accuracy of $\pm 0.02mm$, which on a 10 mm thick sample represents a satisfactory error of 0.2%, but on a typical $GaSe_{x-1}S_x$ sample with thickness 0.5 mm, this represents a rather unsatisfactory error of 4%. Figure 3.12 below shows the uncertainty in the refractive index arising from the measurement uncertainty in the sample thickness. A differ-

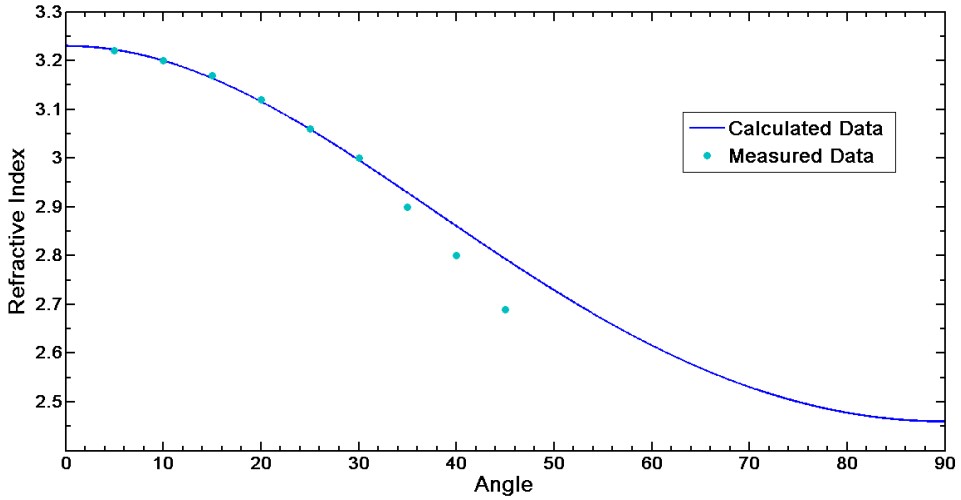

(a) 1 THz

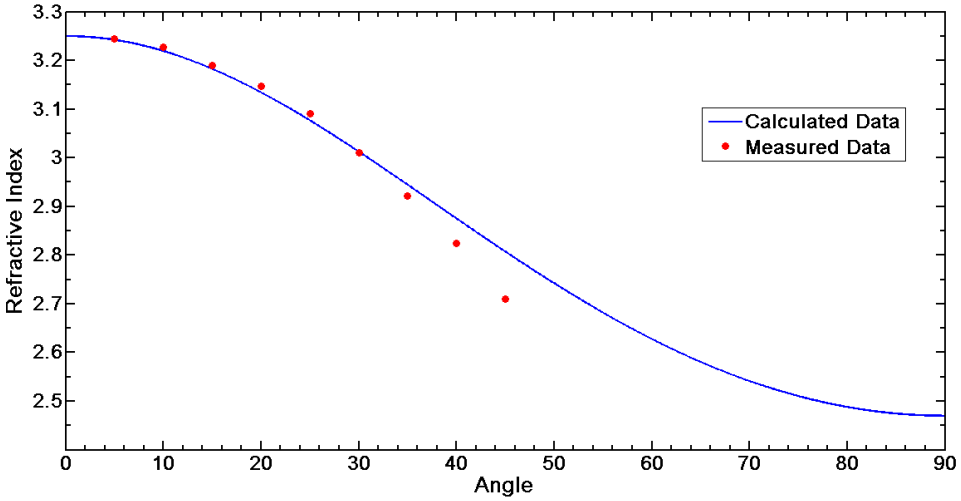

(b) 2 THz

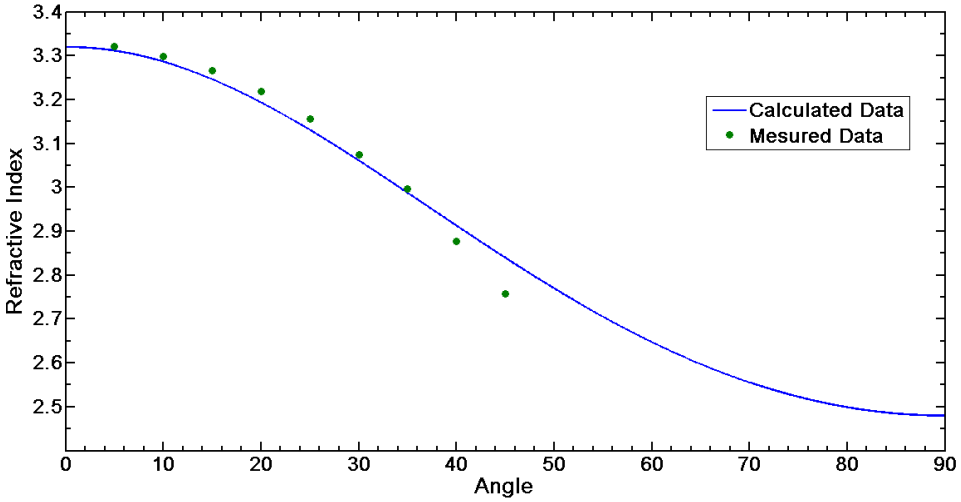

(c) 3 THz

Figure 3.11: Determination of n_e by crystal rotation; the lines represent the data calculated from Egn 2.71, and the dots are the measured results.

ence of 1% in the estimated thickness (corresponding to $\approx 10\,\mu$m) produces a shift in magnitude of refractive index ($\Delta n = 0.02$ at $n = 2.45$) equivalent to a difference in the mixing ratio of about x = 0.18. This is far in-excess of the resolution we require to confidently determine the variation in optical properties of $GaSe_{x-1}S_x$ with doping content.

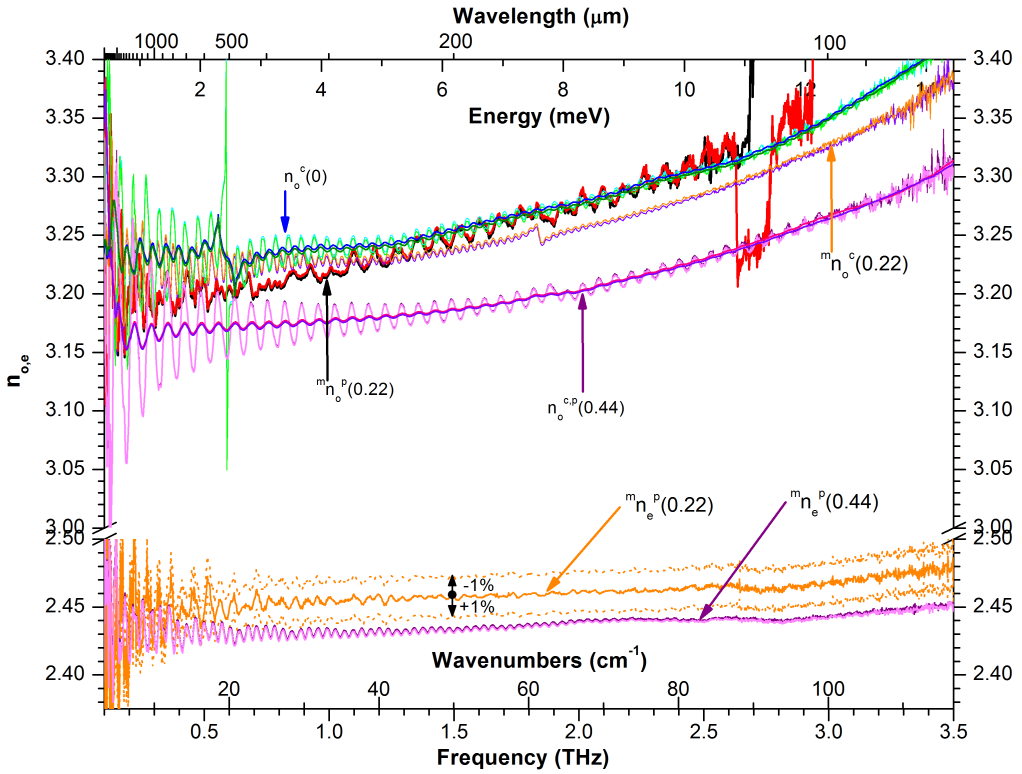

Figure 3.12: Dispersion spectra of a selection of $GaSe_{x-1}S_x$crystals, showing the impact of sample thickness on refractive index, n_o and n_e, refractive index spectra for cleaved and polished (right superscript c and p respectively) $GaSe_{x-1}S_x$ samples. The mixing ratio x is shown in brackets. As measured and smoothed curves are indicated by the left superscript m and s respectively, e.g. ${}^{m}n_o^p(0.22)$ is the as measured o wave refractive index of a cut and polished samples of $GaSe_{x-1}S_x$ x = 0.22 crystal

Clearly it is necessary to use more accurate instruments such as micrometers, where, typically, an accuracy of ± 0.001 mm is achievable, though a figure of ± 0.005 mm is a realistic in practice. One should be careful to avoid applying undue pres-

sure to the samples through the micrometer heads as the crystals, being extremely soft, are easily deformed. Furthermore, it is advisable to make use of ball-ended micrometers to mitigate against scratching of the polished crystal surface, as many micrometers have spindles that rotate as they are closed by the screw mechanism. The error due to thickness inaccuracy in samples of 1 mm thickness is on the order of ± 0.015 in the refractive index measurements of GaSe crystal, approximately twice the measurement to measurement error due to minor angular misalignment ± 0.008. It has been observed that, in thin, low-doped, processed samples, the measurement to measurement variation increases with time and handling. The likely causes are continued shrinking of the polymer after curing, differences in the thermal coefficient of expansion in the crystal, and most significantly, the introduction a high density of cracks from handling. It is therefore recommend that the samples are stored carefully and handled as infrequently as practicable.

3.2.7 Spectrometer Resolution

The rigid mode phonons in GaSe involve the whole crystal ensemble and hence have a high Q, in high quality crystals, with a bandwidth narrower than that of the spectrometer's resolution in typical operation($<$3.75 GHz), the bandwidth of the phonon is estimated to be $<$2.5 GHz (FWHM), the bandwidth of the phonon was later measured as 2.89 GHz (FWHM)using the high resolution of the **Terascan 1550** continuous wave frequency domain spectrometer (Toptica GmHb, Germany). It is not common to see phonons of such a narrow band within THz spectroscopic studies of condensed matter; for example the phonons in common THz materials such as sucrose, fructose, lactose have a bandwidth of around 200 GHz. So they could be easily overlooked, indeed in the author's own initial measurement the presence of the well-known rigid layer phonon mode $E^{(2)}$ at 0.595 THz [224, 274, 275] was not reliably detected at the typical system operating resolution of 15.0 GHz.

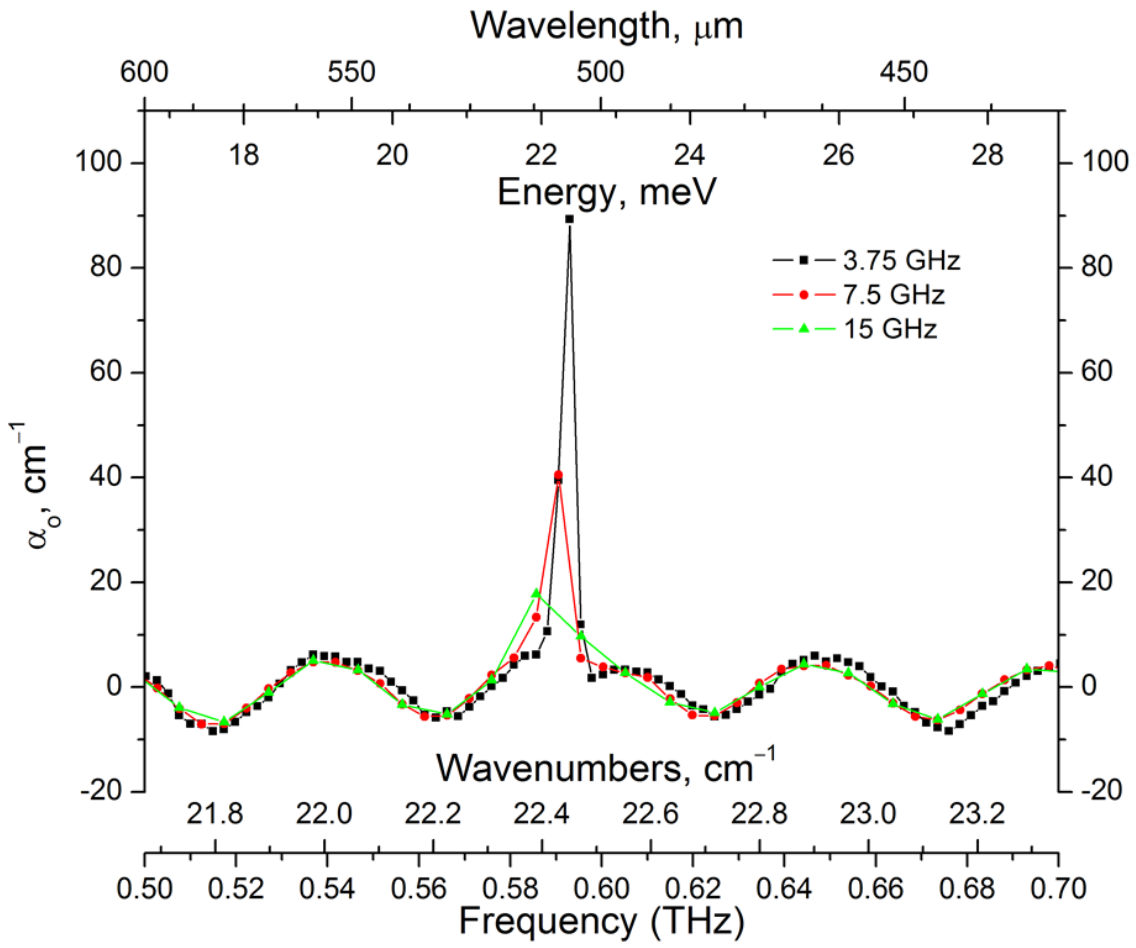

Figure 3.13: Absorption spectrum of the GaSe E'(2) phonon, showing the impact of spectrometer resolution on magnitude of measured phonon absorption.

It is seen in Figure 3.13 that: at 15 GHz resolution the maximum amplitude of $E'^{(2)}$ is measured as $20 \pm 0.1\, cm^{-1}$, when the resolution increased to 3.75 GHz the amplitude increases to $90 \pm 0.5\, cm^{-1}$ and bandwidth narrows to values in agreement with that in the literature. While seemingly an obvious point, key features in THz spectra of GaSe have been continually overlooked in the literature owing to insufficient resolution [219].

3.2.8 Dynamic Range

An important aspect to consider when determining material properties using THz-TDS is the maximum absorption that can be meaningfully measured. Jepsen and

Fisher have addressed this issue [276] and provided an equation which relates the maximum measurable absorption α_{max} to the dynamic range:

$$\alpha_{max} d = 2ln \left[\frac{E_{max}}{E_{min}} \frac{4n}{(n-1)^2} \right] \tag{3.9}$$

where d is the thickness of the samples, $\frac{E_{max}}{E_{min}}$ is the dynamic range of the reference measurement and n is the refractive index. E_{max} is the maximum amplitude of the transmission spectrum and E_{min} is the noise floor. While THz-TDS systems have good dynamic range, the maximum typically occurring about 0.5 - 1 THz and typically quoted as > 2000 it rolls off with increasing frequency, while the absorption tends to increase as we approach the phonon band, so in many cases α_{max} effectively sets the bandwidth of the measurement [265]. We will use Eqn 3.9 throughout the THz-TDS study, to set the validity limits on our measurements.

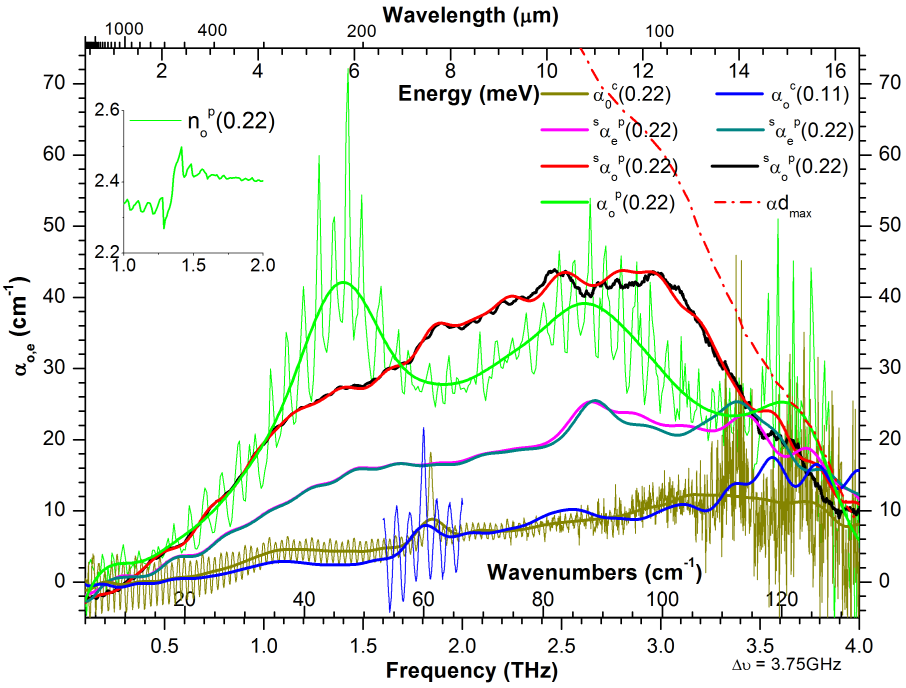

Figure 3.14: Absorption spectra of $GaSe_{x-1}S_x$ (x = 0.11, 0.22) crystals, showing the effect of crystal quality on absorption coefficient as measured at various locations in a, variable quality, polished $GaSe_{x-1}S_x$ (x = 0.22) samples, with absorption spectra of high quality cleaved crystal presented for comparison

3.2.9 Data Selection Rules of Thumb

Examples of THz refractive index and absorption spectra are presented in Figures 3.4 3.12 & 3.15. The crystals are well aligned using the methods presented above, with their facets orthogonal to the incident THz beam. In Figure 3.12 it is seen that as the measured e-wave refractive index of polished $GaSe_{x-1}S_x$ x = 0.22 ($^m n_o^p(0.22)$) curve (the notation is described in the caption of Figure 3.12) has an anomalous variation in its gradient that contrasts with those of the other refractive index spectra. Furthermore its "etalon pattern" (the sinusoidal oscillations around the mean) is highly irregular. When this sample was examined in detail it was found that it contained numerous micro-defects of various kinds, including admixtures of second

phases. The as measured ${}^{m}n_{o}^{p}(0.22)$ is also seen to have irregular oscillations, while they are more regular than that of the ${}^{m}n_{o}^{p}(0.22)$ spectrum, it is certainly less regular than that of as measure e-wave refractive index of polished crystal $({}^{m}n_{e}^{p})(0.44)$. By scanning the measurements site across the aperture of a range of polished (right superscript p) crystals, it was determined that these irregularities are a result of local surface defects caused by processing. It was found that both the density and size of local surface defects are reduced for the harder, higher sulphur content samples (x=0.44), and therefore produce less distortion in the oscillation pattern. Similar effects were observed in the presence of other types of local defects on the surface or within the bulk of certain cleaved samples, such as an occasional precipitate or a local air gap between layers. Clearly, smaller size defects and lower defect density result in greatly improved regularity of the "etalon patterns" and increased measurement reproducibility.

The absorption spectra are plotted in Fig. 3.14 for cleaved and processed $GaSe_{x-1}S_x$, x=0.22, samples. Processed crystals were measured in both o-wave and e-wave transmission. Repeating the measurement at different points on the sample surface, as above, revealed local defects. This is seen in the spectra of smoothed o-wave absorption index of polished crystal $({}^{s}\alpha_{o}^{p})(0.22)$, one of which (green) has an anomalous features at 1.4 THz, indicating that this originated from a local defect. The inset in Fig. 3.14 shows anomalous dispersion caused by this defect.

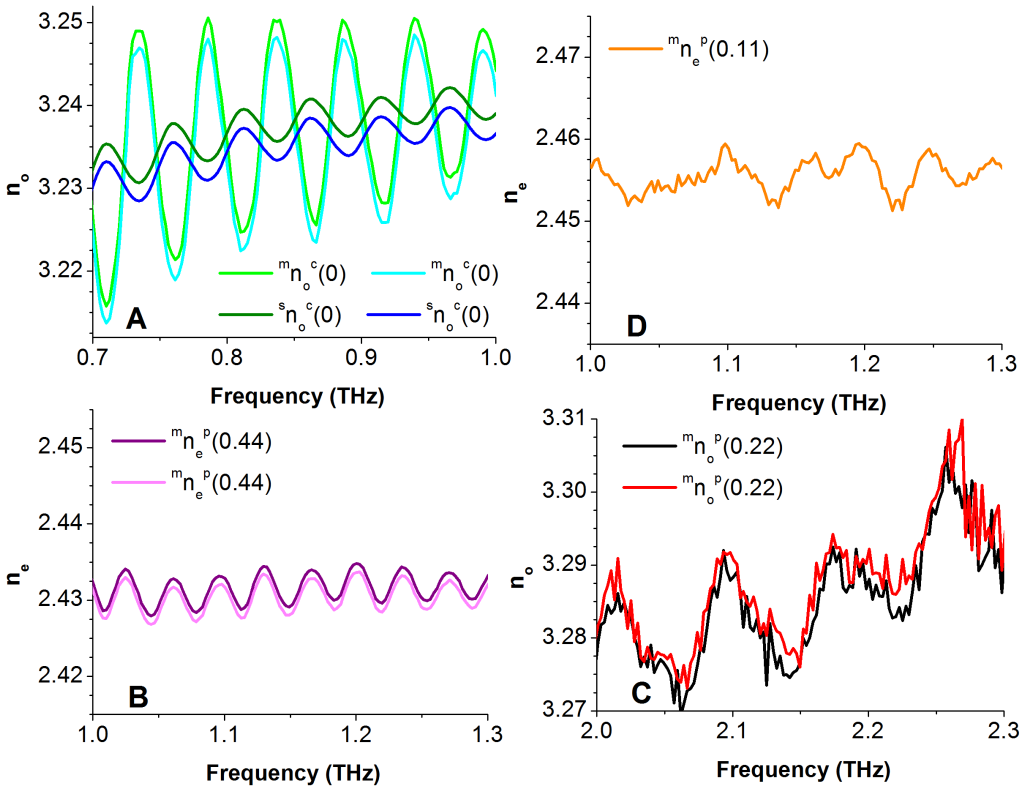

Figure 3.15: A selection of absorption spectra from $GaSe_{x-1}S_x$ crystals, depicting a variety of degraded (A) and a high quality spectra (B, C, D), enabling the Visual selection of accurate THz-TDS data

To overcome these issues and to easily select suitable results, a set of empirical rules of thumb for the assessment of the data were developed. Figure 3.15 presents examples of regular and irregular "etalon patterns" in the refractive index spectra of a series of $GaSe_{x-1}S_x$ crystals. The phase shift in the smoothed oscillations seen in Figure 3.15 (A) are an artefact of the size of smoothing window.

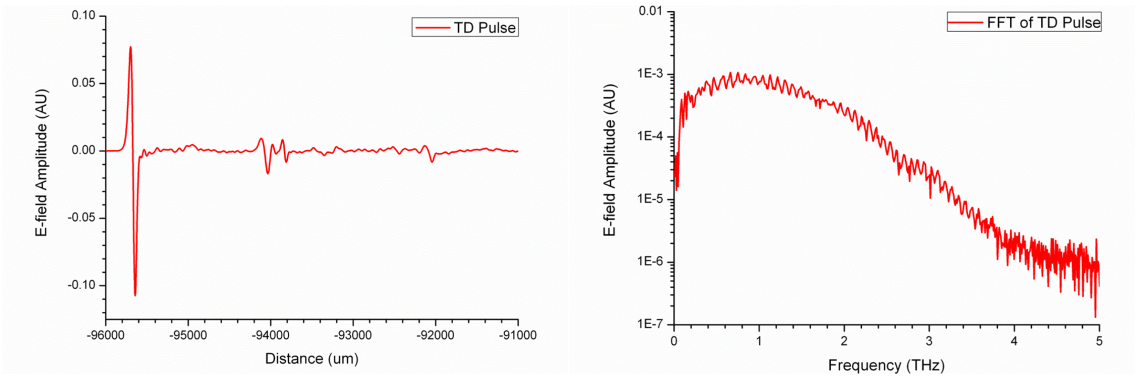

(a) Time Domain (b) Frequency Domain

Figure 3.16: Time and frequency domain representations of a THz pulse. The echoes are observed at -94000 and -92000 μm in time domain and the resulting oscillations are observed in the frequency domain.

The "etalon oscillations" are not the result of standing waves; they are caused by THz "pulse echoes", which result from Fresnel reflections at the crystal-air interface. Travelling twice through the crystal, these delayed pulses appear in the time-domain trace as features delayed from the main pulse peak. Applying Fourier Transform to a time-domain trace containing echoes results in a spectrum with etalon-like sinusoidal oscillations [51], as shown in Figure 3.16.

Figure 3.15 A, above, shows a portion of the refractive index spectra from two measurements of a cleaved GaSe crystal. We can see that both spectra have a smooth highly regular oscillation pattern, the result of a plane-parallel, defect-free sample with high THz transparency. When smoothed to reduce the amplitude of oscillations, the refractive index spectra are seen to be somewhat offset. This is indicative that, while the crystal facets are plane-parallel, one or both of the measurements was made while the crystal was not normal to the incident THz beam.

Figure 3.15 B shows another set of spectra for cut and polished $GaSe_{x-1}S_x$ x = 0.44. Here we can see that both spectra have oscillation patterns that are smooth and regular, indicating that, again, the sample is defect-free, and also the curves are in good coincidence with each other, indicating that both measurements were made at the same angle relative to the incident THz beam. However, the amplitude of the

oscillations vary and decay, which is indicative of a wedged sample. This is because a part of the echo pulse is deflected away from the detector on each reflection. Sample wedging can be caused by the presence of packed or broken layers, by dislocations, by use of polycrystalline boules or through deformation via rough handling.

Figure 3.15 C shows a portion of the refractive index spectra from two measurement of cut & polished $GaSe_{x-1}S_x$ x = 0.22 crystal. We can see that while both spectra are in good coincidence indicating, as before, that measurements were made at the same angle relative to the THz beam, the oscillation pattern remains somewhat regular, though it is no longer smooth. The lack of smoothness is indicative of micro-cracks, leading to multiple paths through the crystal and dispersion of the arrival times of the discrete low amplitude pulses.

In contrast to crystals of high optical quality, samples having surface defects and/or defects in the bulk give rise to highly irregular oscillations instead of regular patterns, because the reflected echo pulses will suffer distortion and loss in travelling through the material. Figure 3.15 D shows another set of spectra for cut and polished $GaSe_{x-1}S_x$ x = 0.11. Here the regularity of the oscillations are entirely lost. This is reflected, upon examination of the crystal, by the heavy cracking and poor surface quality.

Therefore, the oscillation patterns in the refractive index spectra may be used to evaluate the optical quality of the crystal sample, and as a criterion for selecting the most reliable and consistent spectral data sets of crystal spectra. Refractive index spectra with the most regular "etalon" patterns, that are also reproducible in multiple measurements on different areas of the crystal face, are to be judged as the most accurate and reliable.

3.3 THz Absorption of GaSe

For GaSe crystals, a small number of papers report on the absorption spectrum of the crystal in the THz range and these are in the main concerned with the o-wave in cleaved GaSe samples [195]. For the e-wave the number of publications is further reduced and only a very limited amount of data is available for α_e or absorption

anisotropy in the THz range [277, 278, 219, 279]. This is a result of the difficulties in the growth of high quality crystal and in processing samples in crystallographic directions other than parallel to the c-axis.

Within the available data, only a few common features can be deduced, but primarily α_o significantly dominates α_e for the absorption of polarised radiation in the THz range [194, 233, 172]. Moreover the magnitude and spectral behaviour of the o & e-wave differ significantly. As mentioned above the data is widely scattered; in the range 0.5-3 THz, α_o for GaSe has been reported as 70-250 cm^{-1} [234], 40-100 cm^{-1} [280], 5-15 cm^{-1} [212, 281], down to 0.5-8 cm^{-1} [202, 281, 282, 275].

These values are several orders of magnitude higher than the theoretical estimates [283] which have been reproduced elsewhere both correctly [212] and incorrectly [284]. Though it was established later, the theoretical absorption values had been underestimated by up to three times [202].

Some details of the fine structure in o-wave THz absorption can be found in [281]; weakly resolved fine structure can also be identified in [278]. Specific features of the α_o and α_e spectra can also be estimated from the spectral dependency of the power, produced by difference frequency generation in GaSe crystals [93, 194, 284, 285].

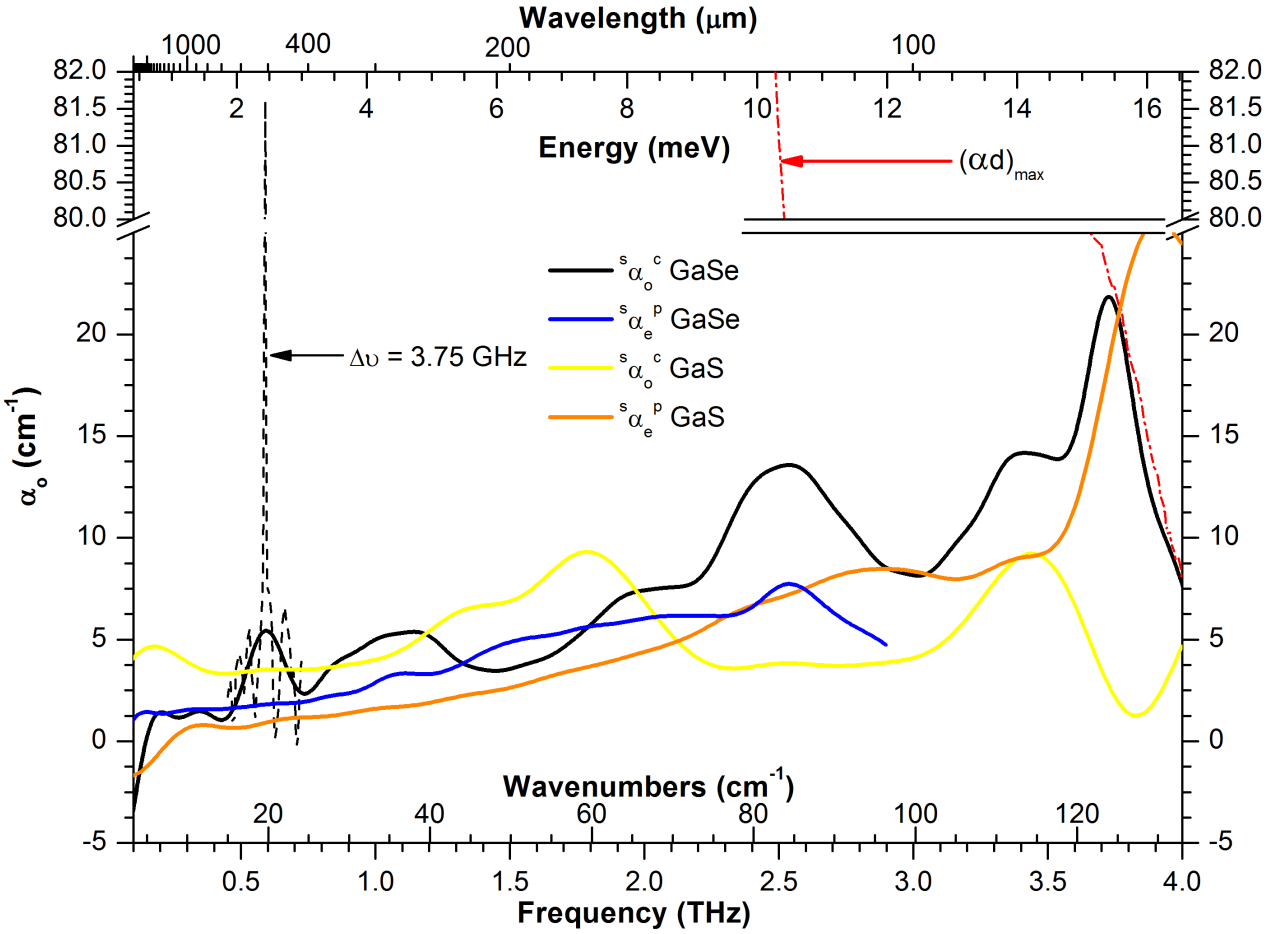

Figure 3.17: Absorption spectra for GaSe and GaS crystals.

3.3.0.1 O-wave absorption of GaSe

Absorption spectra recorded by THz-TDS (smoothed in post-processing [286]) are shown in Figure **??**. The o-wave absorption (α_o) spectra of GaSe agree well with known data in both spectral structure and magnitude [278, 287, 281, 224, 274].

The α_o spectra of GaSe show several distinct features. There is a well known [202, 212, 281, 282, 224] intense absorption peak of the $E'^{(2)}$ rigid layer phonon mode centred at 0.59 THz and two broad absorption features, which have also previously been reported, one centred at 1.0 THz [281, 282, 224, 160] and the other at 2.5 THz [281, 282, 160].

The narrow spectral width of the strongest phonon absorption peak at 0.59 THz (the $E'^{(2)}$ rigid layer mode) indicates the high optical quality and structural homogeneity of the optimally doped crystal [274], since there is no spectral broadening due to site-to-site variation or defects. The $E'^{(2)}$ rigid phonon mode has a maximum measured absorption of $\alpha_o \geq 81.5 \pm 0.4\, cm^{-1}$ for bulk high-quality crystals; in crystals of exceptional quality or thin (micrometric) single domain samples $\alpha_o \geq 90 \pm 0.5\, cm^{-1}$, as illustrated in Figure: 3.18. The general trend of the α_o baseline is to increase with frequency. The baseline absorption, even in the best quality crystals, does not currently reach the low intrinsic absorption figures given in the literature [93]. The optical quality of pure GaSe crystals are degraded by point defects in the crystal lattice, due to Ga vacancies, and residual admixtures of micro-crystal of other polytypes [215], which we will discuss in Chapter 4.

The optical properties in the THz region are dominated by the effects of free carriers and typically the lowest optical phonon. Free carriers in the crystals are not technologically controlled; pure GaSe crystals, grown by the Bridgman method, are invariably p-type semiconductors [288, 289]. However, the contribution of free carriers in the THz optical properties is confined to the low frequency region $\lesssim$ 1 THz, in high quality crystals[280, 290, 10]. At higher frequencies, the optical properties are dominated by the low energy tail of the optical phonon at 213 cm^{-1} [10], which can be described through the simple Lorentz harmonic oscillator model

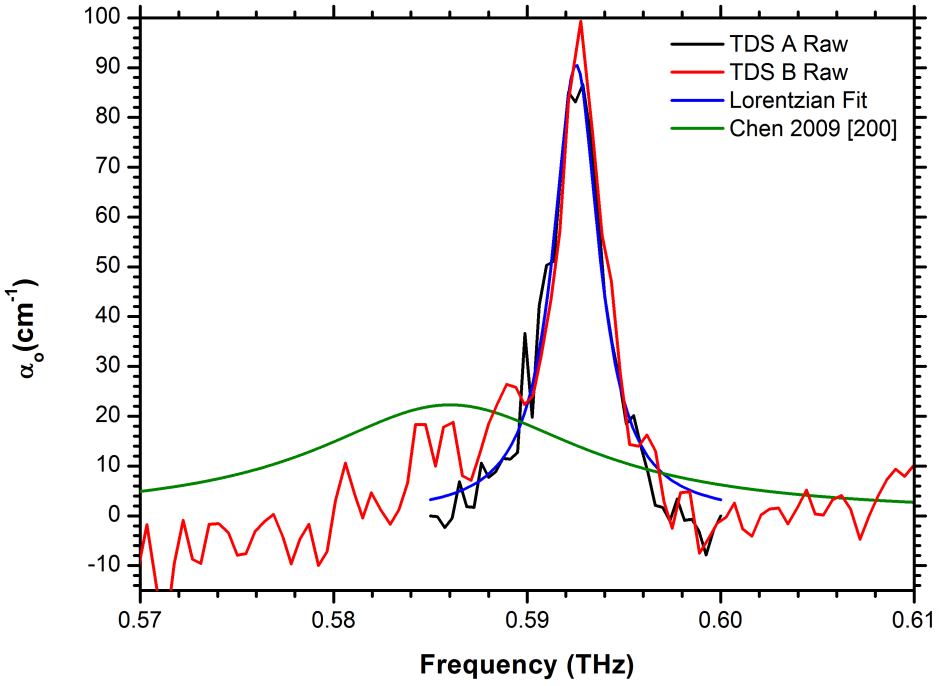

Figure 3.18: Absorption spectra of a thin (200 μm) GaSe around the $E'^{(2)}$ rigid layer mode phonon, as measured by two independent CW THz-TDS systems, and a Lorentzian fit. The Absorption is measured as $\alpha_(o) = 91cm^{-1}$ and a measured bandwidth of $\Delta\nu = 2.89\,GHz$. For comparison the $E'^{(2)}$ data as measured by Chen et al [202] is presented

of electrical permittivity:

$$\varepsilon(\omega) = \varepsilon_L(0) + \frac{f_P}{\omega_P^2 - \omega^2 - i\omega\gamma_P} \tag{3.10}$$

where ε_L is the permittivity of the lattice vibration, ω_P is the frequency of the phonon, f_P is the strength of the phonon and γ_P is a damping constant. The refractive index may then be expressed as:

$$n(\omega) = \Re\left[\sqrt{\varepsilon_r(\omega)}\right] \tag{3.11}$$

And the absorption coefficient as:

$$\alpha(\omega) = \frac{2\omega}{c}\Im\left[\sqrt{\varepsilon_r(\omega)}\right] \tag{3.12}$$

So, the contribution of the transverse optical phonon leads to the increase in absorption and refractive index with increasing frequency.

3.3.0.2 E-wave absorption of GaSe

An intense absorption peak centred at 1.1 THz ($37\,cm^{-1}$) is clearly observed for the first time in the GaSe α_e spectrum in Figure **??**. The absorption peak is just resolved with a resolution of 3.75 GHz, while being barely visible at 15 GHz. The intensity and spectral bandwidth of the absorption peak were found to vary with resolution in a similar fashion to those of the $E'^{(2)}$ phonon absorption peak at 0.59 THz, explaining its omission from previous work. The 1.1 THz phonon mode has a maximum measured absorption of $\alpha_e \geq 27 \pm 0.14\,cm^{-1}$ for the processed GaSe samples, polished with the coarse powder. Although an indication of this phonon was found to be present in the data presented in reference [219], the authors did not identify it as such. It was, however, also observed in one other GaSe sample and identified as phonon absorption peak [291]. Therefore, we propose that given the consistency of observation, the peak at 1.1 THz should be acknowledged as a new phonon absorption peak and should be taken into account in the design of $GaSe_{x-1}S_x$ THz devices [279]. Another broad, low-amplitude, absorption feature can be seen centred around 2.5 THz. The general trend of α_e is to increase with frequency within the validity range of the measurement 0.1 - 3.0 THz. Absorption in GaSe is highly anisotropic, both in spectra features and scale. The magnitude of α_e is significantly less than that of α_o for frequencies greater that 1.8 THz, confirming previous observations [194, 233, 172].

The higher absorption recorded in both the o & e-waves has a significant negative effect on the nonlinear figure of merit, when compared with the value intrinsic absorption, FoM $\backsim$ 2800. The calculated FoM values of 8.5 and 19.8 for the o and e-waves respectively remain competitive with the values for GaAs and GaP, without the challenges of QPM fabrication, see Table 2.2. The lower absorption and higher FOM suggests that the nonlinear generation scheme used should result in an e-wave THz radiation for increased efficiency and wider tunability.

3.4 THz Absorption of GaS

As is explained below, β-polytype crystals were grown in place of ε-polyptype, as GaS preferentially grows in the β form, but the differences in the linear properties are negligible. GaS crystals, in common with GaSe, can be readily cleaved forming optical quality, atomically flat, surfaces. On the other hand, GaS is substantially harder than GaSe crystal, permitting the fabrication of high quality processed samples ($\phi = 90°$), encased in polymer as shown above in Figure 3.7. Examples of the GaS absorption spectra recorded by NPL's THz-TDS are presented in Figure 3.17

3.4.1 O-wave absorption of GaS

From Figure 3.17 it can be seen that GaS crystals possess higher transparency for the o-wave than GaSe. Several broad absorption features are present in the absorption spectrum; two overlapping absorption peak centred around 1.4 and 1.8 THz respectively can be seen; a further absorption feature is present centred around 3.45 THz. The underlying trend of the absorption remains flat across the validity range of these measurements.

3.4.2 E-wave absorption of GaS

Absorption in GaS is strongly anisotropic, the o-wave absorption coefficient dominating the e-wave absorption coefficient α_e by factor of at least 2 to 3 in the range 0.1 - 2.15 THz. The magnitude of α_e increases with frequency, so that for frequencies greater than 2.15 THz, e-wave absorption α_e is dominant. Two broad overlapping absorption features can be seen centred around 2.4 and 2.9 THz respectively.

In contrast to the measured absorption spectra of GaSe crystals, neither the o or e-wave absorption spectra for GaS crystal show the narrow band high-Q phonon modes seen above. The transverse optical phonon for the o & e -waves GaS crystals lies as substantially higher frequencies than in GaSe, 296 & 319 cm^{-1} respectively [292]; hence, their contribution to the optical properties is reduced and consequently the absorption is lower. It should be borne in mind that β-polytype GaS is centrosymmetric and second order nonlinear generation is not possible.

3.5 THz Absorption of $GaSe_{1-x}S_x$

It is evident that the extremely poor mechanical properties, the limited optical quality of available crystals, and the large variability and contradictions in the published data regarding other physical properties, has continually hindered the widespread adoption and utilisation of GaSe crystals in contrast to other materials such as $ZnGeP_2$.

Sulphur (S-) doping of GaSe significantly improves the mechanical properties, due to the substitution of gallium vacancies, which are the dominant defect mechanism, by sulphur atoms, significantly reducing the point defects and stacking faults. The lattice structure is sufficiently strengthened by a low density of interstitials to enable cutting and polishing in arbitrary directions, in particular if the crystal is first set in polymer as described above. Over-doping increases, the density of interstitials, the density of intercalated atoms and leads to the formation of precipitates, which reduce the optical quality of the crystals, deforming its lattice, introducing scattering and increasing absorption [210].

S-doping simultaneously improves the optical properties of the crystals, reducing the mid-IR optical absorption coefficient by a factor of 2-3 [216, 217, 218], while increasing the optical damage threshold fivefold at the optimal mixing ratio [216, 217] and the optical properties in the THz range are also found to improve [172]. Composition dependent transformation of the phonon absorption spectrum for o-wave has been reported [274, 224], but were not confirmed by other researchers [219]. Again, due to limited availability of high quality crystals and lack of capability in processing them, the e-wave absorption spectra of $GaSe_{x-1}S_x$ crystals and therefore the absorption anisotropy in the THz range have rarely been studied [209, 219]

Absorption spectra of the grown $GaSe_{x-1}S_x$ crystals in the 0.1-4.5 THz range were measured using the THz-TDS at NPL, UK. Owing to their small size, the crystal samples were placed at the focus of the THz beam such that they interacted with the incident radiation in either $\vec{E} \perp \vec{c}$ (o-wave) or $\vec{E} \parallel \vec{c}$ (e-wave) geometry, for both cleaved and cut & polished crystals, where E is the electric field vector of the incident THz light and c is the crystal c-axis.

In order to insure the accuracy of the measurements, the precautions detailed above were observed. Furthermore, selected results were further verified by repeating the measurements in two commercial of-the-shelf THz spectrometers systems, a pulsed **K15** THz-TDS (Menlo systems GmHb, Germany) and a continuous wave **Terascan 1550** frequency domain spectrometer (Toptica GmHb, Germany). Examples of the measured absorption spectra for o- and e-wave are depicted in Figures 3.19 & 3.21.

3.5.1 O-wave absorption of $GaSe_{1-x}S_x$

A number of general comments can be made regarding the results. The absorption coefficients measured for cleaved crystals doped with Sulphur mixing ratios x = 0.11 and 0.22 are smaller than those reported for the highest quality pure GaSe crystal [219, 282]. Moreover, it was found that $GaSe_{x-1}S_x$ x =0.22 possesses the lowest absorption coefficient among all the grown crystals, confirming the positive effects of doping on crystal quality, which is consistent with the available published data on optimal sulphur content [216]. The characteristic rigid mode phonon absorption peak $E'^{(2)}$ at 0.59 THz in GaSe is found to disappear from the absorption spectra of $GaSe_{x-1}S_x$ crystals in the mixing range x = 0.11 – 0.22, see Figure 3.19. Instead, a peak appears at 1.8 THz and shifts towards higher frequencies with the increase of sulphur concentration. The evolution and transformation of phonon absorption is discussed in detail below.

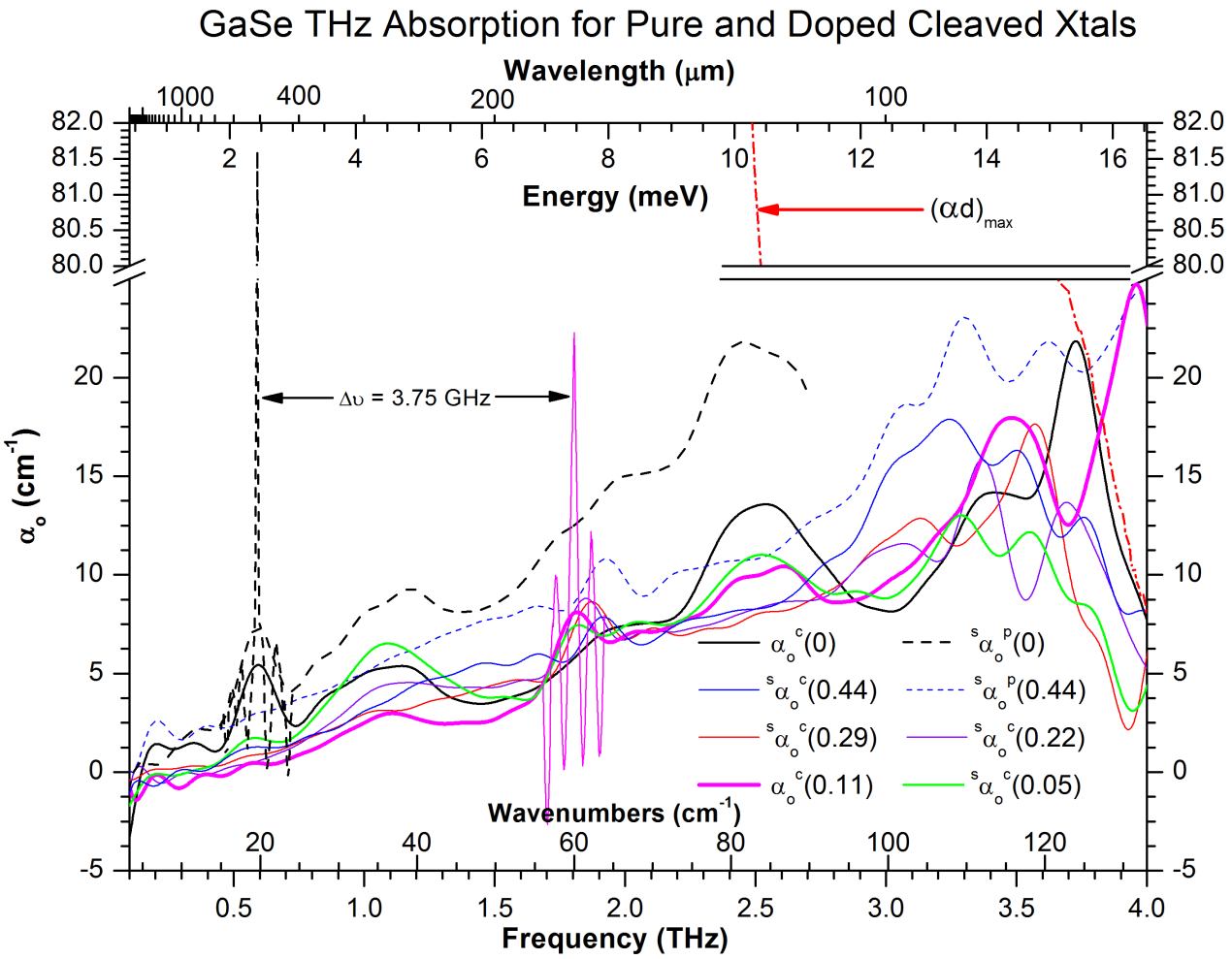

Figure 3.19: O-wave THz absorption spectra for $GaSe_{1-x}S_x$

In Figure 3.19 it is seen that absorption spectra for o-wave for cleaved and cut & polished GaSe crystals possess similar spectral features, as do those for cleaved and cut & polished $GaSe_{x-1}S_x$ crystals; however, cut & polished crystals exhibit higher absorption losses than cleaved ones. The difference in magnitudes of the absorption coefficients between cleaved and cut & polished crystals appears to be frequency-independent, which can be clearly seen in Figure 3.20, by comparing the absorption for two sets of crystals, pure GaSe and $GaSe_{x-1}S_x$ (x = 0.44).

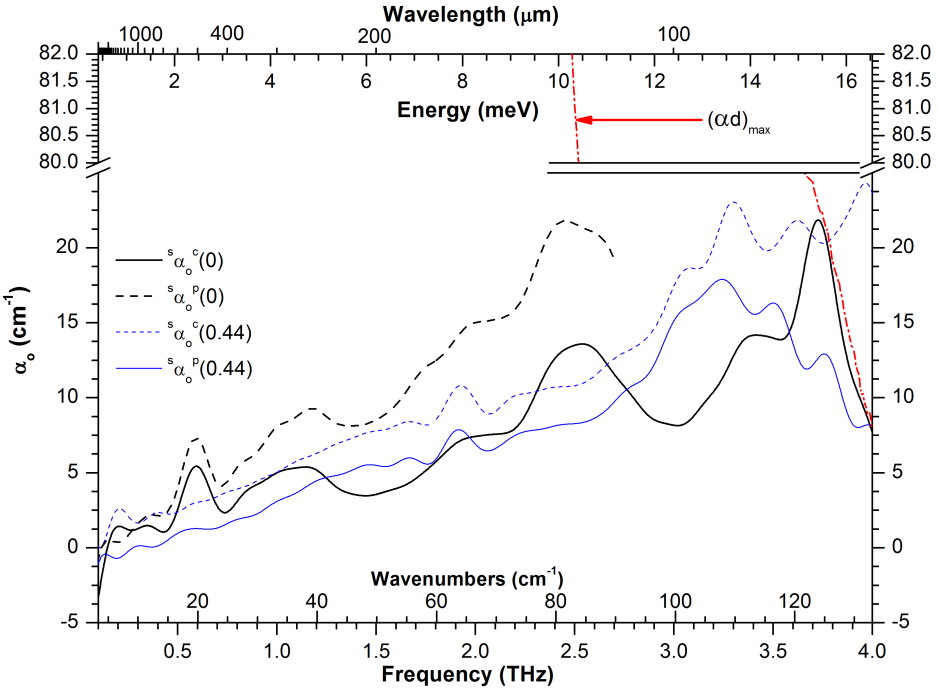

Figure 3.20: Absorption spectra of GaSe and $GaSe_{1-x}S_x$ x = 0.44 crystals for both cleaved and cut & polished samples.

This frequency independence implies that optical losses in these samples are not caused by scattering originating from polishing quality or by absorption by residues of the polishing medium, as we would expect these losses to have frequency dependent components. Indeed, the evidence indicates that higher optical losses in cut & polished samples originate in surface defects related to polishing. It may be proposed that the excess loss is due to increased interface reflections caused by incorporated particles of the polishing powder. The polishing powder consists of a number of

very high refractive index metal-oxide minerals CeO_2 LaO_2 and NdO_2, these form a very thin layer high refractive index layer at the surface, significantly increasing the Fresnel reflection. Investigation are underway to establish the dielectric properties of these materials at THz frequencies and to improve the polishing process.

3.5.2 E-wave absorption of $GaSe_{1-x}S_x$

The absorption spectra for e-wave in cut & polished $GaSe_{x-1}S_x$ crystals were found to be most strongly affected by the perturbing factors, which, as a consequence makes it impossible to perform a detailed quantitative analysis of the data, and for some concentrations it is not possible to present meaningful results at all. A

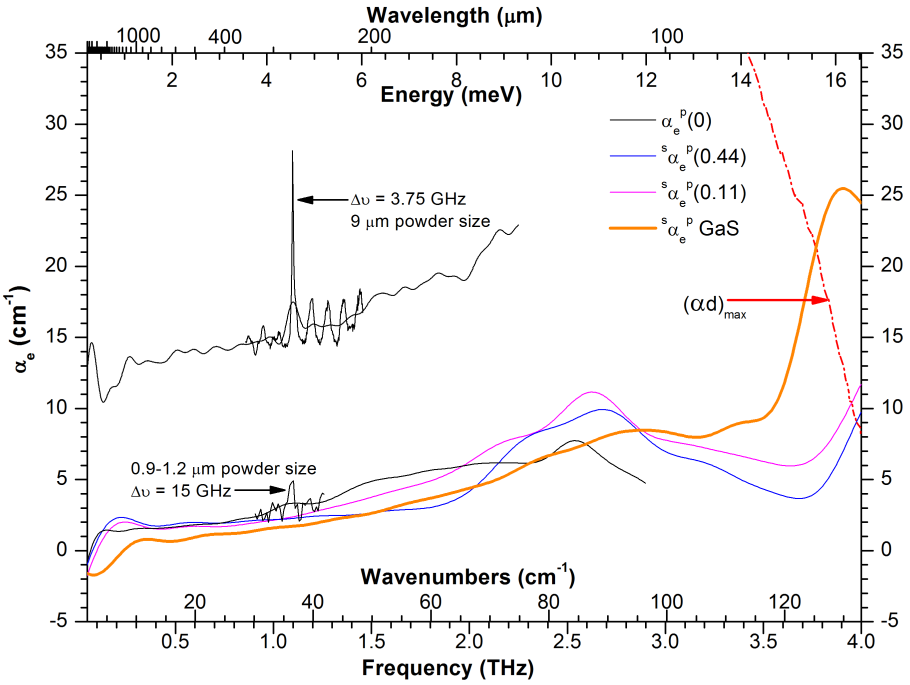

Figure 3.21: E-wave THz absorption spectra for $GaSe_{1-x}S_x$ crystals.

selection of the recorded spectra are presented in Figure 3.21. It can be seen that, for samples which have been processed with the fine polishing powder (1 μm), doped crystals possess the highest optical quality. Their e-wave absorption coefficients are 2-3 times lower than those for o-wave, coinciding well with the published data [194, 219, 172, 222, 209]. It can also be seen that processing $GaSe_{x-1}S_x$ crystals

with the course polishing powder (9 μm) induces an order of magnitude higher loss coefficient than a similar crystal polished with fine powder (0.8–1.2 μm), the loss appears frequency independent and is likely the result of further metallisation of the surface. In the frequency band 0.3–2.0 THz, the absorption coefficient for e-wave in $GaSe_{x-1}S_x$ crystals with high S-concentrations, x = 0.22–0.44, is nearly frequency independent. The intense absorption peak centred at 1.1 THz, which was clearly observed for the first time in the GaSe spectrum, is not found to be present in the e-wave spectra of the measured $GaSe_{x-1}S_x$ crystals presented in Figure 3.21. It may be that, in common with α_o measurements, the phonon decays with increasing sulphur concentration (x), and it would be visible in $GaSe_{x-1}S_x$ crystals, where $x < 0.11$. The phonon peak around 2.5 THz is common for both GaSe and GaS crystals, and so it remains even in heavily S-doped GaSe crystals.

The reduced absorption in both the o & e waves of $GaSe_{x-1}S_x$ x = 0.22 does not compensate for the reduced nonlinear coefficient in the FoM, the values of which are found to be 3.4 and 17, for the o and e-waves respectively. However, the influence of the polishing should be borne in mind and that the actual absorption coefficient is likely lower than those seen in our results. Following the trend from the o-wave case (Figure 3.20), the true value for the e-wave absorption coefficient would be on the order of 1 cm^{-1}, and as a result, the FoM would increase to ≥ 55. Regardless, the result clearly favours the use of e-wave generation. While the FoM may be lower than that of pure GaSe, evidence from the literature shows that it is compensated by: the higher damage threshold, increased strength, improved optical quality in the near-IR, and a shift in the band-gap to higher frequencies.

Low-level Al-doping ($\leqslant 0.01\%$) has be shown to significantly decrease the input of carriers in the lower THz region [210, 215], and as consequence, it reduced the absorption and slightly increased the refractive index. We have calculated, form the values in the literature [210, 215], the FoM for the o-wave in Al-doped GaSe as $\backsim 134$. Gao *et al* report that double doping of crystals changes the optical properties additively. Therefore, as they suggest, double doping with Sulphur and small amounts of Aluminium looks attractive for optimising the optical and mechanical properties

for generation in the THz regime [215]. Accounting additively for the effect of both dopants, we predict a Figure of Merit of 165 for the o-wave in $GaSe_{x-1}S_x$:Al crystals, significantly greater than the values for GaAs and GaP, see Table 2.3 Only weak influence on the e-wave properties is reported for low-level Al-doping in the THz [215] and for both orientation in the near and mid-IR [210]. Such double-doped crystal are currently being grown and future work will investigate their properties in detail. A summary of the results is presented in Table 3.5.2.

Table 3.1: Nonlinear Figure of Merit (FOM) for GaSe, $GaSe_{x-1}S_x$ and Al-doped crystals in the THz regime from measured values. * Estimate value for additive effect of double doping. Results calculated from values measured in this work and those presented in the literature [103, 201, 173, 168, 210, 215]

Crystal	x	o/e-wave	Absorption cm^{-1}	n_{THz}	n_{IR}	d_{eff} pm/V	FOM
GaSe		o	4	3.24	2.63	55	8.5
GaSe		e	3	2.46	2.63	55	19.8
$GaSe_{x-1}S_x$	0.22	o	3.5	3.22	2.59	30	3.4
$GaSe_{x-1}S_x$	0.22	e	1.8	2.44	2.59	30	17
$GaSe_{x-1}S_x$	0.44	o	4	3.16	2.52	15	0.7
$GaSe_{x-1}S_x$	0.44	e	2	2.42	2.52	15	3.7
GaSe:Al		o	1	3.26	2.63	55	134
$GaSe_{x-1}S_x$:Al*	0.22	o	0.5	3.24	2.59	30	165

3.6 THz Refractive Index of GaSe

To successfully design ε-$GaSe_{x-1}S_x$ crystals and fully exploit their potential for efficient nonlinear frequency conversion applications requires, adequate data on dispersion versus mixing ratio of the ordinary (n_o) and extraordinary (n_e) wave refractive indices, over the entire transparency range.

Dispersion equations for the pumping GaSe crystals in the visible and near IR ranges have been published [293] and are recommended by the well known and widely used handbook [294]. However, as with absorption, of the known dispersion equations for GaSe [202, 295, 293, 296, 289, 297, 298, 299, 300, 212], only a limited number are valid in the THz regime [202, 295, 293], due to the difficulty in producing and obtaining high quality crystals for measurement. Some equations [293] are also

in widespread use for THz application despite this being well outside their claimed validity range (0.65 - 18 μm).

Numerous refractive index spectra have been determined experimentally by THz-TDS for n_o in GaSe. But again, data on n_e is extremely limited and largely measured indirectly, due to the difficulty in processing the crystals, though some data has be recorded using processed crystals.

It has been shown [280, 160, 234] that the refractive index is dependent on the quality of the measured crystals and that this can lead to the measured values of refractive index in $GaSe_{x-1}S_x$ varying from $n_o = 3.5$ [234] to $n_o = 3.6$ [280, 160] at ~ 1 THz. The poor quality of these crystals is evident in the figures presented [280] and the deviation of the presented absorption spectra [234] from accepted values for high quality crystals.

So, for accurate determination of the dispersion properties of GaSe, it is crucial that the crystal be of the highest optical quality, i.e. an absorption coefficient of $\leq 0.2\,cm^{-1}$ in the maximum transparency range of the crystal. Indeed it has be seen that even with the same THz-TDS system significant variations (n $\pm$ 0.05) can be observed [275].

Despite the size of these errors, lack of available data and use of dispersion equations outside of their validity range [293], the available experimental data on phase matching angles for o-wave THz generation [213, 301] is consistent with those estimated using [293]. In contrast, mismatches do occur in estimating the generation of e-waves [93, 194, 202, 285]. For long-wave generation ($\geq 300\mu$m), the mismatch amounts to $2 - 3°$. Typically, nonlinear generation in $GaSe_{x-1}S_x$ crystals is via critical phase-matching, so such errors lead to very large a differences in the resulting wavelength; 100s to 1000s of μm variation from what is expected.

As the angular error is quite small, it may be readily compensated for, or indeed go unnoticed in the construction of a typical experimental system, due to the inherent limits on the precision of common optical components and their alignment. However, it hinders the ability to accurately design and estimate the performance of $GaSe_{x-1}S_x$ systems for THz application, and indeed severely limits progress of other

applications such as the manufacture of Brewster surfaces and polarisation optics, where selection of the correct angle is critical. Therefore, the determination of the most suitable dispersion equations, for the full transparency range of $GaSe_{x-1}S_x$ crystals, remains a key issue.

The dispersion in solid solution crystals grown from structurally identical (isostructural), parent crystals can be estimated by using the well-known relation Eqn 3.13, from Ref [302], adapted for use with ε-Ga(Se,S) crystals

$$n^2_{o,e}\left(GaSe_{x-1}S_x\right) = (1-x)\cdot n^2_{o,e}\left(GaSe\right) + x\cdot n^2_{o,e}\left(GaS\right) \tag{3.13}$$

Clearly, the dispersion properties of parent crystals i.e. ε-GaSe (hereinafter GaSe) and ε-GaS, must be well known in order to make use of Eqn 3.13. For this purpose, three sets of dispersion equations for GaSe [202, 295, 293] have been found to be suitable for estimating phase matching (PM) over the whole transparency range.

However, the optical properties of bulk ε-GaS crystals are not available, since to the best of our knowledge crystals of such a polytype have not yet been grown and hence has not been studied. This is a result of GaS crystals growing preferentially as the β-polytype. However it is well known that linear properties of the different polytypes differ negligibly [303, 304]. Thus, it can be proposed that dispersion properties for β-GaS are close to that for ε-GaS (hereinafter, both polytypes are labelled as GaS) and applied for estimating the dispersions of ε-$GaSe_{x-1}S_x$ (hereinafter $GaSe_{x-1}S_x$) by using Eqn 3.13. The only available experimental data reported in [103] presents mid-IR dispersions for β-GaS. Alternatively, they may, of course, be measured directly.

Refractive index spectra of the grown GaSe, GaS & $GaSe_{x-1}S_x$ crystals in the 0.1–4.5 THz range were determined, simultaneously with the absorption spectra, using the THz-TDS at NPL. Due to the small size of the crystals' apertures, the samples were placed at the focus of the THz beam, such that they interacted with the incident radiation in either $\vec{E} \perp \vec{c}$ (o-wave) or $\vec{E} \parallel \vec{c}$ (e-wave) geometries for both cleaved and cut & polished crystals, where E is the electric field vector of the

incident THz light and c is the crystal c-axis.

As THz-TDS uses coherent detection, the absorption and refractive index are recorded simultaneously, so the previous experimental precautions, see above, still apply and the measurements verified in the same fashion.

3.6.1 O-wave refractive index of GaSe

To determine the THz refractive index of the o-wave (n_o) in the GaSe parent crystal, a centimetric thick sample was carefully prepared from a high-quality crystal boule by cleaving, with plane-parallel surfaces. Millimetric thick cut & polished samples were also prepared. The results of the measurements are depicted in Figure 3.22. The rigid mode phonon $E'^{(2)}$ is evident from the strong anomalous dispersion which

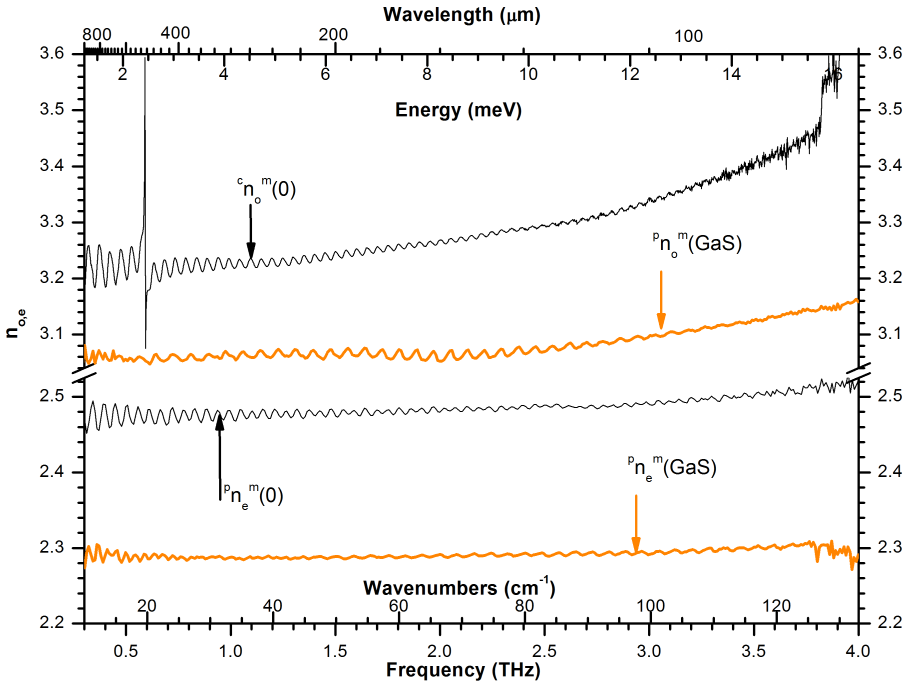

Figure 3.22: THz refractive index for GaSe and GaS crystals.

is seen centred around 0.595 THz. At 0.25 THz, $n_o = 3.25 \pm 0.008$ and its value decreases slightly to $n_o = 3.24 \pm 0.008$ at 1 THz, due to the contribution of the anomalous dispersion around the $E'^{(2)}$ phonon, after which the value of n_o increases with increasing frequency. The errors on these measurements are small, at the level

of angular misalignment, as the GaSe crystal used is thicker than the cut & polished samples. It was found that all the cut & polished samples have a higher refractive index value than the cleaved samples, though the difference was typically within the margin of error. This may be assumed to be due to the lower quality of the cut and polished samples and the impact of polishing as discussed above. The refractive index spectra for the cleaved crystals has a validity range of 0.1-3.5 THz; at 3.5 THz the value of n_o in the GaSe crystal increases rapidly indicating the cut-off point. The lower frequency cut-off in refractive index spectra of the cut & polished samples is further evidence of their somewhat reduced quality, as seen in Figure 3.24.

3.6.2 E-wave refractive index of GaSe

Measurements of the e-wave refractive index spectra were conducted using cut & polished crystals from the same boule used for the cleaved o-wave spectra above; the results are depicted in Figure 3.22. No evidence of the $E'^{(}2)$ rigid mode phonon can be seen in the e-wave refractive index spectra, though the phonon at 1.1 THz is evident, from the anomalous dispersion centred at this frequency in several samples. The value of the e-wave refractive index $n_e = 2.46 \pm 0.015$ is substantially lower than that of the n_o. The measure value of birefringence ($\beta = 0.78$) at 1.5 THz is prodigious and in good agreement with the values estimated by [202] ($\beta = 0.78$) and those measured by [202, 278, 209, 219] ($\beta = 0.78-0.79$); on the other hand, it is twice the value of the estimates resulting from the dispersion equation of [293]($\beta = 0.39$) and also substantially greater than [295] ($\beta = 0.49$). The values calculated from Ref [293, 295] are discounted as they are outside the validity range, and or do not adequately take into account the measured values of n_e. n_e increases nearly linearly with increasing frequency, the slope of the increase is less than that for n_o, so the birefringence increases with frequency, to a value of ($\beta = 0.9$) at 3.5 THz. The lower values of n_e in GaSe crystal, also contributes to the improved FoM, further favouring the use of e-wave generation.

We can have good confidence in these results as the high quality of the crystal has already been established, the measurements were carefully conducted using the

alignment methods detailed above, the large size of the crystal minimises the impact of error in thickness measurement and the selection criteria developed above were used to reject any questionable data. Moreover, this confidence allows us to recommend Chen *et al*'s Sellmeier equations for use in the THz regime [202] as they best available match our data for both the o and e-wave refractive index spectra and also the results found in the literature [202, 278, 209, 219], see Figure 3.23.

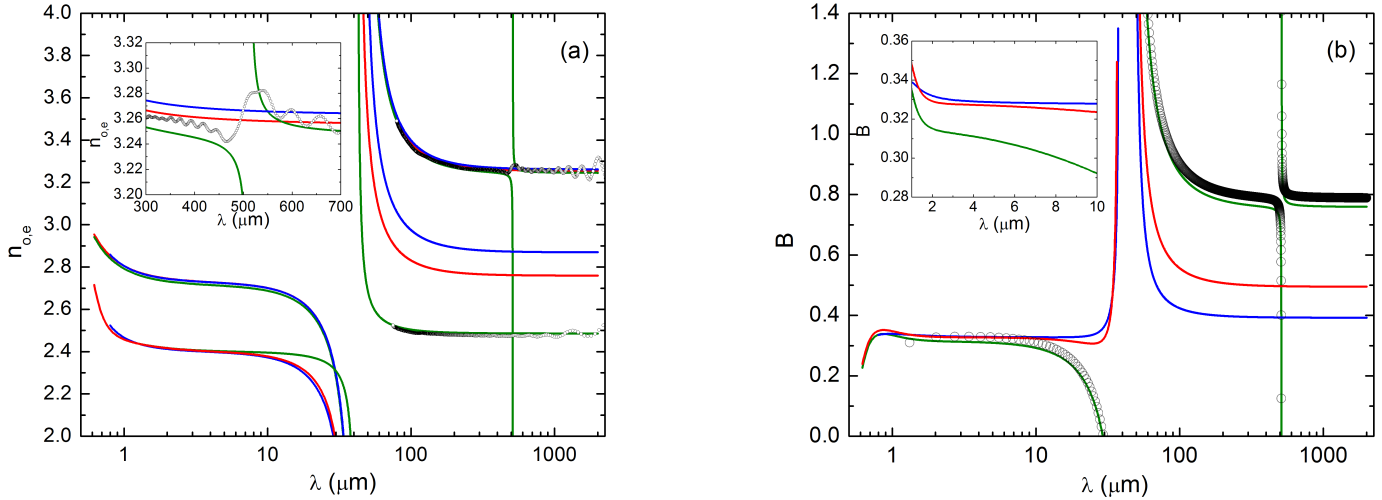

(a) Dispersions

(b) Birefringence

Figure 3.23: GaSe dispersions (a) and birefringence (b) as estimated in the literature [202, 293, 295] and as measured by THz-TDS in this work. Experimental points of the study: black; curves calculated by dispersion equations from Ref [202] : olive, Ref [293] : blue, and Ref [295]: red.

3.7 THz Refractive Index of GaS

High-quality GaS crystals of the β-polytype were specially grown to permit, for the first time to our knowledge, THz-TDS measurements of the dispersions of o-wave (n_o) and e-wave (n_e) refractive indices for GaS crystals. These crystals were grown by the modified Bridgman method described above. Figure 3.22 presents GaS and GaSe dispersions measured via THz-TDS for comparison.

3.7.1 O-wave refractive index of GaS

It can be seen in Figure 3.22 that the magnitude of the GaS o-wave refractive index (n_o) is substantially smaller than that of GaSe. At 1 THz in GaS, $n_o = 3.06 \pm 0.012$, compared with $n_o = 3.24 \pm 0.008$ in GaSe. A very broad, low-amplitude feature can be observed in the refractive index spectra of n_o, between 0.6-2.0 THz, after which the magnitude of n_o grows almost linearly with increasing frequency to a maximum value of $n_o = 3.16 \pm 0.012$ at 4.0 THz. The refractive index spectra for the cut & polished and the cleaved samples were found to be in good agreement, adding further confidence in the results

3.7.2 E-wave refractive index of GaS

The magnitude of the GaS e-wave refractive index is substantially less than that of GaSe, in GaSe $n_e = 2.46$ at 1 THz, while in the measured value in GaS crystals is found to be $n_e = 2.29 \pm 0.012$. In common with GaSe, GaS crystals are found to be strongly birefringent. At 1 THz the measured value of birefringence $\beta = 0.77$ is the same as for GaSe, within the margin of error of the measurements. No regions of abnormal dispersion or significant features can be seen in the refractive index spectra. The magnitude of n_e increases approximately linearly with frequency, the slope of this growth, on the order of $12.5 \cdot 10^{-3}$/THz, which less than that for n_o or indeed n_e in GaSe. The lower refractive index in GaS as with the reduce absorption is a result of the increased frequency separation from the lowest transverse optical phonon.

Having established the refractive index spectra for both the o & e waves in high

quality GaSe and GaS crystals to a good degree of confidence, it is now possible to implement Eqn 3.13 to estimate the refractive index value of $GaSe_{x-1}S_x$ crystals for a given value of x. Furthermore, as both crystals are found to have the same birefringence, we expect that doped crystal will also have a birefringence of $\beta = 0.78$ as Egn 3.13 predicts a linear transformation with x. However, Eqn 3.13 does not include the effects of mixing ratio dependent phonon transformation observed, in the absorption spectra of $GaSe_{x-1}S_x$ crystals.

3.8 THz Refractive Index of $GaSe_{1-x}S_x$

The wide range of refractive index spectra estimated by the available Sellmeier equations can be verified experimentally by THz-TDS. THz-TDS measurements have been previously reported for limited ranges of $GaSe_{x-1}S_x$ compositions, x = 0.01, 0.14, 0.26, 0.37 [305], 0.26 [209] and 0.29 [219], however, the results are inconsistent and contradictory for both the magnitude of the refractive index and its transformation with mixing ratio. To resolve these inconsistencies and to accurately determine the refractive index spectra for $GaSe_{x-1}S_x$, a series of careful measurements were made on, specially gown, high-quality, $GaSe_{x-1}S_x$ crystals. Examples of refractive index spectra, as measured by NPL's THz-TDS, for the set of $GaSe_{x-1}S_x$ crystals, with compositions x = 0.05, 0.11, 0.22, 0.29, 0.44, are depicted in Figure 3.24.

3.8.1 O-wave refractive index of $GaSe_{1-x}S_x$

Several common trend for $GaSe_{x-1}S_x$ can be observed for the n_o refractive index spectra. The magnitude of n_o begins approximately equal to that of GaSe, n_o= 3.25±0.012 for x = 0.05 and reduces as the quantity of sulphur (x) in the composition increases to a minimum value of n_o= 3.16 ± 0.015, at 1 THz, for x = 0.44. The anomalous dispersion observed around the $E'^{(2)}$ rigid mode phonon in GaSe is greatly reduced for $GaSe_{x-1}S_x$ x = 0.05 with only a broad low amplitude feature remaining, and no effect at all is apparent for the other higher sulphur content compositions. A new band of anomalous dispersion begins to arise in ${}^m n_0^c(0.05)$, is fully developed in ${}^m n_0^c(0.11)$ and is present in the remaining higher sulphur content $GaSe_{x-1}S_x$

crystals. This band of anomalous dispersion is associated with the $E''^{(2)}$ phonon absorption peak at 1.8 THz. In common with the earlier GaSe results, the cut & polished samples have a higher refractive index and lower cutoff frequency which maybe there result of the incorporation of a the polishing power particles in a thin layer at the surface and the slightly lower quality of the samples themselves.

A clear example of the variation mentioned above is evident in the value of refractive index for x = 0.29 in [219] $n_o = 3.03$, in [305] $n_o = 3.17$ and in this work $n_o = 3.2 \pm 0.012$ for the same composition at 1 THz. The o-wave refractive index spectra are in good agreement with the published data and measured data for GaSe, together with the high optical quality of the grown crystals providing a firm basis for confidence in the accuracy of the measured dispersion properties of solid solution $GaSe_{x-1}S_x$.

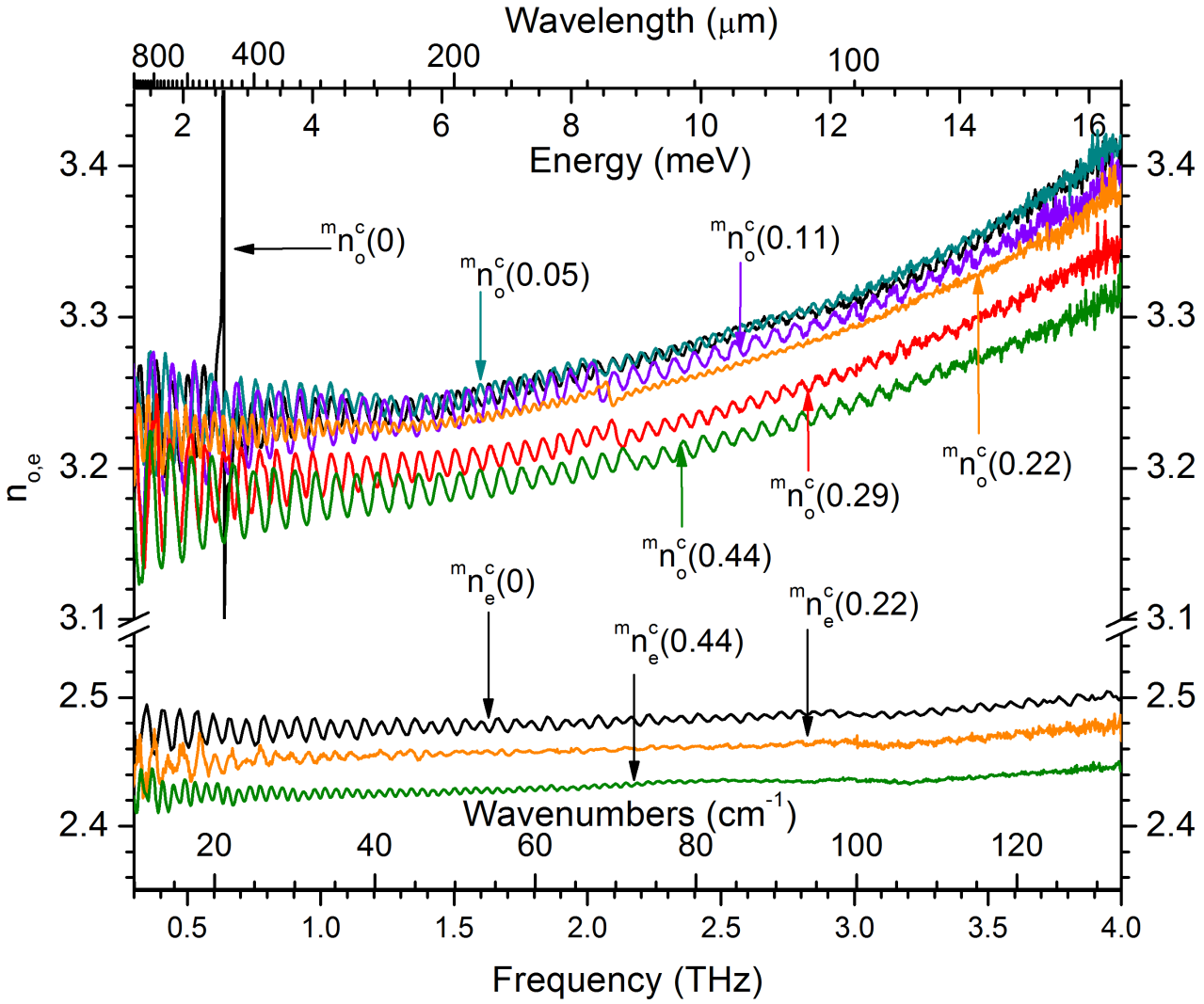

Figure 3.24: THz refractive index spectra for $GaSe_{1-x}S_x$ x = 0.05, 0.11, 0.22, 0.29, 0.44.

3.8.2 E-wave refractive index of $GaSe_{1-x}S_x$

E-wave refractive index measurements of $GaSe_{x-1}S_x$, as with the α_e measurements, are highly sensitive to the quality of the crystals. Repeated handling of the thin samples introduced cracking along the growth layers of some of the crystals. It appears that, for some samples, the higher frequencies in the THz pulses were wave-guiding, or at least propagating through these cracks. Thus, it was not possible to make meaningful measurements for the same wide range of samples as in the o-wave case. Fortunately, good measurements were still available for the key mixing ratios in $GaSe_{x-1}S_x$ x = 0.11, 0.44, which covers the maximum and the optimal doping levels.

The magnitude of e-wave refractive index (n_e) are substantially less than those of the o-wave n_o. At low mixing ratios the magnitude of n_e is approximately equal to that for GaSe. The value of n_e then reduces as the mixing ratio (x) increases, to a minimum value of $n_e = 2.42 \pm 0.015$ at 1 THz for x = 0.44. The anomalous dispersion associated with the newly observed phonon absorption peak in GaSe at 1.1 THz is not observable in the measured $GaSe_{x-1}S_x$ samples. A broad low-amplitude feature centred around 2.5 THz is observable in all samples, associated with the e-wave phonon absorption peak observed above. The magnitude of n_e for all $GaSe_{x-1}S_x$ samples increase with frequency, though the slope of the increase is lower than the slope of n_o in $GaSe_{x-1}S_x$ crystals and moreover, lower than that of n_e in GaSe crystals.

3.8.3 Variation of refractive index in $GaSe_{1-x}S_x$ with doping concentration

The common trend of refractive indices to decrease with rising S-content is clearly seen in Figure 3.26. The variation of refractive index with S-content is characterised by a regular gradient, thus, allowing PM optimisation. Some deviations from this regular trend are observed, which may be attributed to measurement uncertainties, principally in the determination of sample thickness, but also, to differences in the free charge carrier concentrations. While reducing the refractive index has a positive

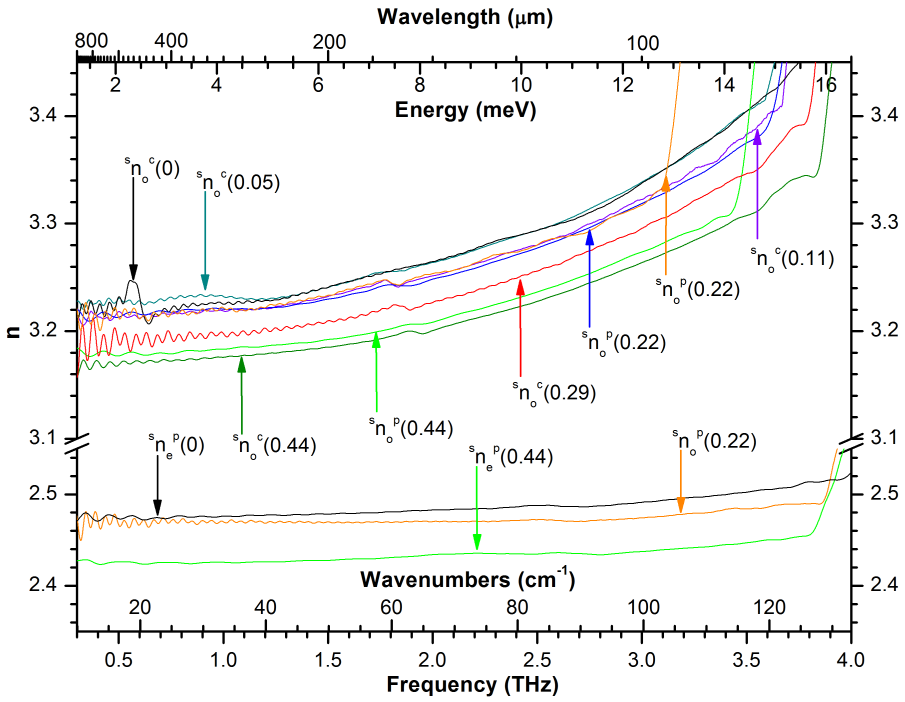

Figure 3.25: Smoothed THz refractive index spectra for $GaSe_{1-x}S_x$ x = 0, 0.05, 0.11, 0.22, 0.29, 0.44.

impact on the FoM, its influence has to be balanced with other factors. While $GaSe_{x-1}S_x$ x = 0.44, has the lowest refractive index for both the o & e-waves for the measured $GaSe_{x-1}S_x$ crystals, its effective nonlinear coefficient is also reduced [103], so the overall result is less attractive.

3.9 Evolution of THz Phonons in $GaSe_{1-x}S_x$ with doping concentration

The dispersion equations of $GaSe_{x-1}S_x$, for the full transparency range, can be estimated to a good degree of accuracy through the available data for the parent crystals using Eqn 3.13. While this method is quick, readily accessible and straightforward, on the other hand, it fails to take account of a variety of factors, among these are the appearance of new phonon absorption peaks in $GaSe_{x-1}S_x$ and their evolution with S-doping. This type of phonon transformation is observed in our results above and

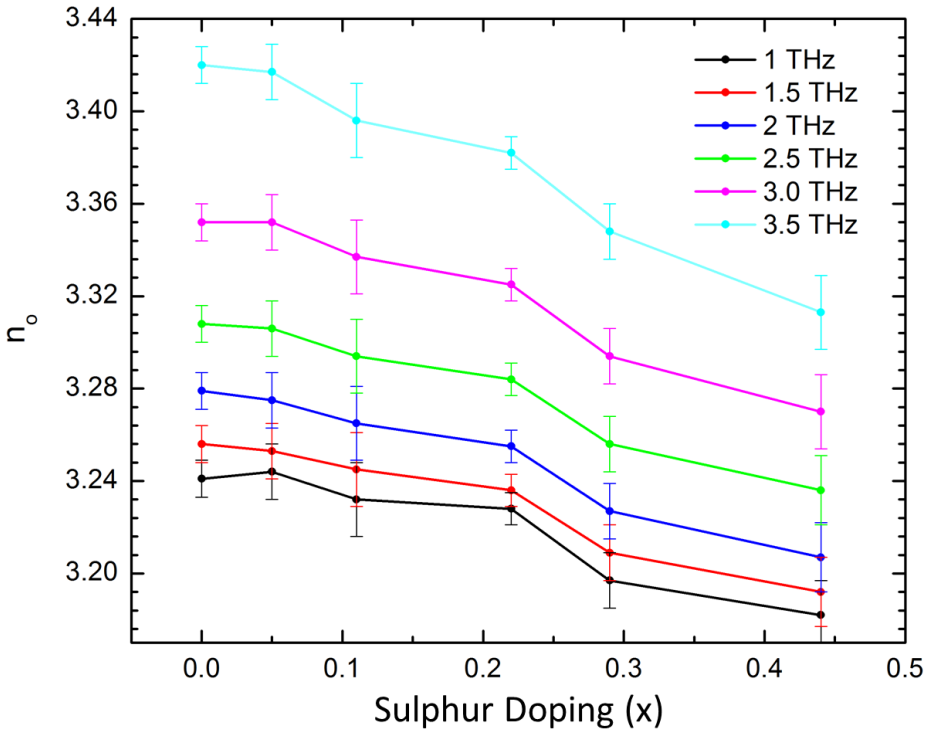

Figure 3.26: Variation of refractive index with doping for $GaSe_{1-x}S_x$ x = 0.05, 0.11, 0.22, 0.29, 0.44

was previously reported in [305, 274] , but it is in contrast with the results of other studies [306] where no new phonon absorption peaks where observed. The rigorous selection of high quality samples, the precautions observed in making the measurements, and the repeated observation of the phenomenon gives us good confidence in stating that the transformations we observe are indeed real.

The presence, appearance and transformation of phonon absorption modes and their profiles should be accounted for in the successful design of efficient THz sources. In particular, the input of the phonon modes to the dielectric response (leading to ranges of abnormal dispersion) should be considered in the formulation of dispersion equations, as is the case with the well known GaSe rigid phonon mode $E'^{(2)}$ at 0.595 THz [202]

To permit the inclusion of these factors into the design of devices it is necessary to study in detail the evolution of phonon structure in $GaSe_{x-1}S_x$ with S-doping using

a dense set of crystals. As discussed above, accurate measurements of the THz phonon modes in GaSe and $GaSe_{x-1}S_x$ require sufficiently high frequency resolution due to their narrow width, the minimum estimated as <2.5 GHz (FWHM). The main THz phonon absorption modes in $GaSe_{x-1}S_x$ are centred at the frequencies of 0.59, 1.0, 2.5 and 3.5 THz.

It is established that the intensity of the rigid layer mode phonon $E'^{(2)}$ at 0.595 THz decreases with increasing s-doping until the mode collapses. At the optimal S-doping level, x = 0.11 – 0.22, the mode is fully immersed. In the e-wave spectrum it was found that, in contrast to [306], the $E''^{(2)}$ mode at 1.7 THz both increase in intensity with S-doping and shifts to higher frequencies with a gradient of 17 GHz/mass% as shown in Figure 3.27, where the absorption spectra of both cleaved and processed crystals are presented.

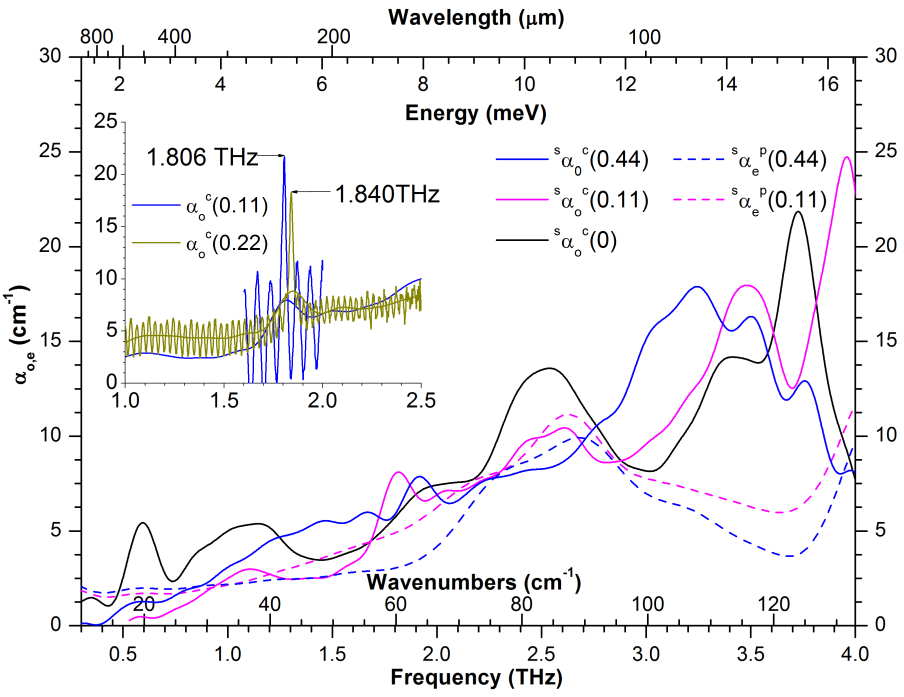

Figure 3.27: Absorption spectrum of $GaSe_{1-x}S_x$ crystals showing the evolution of o & e-wave THz Phonons in with sulphur content.

The increase in frequency of the phonons is related to the mass of the ions in the lattice and the stiffness of spring constants between them; to illustrate this we can

consider the simple case of a one dimensional lattice containing two species of ions. The dispersion of the vibrational mode frequency in the lattice can be described by the equation[10]:

$$\omega^2 = \frac{\kappa_1}{\kappa_2}\left[1 \pm \sqrt{1 - \frac{8\mu_r\kappa_1\kappa_2}{\mu_c(\kappa_1+\kappa_2)^2}(1 - cos\, ka)}\right] \tag{3.14}$$

where $\kappa_{1,2}$ are the spring constants, $\mu_r = \dfrac{m_+m_-}{m_+ + m_-}$ is the reduced mass and $\mu_c = m_+ + m_-$ is the total mass; where $m_\pm$ are the masses of the ions. This relation is defined within the reciprocal unit cell, $-\pi/a < k < \pi/a$. In the long wave limit $k \ll \pi/a$, this can be approximated as [10]:

$$\omega = \sqrt{\frac{\kappa_1 + \kappa_2}{\mu_r}} \qquad \text{i.e. optical branch} \tag{3.15}$$

$$\omega = \sqrt{\frac{\kappa_1\kappa_2}{\mu_c(\kappa_1+\kappa_2)}}(ka) \qquad \text{i.e. acoustic branch} \tag{3.16}$$

We can see that the optical modes are dependent on the reduced mass of the ions and the stiffness of the spring constants. The mass of sulphur atoms is less than that of either Gallium or Selenium, so all other things being equal the frequency of vibration increases, as more sulphur is incorporated into the lattice. This is reflected in the shift of the THz phonons to higher frequencies in our results. The acoustic branch considers the propagation of sound through the lattice.

For the first time the arising and transformation of other phonon peaks, where observed in the e-wave absorption spectra of heavily S-doped crystals, including in $GaSe_{x-1}S_x$ x = 0.44, at 1.9 THz, resulting in regions of abnormal dispersions. Furthermore, an intense phonon peak with a centre frequency at 1.1 THz was observed in the e-wave spectra of GaSe. Having being consistently observed, these modes should be accounted for in the design of THz devices.

In general, the determination of the composition of solid solution $GaSe_{x-1}S_x$ crystal is quite an involved process. The transformation of the short wave edge shows weak dependence on the mixing ratio of parent crystals, at low mixing levels

e.g. GaSe:Al, while transformation of the mid-IR multi-phonon structure becomes apparent earlier [209, 210]. However, as we have observed, the transformation of the rigid mode phonons in the THz regime is very sensitive to the mixing ratio of the parent crystals. The transformation of $GaSe_{x-1}S_x$ phonon structure is particularly sensitive, more so than that observed for other GaSe solid solution crystals such as $GaSe_{1-x}Te_x$ [274].

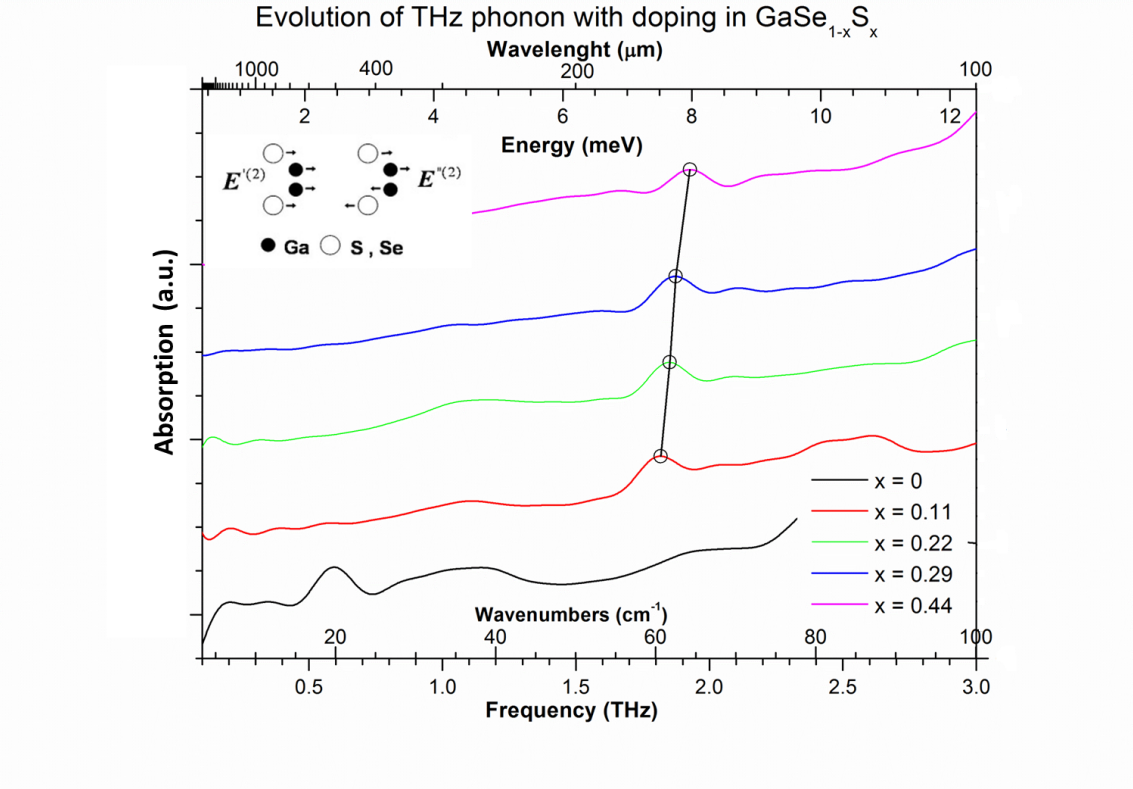

Figure 3.28: Evolution of o-wave THz Phonons in $GaSe_{1-x}S_x$ with sulphur content

Thus, the appearance, transformation and frequency shift of rigid mode phonons in the THz regime, including the rigid modes $E'^{(2)}$ at 0.595 THz and $E''^{(2)}$ at 1.7 THz may be used to quickly determine the mixing ratio of the parent crystal, with a good degree of confidence, as seen in Figure 3.28 where the spectra of set of cleaved crystals are presented. Moreover, they may also be used to determine the optimal doping level for high quality crystals. $E'^{(2)}$ is an interlayer shear mode, while $E''^{(2)}$ in an intralayer shear mode (Figure 3.28 inset), we can suppose that the presence of interstitial atoms in the lattice is suppressing the $E'^{(2)}$ mode, at higher doping concentrations.

The optical properties of the crystals improve with improvements in the structure of the crystal lattice, these improvements are achievable, up to a limit, by doping, which fills the vacant lattice sites. Sulphur atoms are well match to the atomic size of the substituted atoms, so the resulting lattice deformation is limited. The decrease in the vacancies may also reduce the staking fault density, further improving the optical quality [215]. With this improvement in crystal lattice structure, the Q and intensity of the rigid modes phonons increases, reaching a maximum for $GaSe_{x-1}S_x$ at about $0.11 \geq x \leq 0.22$, which has been confirmed through other means, including efficiency of nonlinear conversion, to be the optimal mixing ratio.

3.10 Summary

In this chapter we examined the sources of inaccuracy in the THz-TDS measurements of high refractive index birefringent crystals, such as GaSe, and proposed, a rule of thumb, selection criteria for adequate data, based on the quality of the oscillations in the refractive index curves. The linear refractive index (n) and absorption coefficient (α), for both the o & e waves, in the THz regime (0.1- 4.5 THz) was determined, by direct measurement using Terahertz - Time Domain Spectroscopy, for GaSe and a dense set of $GaSe_{x-1}S_x$ crystals (x = 0.05, 0.11, 0.22, 0.29, 0.44), fabricated with facets perpendicular to the c axis. The presence of a new phonon mode at 1.1 THz was observed with a good degree of confidence for the first time. Measurements of THz dispersion and absorption properties of GaS crystals are performed for the first time. These measurements enable the use of Takaoka *et al*'s Eqn 3.13 [302], to determine the refractive index of $GaSe_{x-1}S_x$ crystals for a given mixing ratio, x. We determined the birefringence for GaSe,GaS and $GaSe_{x-1}S_x$ crystals, and recommend Chen *et al*'s estimates [202], from the existing Sellmeier equations, as those which best fit the experimental data. The transformation of the optical properties of the crystals and their phonon structure, with respect to Sulphur content, is studied and the possibility of using THz-TDS as an assessment tool, for crystal composition and quality, is discussed. The impact of the transformation of the optical properties with sulphur content on the nonlinear Figure of Merit FoM is

discussed, and the optimal doping level recommended.

Chapter 4

FTIR and Raman spectroscopy of GaSe1-xSx

4.1 Introduction

In this chapter we will investigate the possibility of engineering the transparency windows in $GaSe_{x-1}S_x$ crystals by means of doping. The phonon bands of the GaSe, GaS and $GaSe_{x-1}S_x$ crystals will be examined by FTIR and Raman spectroscopy and their transformation with respect to doping is studied. We estimate for the first time the absorption coefficients of the main phonon peak in the set of $GaSe_{x-1}S_x$ crystals using thin (10s of μm) exfoliated samples. The polytype of the grown $GaSe_{x-1}S_x$ is investigated and the appropriate relations for calculating d_{eff} is identified. Sellmeier equations for the full transparency range of GaSe and GaS crystals, designed in part from the results found in this work, are presented.

Doping of semiconductor crystals is common practice for engineering a variety of desirable properties, both optical and electrical, such as the fabrication of high resistance crystals for nonlinear optical frequency conversion. These impurities are known to modify the phonon structure of the host material. The transformation of the phonon band in doped GaSe crystals is more sensitive to mixing ratios than the short-wave edge, suggesting that transformation of the phonon band may be a convenient assessment tool for monitoring doping levels [266, 209, 210, 307]; though, as we have seen in Chapter 3, THz-TDS is more sensitive and in many respects more

convenient.

Determining the amplitude of the main IR active phonon mode, at 213 cm^{-1}, and its evolution with sulphur content (x) are key to understanding the dispersion properties of $GaSe_{x-1}S_x$ crystals and determining the efficiency of Mid-, Far-IR and THz frequency generation [212]. Accurate Sellmeier equations for the full transparency range are predicate on establishing the main phonon. Inaccurate estimations of the amplitude of the main phonon peak in GaSe and its reproduction elsewhere in the literature has lead to the development of several sets of incorrect dispersion equations [283, 284, 202].

Furthermore, the absorption edges of the phonon band set the practical lower limit for nonlinear optical frequency conversion in the IR and the upper limit for THz generation. As we have seen from Eqn 3.10 the contribution of the lowest transverse optical phonon mode dominates the optical properties of the crystals at higher THz frequencies. Furthermore, we have also seen from Eqn 3.15 that lighter elements shift the phonon modes to frequencies, while heavier elements shift the phonon modes to lower frequencies. So, it has been suggested that doping GaSe with lighter elements could perhaps shift of the phonon band to higher frequencies, providing access to higher frequency regions of the THz regime for nonlinear frequency conversion [212], increasing the bandwidth of such devices.

A large number of Raman spectroscopy studies have been conducted on GaSe, $GaSe_{x-1}S_x$ and GaS crystals. It is possible using Raman techniques to determine the polytypes present in $GaSe_{x-1}S_x$ crystal; however, in common with other areas, the literature, surrounding these studies, is often in contradiction with the results scattered. On the other hand, Raman spectroscopy readily resolves the phonon frequencies, their transformation and their relative intensities, but measurements of their absorption coefficients is out of reach; furthermore, not all phonon modes are both Raman and IR active due to selection rules. However, as GaSe is a noncentrosymmetric crystal, modes that are both IR and Raman active are permitted and we can investigate the evolution of the principle phonons modes, TO and LO, to some degree. Conversely, FTIR spectroscopy systems are ideally suited to making

measurements of the absorption spectra of crystals, though, due to the lack of sufficient dynamic range or sensitivity, the main phonon band in GaSe and $GaSe_{x-1}S_x$ has not been widely investigated [212].

4.2 FTIR Spectroscopy of GaSe1-xSx

A significant number of FTIR studies have also been carried out for GaSe [308, 309, 221, 212, 211, 310, 202, 266, 307], $GaSe_{x-1}S_x$ [221, 311, 312, 307, 310] and other doped GaSe crystals [211, 313, 209, 274, 210]. However, unlike Raman measurements, the phonon peaks are not readily resolvable. The main IR phonon mode in GaSe and $GaSe_{x-1}S_x$ is extremely intensive, so in most instances it is not possible to determine its amplitude [314, 212], as the detectors in conventional FTIR systems lack sufficient dynamic range. Alternatively, reflection geometries have been used to examine the reflection spectra in some instances [315, 316]. Moreover, many of the instruments employed to conduct spectroscopic studies in GaSe and $GaSe_{x-1}S_x$ have a lower limit of sensitivity around 25 μm or 400 cm^{-1}. While more than acceptable for investigating the transparency window of GaSe crystals, in the range 0.6-20 μm, it falls sort of the range needed to examine the main phonon band in the range 40-50 μm [202, 212].

4.2.1 Experimental details

Spectroscopy measurements were performed on 4 different FTIR systems in this study. In two systems (Cary and Bruker, Vertex 80) the measurements were conducted in ambient atmosphere where the high density of water lines resulted in problematic and highly unsatisfactory measurements. Using an instrument (Bruker, Vertex 80) purged with N_2, the majority of the waterlines were removed, improving the results, but at the cost of a highly variable background. Only the evacuated system (Bruker, Vertex 80V) produced acceptable results. The measurements presented here were conducted at a resolution of 0.25 cm^{-1}, using an unpolarised light source and a liquid He cooled detector. The cleaved samples were installed on an 8 mm aperture, such that $E \perp c-axis$, in an evacuated chamber ($> 10^{-6}$ torr) at 300

K.

As mentioned above, the main IR phonon mode in GaSe and $GaSe_{x-1}S_x$ is extremely intensive and the detectors in conventional FTIR systems lack sufficient dynamic range to fully resolve them. This necessitates the special preparation of extremely thin samples ($10's\,of, \mu$m). Thin samples do have the advantage of eliminating the majority of the interference effects present in thicker samples.

Such samples were obtained though repeated exfoliation using scotch tape. The samples were pressed between two Silicon (Si) plates to ensure plane surfaces. Initial trials of samples using singly exfoliated $GaSe_{x-1}S_x$ produced $100's$ of μm thick layers which proved too absorbing and curled readily, hindering measurements. For clean exfoliation the edge of the crystals should be dressed to a steep chamfer using a keen scalpel. Care should be taken in applying the scotch tape for exfoliation, insuring no wrinkles or air bubbles are present and that there is good contact with the surface before exfolitaion. Prepared samples should be checked carefully for the presence of micro-holes.

A range of samples were prepared including, one GaSe sample 16 μm thick and several $GaSe_{x-1}S_x$ samples x = 0.11, 0.22, 0.44 with thicknesses of 21, 25 & 8 μm respectively. The thickness of these samples were determined to an error of 2% by G. Moschetti of the Engineering Measurement group at NPL, using his well-characterised home-built Wavelength Scanning Interferometer [317, 318] .

4.2.2 Absorption and Evolution of the main phonon band of GaSe1-xSx

In Figure 4.1 we can see, that by using thin samples, the phonon bands in $GaSe_{x-1}S_x$ x = 0, 0.11, 0.22, 0.44 have been successfully resolved. Several features are quickly apparent, the main phonon mode E'(TO) at 213 $\pm 0.25\,cm^{-1}$ (46.7 μm) shifts to higher frequencies with increasing sulphur content. In the presence of sulphur doping several new phonons arise in the range 260-360 $\pm 0.25\,cm^{-1}$ (28-38.5 μm), and the evolution of the phonon band with doping is complex.

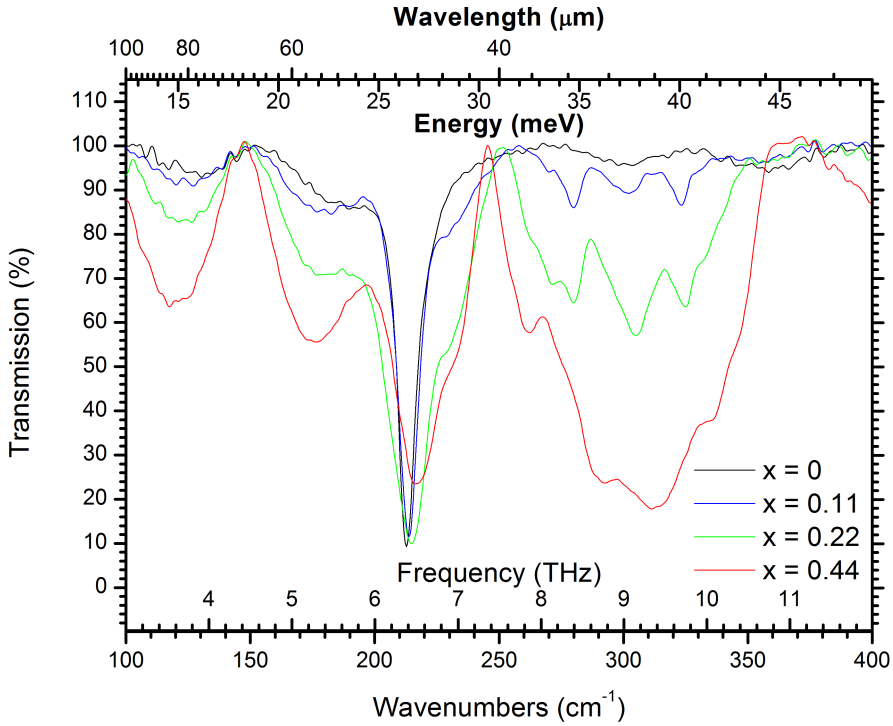

Figure 4.1: FTIR transmission spectra for thin samples of GaSe, $GaSe_{x-1}S_x$ (x = 0.11, 0.22, 0.44).

The absorption structure of the IR active modes in GaSe has been measured in transmission by Chen *et al* [202], while reflection studies had previously established the centre frequencies of the principle modes [319, 277, 320, 316], including the transverse optical E'(TO) at 213.5 cm^{-1} (46.8 μm, 6.4 THz) and the longitudinal optical $E'(LO)$ at 255.1 cm^{-1} (39.2 μm, 7.65 THz). While we clearly observed the TO phonon at 46.7 μm for GaSe crystals, the LO phonon has not been observed at 255.1 cm^{-1} in any of our measurements across the full range of samples and a variety of sample thicknesses (10-100 μm). A phonon peak does emerge from the shoulder of the TO phonon at $230.5 \pm 0.25\, cm^{-1}$ (43.4 μm, 6.91 THz) which follows a similar shape-form to that observed by Chen *et al* [202]. But from Chen *et al*'s discussion we attribute this feature to the A_1' phonon mode. As the thickness of the samples is increased, the width to the phonon peak broadens considerably and in an asymmetrically form, growing to the higher frequency side. Chen *et al*'s samples were almost an order of magnitude thicker (170 μm) than those used in this study,

suggesting that E'(LO) phonon may appear at the observed frequencies in thicker samples.

Table 4.1: IR active phonons observed in the absorption spectra of thin GaSe and $GaSe_{x-1}S_x$ crystals.

Crystal	x			$E'(TO)$	A_1'			
		cm^{-1}	cm^{-1}	cm^1	cm^{-1}	cm^{-1}	cm^{-1}	cm^{-1}
GaSe		123.4	177.5	212.7	-	-	-	-
$GaSe_{x-1}S_x$	0.11	125.4	180.8	218.1	-	270	290.3	323.1
$GaSe_{x-1}S_x$	0.22	134.9	179.9	214.6	227.5	272	279.7	325
$GaSe_{x-1}S_x$	0.44	135.4	177.9	218	230	261.4	280.2	334.2

The newly arisen phonons at 271, 279 $\pm 0.25\,cm^{-1}$ (37, 36 μm) have not been previously noted by Chen *et al* [212, 202] or others [319, 315, 308, 316]. They also do not correspond to the phonon frequencies for known GaSe impurities [314]. The mode at 324 $\pm 0.25\,cm^{-1}$ (31 μm) has previously been observed by Chen *et al*, while 302 cm^{-1} (33.1 μm) present in their work is missing here [212]. Hence, given the observation and growth of these news mode in the presence of sulphur doping, we conclude that they are due to the influence of the GaS parent crystal, which is reflected in earlier measurements of GaS crystals in the range 18-25 μm. Figure 4.2 shows phonon modes observed in transmission from a thin $GaSe_{x-1}S_x$ x =0.44 sample. The evolution of 7 of those modes with sulphur doping is presented in Figure 4.3. Three of the modes (A,B & C) are present in all the samples and originate from the GaSe parent crystal. The four high frequency modes (D, E, F, G) present themselves in the sulphur doped crystals, though from the literature, mode D at 230.5 $\pm 0.25\,cm^{-1}$ likely originates from the GaSe parent crystal. The evolution of the modes is complex and no general rule presents itself. However, it is to be noted that in the region of optimal doping x = 0.11-0.22 the frequency distribution of the modes decreases significantly and they move towards the centre of their respective photon bands, either $GaSe_{x-1}S_x$, or the proposed GaS band.

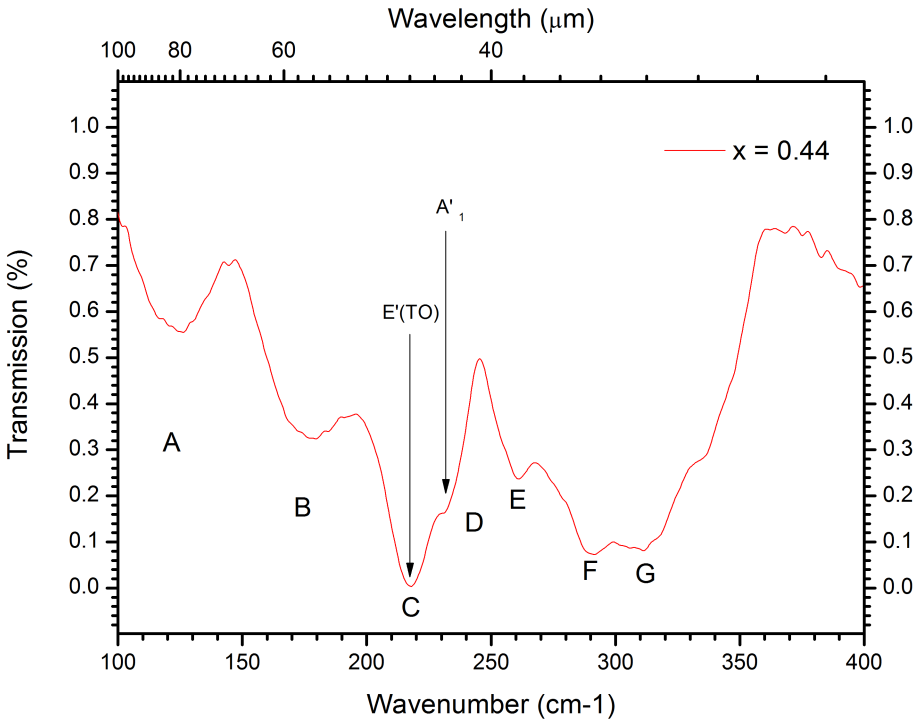

Figure 4.2: Observed phonon modes in a thin $GaSe_{x-1}S_x$ sample x = 0.44.

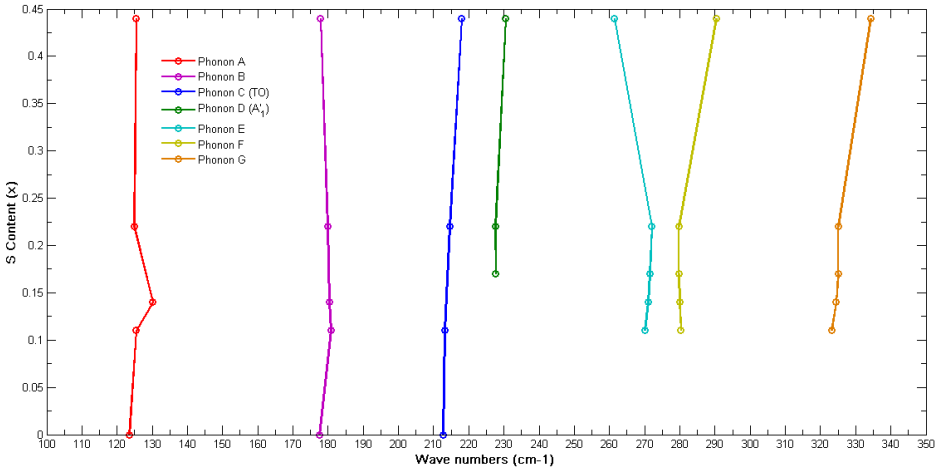

Figure 4.3: Evolution of IR active phonons in FTIR spectra of GaSe and $GaSe_{x-1}S_x$ samples x = 0.05, 0.11, 0.22, 0.27, 0.44.

Modes A at 123.4 $\pm 0.25\,cm^{-1}$ (81 μm) and B at 177.5 $\pm 0.25\,cm^{-1}$ (56.3 μm) shift by 5.45 GHz and 9 GHz in the presence of sulphur doping but then remain relatively stable as the doping increases. The main phonon peak E'(TO) (C) is

observed to shift linearly to higher frequencies by 15 GHz/mass% in the presence of sulphur from 213 $\pm 0.25\,cm^{-1}$ (46.8 μm) to 218 $\pm 0.25\,cm^{-1}$ (45.9 μm). The A_1' mode (D) follows a similar trend. The GaS associated modes follow a more complex transformation. Modes E at 270 $\pm 0.5\,cm^{-1}$ (36 μm) and F at 280 $\pm 0.25\,cm^{-1}$ (37 μm) first move closer together in the optimal doping range, before diverging rapidly, to 261.4 $\pm 0.25\,cm^{-1}$ (38.2 μm) and 290.3 $\pm 0.25\,cm^{-1}$ (34.45 μm) respectively, at higher sulphur concentrations. Phonon G at 325 $\pm 0.25\,cm^{-1}$ (31 μm) follows the same general trend as F, shifting to 334.2 $\pm 0.25\,cm^{-1}$ (29.92 μm) at higher sulphur concentrations.

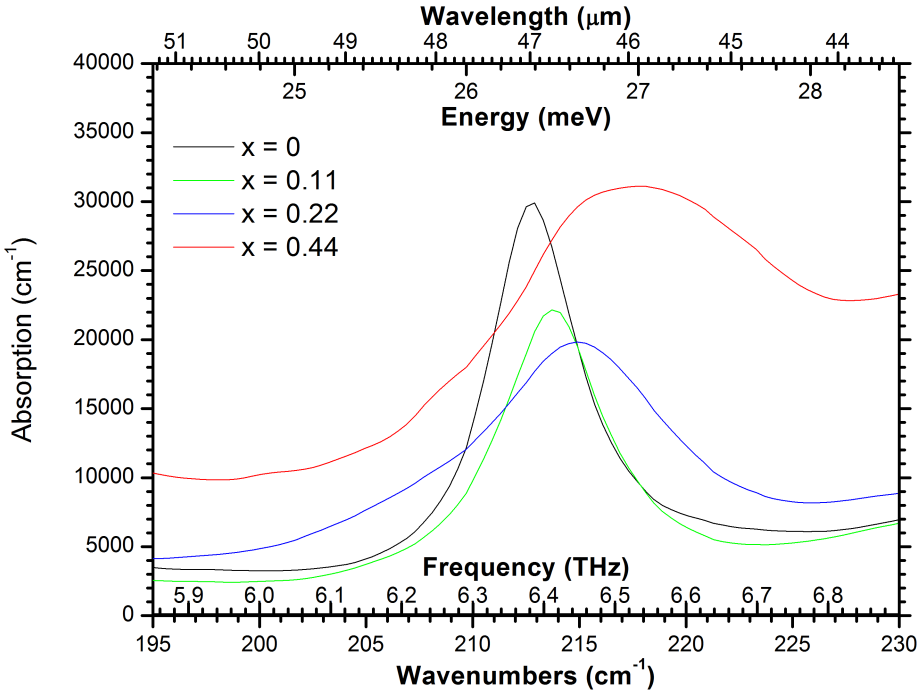

Figure 4.4: Absorption spectra of the E'(TO) mode in GaSe, $GaSe_{x-1}S_x$ samples x = 0.11, 0.22, 0.44.

Figure 4.6 presents, for the first time, the evolution of the estimated absorption coefficients for $GaSe_{x-1}S_x$ crystals, x = 0.11, 0.22 0.44, calculated using the relation:

$$\alpha = \frac{2}{d} ln \left[\frac{I}{I_0 T} \right] \tag{4.1}$$

where d is the thickness of the crystal, I is the transmitted intensity, I_0 is the incident

intensity, $T = 1 - \left[\frac{n-1}{n+1}\right]^2$ is the transmission factor and n is the refractive index. The estimates were calculated using the value of refractive index n for GaSe crystals found in the literature [315, 202]. It can be seen that the intensity of the phonon decreases in intensity with increased doping, from $\alpha = 3 \pm 0.75 \times 10^4\, cm^{-1}$ in GaSe to $\alpha = 2.3 \pm 0.6 \times 10^4\, cm^{-1}$ in $GaSe_{x-1}S_x$, x = 0.11, and $\alpha = 2 \pm 0.4 \times 10^4\, cm^{-1}$ for x =0.22. The results for x = 0.44, show an increase in absorption $\alpha = 3.3 \pm 0.8 \times 10^4\, cm^{-1}$, this varies from the expected continuing decay of the phonon mode. The values for the absorption coefficient can be assumed to have significant errors $\sim 20\%$. These error are a result of the extreme thinness of the samples, the variable baseline on the measurement (x = 0.44 in particular) and the sensitivity of the transmission factor due to the strong anomalous dispersion around the phonon mode. So, the estimated value for GaSe is found to be in reasonable agreement with those found in the literature: $\alpha = 4 \times 10^4\, cm^{-1}$ [212, 202, 283]

As seen, sulphur doping significantly transforms the structure of the phonon band in GaSe crystals. The THz regimes benefits from the lower absorption and refractive index associated with the decay of main phonon mode and its slight shift to higher frequencies, the effect of which is evident in the results in Chapter 3. However, the $E'(TO)$ mode remains intensive and significant increase in the bandwidth of a THz OPO would not be forthcoming, as absorption will remain large at higher frequencies. On the other hand, the longwave edge of the main transparency window, shifts significantly to higher frequencies, as a result of the phonons arising from sulphur doping, which is reflected in the literature, where the effects may be observed at wavelengths in the range 16-22μm [221, 311, 310, 312, 266, 209], so the ability to FIR generation in this range would be seriously reduced.

4.3 Raman Spectroscopy of GaSe1-xSx

Since the 1960's, a significant number of Raman spectroscopy studies, both theoretical and experimental have also been conducted , first on GaSe and GaS [321, 322, 323, 237, 291, 102] and later on $GaSe_{x-1}S_x$ [324, 321, 325, 103, 326, 327, 237, 328, 291], as well as other doped GaSe crystals [329, 291]. As with all the literature encountered to date, the results tend to be scattered, inconsistent and contradictory, in particular the discussion and interpretation of results. However, Raman spectroscopy studies are relatively easy to conduct, transformation of the centre frequency of the $E'(TO)$ mode can be observed, and due to the ubiquity of commercial instruments, the main features of the crystals' spectra are well established.

The determination of the polytype composition of the crystals is important for optimising the crystal growth process, higher quality crystals having reduced admixtures. Furthermore, while the linear optical properties of the different polytypes are largely the same, the nonlinear properties vary significantly. The effective nonlinear coefficient is dependent on the crystal polytype, the relations for determining d_{eff} in each are given in Table 4.3 [214].

Table 4.2: Relations for determining effective nonlinear coefficient (d_{eff}) for ε, γ & δ-polytypes of GaSe crystals.

Polytype	Type-I interaction	Type-II interaction
ε	$d_{22} cos\,\theta\, sin\, 3\phi$	$d_{22} cos^2\,\theta\, sin\,\phi$
γ	$d_{22} sin\,\theta\, -\, d_{22} cos^2\,\theta\, sin\,\phi$	$d_{22} cos^2\,\theta\, sin\, 3\phi$
δ	$d_{22} sin\,\theta$	0
β	0	0

From these relations, using the values for the optical properties from before, and assuming the ϕ-angle is maximised, the angle dependent effective nonlinear coefficient is calculated for ε, γ & δ-polytypes and the results presented in Figure: 4.5. As β is a centrosymmetric crystal, the second order nonlinear coefficient vanishes. From these results the Figure of Merit, in the THz regime, is calculated and presented in Table 4.3. We can see that, the nonlinear FoM, and thus, the efficiency of nonlinear frequency conversion and the most appropriate interaction type, are effected by the crystal polytype; the ε-polytype is preferred as it maximise conversion

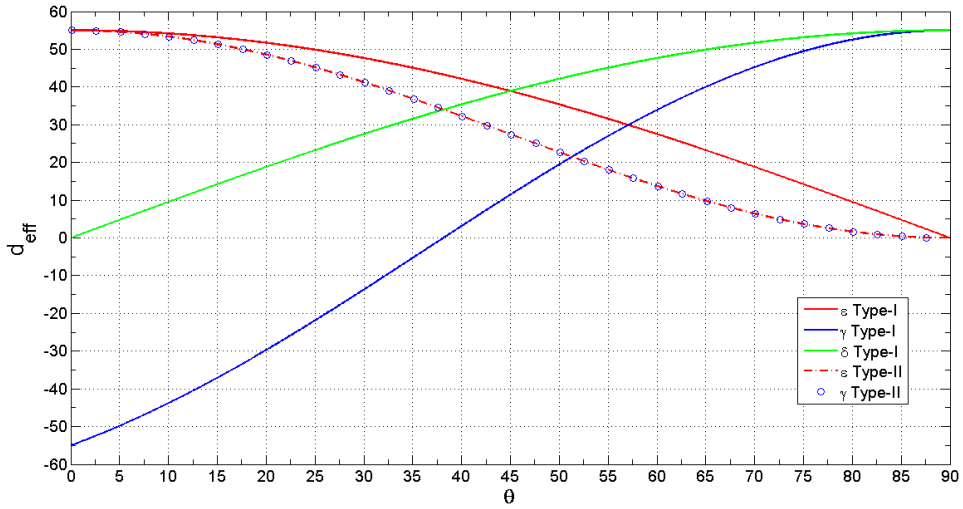

Figure 4.5: Angle dependent d_{eff} for Type I & II interactions in the ε, γ & δ-polytypes of GaSe.

efficiency in the THz regime. So, for high quality crystals and optimised efficiency the polytypism of the crystals should be well controlled.

Table 4.3: Nonlinear Figure of Merit (FOM) for the ε, γ & δ-polytypes of GaSe crystals.

Crystal	Type	ε-Polytype FoM	γ-Polytype FoM	δ-Polytype FoM
GaSe	I	19.8	12.5	0.6
GaSe	II	19	19	-

4.3.1 Introduction to Raman spectroscopy

Raman spectroscopy differs from FTIR and THz-TDS in several respects. IR spectroscopy is based on the absorption of photons, whose energies correspond to the energy difference between vibrational states of molecules, from a polychromatic source. Raman spectroscopy relies on the inelastic scattering of monochromatic photons from these molecules. The energy difference between the incident photons ($h\omega_L$) and the scattered photons ($h\omega_R$) is equal to the transition energy of the vibrational states ($h\omega_k$):

$$h\omega_R = h\omega_L \pm h\omega_k \tag{4.2}$$

The energy differences are in the same range as the absorbed photons in IR spectroscopy, but may be interrogated by UV, visible and near-IR sources. Due to selection rules, vibrational modes which are Raman active are not IR active and vice-versa, however, in non-centrosymmetric crystals, such as GaSe, some modes maybe be both IR and Raman active. The intensity of absorbed light in IR spectroscopy is dependent on the change in the dipole moment $I_{IR} \propto \left(\frac{\partial \mu}{\partial q}\right)^2$, where as the intensity of Raman scattering is dependent on the change in the polarisation $I_R \propto \left(\frac{\partial \alpha}{\partial q}\right)^2$; so, Raman spectroscopy often presents spectra which are complimentary to those of FTIR spectroscopy.

Inelastic scattering can be described classically; if we consider a molecule in an electrical field, then the induced dipole moment is give by [330]:

$$\mu_{induce} = \alpha E \tag{4.3}$$

where α is the polarisability tensor, which is characteristic of the material and E is the electric field. Provided that the electric field is not too strong the induced dipole moment remains linear with E. In an oscillating electric field $E = E_0 cos(\omega t)$, the induced dipole becomes:

$$\mu_{induced} = \alpha(\omega) E_0 cos(\omega t) \tag{4.4}$$

where $\alpha(\omega)$ contains both a static component and a time varying component related to the vibrational modes of the molecule at some frequency ω_k, given as:

$$\alpha(\omega) = \alpha_0 + \alpha_1 cos(\omega_k t) \tag{4.5}$$

Substituting Eqn 4.5 in to Eqn 4.4 we can find:

$$\mu_{induced} = \left[\alpha_0 + \alpha_1 cos(\omega_k t)\right] E_0 cos(\omega t) \tag{4.6}$$

$$= \alpha_0 E_0 cos(\omega t) + \frac{1}{2}\alpha_1 E_0 \left\{cos\left[(\omega + \omega_k)t\right] + cos\left[(\omega - \omega_k)t\right]\right\} \tag{4.7}$$

resulting in three terms:

$$\alpha_0 E_0 cos(\omega t) \qquad \text{Rayleigh Scattering}$$

$$\alpha_1 E_0 cos\left[(\omega - \omega_k)t\right] \qquad \text{Stokes}$$

$$\alpha_1 E_0 cos\left[(\omega + \omega_k)t\right] \qquad \text{Anti-Stokes}$$

In Rayleigh scattering, the energy of the incident and scattered light are the same. In the two Raman scattering terms, the energy of the scattered light either is reduced by the transition energy of the vibrational mode, $h(\omega - \omega_k)$ (Stokes), or is increased by the transition energy of the vibrational mode, $h(\omega + \omega_k)$ (Anti-Stokes).

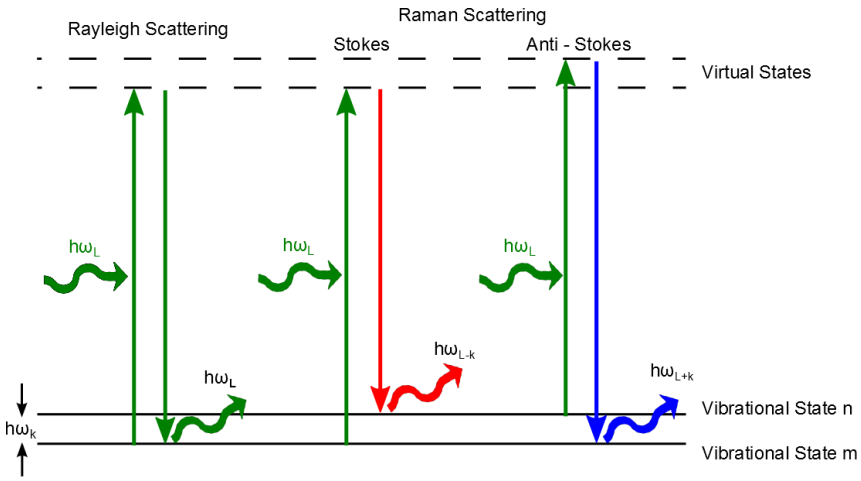

Figure 4.6: Schematic representations of Rayleigh and Raman scattering.

The efficiency of inelastic scattering is quite low, ≈ 1 in 10^6, so the majority of photons are scattered elastically as Rayleigh scattering. At room temperature, the majority of molecules tend to be in the lower vibrational states, so the number of inelastically scattered Anti-Stokes photons is much lower than the number of Stokes photons.

4.3.2 Experimental details

Raman spectroscopy was conducted using Raman microscope (inViva Renishaw, UK), with a 1064 nm Nd:YAG pump source. The beam was aligned for optimal focus and shape using a collinearly propagating HeNe, in advance of measurements.

Using a 1064 nm laser reduces unwanted two photon absorption, scattering and fluorescence. The lower limit of the measurement range for this instrument is $100\,cm^{-1}$ ($100\,\mu$m) as a result of the filter bandwidth. The Anti-Stokes spectra were not recorded. Prior to, during and after the measurement the instrument was calibrated using the well known Raman peak in Silicon (Si) wafer at 520.7 cm^{-1}

Both cleaved and cut & polished crystal samples were measured. Materials were carefully handled to avoid contamination, samples were placed on, fresh, clean microscope slide prior to installation in instrument. The slide was checked for Raman peaks before measurement, to avoid any artefacts in the results, and the slide background spectrum was removed from measurement results in software processing. Measurements of cleaved samples were made on freshly exfoliated samples ensuring a clean surface.

The extinction level was set using variable filters, such that the intensity of the strongest phonon mode was at approximately 80% of saturation level. All subsequent measurements were performed at this setting to allow direct comparison. The results are an average of 5 sets of measurements across the sample surface. Each set of measurements consisted of an average of 5 measurements of 10 s duration. The optical microscope was used to ensure measurements were made on clean defect-free areas of the crystals.

The Raman microscope system has no defined polarisation axis on the input or output and detection is not polarised, so, in spite of efforts, negligible change in measurement results is observed through rotation of the cut and polished samples. All measurements were conducted at 300 K, at sea level, and in normal atmospheric conditions.

4.3.3 Results

The Raman spectra of pure ε-polytype GaSe crystals are relatively simple being characterised by 3 intense narrow phonon lines A_1' at 133 cm^{-1}, $E'(TO)$ at 213 cm^{-1} A_1' at 307 cm^{-1} and a weaker line $E'(LO)$ at 250 cm^{-1}, as depicted in Figure 4.8. These lines correspond to the the vibrational modes within the crystal's covalently

bonded Se-Ga-Ga-Se primitive layers [237]. The labelling of vibrational modes for the crystals follows the nomenclature set out in the literature [291, 327] and is depicted in Figure 4.7. Lines labelled 'E' represents shear modes, while those labelled

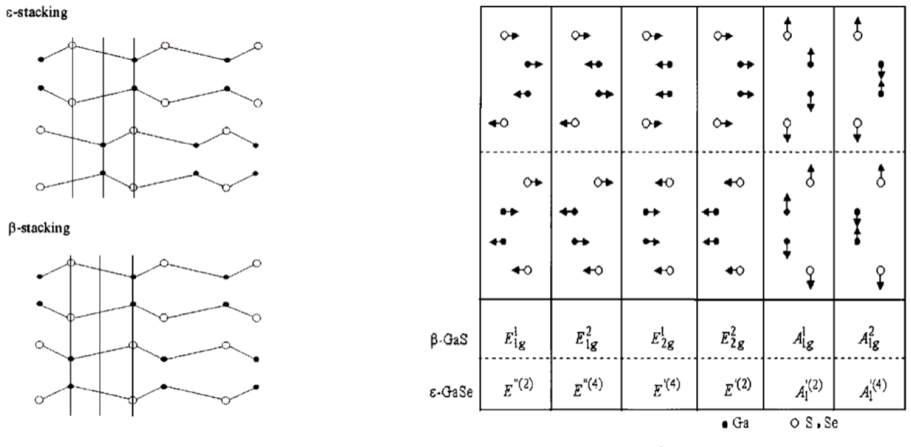

Figure 4.7: The β and ε polytypes of GaSe, $GaSe_{x-1}S_x$ & GaS crystals [327].

as 'A' represents compression modes. The GaSe phonon at 133 cm^{-1} is extremely intense. It has an amplitude 3 times that of the strongest GaS line at 188 cm^{-1} as shown in Figure 4.8. The Raman spectra of β-polytype GaS crystals are also

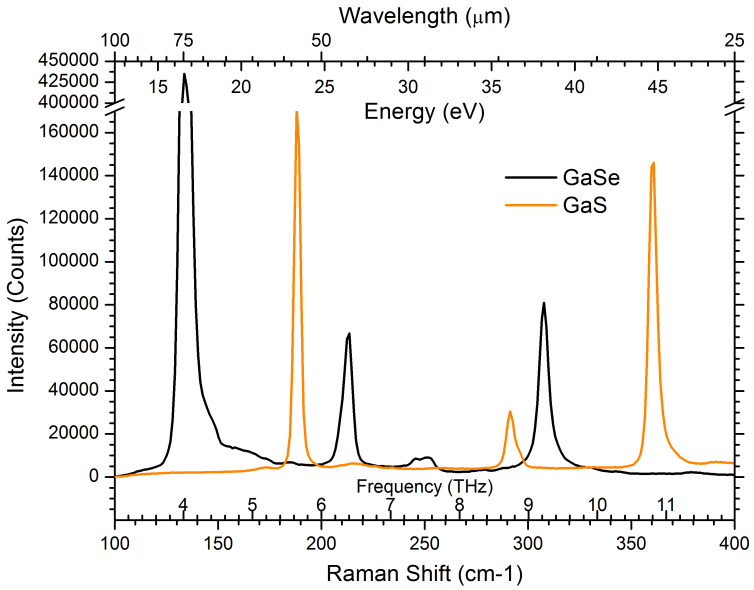

Figure 4.8: Raman spectra of pure GaSe and GaS crystals

relatively simple, characterised by 2 strong phonon lines A^1_{1g} at 188 cm^{-1} and A^2_{1g} at 360 cm^{-1}, with weaker lines E' at 215 cm^{-1} and E^1_{2g} at 291 cm^{-1}, as shown

in Figure 4.8. The arrangement of atoms within the layers of GaS is similar to those GaSe, but the Selenium atoms are replaced by Sulphur, forming S-Ga-Ga-S cells [327]. As described above, the arrangement of atoms with the layers of GaSe

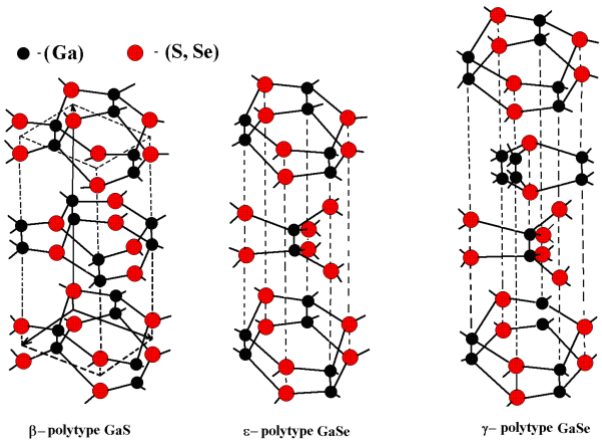

Figure 4.9: The β, ε & γ polytypes of GaSe, $GaSe_{x-1}S_x$ & GaS crystals [331].

and $GaSe_{x-1}S_x$ are very similar, consisting of two layers of Ga atoms sandwiched between layers of Se and S atoms respectively [237, 327]. Five regular stacking polytypes have been identified in the literature for GaSe; the β, ε & γ polytypes are represented schematically in Figures 3.8, 4.7 & 4.9. The centrosymmetric β-polytype has a unit cell that includes sections of two crystal layers, with the space group symmetry D^4_{6h}. The non-centrosymmetric ε-polytype, the main component of "from the melt grown" crystals, belongs to the D^1_{3h} space group symmetry and its unit cell also includes two primitive layers [102]. The γ-polytype belonging to $C^5_{3\nu}$ space group symmetry has a unit cell that contains only one primitive layer and is also non-centrosymmetric. The four-layer δ-polytype of $C^4_{6\nu}$ is usually obtained from the vapour phase [320]. Investigations by Allakhverdiev *et al* have suggest that there also exists a polytype with 8 layers in the unit cell [102]. GaSe crystals grown by Bridgman techniques and used in nonlinear devices, as is the case here, are commonly of ε-polytype, but can contain admixtures of other polytypes. [102] The stacking of the layers in GaS crystal grown from the melt is invariably of the centrosymmetric β-polytype [332], though even in crystals of pure GaS Maker fringe experiments produce weak SHG generation [333]. So, it is the case that GaS can also contain an admixture of ε and γ polytypes.

4.3.4 Evolution of Raman active phonons in GaSe1-xSx with doping

The transformation of the Raman spectra of $GaSe_{x-1}S_x$ with Sulphur doping is complex as a result of the multiplicity of polytypes that can exist within the parent GaSe and GaS crystals. Similar to parent crystals, the unit cell of the solid solution crystals contain up to fourfold primitive layers; stacking then gives rise to at least four well known structural modifications: ε, β, δ and γ. GaSe and GaS crystals form a continuum $GaSe_{x-1}S_x$ compounds, where the mixing ratio varies from x = 0 to 1. In solid solution single crystals this can lead to the presence of a range of dissimilar crystallised phases, depending on the differing composition and its tendencies towards GaSe or GaS, [326], which is reflected in the phonon structure [237]. The transformation of the phonon band reflects not only the polytype but also the gradual incorporation of sulphur into the GaSe lattice. The S atoms being lighter than the Se atoms lead to a shift in the lattice vibrations to higher frequencies. The shift and splitting of the phonon lines can be used to deduce the ratio of Selenium to Sulphur content [237].

Examples of the obtained Raman spectra for GaSe, $GaSe_{x-1}S_x$ & GaS crystals are presented in Figure 4.10. We can see that as the sulphur content increases, the 133 cm^{-1} phonon begins to collapse, first one (145 cm^{-1}) and then a second (155 cm^{-1}) additional peak rise up and out of its shoulder. The trend of these new peaks is to grow in intensity with doping and shift to higher frequencies closer to the main GaS phonon mode at $188cm^{-1}$ at a rate of 24.5 cm^{-1}/x and 34 cm^{-1}/x respectively. A third mode begins to develop at 164 cm^{-1} in $GaSe_{x-1}S_x$, x = 0.44, appearing as a shoulder on the higher frequency 168 cm^{-1} line. It has been proposed that these multi-peak phonon modes are as a result of single crystal formation, and these modes have previously been decomposed into different crystal species [327], the 133 cm^{-1} (A) mode as Se-Ga-Ga-Se and the 168-188 cm^{-1} (D) mode as S-Ga-Ga-S; with the intermediate modes (B & C) representing Se-Ga-Ga-S lattice vibrations, as shown in detail in Figure 4.11.

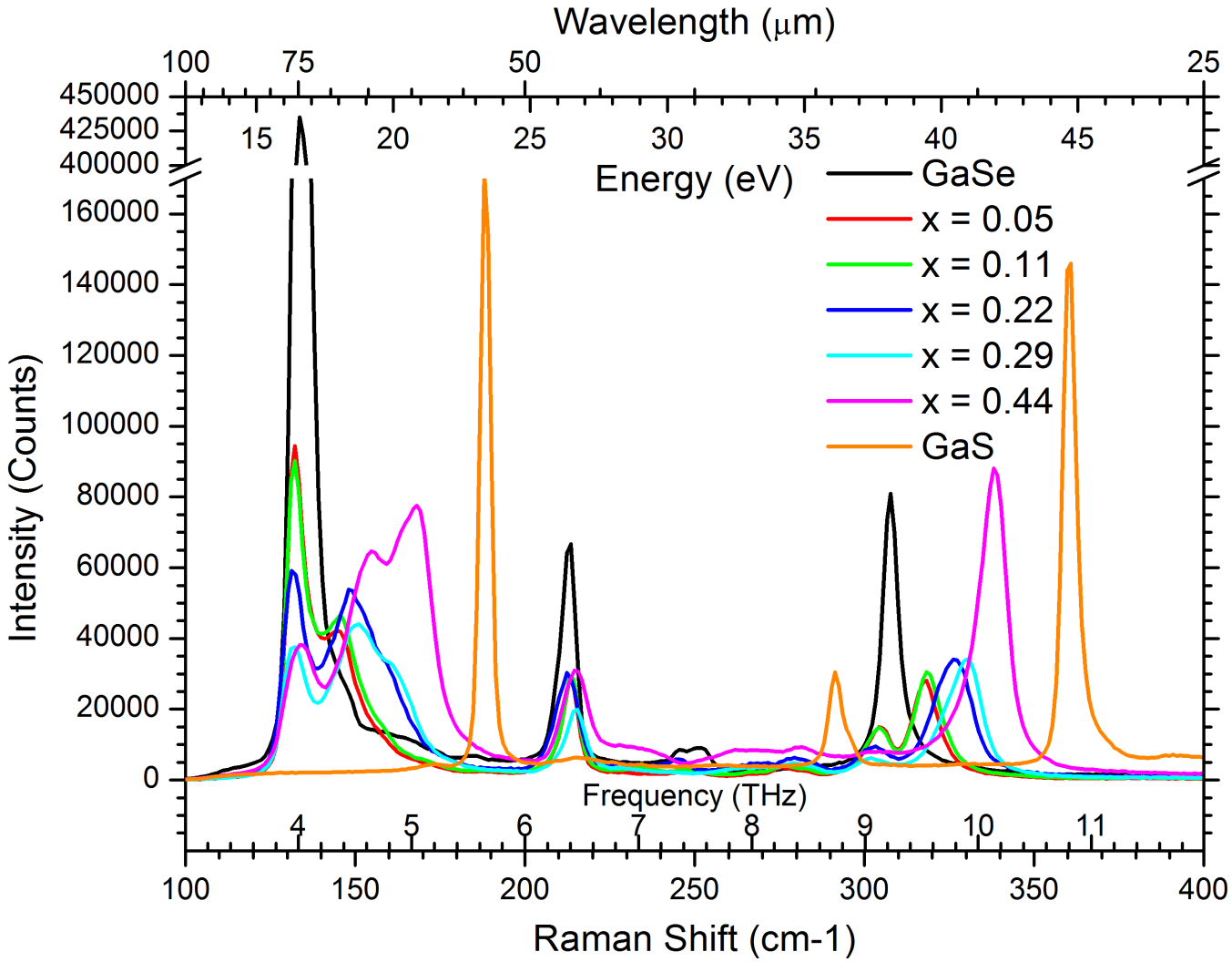

Figure 4.10: Raman spectra of GaSe, $GaSe_{x-1}S_x$ (x = 0.05, 0.11, 0.22, 0.27, 0.44) and GaS.

Table 4.4: Raman active phonons observed in GaSe GaS and $GaSe_{x-1}S_x$ crystals.

Crystal	x	A_1' cm^{-1}	A_{1g}^1 cm^{-1}	cm^{-1}	$E'(TO)$ cm^{-1}	cm^{-1}	$E'(LO)$ cm^{-1}	A_1' cm^{-1}	E_{2g}^1 cm^{-1}	A_{1g}^2 cm^{-1}
GaSe		133.64	-	-	213.54	-	249.85	-	307.76	-
$GaSe_{x-1}S_x$	0.11	132.235	145.62	157.86	214.36	234.19	248.47	276.95	304.21	318.35
$GaSe_{x-1}S_x$	0.22	132.235	148.13	159.27	214.65	233.34	245.46	279.14	303.41	327.32
$GaSe_{x-1}S_x$	0.44	133.64	154.82	168.16	215.74	232	-	280.51	302.32	338.16
GaS		-	-	188.11	215.74	-	-	291.42	291.42	360.86

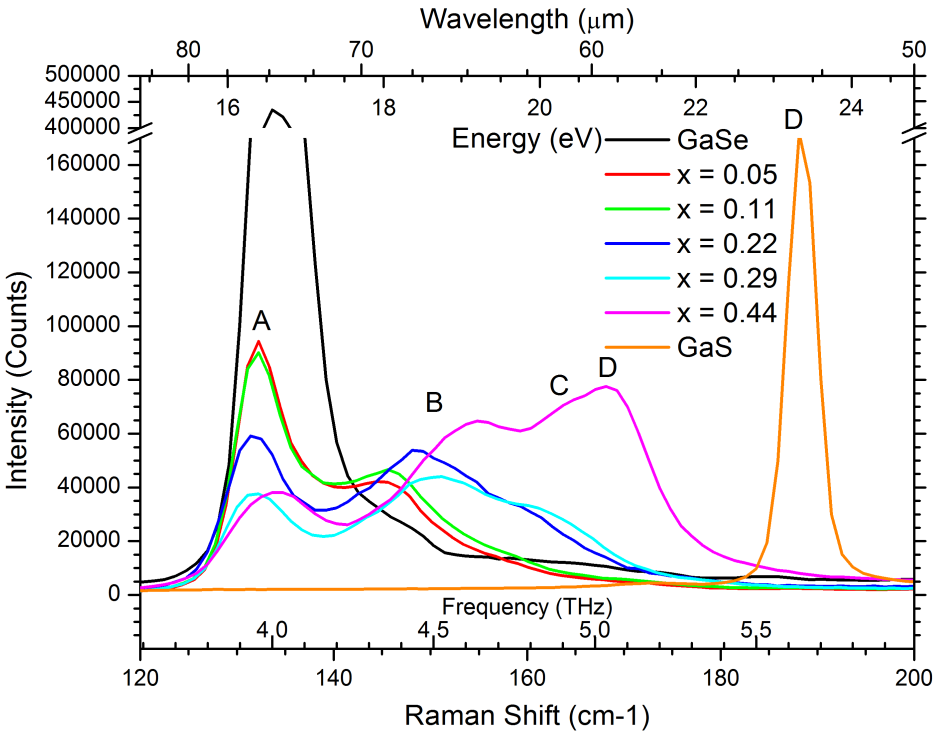

Figure 4.11: Composition of the complex multi-peak phonon mode in $GaSe_{x-1}S_x$, with GaSe and GaS.

Even after significant doping (x = 0.44), the 133 cm^{-1} is still present and no shift in frequency is observed as shown in Figure 4.12. However, the mode does begin to collapse as a result of doping and its relative intensity is reduced by >10 times. The main GaS phonon at 188 cm^{-1} is intensive, but still 3 time less intense than that of the main GaSe Raman mode.

The phonon at 213-215 cm^{-1} which is the main IR phonon absorption mode, is common to GaSe and GaS, and while quite intense for GaSe, it is drastically reduced for GaS (10x) as seen in Figure 4.10. The greatly reduced $E'(TO)$ phonon in GaS is to be expected, as it is a centrosymmetric crystal. A linear shift of the $GaSe_{x-1}S_x$ phonons to the higher frequencies with doping is observed, with a slope of 4.5 cm^{-1}/x (15 GHz/mass %)as shown in Figure 4.12. This is in good agreement with the results of the FTIR measurements above.

Low amplitude features are seen at 250 cm^{-1} in GaSe shifting to 245 cm^{-1} in $GaSe_{x-1}S_x$, x = 0.22; its presence is not detected in higher doping levels (Figure

4.10). The amplitude of this phonon decays with increasing sulphur concentrations. This is in contrast to the findings of Perez-Leon *et al* who observed the growth and strengthening of the feature with doping and attributed it to the presence of γ-polytype domains [237].

Another low amplitude feature appears in $GaSe_{x-1}S_x$ crystals around 234 cm^{-1}, for x= 0.11 and shifts to 232 cm^{-1} for x = 0.44 (Figure 4.10). It remains weak, again, in contrast to the findings of Perez-Leon *et al* who, once more, observed the growth and strengthening of the feature with doping and attributed it to the presence of γ-polytype domains[237].

The phonon feature at 308 cm^{-1} rapidly collapses with doping in $GaSe_{x-1}S_x$; as the mode collapses, it splits into two components as shown in 4.10. One component, the lesser of the two, continues to collapse with increasing x and shifts toward lower frequencies and the GaS mode at 291 cm^{-1} at a rate of 16 cm^{-1}/x. The other component, after the initial collapse, grows in magnitude with doping and shifts towards higher frequencies the intense GaS phonon mode at 360 cm^{-1} at a rate of 46 cm^{-1}/x 4.12. The collapse of the low frequency components of split modes while high frequency components continue to grow reflect the Se:S balance in the crystal.

4.3.5 Discussion

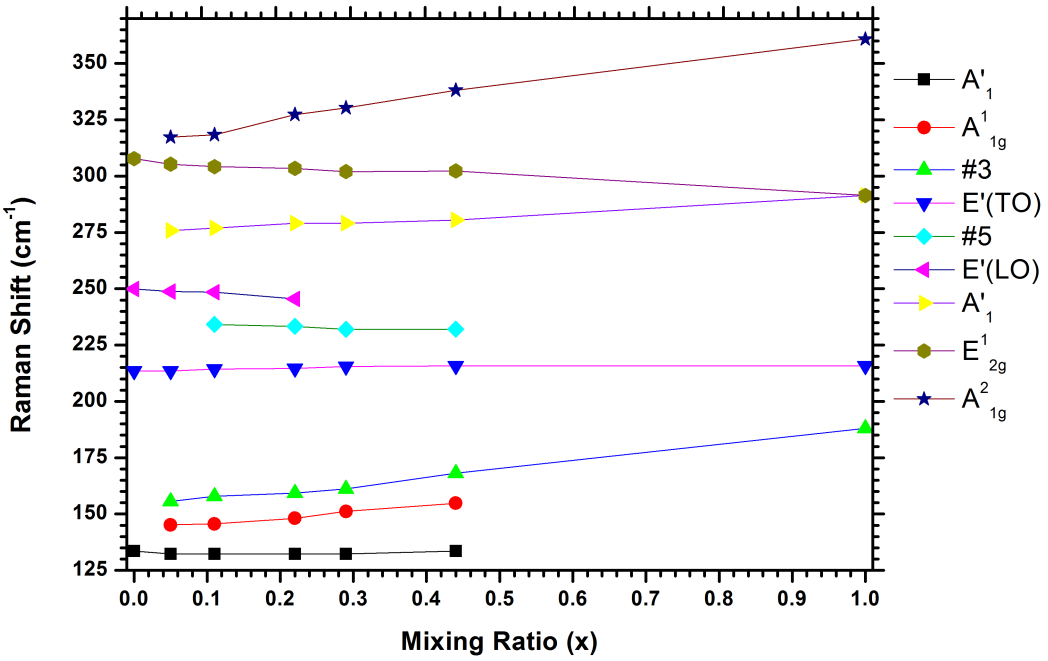

Figure 4.12: Evolution of Raman spectra of GaSe, $GaSe_{x-1}S_x$ (x = 0.05, 0.11, 0.22, 0.27, 0.44) and GaS with doping.

It can be seen that for mixing ratios $x \leq 0.11$ and, in particular, $0.05 \geq x \geq 0.11$, the change between the Raman spectra are not as dramatic as for other values. This is ascribed to the weak effect of this level of doping on the crystal lattice parameters and borne out by measurments made by colleagues at the Siberian Physical-Technical Institute of Tomsk State University (Figure 4.13). In contrast to Vegard's law, a flat dependence on sulphur content is observed for $x \leq 0.11$, which may be due to a nonlinear response of the defect concentration to Sulphur doping.

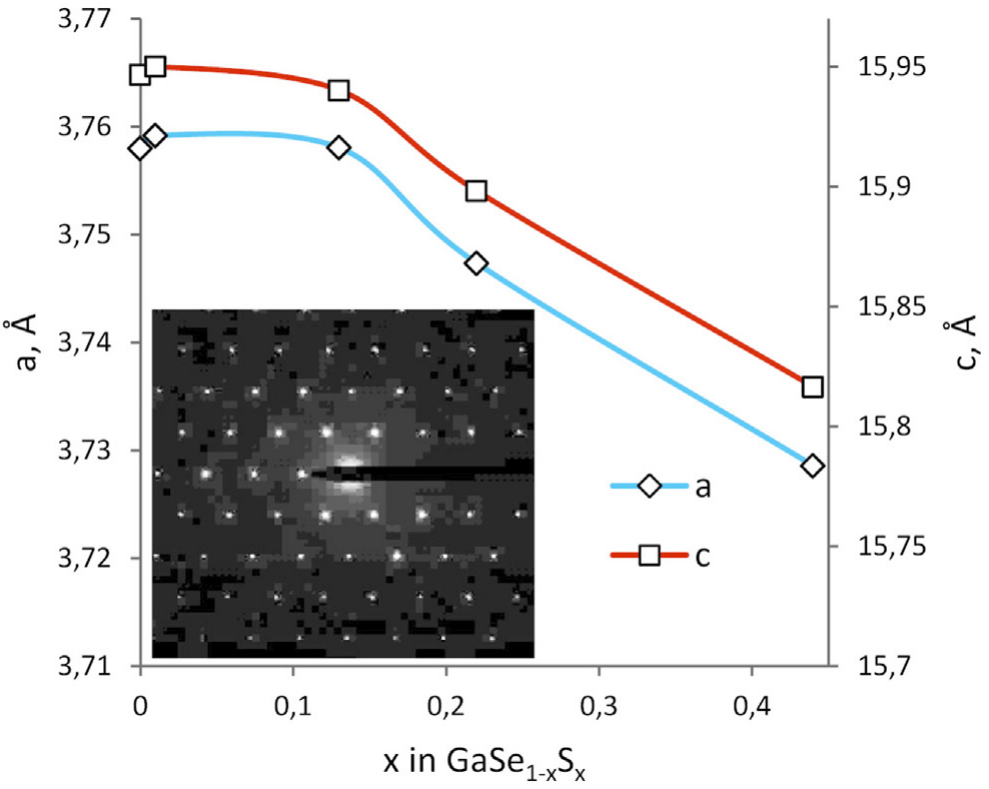

Figure 4.13: Lattice parameters versus S-doping for $GaSe_{x-1}S_x$crystals, Inset:SAED pattern observed by TEM for $GaSe_{x-1}S_x$ x = 0.44.

Brebner & Ficher (1964) gave the limits of possible mixing ratio limits for ε and γ- polytypes in GaSe1xSx as $0 \leq x \leq 0.1$, while the centrosymmetric β-polytype dominates at $x \geq 0.6$ [324]. However, Allakhverdiev *et al* and others have observed SHG crystals with a sulphur content up to x = 0.8 [103, 237], indicating the presence of noncentrosymmetric components. Later, the mixing ratio limits were given as $0 \leq x \leq 0.01$ for ε-polytype, $0.01 \leq x \leq 0.03$ for ε and γ-polytype admixtures, $0.05 \leq x \leq 0.4$ for γ-polytype and $0.5 \leq x \leq 1$ for β-polytype in [325]. While, Ref [103] states that the phase transition from the ε- to the β-polytype takes place for $0.2 \leq x \leq 0.3$m and [326] placed this transition at = 0.4. More recent studies have associated the $0 \leq x \leq 0.4$ region with mixtures of ε and γ-polytype, while mixtures of ε, γ and β-polytypes were observed for the $0.5 \leq x \leq 1$ region [238], similar limits were found for mixing ratios of β and γ-polytypes in [237].

From Perez-Leon *et al*'s discussion, the phonon modes at 234 cm^{-1} and 250 cm^{-1} which are indicative of the presence of γ-polytype [237]; we found that these

modes remain weak or decay with increasing sulphur content, up to x = 0.44. Thus, our results show we have ε-polytype with only a weak presence or a decrease in the admixture of γ-polytype in the crystal with increased doping and improved lattice structure.

The question of which mixing ratio leads to what polytype is rather complex, with a satisfactory solution yet to be found while the literature surrounding $GaSe_{x-1}S_x$ compounds remains scattered, inconsistent and contradictory. There are however strong indications that other factors in the growth process, outside of the mixing ratio, play an important role in determining the polytypism of the crystals [237, 334], this is reinforced by the variation in polytypism that has been found along the growth axis of $GaSe_{x-1}S_x$ crystals [237]

Using X-ray methods to identify different polytypes and analysis of their relative content and location within a sample is also challenging as the 2θ angles of the most intensive diffraction lines for β, ε, γ, δ-polytypes are very close, and non-destructive characterization by X-ray reflection from the surface can only analyse a thin layer of the sample [214]. A non-linear optical method proposed by Andreev *et al* does not allow the identification of β-polytype [214].

Furthermore the difficulty in determining the as grown crystal composition, due to strong effect of low doping concentrations on physical properties of GaSe, e.g. in the case of Al-doping [103], adds an additional layer to ambiguity to the problem.

However, it remains the case that, only weak indication of other polytype admixtures were found in the measured crystals, thus we can conclude that the grown crystals are of a high quality and that we are free to use the effective nonlinear coefficient relations for ε-polytype. Hence, the efficiency of generation for both Type-I & II interactions is maximised.

4.4 New Sellmeier Equations for full transparency range for GaSe and GaS

As discussed previously, of the known sets of Sellmeier equations, only 3 are suitable for use in the THz regime [202, 295, 293]. Of these 3, Vodopyanov's equations are in widespread use for THz applications despite this being well outside their claimed validity range (0.65 - 18 μm) [293]. The values predicted by Refs [295, 293] are not in good agreement with the results in this work or those found in the literature; Chen *et al*'s equations are found to be the best fit of existing estimates.

Using the result in this work for the optical properties of GaSe and GaS crystals in the THz and FIR regimes, described above, and the best available mid-IR data, from phase matching experiments and the literature [294, 103], colleagues at the Siberian Physical Technical Insitute of Tomsk State University, designed by nonlinear methods new Sellmeier equations, presented below and depicted in Figure 4.14, for the full transparency range of both GaSe and GaS crystals, i.e. 0.8–20 μm and 4–0.2 THz; the relations for GaSe allow for the anomalous dispersion around the $E'^{(2)}$ rigid layer phonon mode at 0.595 THz.

Sellmeier equations of GaSe crystals

$$n_o^2 = 10.6409 + \frac{0.3788}{\lambda^2 - 0.1232} + \frac{6963.32}{\lambda^2 - 2198.85} + \frac{0.017\lambda^2}{\lambda^2 - 262177.5577} \tag{4.8}$$

$$n_e^2 = 5.76 + \frac{0.3879}{\lambda^2} + \frac{0.2288}{\lambda^4} + \frac{0.1223}{\lambda^6} + \frac{0.3706\lambda^2}{\lambda^2 - 1780.3} \tag{4.9}$$

Sellmeier equations of GaS crystals

$$n_o^2 = -\frac{0.01129}{\lambda^6} + \frac{0.03648}{\lambda^4} + \frac{0.51402}{\lambda^2} + 6.59624 + \frac{2.71047\lambda^2}{\lambda^2 - 1025.42116} \tag{4.10}$$

$$n_e^2 = \frac{0.0113}{\lambda^6} + \frac{0.10569}{\lambda^4} + \frac{0.44573}{\lambda^2} + 4.92114 + \frac{0.315\lambda^2}{\lambda^2 - 720.12225} \tag{4.11}$$

(a) Dispersions

(b) Birefringence

Figure 4.14: GaSe dispersions (a) and birefringence (b) as reported in the literature [202, 293, 295] and new estimates based on the measurements in this work. New Estimates: black; curves calculated by dispersion equations from Ref [202] : olive, Ref [293] : blue, and Ref [295]: red.

4.5 Summary

In this chapter, we have studied the main phonon band of GaSe, $GaSe_{x-1}S_x$ & GaS crystals by both FTIR and Raman spectroscopy. The transformation of the main $E'(TO)$ phonon has been studied and its absorption coefficient estimated for GaSe and $GaSe_{x-1}S_x$, x = 0.11, 0.22 & 0.44. The results of these estimates are found to be in agreement with the published result for GaSe crystals within the margin of error. The amplitude of the $E'(TO)$ phonon is found to decay with increased sulphur doping and the centre frequency to shift to short wavelengths at a rate of 375 GHz/x (15 GHz/mass% or 4.5 $cm^{-1}/mass\%$) in both the absorption and Raman spectra. While this shift and decay improve the optical properties in the THz regime, increasing the efficiency of nonlinear generation, the ability of OPOs to operate at higher THz frequencies is not greatly enhanced. All the measured GaSe and $GaSe_{x-1}S_x$ crystals were found to be of the ε-polytype, the admixture of other polytypes are found to be small and their content decrease with increased doping, indicating the high quality of the crystals. Furthermore, as discussed, the ε-polytype has the greatest effective nonlinear coefficient, maximising the frequency conversion efficiency in $GaSe_{x-1}S_x$ crystals. Sellmeier equations valid for the full transparency range (0.8–20 μm & 4–0.2 THz) of GaSe and GaS designed by colleagues based, in part, on the optical properties determined in this work are presented.

Chapter 5

Nonlinear Optical properties of GaSe1-xSx

5.1 Introduction

In this chapter, we will report on attempts to determine the key nonlinear optical properties d_{eff} and n_2 in the FIR and THz regimes for GaSe and $GaSe_{x-1}S_x$ crystals by the classic Maker fringe and Z-scan methods, pumped using the Felix free electron laser. Measurements of these properties, which are crucial for designing efficient nonlinear optical frequency conversion sources, have to date been largely confined to around 1.064 μm.

It is obvious that a high $\chi^{(2)}$ nonlinearity, the mechanism we wish to exploit for the parametric generation of THz radiation, is desirable. As we have seen, $\chi^{(2)}$ is a key parameter in determining the efficiency of nonlinear frequency conversion of radiation (Eqn 2.65) and the threshold of optical parametric oscillators (Egn 2.45) [335]. So to optimise the design of nonlinear systems for efficient generation it is necessary to know the magnitude of $\chi^{(2)}$. However, at longer wavelengths, where, from the Manly-Rowe relations, the efficiency of generation of THz radiation is increased, the value of $\chi^{(2)}$ has not typically been measured. Little direct data exist for the Mid Infra-Red (Mid-IR) or FIR, with the exception of measurements in and around 10 μm by means of CO_2 lasers [297]. Nothing at all exists for the THz regime. Generally the values are inferred from the system performance in the Mid-IR range

and the values of nonlinear coefficients in FIR & THz regime are presumed to follow on from those. Furthermore even in well established nonlinear materials such as Potassium titanyl phosphate KTi_2PO_4 (KTP) and $LiNbO_3$ the value of $\chi^{(2)}$ varies considerably [335], likely a result of production process variation, as Armstrong noted "not all KTP crystals are created equal" [336]. The values of the nonlinear coefficient of $GaSe_{x-1}S_x$ has been found to decrease with increased sulphur doping [103, 215], though significant improvements in other areas compensate the efficiency of nonlinear generation.

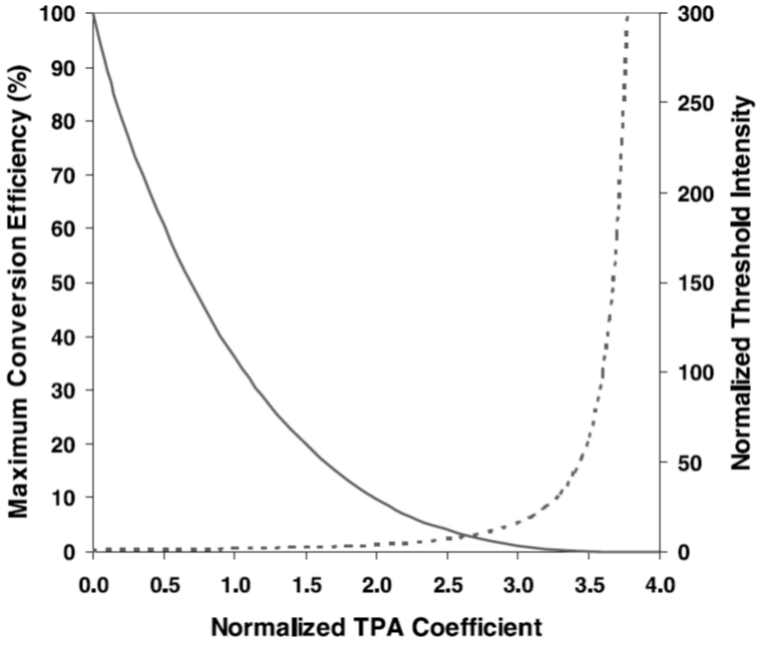

Figure 5.1: The effect of two-photon absorption on the frequency conversion efficiency and oscillation threshold of a backward OPO [337]

$\chi^{(3)}$ nonlinearity is responsible for the Kerr Effect, two-photon absorption and self-focusing, which can lead to laser induced damage of materials. As such, it can also play an important roll in the design, operation and efficiencies of nonlinear frequency conversion sources; Zotova & Ding showed that two-photon absorption increases the threshold oscillation for OPOs and at high values prevents oscillation entirely [337], the increased threshold $I_{Thres,B}$ being described by the relation:

$$I_{Thres,B} = \left(\frac{4}{4-\beta'}\right)^2 I_{Thres} \tag{5.1}$$

where β' is the two-photon absorption for the given pump intensity and length of the nonlinear medium and I_{Thres} is the oscillation threshold in the absence of two-photon absorption.

$\chi^{(3)}$ effects are most easily observed and measured through nonlinear refractive index n_2 via the Kerr effect. The Kerr effect is the induced change of refractive index of a material due to the effect of an intense beam of light propagating through it. The intensity dependent refractive index is defined as:

$$n = n_0 + 2\overline{n}_2|E(\omega)|^2 \tag{5.2}$$

where n_0 is the linear refractive index, $\overline{n}_2$ is the time averaged nonlinear refractive index and $E(\omega)$ is the incident electric field. The imaginary component of nonlinear refractive index, nonlinear or multi-photon absorption has been widely studied at 1.064 μm [338, 339, 340, 341, 342] in order to determine the performance of ns and ps Nd:YAG pumped OPOs and other nonlinear schemes [343]. As with other optical data relating to GaSe and $GaSe_{x-1}S_x$, it is highly scattered and contradictory [341]. Little work is to be found relating to the real component of nonlinear refractive index n_2, and in some case, the authors designed the experimental set up to negate its observation [338], or failed to report the results [339].

Measurement of the nonlinear coefficients in the THz regime has, without doubt been hampered by the lack of suitable sources. The pump source for such measurements has several requirements. The laser should be of high power to enable the measurement of nonlinear phenomena. It is desirable that the source laser is short pulsed to achieve high peak power while reducing the impact of heating on the crystal and, hence, the resulting thermal lensing that may distort the measurements. Tunability and narrow linewidth are required to select a number of fundamental pump and generated wavelengths while avoiding absorption features that would negatively effect the efficiency of SHG [344]. Currently, free electron lasers are the only source that can readily meet those requirements for the THz range, as seen in Figure 5.2 [345].

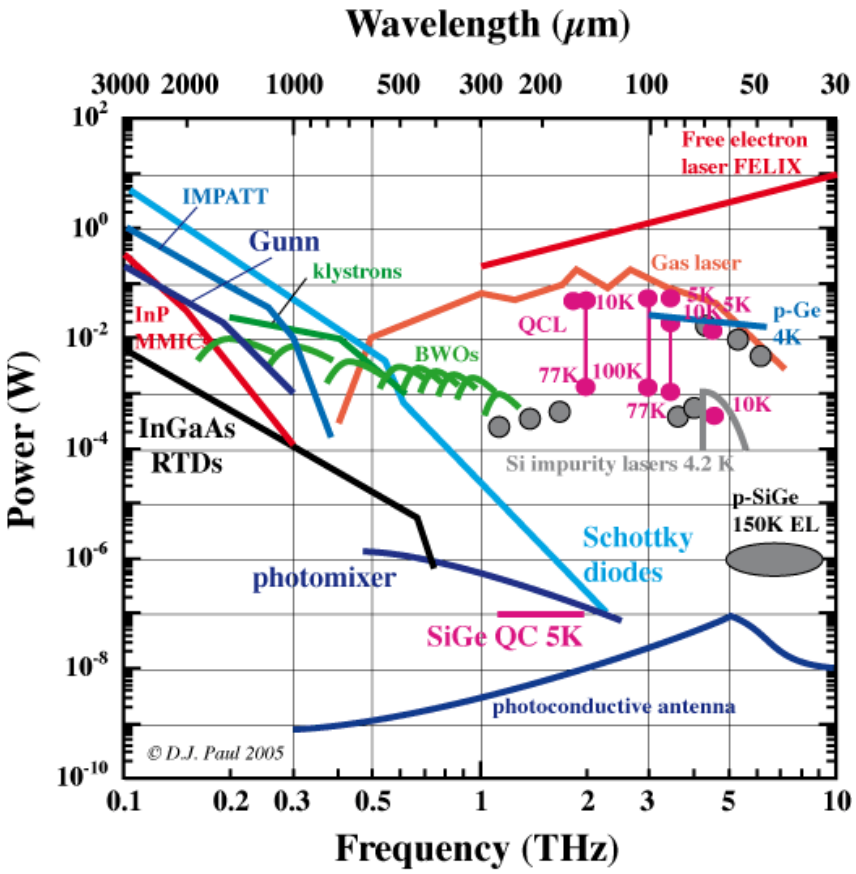

Figure 5.2: Power and tunability of the Felix free electron laser at Radbout University, Nijmegen, the Netherlands, compared against other current THz sources [345].

Following the competitive submission of a proposal to determine the nonlinear coefficients of a range of semiconductor and nonlinear crystals, we were awarded beam time on the FELIX and FLARE instruments at free electron laser facility in Radbout University, Nijmegen, the Netherlands.

5.2 $\chi^{(2)}$ Nonlinearity

Direct determination $\chi^{(2)}$ is normally achieved through the analysis of second harmonic generation in the material. It is difficult to accurately analyse the data due to a large number of parameters that must be considered, so the values often have large uncertainties [346, 347, 348]. Phase-matched methods of determining $\chi^{(2)}$ are restrictive, as for a fixed frequency pump beam there is generally only a limited

set of propagation angles that may be accessed. In most cases, this prevents the determination of the full nonlinear tensor [335, 348].

Due to the high refractive index of GaSe, it is difficult to make phase matched SHG as the internal angles required often exceed the critical angle for Total Internal Reflection and the generated wave can not be readily coupled out of the crystal [349]. Kador *et al* overcame this issue by means of specially fabricated semicircular prisms [349]. Abdullaev *et al* determined the nonlinear coefficient of GaSe as $d_{22} = 86 \pm 17\, pm/V$ by phase-matched SHG at 10.6 μm using a CO_2 laser [350, 102]. GaSe has only one independent component, d_{22}, in the polarisability tensor. Non phase-matched techniques like the Maker Fringe method allow the light to propagate in any arbitrary direction so the full nonlinear tensor may be determined [351, 336, 348].

In 1962, following Frankin's demonstration of Second Harmonic Generation, Maker et al placed a quartz plate in the focus of a Ruby laser beam (0.694 μm) and measured the variation in intensity of the generated second harmonic radiation (0.327 μm) as the angle of inclination of the crystal relative to the laser beam was varied by around the z-axis [107]. The fringe pattern in Figure 5.3 was observed, where the intensity of the generated second harmonic radiation $I_{2\omega}$ varies with a $sinc^2(\Delta kL)$ dependence, as the crystal rotates [107].

The fringes that result are due to the variation in the dispersion between the fundamental at ω and the second harmonic at 2ω. The individual waves E_ω and $E_{2\omega}$ are not phase-matched and, as they propagate, the energy flows back and forth between the fundamental and second harmonic, as can be seen in Figure 5.3 belwo and shown in Eqn 2.34. Rotating the crystal changes the distance over which the two beams propagate and, thus, the intensity of the second harmonic $I_{2\omega}$ observed at the output face of the crystal.

Jerphagon and Kurtz, in their 1970, paper analysed the variation in $I_{2\omega}$ and related it to the second order nonlinear coefficient. Since then, the Maker Fringe method has effectively been the standard means of establishing the value of $\chi^{(2)}$ nonlinearity [352, 335], with the theory and methods being improved over time. Hayden and Herman refined the theory further, to account for absoption of E_ω and

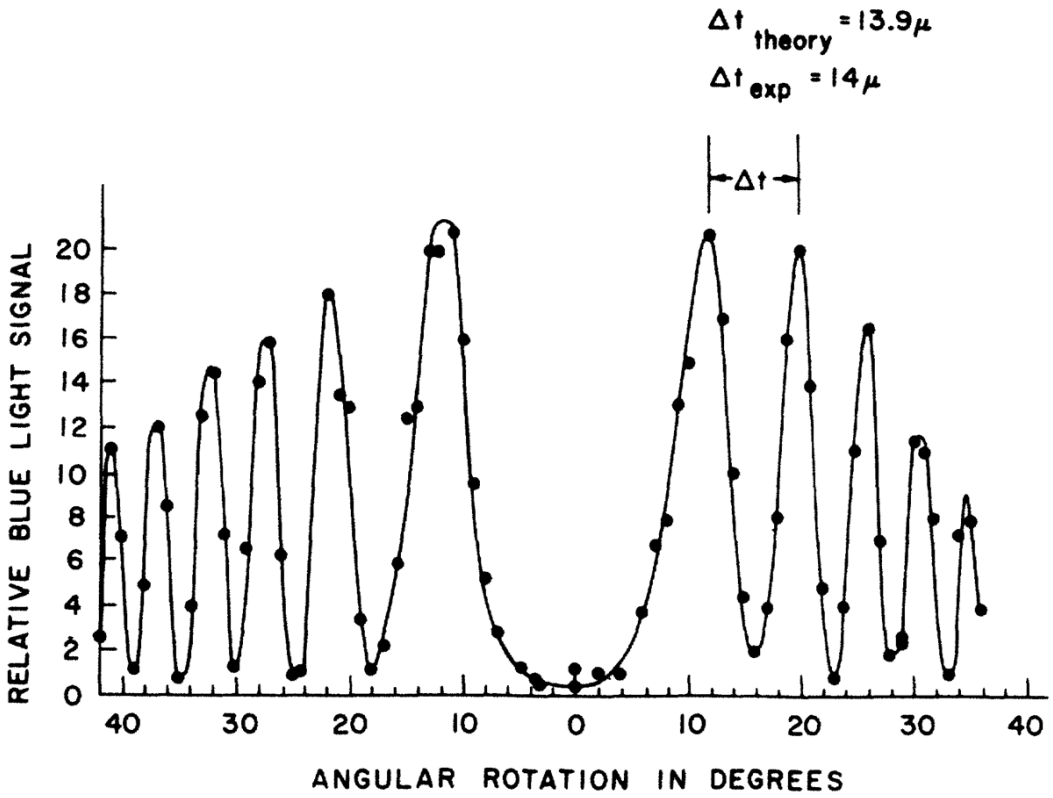

Figure 5.3: Intensity variation (Maker Fringes) in the generate second harmonic radiation as a function of angle, observed by Maker et al for a quartz plate in the focus of a ruby laser [107]

$E_{2\omega}$, dispersion in the crystal and multiple reflection [352]. *Kador et al* measured the nonlinear coefficient of GaSe as $d_{22} \geq 72 \pm 6pm/V$ at 1.579 μm, by the maker fringe method [353]. The Maker Fringe method has also been applied to $GaSe_{x-1}S_x$ crystals at 1.30 and 1.55 μm using cw laser diodes [344], but, unfortunately the values for the nonlinear susceptibility were not provided.

A variation of the maker fringe method is the translate wedge [335], which has several attractive advantages over the conventional rotational Maker Fringe method. However, specially processing the crystals to a sufficient quality is non-trivial, and given the limited stock of high quality crystals available it was not undertaken here. Furthermore the results between the two methods have been found to be in good agreement [335].

We assume that, through careful selection of the fundamental (ω) and second harmonic (2ω), the effects of absorption will be minimised, and thus, will follow

Herman & Hayden's analysis for determine $\chi^{(2)}$ in birefringent media [352], which is summarised below.

The intensity of the transmitted second harmonic beam from a birefringent uniaxial crystal, with negligible absorption, as a ratio of the pump beam and a function of angle is defined by Herman & Hayden as Eqn 5.3 [352]; in the case of crystals with standing waves, it describes the envelope of the generated second harmonic. We can see that Eqn 5.3, closely resembles Eqn 2.65 from earlier, with additional factors to account for the transmission loss of both the pump and SHG beams and the variation of refractive index with angle in birefringent crystals.

$$\frac{I_{2\omega}}{I_{\omega}^{2}} = \left\{ \frac{128\pi^{3}}{c} \frac{t_{\omega}^{4} t_{2\omega}^{2}}{n_{2\omega}^{2}(\theta_{2\omega}) cos^{2}\gamma_{2\omega} cos^{2}(\theta_{2\omega} - \gamma_{2\omega})} \left(\frac{2\pi L}{\lambda_{\omega}}\right)^{2} \right. \\ \left. \times d_{eff}^{2} \left[\frac{n_{2\omega}(\theta_{\omega})}{n_{2\omega o}}\right]^{4} \left[\frac{(n_{\omega}^{2}(\theta_{\omega}) - n_{2\omega}^{2}(\theta_{2\omega})}{n_{\omega}^{2}(\theta_{\omega}) - n_{2\omega}^{2}(\theta_{\omega})}\right]^{2} \frac{sin^{2}\Psi}{\Psi} \right\} \tag{5.3}$$

where t_m is the angle dependent transmission Eqn 5.9 & 5.10, $n_m(\theta_m)$ is the angle dependent refractive index, Eqn 5.7, γ is the walk of angle, Eqn 5.11, L is the length of the crystal and λ_ω is the wavelength of the fundamental pump beam. The index $m = (\omega, 2\omega)$ represents the fundamental and second harmonic respectively.

The phase mismatch Ψ is define as:

$$\Psi = \left(\frac{2\pi L}{\lambda}\right) \left[n_{\omega}^{2} cos\theta_{\omega} c_{\omega} - n_{2\omega} c_{2\omega}\right] \tag{5.4}$$

where s_m and c_m are:

$$s_m = \left(\frac{1}{n_m}\right) sin\theta \tag{5.5}$$

$$c_m = \sqrt{1 - s_m^2} \tag{5.6}$$

As $GaSe_{x-1}S_x$ is a birefringent crystal, it is necessary to account for the variation in refractive index with angle. The Fresnel transmission and Snell's law of refraction

must be adapted to account for this.

The angle dependent refractive index is defined as:

$$n_m(\theta_m) = \left(\frac{cos^2\theta_m}{n_{mo}^2} + \frac{sin^2\theta_m}{n_{me}^2} \right)^{-\frac{1}{2}} \tag{5.7}$$

$$n_{2\omega}(\theta_\omega) = \left(\frac{cos^2\theta_\omega}{n_{2\omega o}^2} + \frac{sin^2\theta_\omega}{n_{2\omega e}^2} \right)^{-\frac{1}{2}} \tag{5.8}$$

The angle dependent Fresnel transmission for the fundamental wavelength is defined as:

$$t_\omega = \begin{cases} \frac{2cos\theta}{cos(\theta_\omega - \gamma_\omega) + n_\omega(\theta_\omega)cos\gamma_\omega cos\theta}, & p\ polarised \\ \frac{2cos\theta}{cos\theta_\omega + n_{\omega o}cos\theta}, & s\ polarised \end{cases} \tag{5.9}$$

The angle dependent Fresnel transmission for the second harmonic is defined as:

$$t_{2\omega} = \frac{2n_{2\omega}(\theta_{2\omega})cos\gamma_{2\omega}cos(\theta_{2\omega} - \gamma_{2\omega})}{cos(\theta_{2\omega} - \gamma_{2\omega}) + n_{2\omega}cos\gamma_{2\omega}cos\theta} \tag{5.10}$$

$$\gamma_m = cos^{-1}\left(\frac{n_{mo}n_{me}}{n_m(\theta_m)\left[n_{mo}^2 + n_{me}^2 - n_m(\theta_m)^2\right]^{\frac{1}{2}}} \right) \tag{5.11}$$

The internal angle of propagation for the propagating beam is defined as:

$$\theta_m = sin^{-1}\left(\frac{n_{me}sin(\theta)}{\left[(n_{mo}n_{me})^2 + (n_{me}^2 - n_{mo}^2)sin^2(\theta)\right]^{\frac{1}{2}}} \right) \tag{5.12}$$

Samples are of millimetric thickness and given that the wavelengths are of the order of 100 μm and the rate of increase in the refractive index is low, so walk-off is not of great concern and helps reduce the effects of multiple reflections

5.3 $\chi^{(3)}$ Nonlinearity

As we have seen above in Eqn 5.2, the refractive index of a material n can be altered by an intense beam of light propagating through it. The measured value of the nonlinear refractive index can be used to derive the value of $\chi^{(3)}$. Measurements

of n_2 can be performed in a number of ways such as by optical phase conjugation and optical Kerr gating. However, by far the simplest and most straightforward to analyse method is the Z-scan technique developed by Sheik-Bahae *et al* in their classic 1989 paper and whose method we will follow and summarise below [354, 355]. Z-scan allows the magnitude and sign of $\chi^{(3)}$ to be measured, with a relatively straightforward set up and not overly involved interpretations [355].

In the Z-scan technique, a Gaussian laser beam is brought to a focus while passing through the nonlinear sample of interest as shown in Figure 5.4 (A). The light then passes through an aperture placed in the far field at z_{ap}, where $z_{ap \gg Z_R}$, and $Z_R = \frac{\pi\omega_0^2}{\lambda}$ is the Rayleigh range, sometimes called the diffraction length. ω_0 is the $\frac{1}{e^2}$ beam radius at the focal point. Typically, the aperture limits the transmission of the beam S to 10% - 50% i.e. S = 0.1-0.5. [355] The sample to be measured is moved along the beam axis, through the focus and the transmitted radiation recorded as a function of z, the distance to the focal plane. As the sample moves along the z-axis, the intensity of the incident radiation increases in a known fashion, and, at high intensities, a change in refractive index is induced. The change in refractive index, alters the beam propagation and more or less radiation is transmitted through the aperture.

In order to improve the accuracy of the results, is important to remove the measurement background. In these measurements, the background was removed by recording the transmission of the circular sample holder as a function of distance from the focal plane (z) and dividing the measurement data by the result. The laser power was monitored on a separate channel to compensate for pulse to pulse variation.

The presence of strong nonlinear absorption prevents the accurate determination of n_2. Two-photon absorption dominates the nonlinear absorption as typically $\alpha_{2PA} \gg \alpha_{3PA}, \alpha_{4PA} \cdots$. The effect of the nonlinear absorption, β can be mitigated by performing an open aperture scan [354]. The sample is place in the beam and transmission recorded as it is scanned along the z-axis. The aperture is opened or removed so that the beam transmission is uninhibited and all radiation is collected.

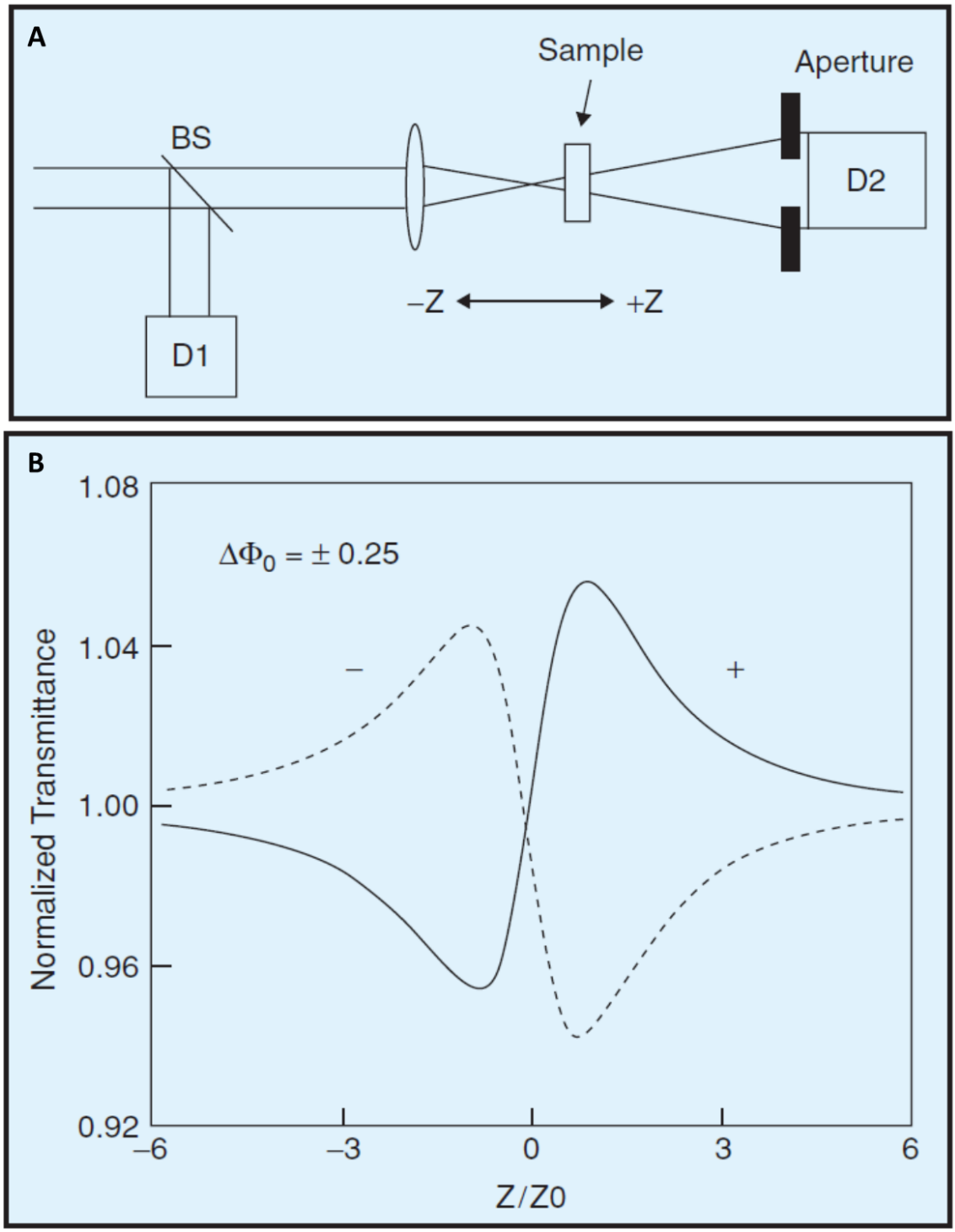

Figure 5.4: (A) Sheik-Bahae's experimental set-up for Z-scan measurments, (B) Calculated Z-scan transmission for both positive and negative 3^{rd} order nonlinearity[354]

The intensity dependent change in absorption $\Delta\alpha$ is defined as:

$$\Delta\alpha = \beta I \tag{5.13}$$

To remove the effect of β, one needs to simply divide the normalised closed aperture measurement by the normalised open aperture measurement [355]. The now background free change in the normalised transmittance for the sample, ΔT_{pv}, can be related to the induced phased distortion, $\Delta\Phi_0$, by Sheik-Bahae's empirically derived relation [354]:

$$\Delta T_{pv} \cong 0.406(1-S)^{0.27}|\Delta\Phi_0| \tag{5.14}$$

where $T_{pv} = T_p - T_v$, the transmittance at the peak and the valley respectively, S is the aperture transmission as above and $\Delta\Phi_0$ is defined as

$$\Delta\Phi_0 = \frac{2\pi}{\lambda} n_2 I_0 L_{eff} \tag{5.15}$$

where L_{eff} is the effective length of the crystal and I_0 is the on axis irradiance at the focus defined as:

$$I_0 = \frac{E_{macro}[J]}{N_{micro}\tau_{mirco}[s]} \frac{1}{\pi w_0^2[cm^2]} \tag{5.16}$$

where E_{macro} is the energy of the laser macropulse, N_{micro} is the number of micropulses per macropulse and τ_{mirco} is the length of a micropulse. The effective length is defined as:

$$L_{eff} = \frac{(1-e^{-\alpha L})}{\alpha} \tag{5.17}$$

where α is linear absorption and L is the thickness of the crystal. From $\Delta\Phi_0$ we may find n_2, the nonlinear refractive index, which can be used to find the real component of $\chi^{(3)}$ using the relation below [101]:

$$n_2 = \frac{3}{4n_0^2\varepsilon_0 c}\chi^{(3)} \tag{5.18}$$

Having performed open aperture scans to remove the distortion of nonlinear absorption on the n_2 measurement, we may also find the third order nonlinear absorption coefficient β. The radiation induced absorption leads to a change in the transmitted radiation incident on the detector $\Delta T(z)$, which for normalised transmisison is

defined as:

$$\Delta T(z) \approx -\frac{q_0}{2\sqrt{2}} \frac{1}{1+\frac{z^2}{Z_R^2}} \tag{5.19}$$

where $q_0 = \beta I_0 L_{eff}$ and I_0 & L_{eff} are as defined above, in Eqn 5.16 & 5.17 respectively.

$$\beta = \frac{q_0}{I_0 L_{eff}} \tag{5.20}$$

5.4 THz Maker Fringe Experiment

5.4.1 Experimental Setup

The FLARE instrument was run at 44 cm^{-1} in 20 MHz mode. Each laser pulse or macropulse was 8 μs long and consisted of a train of 100 micropulses. The micropulses had a repetition rate of 20 MHz and the macropulses a repetition rate of 5 Hz, with an average power of 3 mW. Both Felix and Flare are provided with a red alignment laser that propagates collinearly with the main Mid-IR/FIR beam.

To enable analysis of the nonlinear effects it is important to have a clean Gaussian beam. To achieve a good beam profile the output of the Flare beam was focused to a tight spot using a 100 mm Off-Axis Parabolic (OAP) mirror (M1). The beam profile is then spatially filtered using an aperture that transmitted 50 % of the incident energy (A1) and the beam was then re-collimated (M2). In the measurement position between 125 mm OAP mirrors M5 and M6 the beam is brought to a focus.

The sample holder was a rotation mount on top of a rotation stage, enabling rotation about the θ and ϕ angles respectively. The rotation stage itself was mounted on an xyz translation stage to enable accurate placement of the samples in the focus of the beam and along the axis of propagation between mirrors M5 and M6. An aperture was placed in the sample holder and the system aligned for transmission along the length of the stage. Detection was via a liquid Helium cooled GaGe photoconductor. The sensitivity of the detector is shown below in Figure 5.6.

The energy of the fundamental beam readily saturates the photoconductor. Given the difficulty in obtaining good optical filters at the higher end of the frequency regime, selecting an appropriate fundamental wavelength is vital. The GaGe

photodetector has its low frequency cut-off at 50 cm^{-1} (200 μm), so selecting a wavelength longer than this will reduce impact of fundamental wavelength on the measurement. Pumping at 44 cm^{-1} (227 μm) is well below the cut-off point while the second harmonic 88 cm^{-1} (114 μm) is in the centre of the longer wavelength sensitivity region. Furthermore, both wavelengths avoid the strongest THz phonons in the crystals, allowing us to use the zero absorption case outlined above.

5.4.2 Measurement

Large aperture, high quality crystals are desired for this experiment so that the full range of angles can be measured. $GaSe_{x-1}S_x$, x = 0.44, was selected, as it is the $GaSe_{x-1}S_x$ crystal with the largest diameter and has high optical quality throughout, a $\approx 1.5\,mm$ thick sample was prepared. In addition to $GaSe_{x-1}S_x$, x = 0.44, number of other high quality samples of nonlinear optical crystals were measured including GaAs and Quartz (SiO_2). The samples were rotated from -90° to +90° relative to the incident fundamental beam, althrough the sample mount reduce the effective measurment range to -70° to +70° or less depending on samples size and fringes were observed in all cases, as shown in Figures 5.7 & 5.8.

A blazed grating, with a period of 0.75 mm and an blazed angle of 16.5° cut from stainless steel, was employed to separate the two wavelengths. The grating

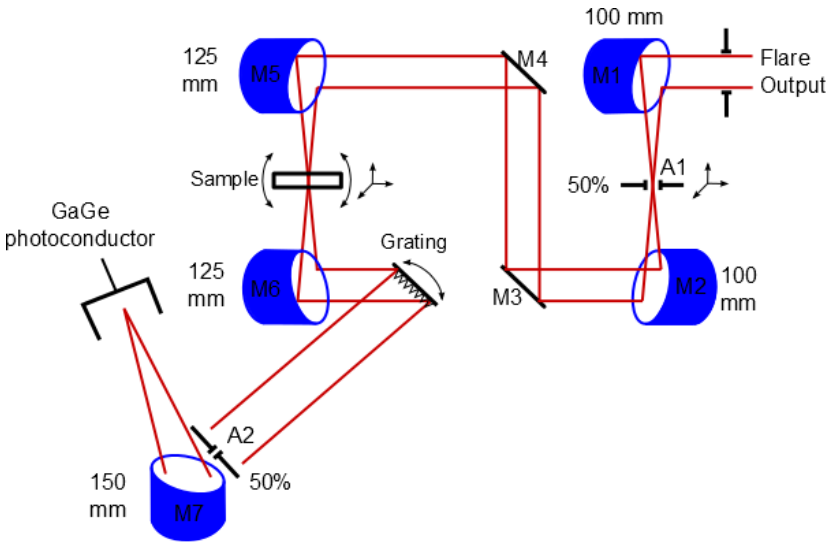

Figure 5.5: Schematic of the experimental setup used for the Maker fringe experiments.

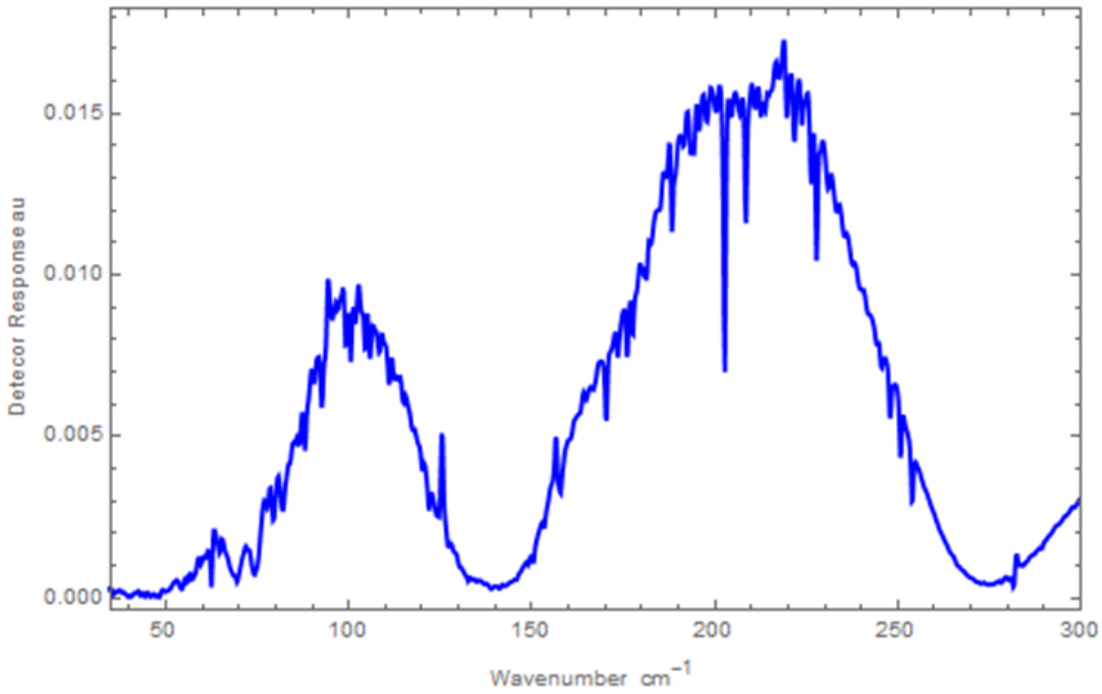

Figure 5.6: Variation in the response of the liquid Helium cooled GaGe photoconductor with frequency.

proved largely ineffective and could not readily separate the second harmonic which was too far outside the gratings effective range. As the efficiency of generation for the SHG is low, and in spite of pumping at 44 cm^{-1}, below the responsivity cut-off, the residual signal from the fundamental beam is still dominates the measurement.

In order to demonstrate that the origin of the fringes is not a transmission artefact of the fundamental beam measurements were recorded for centrosymmetric Ge wafers; Ge's crystal structure is face-centred diamond cubic, and no Maker fringes were observed, as seen in Figure 5.8 (b).

The inability to separate the fundamental beam from the generated second harmonic in the Maker fringes currently negates the possibility to make a quantitative determination of the $\chi^{(2)}$. On the other hand, we have observed the presences of fringes and demonstrated that it is possible to perform these measurements in the THz regime, using free electron lasers. A new grating is to be fabricated and an additional measurement campaign pursued to determine the value of the second order nonlinear tensor. For future experiments it should be considered to conduct

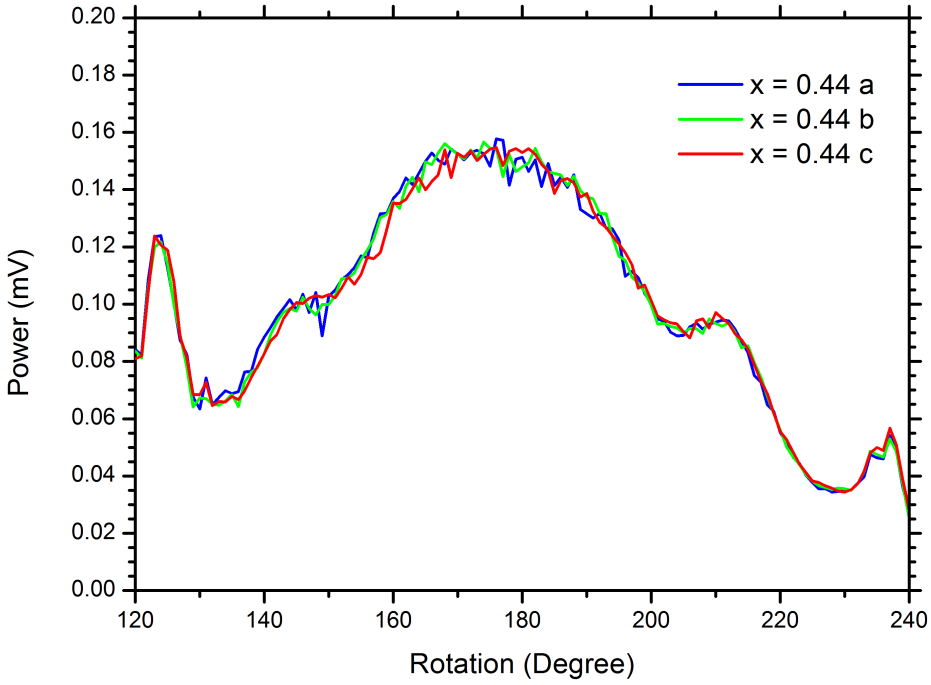

Figure 5.7: Maker fringes observed in several measurements of $GaSe_{x-1}S_x$, x =0.44, at $\lambda = 113.5\mu m$ with a background from the fundamental at $\lambda = 227\mu m$

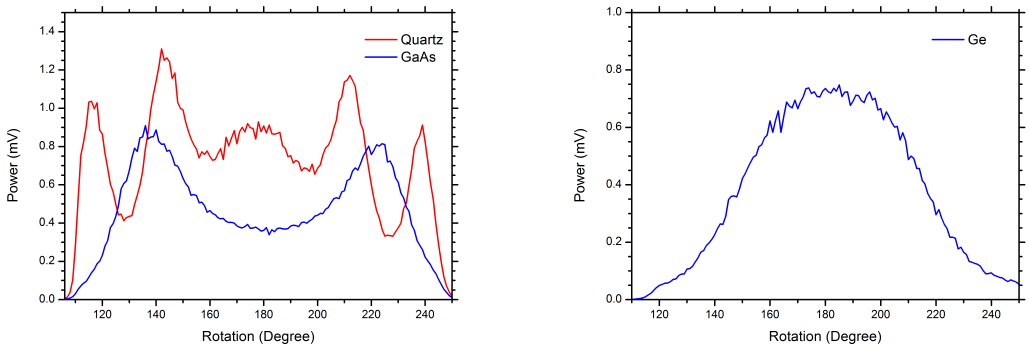

(a) GaAs & quartz

(b) Germanium (Ge)

Figure 5.8: Maker fringes observed in GaAs and Quartz at $\lambda = 113.5\,\mu m$ with a background from the fundamental at $\lambda = 227\,\mu m$ and fringe free transmission of the fundamental beam through a centrosymmetric Ge wafer.

measurements at low powers, where SHG is not observed, to compensate the fundamental transmission through the nonlinear crystals.

5.5 Z-scan Experiment

5.5.1 Experimental Setup

The experimental set up is depicted schematically below in Figure 5.9. After the FELIX output port, a beam splitter was installed to pick of a portion off the beam to monitor laser performance. The light was focused on to a pyro-electric detector and the laser power recorded in parallel with measurements. A HeNe laser propagates collinearly with the FELIX beam to ease the processes of alignment.

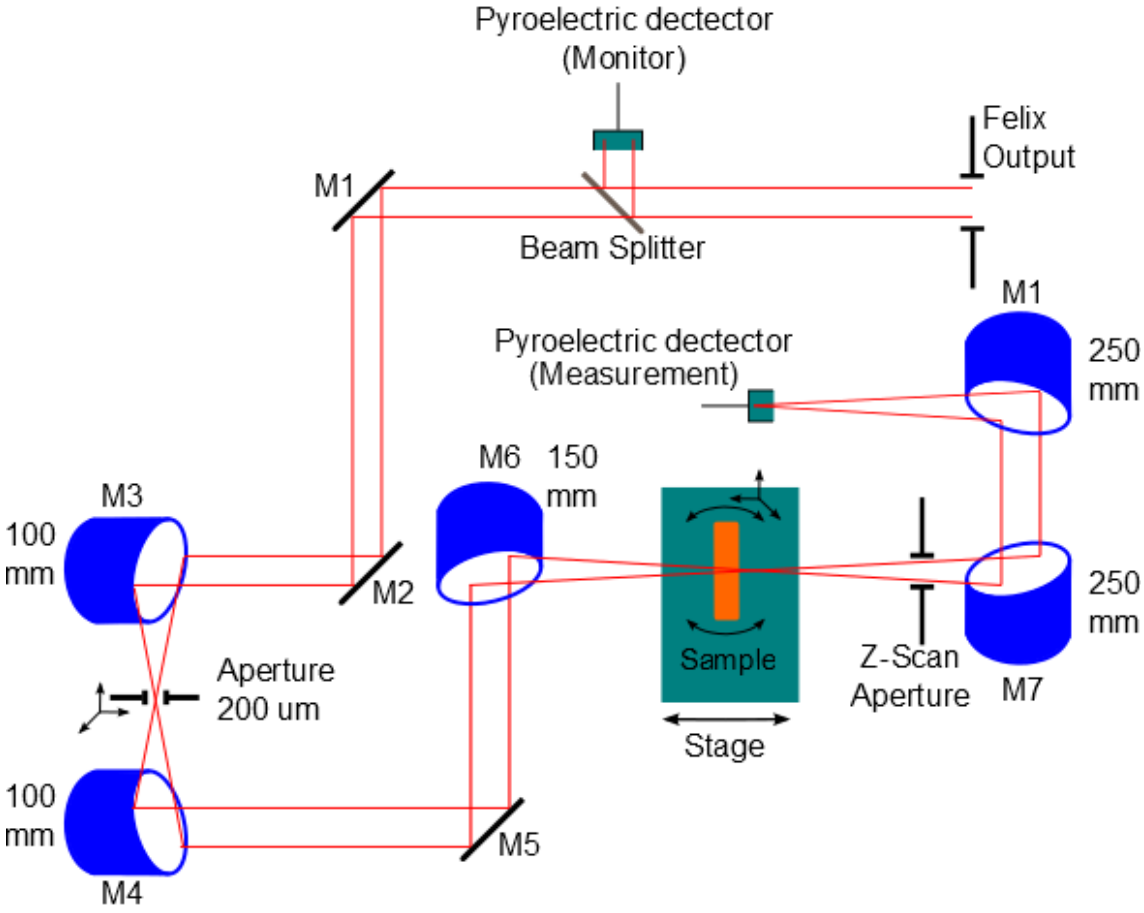

Figure 5.9: Schematic of the experimental setup for Z-scan measurements.

A clean Gaussian beam is desired for simple analysis of the results. To achieve a good beam profile the available FELIX beam was focused to a tight spot using an

OAP mirror (M3) Focal Length (FL) = 100 mm. The beam profile is then spatially filtered using a pinhole (200 and 1000 μm), slightly smaller than the first minimum of the diffraction limit point spread function $a = 1.22\frac{\lambda f}{d}$, transmitting $\approx 90\%$ of the incident energy. The pinhole was mounted on a xyz translation stage to allow precise alignment at the focal point. The beam was then re-collimated by another OAP mirror (M4) FL = 100 mm. In the measurement position between OAP mirrors M6 FL = 150 mm and M7 FL = 250 mm, the beam is brought to a focus.

The samples were mounted in a circularly symmetric holder, with a clear circular aperture of 9.4 mm, on top a xyz translation stage to enable placement of the samples in the focus of the beam and translation along the axis of propagation between mirrors M6 and M7. An aperture was placed in the sample holder and the system aligned for transmission along the length of the stage. The transmitted radiation was re-collimated by M7 and focused on a pyro-electric detector, by OAP mirror (M8) FL = 250 mm.

The FELIX instrument was run in 20 MHz mode. Each laser pulse or macropulse consists of a train of 110 micropulses. The micropulses have duration $\tau_{micro} = 0.1$ ns and a repetition rate of 20 MHz. The macropulses have a duration of 5.5 μs, and a repetition rate of 5 Hz. The macropulse energy E_{macro} is dependent on the operating wavelength of the laser, measured at the sample position $E_{macro} = 0.7$ mJ for $\lambda = 20\,\mu m$ and $E_{macro} = 0.15$ mJ for $\lambda = 87\,\mu m$.

The beam parameters in the measurement arm were determined, Figure 5.10. When operating at $\lambda = 20\,\mu m$ the beam waste was found to be $w_0 = 165\,\mu m$. At the focusing parabolic z = -152 mm the beam diameter was calculated as: $w(z) = 11.8mm$ The Rayleigh length was calculated to be $Z_R = 3.1\,mm$. For $\lambda = 87\,\mu m$ the beam waist was $w_0 = 420\,\mu m$ and the Rayleigh range calculated as $Z_R = 6.5 \pm 0.5\,mm$.

5.5.2 Measurement

One GaSe sample and three $GaSe_{x-1}S_x$ samples x = 0.11, 0.17, 0.22 were measured by the Z-scan technique at 20 μm and 87 μm using the FELIX instrument. It is

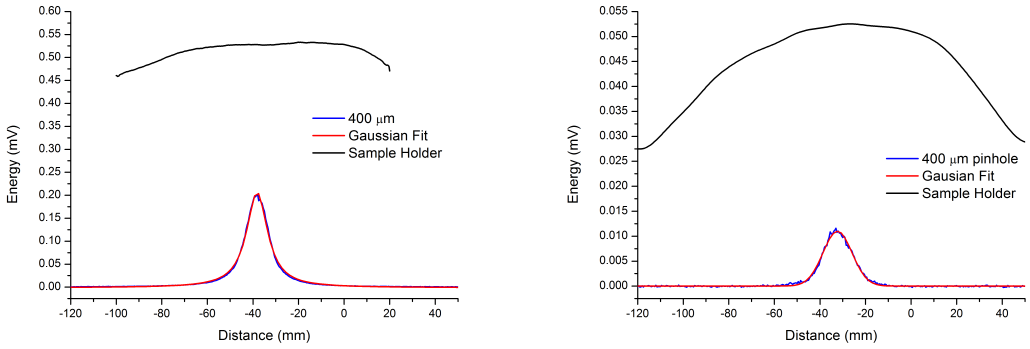

(a) $\lambda = 20\mu m$ (b) $\lambda = 87\mu m$

Figure 5.10: Transmitted energy of Felix instrument though both a pinhole and sample holder as they are scanned along beam path a the measurement position.

necessary to have sufficiently large crystals so that the beam may pass through the crystal without been clipped, preferably for a distance $z > 5Z_R$ [355]. The crystals should also be thin, with the crystal thickness $l \leq Z_R$, though it is possible to use thick crystals with a more complex analysis. The sample holder (diameter 9.4 mm) was scanned long the beam path to find the range in which there would be no clipping of the beam and to establish a background shown in Figure 5.10.

A strong broad induced increase in the transmission curves is observed for all crystals at both $\lambda = 20$ & $87\,\mu$m. When normalised to the transmission profile of the sample holder this broad increase is found to have nominally a Gaussian profile. We assumed it to be the result of thermal lensing in the crystals [354] and remove it in data processing, using a Gaussian fit as shown in Figure 5.11.

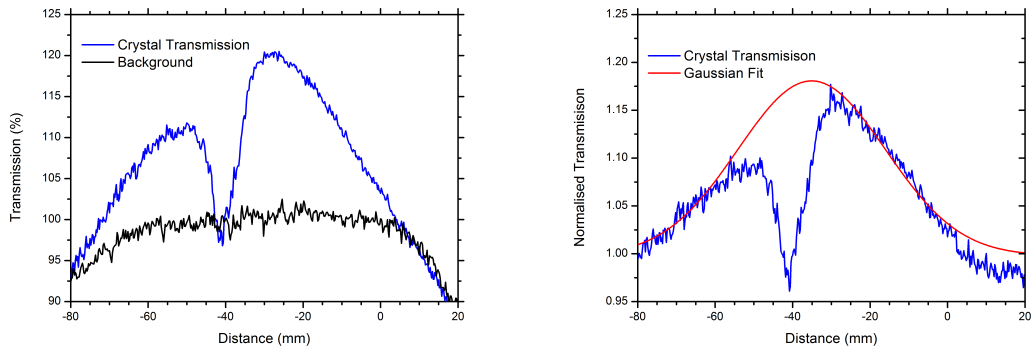

(a) Crystal Transmission (b) Background Removed

Figure 5.11: The effect of thermal lensing on crystal transmission, and normalised transmission with background removed in there presence of thermal lensing.

With the background and the effect of thermal lensing removed we are left with the multiphoton absorption curves, as presented in Figure 5.12 (b) and others, which is fitted with a Lorentzian function [355]. By measuring the depth of the absorption peak, we may calculate the third order nonlinear absorption coefficient β as described above using Eqns 5.19 & 5.20.

To obtain the nonlinear refractive index, we divide the normalised crystal transmission for closed aperture by the normalised crystal transmission for the open aperture; the resulting curves for nonlinear refractive index is presented below in Figure 5.12 (a) and others.

By inspection we can see that the sign of the change in refractive index is positive, the transmission first decreases before the focus and increases after in all samples, in keeping with Sheik-Bahae's results depicted in Figure 5.4 (B) [354, 355]. This is analogous to placing a thin positive lens in the beam path; in advance of the beam focus, the additional focusing of thin lens increases divergence in the far field, while after the focus the thin lens collimates the beam, increasing transmission [354]. By measuring the peak-to-valley change in transmission, ΔT_{pv}, the magnitude of the nonlinear refractive index, n_2, can be calculated as described above, using Eqns 5.14 & 5.15, and hence obtain $\chi^{(3)}$ using Eqn 5.18.

5.6 FIR Nonlinearity of GaSe1-xSx

The results of the measurements for the FIR regime are presented in Table 5.6. The improvement in the shape form of the curves for the measurements from GaSe to $GaSe_{x-1}S_x$, x =0.11, can be attributed to the improvement in the crystal quality near optimal doping. The measurements are seen to become noisier for $GaSe_{x-1}S_x$, x = 0.17 & 0.22 (Figures 5.15 & 5.14), which can be explained by the increase in absorption at $\lambda = 20\,\mu m$, as the increase in sulphur content shifts the edge of the transmission window to shorter wavelengths.

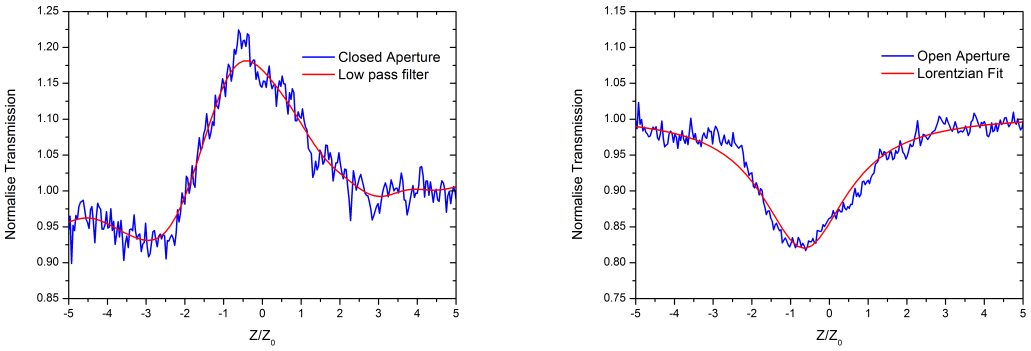

(a) Nonlinear Refractive Index (b) Nonlinear Absorption

Figure 5.12: Normalised transmission though the crystals samples for both closed (a) and open (b) aperture Z scan measurements, showing the effect of nonlinear refractive index (n_2) and nonlinear absorption (β) on the normalised transmission of GaSe at $\lambda = 20\,\mu$m.

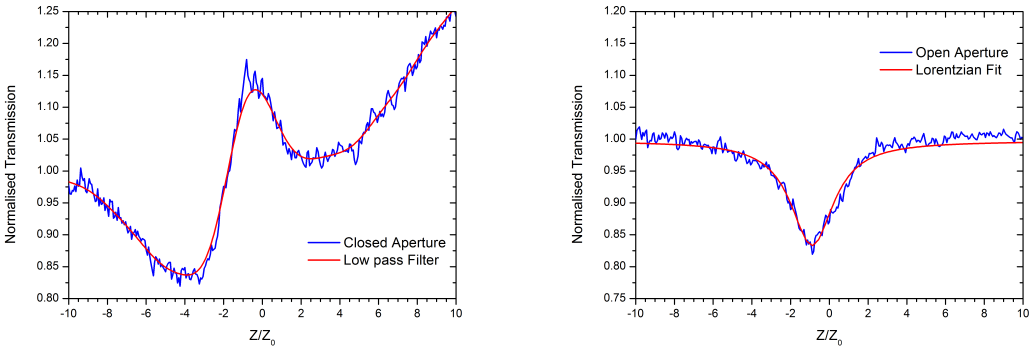

(a) Nonlinear Refractive Index (b) Nonlinear Absorption

Figure 5.13: Normalised transmission though the crystal samples for both closed (a) and open (b) aperture Z scan measurements, showing the effect of nonlinear refractive index (n_2) and nonlinear absorption (β) on the normalised transmission of $GaSe_{x-1}S_x$ x = 0.11 at $\lambda = 20\,\mu$m.

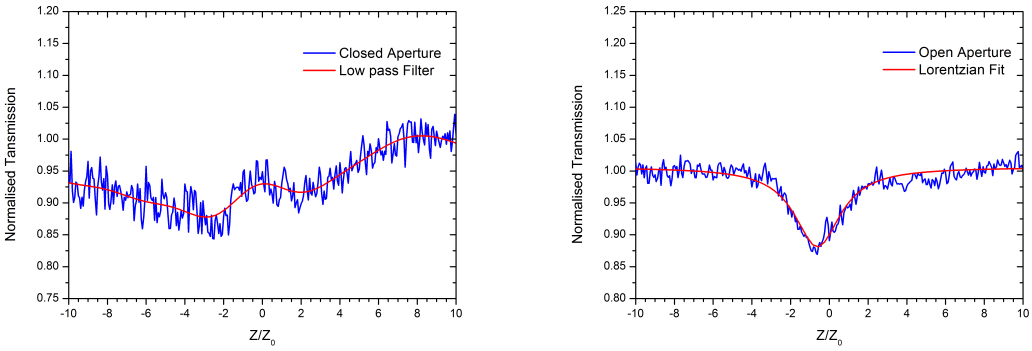

(a) Nonlinear Refractive Index (b) Nonlinear Absorption

Figure 5.14: Normalised transmission though the crystal samples for both closed (a) and open (b) aperture Z scan measurements, showing the effect of nonlinear refractive index (n_2) and nonlinear absorption (β) on the normalised transmission of $GaSe_{x-1}S_x$ x = 0.17 at $\lambda = 20\,\mu$m.

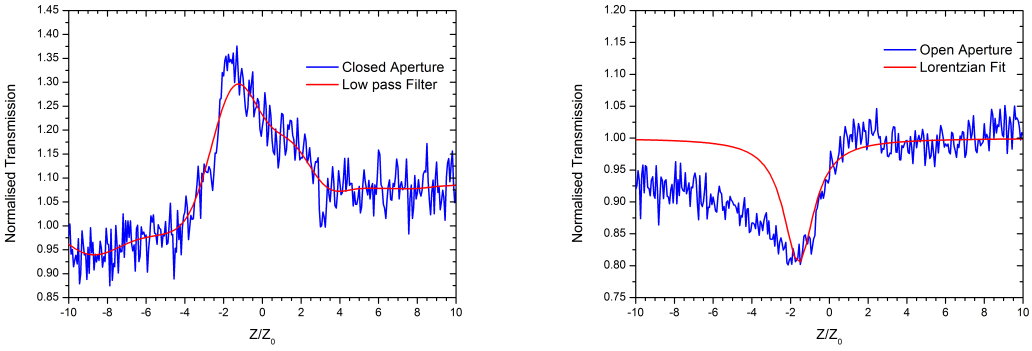

(a) Nonlinear Refractive Index (b) Nonlinear Absorption

Figure 5.15: Normalised transmission though the crystal samples for both closed (a) and open (b) aperture Z scan measurements, showing the effect of nonlinear refractive index (n_2) and nonlinear absorption (β) on the normalised transmission of $GaSe_{x-1}S_x$ x = 0.22 at $\lambda = 20\,\mu$m.

Table 5.1: Nonlinear absorption (β), nonlinear refractive index (n_2) and 3^{rd} nonlinear optical coefficient ($\chi^{(3)}$) for $GaSe_{x-1}S_x$ crystals at $\lambda = 20\mu m$

.

Wavelength μm	$GaSe_{x-1}S_x$ x	β cm/W	n_2 cm^2/W	$\chi^{(3)}$ m^2/V^2
20	0	$6.0 \pm 0.6 \times 10^{-7}$	$3.3 \pm 0.3 \times 10^{-7}$	$1.3 \pm 0.1 \times 10^{-12}$
20	0.11	$5.5 \pm 0.4 \times 10^{-7}$	$5.4 \pm 0.5 \times 10^{-7}$	$2.1 \pm 0.2 \times 10^{-12}$
20	0.17	$3.8 \pm 0.6 \times 10^{-7}$	$3.2 \pm 0.5 \times 10^{-7}$	$5.9 \pm 0.1 \times 10^{-13}$
20	0.22	$7.3 \pm 0.7 \times 10^{-7}$	$7.4 \pm 0.6 \times 10^{-7}$	$2.8 \pm 0.2 \times 10^{-12}$

5.7 THz Nonlinearity of GaSe1-xSx

The results of the measurements for the THz regime are presented in Table 5.7. An increase in the multiphoton absorption is observed in all crystals at $\lambda = 87\,\mu m$, as compared with that at $\lambda = 20\,\mu m$, while perhaps initially somewhat counter-intuitive, the two-phonon edge i.e. half the wavelength is now at $\lambda = 43.5\,\mu m$, in the centre of the main phonon absorption band. An enhancement in the value of n_2 is also observed, the origin of which is yet to be identified.

The results for $GaSe_{x-1}S_x$, x = 0.17 & 0.22, are very noisy and unreliable for determining the nonlinear refractive index. The curves are presented in Figures 5.18 & 5.19, but values are excluded from the results. The noise is a result of instability that developed in the laser mode operating a $87\,\mu$m.

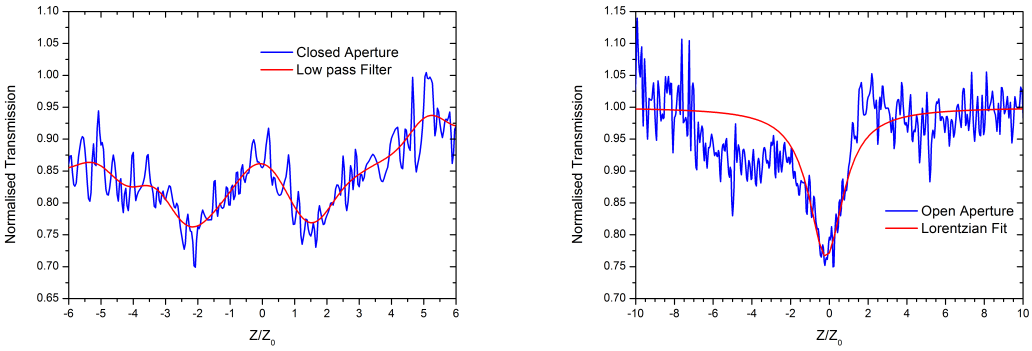

(a) Nonlinear Refractive Index (b) Nonlinear Absorption

Figure 5.16: Normalised transmission though crystal samples for both closed (a) and open (b) aperture Z scan measurements, showing the effect of nonlinear refractive index (n_2) and nonlinear absorption (β) on the normalised transmission of GaSe at $\lambda = 87\,\mu$m.

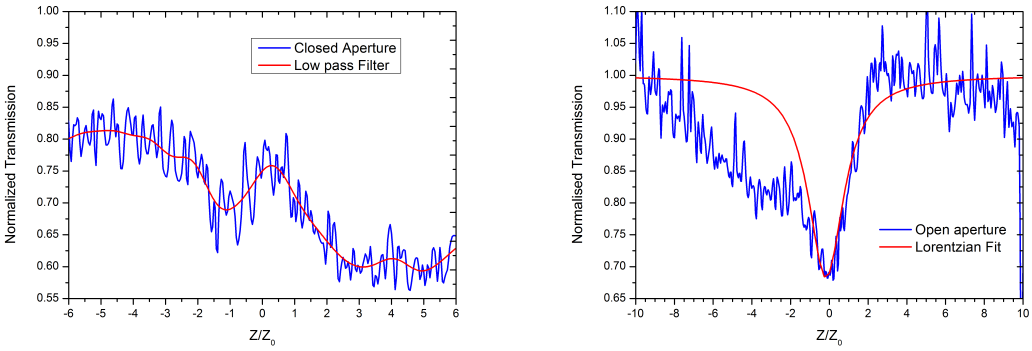

(a) Nonlinear Refractive Index (b) Nonlinear Absorption

Figure 5.17: Normalised transmission though the crystal samples for both closed (a) and open (b) aperture Z scan measurements, showing the effect of nonlinear refractive index (n_2) and nonlinear absorption (β) on the normalised transmission of $GaSe_{x-1}S_x$, x = 0.11, at $\lambda = 87\,\mu$m.

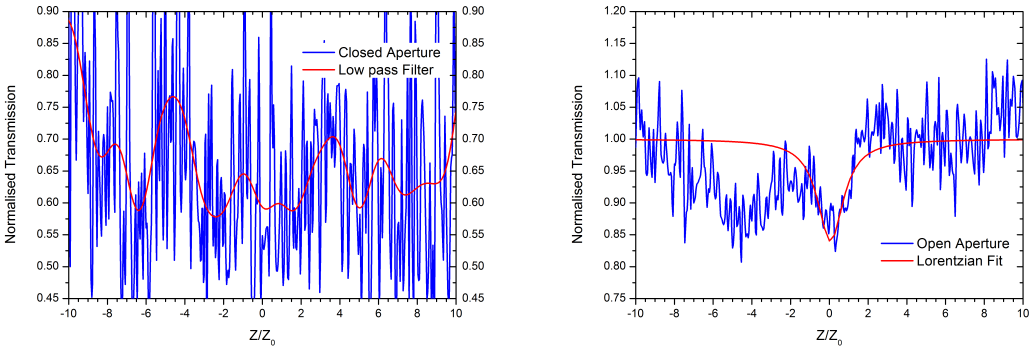

(a) Nonlinear Refractive Index (b) Nonlinear Absorption

Figure 5.18: Normalised transmission though the crystal samples for both closed (a) and open (b) aperture Z scan measurements, showing the effect of nonlinear refractive index (n_2) and nonlinear absorption (β) on the normalised transmission of $GaSe_{x-1}S_x$, x = 0.17, at $\lambda = 87\,\mu$m.

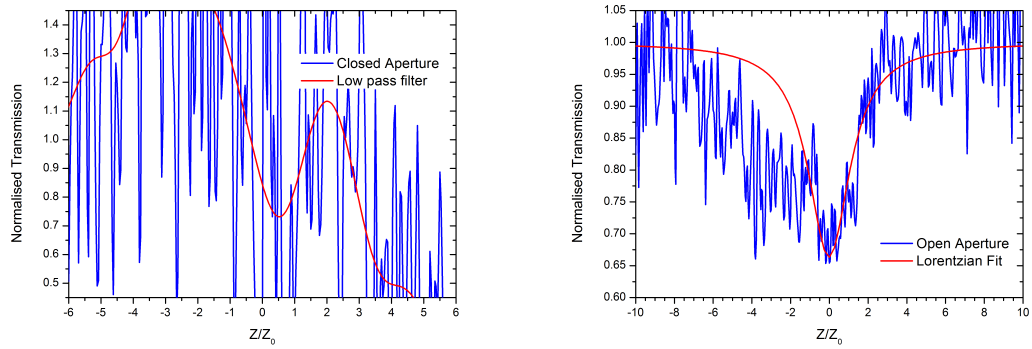

(a) Nonlinear Refractive Index (b) Nonlinear Absorption

Figure 5.19: Normalised transmission though the crystals samples for both closed (a) and open (b) aperture Z scan measurements, showing the effect of nonlinear refractive index (n_2) and nonlinear absorption (β) on the normalised transmission of $GaSe_{x-1}S_x$, x = 0.22, at $\lambda = 87\,\mu$m.

As previously stated, the values provided in the literature for nonlinear optical properties in GaSe are limited in number, scattered and often in contradiction [356, 339, 341] and even considered *"chaotic"* [341]. It may be better characterised as a complex problem where all factors have not be adequately addressed, β is found to be

Table 5.2: Nonlinear absorption (β), nonlinear refractive index (n_2) and 3^{rd} nonlinear optical coefficient ($\chi^{(3)}$) for $GaSe_{x-1}S_x$ crystals at $\lambda = 87\,\mu m$.

Wavelength μm	$GaSe_{x-1}S_x$ x	β cm/W	n_2 cm^2/W	$\chi^{(3)}$ m^2/V^2
87	0	$3.9 \pm 0.8 \times 10^{-6}$	$2.3 \pm 1.0 \times 10^{-5}$	$8.8 \pm 2.5 \times 10^{-11}$
87	0.11	$5.4 \pm 0.8 \times 10^{-6}$	$1.1 \pm 0.5 \times 10^{-5}$	$4.0 \pm 1.7 \times 10^{-11}$
87	0.17	$2.4 \pm 0.8 \times 10^{-6}$	–	–
87	0.22	$5.2 \pm 0.8 \times 10^{-6}$	–	–

dependent on crystal quality [341], pump wavelength [356], pump energy [339, 340] and pulse duration [356, 339, 340, 341]. Furthermore, the absorption has been found not to be a strictly two-photon process with contributions from three and higher multiphonon processes [356, 341], and at still higher intensities saturable absorption has been observed [339, 339, 342]. Results for doped crystals GaSe are rarer still [272, 339, 340, 342] and for $GaSe_{x-1}S_x$ we found two publications [341, 217]. The majority of studies were conducted using Nd:YAG at 1.064 μm or shorter sources. It has been observed that there is strong anisotropy in the multiphoton absorption coefficient [272, 341] and that doping leads to a reduction of induced absorption under fs pumping [217].

In spite of these complications, it can be seen that pumping with ns pulse lengths has consistently led to results for β two orders of magnitude greater than for ps or fs pumping [356, 339, 102, 340, 341, 217]. The increase is the result of long lifetime, thermally induced carriers [356, 339, 340, 341], evidence of which is clearly found in our figures from their asymmetric shape forms with long tails after the focus [354], e.g. Figure 5.15 (a).

Furthermore, following processing the nonlinear refractive index curves presented for both the FIR and THz regime can be seen to deviate from ideal shape form as presented in Sheik-Bahae *et al*, following from their discussion these distortions can be assumed to be due to the influence of the crystal samples [354]. It is recommended that a low power scan of the crystal be preformed to compensate [354]; in future measurement this precautions will be followed.

Regardless, our result for multiphoton absorption at $20\mu m$ are found to be in reasonable agreement, within the margin of error, with the results in the literature

for ns pumping with intensities at about $0.1\,GW/cm^2$ for both pure and doped GaSe crystals, with $\beta = 3.30 \times 10^{-7} cm/W$ for GaSe [340], $\beta = 4.72 \times 10^{-7} cm/W$ for $GaSe_{1-x}Sn_x$, x =0.5 [339] and $\beta = 3.20 \times 10^{-7} cm/W$ for $GaSe_{1-x}Ge_x$, x =0.5 [340], as well as with the early results referred to in Zotova and Ding [356]. This agreement lends some confidence to our results for nonlinear refractive index n_2 and $\chi^{(3)}$ which are less well investigated. So, the effect of multi-photon absorption at long wavelengths is at least a no more serious impediment to nonlinear frequency conversion than at 1.064 μm. At somewhat shorter wavelengths away from the phonon absorption e.g. 10 μm and shorter pulse durations, the situation may even be improved.

5.8 Summary

In this chapter, we investigated to possibility of determining the nonlinear properties of GaSe, $GaSe_{x-1}S_x$ and other nonlinear optical crystals in the FIR and THz regimes using the classic Maker Fringe and Z-scan techniques. Maker fringes have been observed in the nonlinear crystals measured, but the experimental method requires improvement to adequately separate the pump and second harmonic beams and enable analysis of the result. Herman & Hayden's Eqn 5.3 should be adapted to account for the angle dependence of d_{eff}. However, we have demonstrated that it is possible to perform these measurements in the THz regime using free electron lasers, and the experiment will be revisited with an improved setup.

The Z-scan measurement were conducted successfully, in both the FIR and THz regimes, and the measurement results in the FIR were found to be in reasonable agreement with the available literature. Two-photon absorption was seen to increase by an order of magnitude between at 20 μm and 87 μm, as a result of the main optical phonon band centred at 47 μm. The nonlinear refractive index n_2 is also found to increase below the main phonon band. At 20 μm, two-photon absorption, β, was found to decrease with doping and as the quality of the results improve for $GaSe_{x-1}S_x$, x =0.11. However, further detailed comparison between individual crystals is hampered as the linear absorption at 20 μm increases with doping,

pumping with ns pulses leads to thermal carriers, which significantly distort the form of the transmission curves, the samples are small for measurements at 87 μm, beam distortion due to the samples and the instability in the laser; these less than ideal experimental conditions introduce additional inaccuracies into the measured values, which we may conclude exceed the calculated errors, based on measurement uncertainties. The measurements will be revisited using larger crystals samples at different wavelengths in both the FIR and THz regimes to reduce linear absorption and allow more stable laser oscillation. Low power scans will be performed to eliminated the effect of beam distortion due to the sample. However, we can conclude that mulit-photon absorption in the FIR is no more an impediment to pumping, GaSe based, nonlinear frequency conversion devices that in the near-IR.

Chapter 6

Conclusion and Future Work

A coherent, table top source of Terahertz (30-1000 μm) radiation, which is, high power, narrow bandwidth, and broadly tunable is highly desired for a wide variety of applications across the physical sciences as well as in engineering, manufacturing and security sectors. Sulphur-doped solid solution ε-polytype Gallium Selenide ($GaSe_{x-1}S_x$) crystals have the potential for efficient generation of THz radiation and broadband tunability throughout the majority of this regime; unfortunately, the literature relating $GaSe_{x-1}S_x$ is highly scattered and often contradictory. The aim of the work presented in this thesis was to develop a robust understanding of the linear and nonlinear optical properties of $GaSe_{x-1}S_x$ crystals, to enable their successful exploitation in DFG and OPO devices at THz frequencies, and where possible, clarify discrepancies in the literature. Investigations of the linear optical properties of GaSe, GaS & $GaSe_{x-1}S_x$ crystals the THz and FIR regimes were conducted using of THz-TDS, FTIR and Raman spectroscopy. Investigations of the nonlinear optical properties in the THz and FIR regimes were conducted using the classic Maker fringe and z-scan techniques.

6.0.1 Chapter 3

Besides the poor mechanical properties, the scattered and contradictory results in the literature around GaSe crystals, in particular for the THz region, have hindered its widespread adoption for nonlinear frequency conversion. To resolve some of the ambiguities, we examined the sources of inaccuracy in the THz-TDS measurements

of high refractive index, birefringent layered crystals, and propose a Rule of Thumb for the selection of adequate data, based on the quality of the oscillations in the refractive index curves.

The linear refractive index (n) and absorption coefficient (α) of both the o & e-waves in for GaSe and a dense set of $GaSe_{x-1}S_x$ crystals (x = 0.05, 0.11, 0.22, 0.29, 0.44) was determined in the THz regime (0.1- 4.5 THz) by direct measurement using Terahertz - Time Domain Spectroscopy. Measurements of THz dispersion and absorption properties of GaS crystals were performed for the first time. The crystals were fabricated with facets perpendicular to the c-axis, to enabling access to the n_e direction.

The refractive indices in GaSe at 1.5 THz was found to be $n_o = 3.24 \pm 0.015$ and $n_e = 2.46 \pm 0.015$, while the refractive index values for GaS were found to be $n_o = 3.06 \pm 0.012$ and $n_e = 2.29 \pm 0.012$, so that the birefringence in both crystals are equal within the margin of error of the measurements. These measurements allow the calculation of refractive index for any $GaSe_{x-1}S_x$ crystal using Takaoka *et al*'s Eqn 3.13 [302]. Of the existing Sellmeier equations, Chen *et al*'s estimates [202] were found to be the best fit to our results and also the results found in the literature. Improved Sellmier equations are presented, which were designed by colleagues, based, in part, from the results in this work. Both the o & e-wave refractive indices of $GaSe_{x-1}S_x$ crystals were measured and found to change linearly with doping at a rate of -0.14/x (-0.006/mass%) at 1.5 THz, between the value of the two parent crystals GaSe and GaSe.

O-wave absorption is found to be dominant in all GaSe and $GaSe_{x-1}S_x$ crystals. Doping reduces absorption for both the o & e-waves, with $GaSe_{x-1}S_x$, x = 0.22, found to have the lowest absorption. Phonons in the o-wave absorption spectra is seen to transform with doping, the $E'^{(2)}$ rigid layer mode at 0.595 THz is found to collapse with increased sulphur content, and a new mode $E''^{(2)}$ arises at $\approx$ 1.7 THz, shifting to higher frequencies at a rate of 425 GHz/x (17 GHz/mass%). A nearly frequency-independent absorption is observed for the e-wave, between 0.1 - 2 THz, in $GaSe_{x-1}S_x$, x = 0.22-0.44, crystals. A phonon at 1.1 THz was observed, with

confidence for the first time in the e-wave absorption spectra of GaSe. The reduced refractive index and absorption in the e-wave properties clearly favours conversion schemes that result in an extraordinarily polarised THz beam.

The optical properties of the crystals and their phonon structure, transform in proportion to their Sulphur content. The transformation of the absorption spectra in the THz range is found to be more sensitive to doping content than at the band gap edge or in the mid to far-IR multiphonon bands. Furthermore absorption is found to decrease and the intensity of the rigid mode phonons to increase as the quality of the crystals improve. Thus, THz-TDS looks like a promising assessment tool, for crystal composition and quality. Neither GaSe nor $GaSe_{x-1}S_x$ reach the nonlinear Figure of Merit estimated from the literature as 3375, as even in the best available quality crystals the absorption coefficient remains $> 1\,cm^{-1}$; the e-wave FoM for the measured GaSe and $GaSe_{x-1}S_x$ was found to be 19.8 and 17 respectively. While the absorption and refractive index of $GaSe_{x-1}S_x$ crystals are reduced as a result of doping, so too is the second order nonlinear optical coefficient and, hence, the reduced Figure of Merit. In spite of this, improvements in the optical quality has been shown to compensate for the reduced nonlinearity and the optimal doping level is recommended as $x \approx 0.22$.

6.0.2 Chapter 4

The main phonon bands of the GaSe, GaS and $GaSe_{x-1}S_x$ crystals were investigated by FTIR and Raman spectroscopy and their transformation with respect to doping is studied. The transformation of the main $E'(TO)$ phonon has been studied. The absorption coefficient was estimated for the first time in $GaSe_{x-1}S_x$, x = 0.11, 0.22 & 0.44. The results of the estimates for GaSe, $\alpha = 3 \pm 0.75 \times 10^3\ cm^{-1}$, are found to be in agreement with the published results for GaSe crystals, within the margin of error. The amplitude of the $E'(TO)$ phonon is found to decay with increased sulphur doping and the centre frequency to shift to short wavelengths at a rate of 375 GHz/x (15 GHz/mass% or 4.5 $cm^{-1}/mass\%$) in both the absorption and Raman spectra. The possibility of engineering the transparency windows in $GaSe_{x-1}S_x$ crystals by

means of doping had been suggested. While the intensity of the phonon mode is somewhat reduced and the centre frequency shifted to shorter wavelengths, leading to the improved optical properties in the THz, the mode remains intensive and no significant increase in bandwidth is achieved. Conversely, Sulphur doping leads to a significant increase in absorption at 20 μm, due to the emergence of GaS associated phonons, reducing the efficiency of FIR generation.

While the polytype of the crystals has negligible impact on the linear optical properties, this is not the case for the nonlinear optical properties, where the polytype influences both the effective nonlinear coefficient (d_{eff}) and the most suitable interaction type. In contrast to other studies in the literature, all the measured crystals are of the ε-polytype and the admixture of other polytypes is found to be small. Furthermore, the admixture content is seen to decrease with increased doping, indicating the high quality of the crystals. The ε-polytype, has the largest d_{eff} for both Type-I and II interactions at THz frequencies, maximising the nonlinear Figure of Merit. Sellmeier equations, valid for the full transparency range (0.8–20 μm & 4–0.2 THz) of GaSe and GaS, designed by colleagues and based, in part, on the optical properties determined in this work, were presented.

6.0.3 Chapter 5

Measurements of the second order nonlinear coefficient ($\chi^{(2)}$) and the two-photon absorption coefficienct (β) have to date been largely confined to around 1.064 μm, or been inferred from system performance. $\chi^{(2)}$ and β are a key parameters in determining the efficiency of nonlinear frequency conversion and the threshold of optical parametric oscillators. However, at longer wavelengths, where, from the Manly-Rowe relations, the efficiency of generation of THz radiation is increased, the value of $\chi^{(2)}$ and β have not typically been measured. Attempts to determine the nonlinear optical properties of the crystal in the THz and FIR regimes were undertaken using the classic Maker fringe and z-scan techniques pumped by the Felix free electron laser at Radboud University, Nijmegen, the Netherlands.

Maker fringes experiment was attempted with a 44 cm^{-1} fundamental beam,

such that the major THz absorption features would be avoided and the response of the detector to the generates SHG signal would be maximised. While Maker fringes have been observed in $GaSe_{x-1}S_x$, GaAs and quartz crystals, the experimental method requires improvement to adequately separate the pump and second harmonic beams and enable meaningful analysis of the result. To confirm the origin of the fringes, a centrosymmetric Ge wafer was also measured and no fringes were observed. However, we have demonstrated that it is possible to perform these measurements in the THz regime using free electron lasers, and the experiment will be revisited with an improved setup.

Z-scan measurements were conducted successfully in both the FIR and THz regimes. Two-photon absorption was seen to increase by an order of magnitude between 20 μm and 87 μm, as a result of the main optical phonon band centred at 47 μm. The measurement results for two-photon absorption in the FIR (20 μm), $\beta = 3.8 - 6 \pm 0.6 \times 10^{-7} cm/W$, were found to be in reasonable agreement with the available literature, $\beta = 3.2 - 4.7 \times 10^{-7} cm/W$, for ns pumping with intensities at about $0.1\, GW/cm^2$ in both pure and doped GaSe crystals. β was found to decrease with doping as seen in $GaSe_{x-1}S_x$, x =0.11. However, further detailed comparison between individual crystals is hampered, as the linear absorption at 20 μm increases with doping, pumping with ns pulses leads to thermal carriers (which significantly distort the form of the transmission curves). These problems are further exacerbated by small samples size for measurements at 87 μm, the beam distortion due to the samples, and the instability in the laser operation. The measurements will be revisited using larger crystal samples at different wavelengths, in both the FIR and THz regimes, to reduce linear absorption and allow more stable laser oscillation and low power scans will be performed to eliminated the effect of beam distortion due to the sample. However, we can conclude that mulit-photon absorption in the FIR is no more an impediment to pumping, GaSe based, nonlinear frequency conversion devices that in the near-IR.

6.1 Future Work

As we discussed in Chapter 5, current high power sources of narrow linewidth, broadly tunable, short pulse terahertz radiation are largely restricted to Free-Electron Laser (FEL), such as the Felix instrument. Unfortunately FELs are large, expensive, cumbersome devices, requiring dedicated specialist facilities and a large team of scientists and engineers to operate and maintain, and thus, are restricted to a few large facilities. Even table top systems, that are much less flexible than a FEL, would be highly desirable for many of the applications where FELs are currently used i.e. molecular biology, biophysics and solid state quantum devices [357]. As we seen in Chapter 2, table top sources of tunable [90, 177, 182, 1, 184, 158, 180], narrow linewidth THz radiation have been demonstrated in $LiNbO_3$ [178, 183] below 3 THz and are commercially available in the range 1.2-3 THz [175]. Unfortunately this tuning range is below the transition energies for many the dopants of interest in solid state quantum devices.

Figure 6.1: Inside the radiation vault housing the Felix FEL, showning an engineer for scale (http://www.ru.nl/felix/).

From the work presented in this thesis, it is clear that doped GaSe crystals represent an attractive option for the generation of THz radiation by nonlinear frequency generation. While GaSe's large second order nonlinear coefficient has been reported to be reduced by doping [215, 103], the improvements in the optical quality and mechanical properties more than adequately compensate this reduction; increases in conversion efficiencies of up to 15 times has been reported for $GaSe_{x-1}S_x$. [215].

This situation can be further improved by means of double-doping GaSe crystals with sulphur and aluminium. Light Al-doping has been found to significantly strengthen the crystal and reduce absorption in the GaSe to $\alpha < 1cm^{-1}$ [215]. Gao *et al* state that the effects of two-element doping is additive and we estimated the nonlinear Figure of Merit for THz o-wave generation in $GaSe_{x-1}S_x$:Al, x = 0.22, to be 165, almost an order of magnitude greater than for $GaSe_{x-1}S_x$, x = 0.22, alone; such crystals are currently being grown.

We intend to exploit these crystals in an table top FEL substitute source, based on DFG. The desired tunability range is 0.05–30 THz with gaps due to phonon absorption and a linewidth of $0.1\,cm^{-1}$. A variety of pumping schemes will be investigated including: Q-switched Nd:YAG laser, near-IR OPAs, Mid-IR OPOs and pulsed CO_2 laser. Following successful trials and further crystal optimisation, an OPO system will be developed.

Solid-state quantum devices show great potential in that they are integrable with currently industrial scale silicon wafer processes and existing microelectronic devices. The operation of implanted silicon devices, such as phosphorous in silicon (Si:P), calls for a source of intense narrowband and tunable THz frequency pulses. This source will be employed for the coherent control of spin orbitals, that is essential for entangling neighbouring P atoms, development of quantum memory and the reading and writing of data to such devices [358, 359, 360].

References

[1] D. J. Paul, "The progress towards terahertz quantum cascade lasers on silicon substrates," *Laser & Photonics Reviews*, vol. 4, no. 5, pp. 610–632, 2010.

[2] M. Sheik-bahae, a. a. Said, and E. W. Van Stryland, "High-sensitivity, single-beam n_2 measurements," *Optics Letters*, vol. 14, no. 17, p. 955, 1989.

[3] T. J. Edwards, D. Walsh, M. Spurr, C. F. Rae, M. H. Dunn, and P. G. Browne, "Compact source of continuously and widely-tunable terahertz radiation.," *Optics express*, vol. 14, pp. 1582–9, feb 2006.

[4] M. Tonouchi, "Cutting-edge terahertz technology," *Nature Photonics*, vol. 1, pp. 97–105, 2007.

[5] D. Saeedkia, S. Safavi-naeini, and I. Paper, "Terahertz Photonics : Optoelectronic Techniques for Generation and Detection of Terahertz Waves," *Journal of Lightwave Technology*, vol. 26, no. 15, pp. 2409–2423, 2008.

[6] T. Hochrein, "Markets, Availability, Notice, and Technical Performance of Terahertz Systems: Historic Development, Present, and Trends," *Journal of Infrared, Millimeter, and Terahertz Waves*, vol. 36, no. 3, pp. 235–254, 2014.

[7] J. F. Federici, B. Schulkin, F. Huang, D. Gary, R. Barat, F. Oliveira, and D. Zimdars, "THz imaging and sensing for security applicationsexplosives, weapons and drugs," *Semiconductor Science and Technology*, vol. 20, pp. S266–S280, jul 2005.

[8] A. J. Fitzgerald, E. Berry, N. N. Zinovev, G. C. Walker, M. A. Smith, and J. M. Chamberlain, "An introduction to medical imaging with coherent terahertz

frequency radiation," *Physics in Medicine and Biology*, vol. 47, no. 7, p. R67, 2002.

[9] P. H. Siegel, "Terahertz technology in biology and medicine," *IEEE Transactions on Microwave Theory and Techniques*, vol. 52, no. 10, pp. 2438–2447, 2004.

[10] D. J. Cook and R. M. Hochstrasser, "Intense terahertz pulses by four-wave rectification in air.," *Optics letters*, vol. 25, no. 16, pp. 1210–1212, 2000.

[11] D. Grischkowsky and D. Mittleman, "Introduction," in *Sensing with Terahertz Radiation* (D. Mittleman, ed.), vol. 85 of *Springer Series in Optical Sciences*, pp. 1–38, Springer Berlin Heidelberg, 2003.

[12] Y. S. Lee, *Principles of Terahertz Science and Technology*. Springer US, 2010.

[13] R. Ulbricht, E. Hendry, J. Shan, T. F. Heinz, and M. Bonn, "Carrier dynamics in semiconductors studied with time-resolved terahertz spectroscopy," *Rev. Mod. Phys.*, vol. 83, pp. 543–586, jun 2011.

[14] J. D. Buron, F. Pizzocchero, P. U. Jepsen, D. H. Petersen, J. M. Caridad, B. S. Jessen, T. J. Booth, and P. Bøggild, "Graphene mobility mapping," *Scientific Reports*, vol. 5, p. 12305, 2015.

[15] J. D. Buron, D. H. Petersen, P. Bøggild, D. G. Cooke, M. Hilke, J. Sun, E. Whiteway, P. F. Nielsen, O. Hansen, A. Yurgens, and P. U. Jepsen, "Graphene Conductance Uniformity Mapping," *Nano Letters*, vol. 12, no. 10, pp. 5074–5081, 2012.

[16] M. F. Kimmitt, "Restrahlen to T-rays - 100 Years of terahertz radiation," in *Journal of Biological Physics*, vol. 29, pp. 77–85, 2003.

[17] W. Herschel, "Philosophical Transactions of the Royal Society of London.," *Philosophical Transactions of the Royal Society of London*, vol. 90, no. 1800, pp. 284–292, 1800.

[18] H. Rubens and B. W. Snow, "II. On the refraction of rays of great wave-length in rock-salt, sylvite, and fluorite," *Philosophical Magazine Series 5*, vol. 35, no. 212, pp. 35–45, 1893.

[19] E. F. Nichols, "A method for energy measurements in the infra-red spectrum and the properties of the ordinary ray in quartz for waves of great wave length," *Phys. Rev. (Series I)*, vol. 4, pp. 297–313, jan 1897.

[20] J. M. Chamberlain, "Where optics meets electronics: recent progress in decreasing the terahertz gap.," *Philosophical transactions. Series A, Mathematical, physical, and engineering sciences*, vol. 362, pp. 199–211; discussion 212–3, feb 2004.

[21] E. Nichols, *Ernest Fox Nichols 18691924*. Washington, D.C.: National Academy of Sciences, 1929.

[22] H. Rubens and E. F. Nichols, "Heat Rays Of Great Wave Length," jan 1897.

[23] H. Rubens and E. F. Nichols, "Certain Optical and Electro-Magnetic Properties of Heat Waves of Great Wavelength, I.," *Physical Review (Series I)*, vol. 5, no. 2, pp. 98–112, 1897.

[24] H. Rubens and E. F. Nichols, "Certain properties of heat waves of great wavelength. II," *Physical Review (Series I)*, vol. 5, no. 3, pp. 152–169, 1897.

[25] P. C. Hewitt, "Method of manufacturing electric lamps.," 1901.

[26] H. Rubens and O. von Baeyer, "LXXX. On extremely long waves, emitted by the quartz mercury lamp," *Philosophical Magazine Series 6*, vol. 21, no. 125, pp. 689–695, 1911.

[27] R. W. Wood, "LXXXV. The echelette grating for the infra-red," *Philosophical Magazine Series 6*, vol. 20, no. 118, pp. 770–778, 1910.

[28] B. R. M. Badger, "Absolute intensities in the hydrogen-chloride rotation spectrum," *Proceedings of the National Academy of Sciences*, vol. 13, no. 6, pp. 408–413, 1927.

[29] C. E. Cleeton and N. H. Williams, "Electromagnetic Waves of 1.1 cm Wave-Length and the Absorption Spectrum of Ammonia," *Phys. Rev.*, vol. 45, pp. 234–237, feb 1934.

[30] S. P. Langley, "The bolometer and radiant energy," in *Proceedings of the American Academy of Arts and Sciences*, pp. 342–358, JSTOR, 1880.

[31] M. Jammer, *The conceptual development of quantum mechanics*. International series in pure and applied physics, McGraw-Hill, 1966.

[32] E. F. Nichols and J. D. Tear, "Short Electric Waves," *Phys. Rev.*, vol. 21, pp. 587–610, jun 1923.

[33] A. G. Arkadiewa, "Short electromagnetic waves of wave-length up to 92 μ," *Nature*, vol. 113, p. 640, 1924.

[34] M. J. E. Golay, "A Pneumatic InfraRed Detector," *Review of Scientific Instruments*, vol. 18, no. 5, 1947.

[35] D. H. Andrews, W. F. Brucksch, W. T. Ziegler, and E. R. Blanchard, "Attenuated Superconductors I. For Measuring InfraRed Radiation," *Review of Scientific Instruments*, vol. 13, no. 7, 1942.

[36] D. H. ANDREWS, R. M. MILTON, and W. DESORBO, "A Fast Superconducting Bolometer," *J. Opt. Soc. Am.*, vol. 36, pp. 518–521, sep 1946.

[37] R. H. Varian and S. F. Varian, "A High Frequency Oscillator and Amplifier," *Journal of Applied Physics*, vol. 10, no. 5, 1939.

[38] N. Devyatkov and E. Daniltcev, "On the vibrational modes of the klystronl," *IEST*, 1940.

[39] H. A. H. Boot and J. T. Randall, "Historical Notes on the Cavity Magnetron," *IIIEE TRANSACTIONS ON ELECTRON DEVICE*, vol. 23, no. 7, pp. 724–729, 1976.

[40] P. Guenard, O. Doehler, B. Epsztein, and R. Warnecke, "New UHF tubes with wide electronic tuning. range," *CR Acad. Sci.(Paris)*, vol. 235, p. 235, 1952.

[41] R. Kompfner and N. T. Williams, "Backward-Wave Tubes," *Proceedings of the IRE*, vol. 41, pp. 1602–1611, nov 1953.

[42] R. Beringer, "The Absorption of One-Half Centimeter Electromagnetic Waves in Oxygen," *Phys. Rev.*, vol. 70, pp. 53–57, jul 1946.

[43] W. C. King and W. Gordy, "One to Two Millimeter Wave Spectroscopy. I," *Phys. Rev.*, vol. 90, pp. 319–320, apr 1953.

[44] W. Gordy, W. V. Smith, and R. F. Trambarulo, *Microwave spectroscopy*. Dover Publications, 1953.

[45] C. A. Burrus and W. Gordy, "Millimeter and Submillimeter Wave Spectroscopy," *Phys. Rev.*, vol. 101, pp. 599–602, jan 1956.

[46] E. V. Loewenstein, "The history and current status of fourier transform spectroscopy.," *Applied optics*, vol. 5, no. 5, pp. 845–854, 1966.

[47] H. A. Gebbie and G. A. Vanasse, "Interferometric spectroscopy in the far infra-red," *Nature*, 1956.

[48] K. L. Chopra, "Helium II Film Filter," *Review of Scientific Instruments*, vol. 28, no. 2, 1957.

[49] N. L. Alpert, F. Behnke, and P. A. Strauss, "A New Infrared Spectrometer in the 12.5-25 Micron Region," *Appl. Spectrosc.*, vol. 13, pp. 130–132, oct 1959.

[50] W. S. BOYLE and J. R. K. F. RODGERS, "Performance Characteristics of a New Low-Temperature Bolometer," *J. Opt. Soc. Am.*, vol. 49, pp. 66–69, jan 1959.

[51] S. J. Fray and J. F. C. Oliver, "Photoconductive detector of radiation of wavelength greater than 50 μ," *Journal of Scientific Instruments*, vol. 36, no. 4, p. 195, 1959.

[52] J. B. Gunn, "Microwave oscillations of current in IIIV semiconductors," *Solid State Communications*, vol. 1, no. 4, pp. 88–91, 1963.

[65] T. H. Maiman, "Stimulated optical radiation in ruby," *Nature*, vol. 187, pp. 493–494, 1960.

[66] A. Einstein, "Uber einen die Erzeugung und Verwandlung des Lichtes betreffenden heuristischen Gesichtspunkt," *Annalen der Physik*, vol. 17, no. null, pp. 132–148, 1905.

[67] A. Einstein, "Strahlungs-Emission und -Absorption nach der Quantentheorie," *Deutschen Physikalischen Gesellschaft, Verhandlungen der*, vol. 18, no. null, pp. 318–323, 1916.

[68] A. Einstein, "Zur quantentheorie der strahlung," *Physik.Zeitschr*, vol. 18, no. null, pp. 121–128, 1917.

[69] N. G. Basov and a. M. Prokhorov, "Possible methods of obtaining active molecules for a molecular oscillator," *Soviet Physics JETP*, vol. 1, no. 3, pp. 184–185, 1955.

[70] A. Manenkov and A. Prokhorov, "The fine structure of the spectrum of the paramagnetic resonance of the ion Cr3+ in chromium corundum," *Sov. Phys.-JETP.*, vol. 28, p. 762, 1955.

[71] N. Bloembergen, "Proposal for a New Type Solid State Maser," *Phys. Rev.*, vol. 104, pp. 324–327, oct 1956.

[72] G. M. Zverev, L. S. Kornienko, A. A. Manenkov, and A. M. Prokhorov, "A chromium corundum paramagnetic amplifier and generator," *Soviet Physics JETP*, vol. 7, pp. 1141–1142, 1958.

[73] A. M. Prokhorov, "Molecular amplifier and generator for submillimeter waves," 1958.

[74] R. G. Gould, "The LASER, light amplification by stimulated emission of radiation," in *The Ann Arbor conference on optical pumping, the University of Michigan*, vol. 15, p. 128, 1959.

[75] N. G. Basov and A. M. Prokhorov, "Application of molecular beams for the radiospectroscopic study of rotational molecular spectra," *Zh. Eksp. Teor. Fiz*, vol. 27, no. 4, pp. 431–438, 1954.

[76] J. P. Gordon, H. J. Zeiger, and C. H. Townes, "Molecular microwave oscillator and new hyperfine structure in the microwave spectrum of NH3 [7]," *Physical Review*, vol. 95, pp. 282–284, 1954.

[77] A. L. Schawlow and C. H. Townes, "Infrared and Optical Masers," *Phys. Rev.*, vol. 112, pp. 1940–1949, dec 1958.

[78] C. Townes, "How the Laser Happened: Adventures of a Scientist," *Oxford University Press*, 1999.

[79] a. Javan, W. R. Bennett, and D. R. Herriott, "Population inversion and continuous optical maser oscillation in a gas discharge containing a He-Ne mixture," *Physical Review Letters*, vol. 6, pp. 106–110, 1961.

[80] J. Hecht, "Short history of laser development," *Optical Engineering*, vol. 49, no. 9, pp. 91002–91023, 2010.

[81] E. Snitzer, "Optical Maser Action of {\mathrm{Nd}}ˆ{+3} in a Barium Crown Glass," *Phys. Rev. Lett.*, vol. 7, pp. 444–446, dec 1961.

[82] L. F. Johnson and K. Nassau, "Infrared fluorescence and stimulated emission of Nd3+ in CaWO4," *Proc. IRE*, vol. 49, no. 11, pp. 1704–1705, 1961.

[83] R. N. Hall, G. E. Fenner, J. D. Kingsley, T. J. Soltys, and R. O. Carlson, "Coherent light emission from GaAs junctions," *Physical Review Letters*, vol. 9, no. 9, pp. 366–368, 1962.

[84] N. Holonyak and S. F. Bevacqua, "COHERENT (VISIBLE) LIGHT EMISSION FROM Ga(As1xPx) JUNCTIONS," *Applied Physics Letters*, vol. 1, no. 4, 1962.

[85] M. I. Nathan, W. P. Dumke, G. Burns, F. H. Dill, and G. Lasher, "STIMULATED EMISSION OF RADIATION FROM GaAs pn JUNCTIONS," *Applied Physics Letters*, vol. 1, no. 3, 1962.

[86] T. M. Quist, R. H. Rediker, R. J. Keyes, W. E. Krag, B. Lax, A. L. McWhorter, and H. J. Zeigler, "SEMICONDUCTOR MASER OF GaAs," *Applied Physics Letters*, vol. 1, no. 4, 1962.

[87] F. J. McClung and R. W. Hellwarth, "Giant Optical Pulsations from Ruby," *Journal of Applied Physics*, vol. 33, no. 3, 1962.

[88] L. E. Hargrove, R. L. Fork, and M. A. Pollack, "LOCKING OF HeNe LASER MODES INDUCED BY SYNCHRONOUS INTRACAVITY MODULATION," *Applied Physics Letters*, vol. 5, no. 1, 1964.

[89] J. E. Geusic, H. M. Marcos, and L. G. Van Uitert, "LASER OSCILLATIONS IN NdDOPED YTTRIUM ALUMINUM, YTTRIUM GALLIUM AND GADOLINIUM GARNETS," *Applied Physics Letters*, vol. 4, no. 10, 1964.

[90] W. B. Bridges, "Laser action in singly ionized krypton and xenon," *Proceedings of the IEEE*, vol. 52, no. 7, pp. 843–844, 1964.

[91] C. Patel, "Continuous-Wave Laser Action on Vibrational-Rotational Transitions of CO2," *Physical Review*, vol. 136, no. 5A, pp. 1187–1193, 1964.

[92] K. Kawase, J.-i. Shikata, and H. Ito, "Terahertz wave parametric source," *Journal of Physics D: Applied Physics*, vol. 34, p. R1_R14, feb 2001.

[93] X. Xie, J. Dai, and X.-C. Zhang, "Coherent Control of THz Wave Generation in Ambient Air," *Phys. Rev. Lett.*, vol. 96, p. 75005, feb 2006.

[94] J. Dai, X. Xie, and X. C. Zhang, "Detection of broadband terahertz waves with a laser-induced plasma in gases," *Physical Review Letters*, vol. 97, no. 10, pp. 8–11, 2006.

[95] W. Shi and Y. J. Ding, "A monochromatic and high-power terahertz source tunable in the ranges of 2.738.4 and 58.23540 μm for variety of potential applications," *Applied Physics Letters*, vol. 84, no. 10, p. 1635, 2004.

[96] P. A. Franken, A. Hill, C. Peters, and G. Weinreich, "Generation of Optical Harmonics," *Physical Review Letters*, vol. 7, no. 4, pp. 118–120, 1961.

[97] J. Kerr, "A new relation between electricity and light: Dielectrified media birefringent," *Philosophical Magazine Series 4*, vol. 50, no. 332, pp. 337–348, 1875.

[98] N. Bloembergen, "Nonlinear Optics: Past, Present, and Future," *IEEE J. Sel. Top. Quantum Electron.*, vol. 6, no. 6, pp. 876–880, 2000.

[99] M. H. Dunn, "Parametric Generation of Tunable Light from Continuous-Wave to Femtosecond Pulses," *Science*, vol. 286, pp. 1513–1517, nov 1999.

[100] R. L. Byer and R. L. Herbst, *Parametric oscillation and mixing*, ch. Parametric, pp. 81–137. Berlin, Heidelberg: Springer Berlin Heidelberg, 1977.

[101] S. Hayashi and K. Kawase, "Terahertz wave parametric sources," in *Recent Optical and Photonic Technologies*, pp. 109–124, Spie, 2010.

[102] W. Koechner, "Nonlinear devices," in *Solid-State Laser Engineering*, pp. 587–679, Springer, 2006.

[103] R. W. Boyd, *Nonlinear optics*. Academic press, 1998.

[104] K. R. Allakhverdiev, M. Ö. Yetis, S. Özbek, T. K. Baykara, and E. Y. Salaev, "Effective nonlinear GaSe crystal. Optical properties and applications," *Laser Physics*, vol. 19, pp. 1092–1104, may 2009.

[105] K. R. Aliakhverdiev, R. I. Guliev, E. Y. Salaev, and V. V. Smirnov, "Investigation of linear and nonlinear optical properties of GaSxSe1-x crystals," *Soviet Journal of Quantum Electronics*, vol. 12, no. 7, pp. 947–948, 1982.

[106] K. L. Vodopyanov, "Parametric generation of tunable infrared radiation in ZnGeP_2 and GaSe pumped at 3 m," 1993.

[107] R. L. Byer, "Nonlinear optics and solid-state lasers: 2000," *IEEE Journal on Selected Topics in Quantum Electronics*, vol. 6, no. 6, pp. 911–930, 2000.

[108] J. A. Giordmaine, "Mixing of Light Beams in Crystals," *Physical Review Letters*, vol. 8, no. 1, pp. 19–21, 1962.

[109] P. D. Maker, R. W. Terhune, M. Nisenoff, and C. M. Savage, "Effects of dispersion and Focusing on the Production of Optical Frequencies," *Physical Review*, vol. 8, no. 1, pp. 21–23, 1962.

[110] M. Bass, P. A. Franken, A. Hill, C. Peters, and G. Weinreich, "Optical Mixing," *Physical Review Letters*, vol. 8, no. 1, 1962.

[111] D. C. Laine, "A Proposal for a Tunable Source of Radiation for the Far Infrared using Beats between Optical Masers," *Nature*, vol. 191, pp. 795–796, 1961.

[112] J. Armstrong, N. BLOEMBERGEN, J. Ducuing, and P. Pershan, "Interactions between Light Waves in a Nonlinear Dielectric," *Physical Review*, vol. 127, no. 6, pp. 1918–1939, 1962.

[113] Y. S. Luh, M. M. Fejer, R. L. Byer, and R. S. Feigelson, "Stoichiometric LiNbO 3 single-crystal fibers for nonlinear optical applications," *Journal of Crystal Growth*, vol. 85, no. 1, pp. 264–269, 1987.

[114] G. A. Magel, M. M. Fejer, and R. L. Byer, "Quasi-phase-matched second-harmonic generation of blue light in periodically poled LiNbO3," *Applied Physics Letters*, vol. 56, no. 2, pp. 108–110, 1990.

[115] D. H. Jundt, G. A. Magel, M. M. Fejer, and R. L. Byer, "Periodically poled LiNbO3 for high-efficiency second-harmonic generation," *Applied physics letters*, vol. 59, no. 21, pp. 2657–2659, 1991.

[116] R. H. Kingston, "Parametric Amplification and Oscillation at Optical Frequencies," *Proc of IRE*, vol. 50, no. 4, p. 472, 1962.

[117] S. A. Akhmanov and R. V. Khokhlov, "Concerning one possibility of amplification of light waves," *Soviet Physics JETP*, vol. 16, no. 3, pp. 252–254, 1962.

[118] N. M. Kroll, "Parametric Amplification in Spatially Extended Media and Application to the Design of Tuneable Oscillators at Optical Frequencies," *Phys. Rev.*, vol. 127, pp. 1207–1211, aug 1962.

[119] G. D. Boyd, R. C. Miller, K. Nassau, W. L. Bond, and A. Savage, "LiNbO3: AN EFFICIENT PHASE MATCHABLE NONLINEAR OPTICAL MATERIAL," *Applied Physics Letters*, vol. 5, no. 11, pp. 234–236, 1964.

[120] S. A. Akhmanov, A. I. Kovrigin, A. Kolosov, A. Piskarskas, V. Fadeev, and R. V. Khokhlov, "Tunable Parametric Light Generator with KDP Crystal," *Soviet Physics JETP*, vol. 3, no. 9, pp. 372–378, 1966.

[121] G. D. Boyd and A. Ashkin, "Theory of Parametric Oscillator Threshold with Single-Mode Optical Masers and Observation of Amplification in LiNbO," *Physical Review*, vol. 148, no. 1, pp. 187–198, 1966.

[122] A. Yariv, "Parametric Interactions of Optical Modes," *IEEE Journal of Quantum Electronics*, vol. 2, no. 2, pp. 30–37, 1966.

[123] A. Yariv, "Theory of the Optical Parametric Oscillator," *IEEE Journal of Quantum Electronics*, vol. 2, no. 9, pp. 418–424, 1966.

[124] G. D. Boyd and D. A. Kleinman, "Parametric Interaction of Focused Gaussian Light Beams," *Journal of Applied Physics*, vol. 39, no. 8, pp. 3597–3639, 1968.

[125] A. W. Nordland and R. C. Miller, "Tunable LiNbO3 Optical Pscillator with External Mirrors," *Applied Physics Letters*, vol. 10, no. 2, pp. 53–55, 1967.

[126] L. Kreuzer, "Ruby-Laser-Pumped Optical Parametric Oscillator with Electro-Optic tuning," *Applied Physics Letters*, vol. 10, no. 12, pp. 366–338, 1967.

[53] W. T. Read, "A Proposed High-Frequency, Negative-Resistance Diode," *Bell System Technical Journal*, vol. 37, no. 2, pp. 401–446, 1958.

[54] R. L. Johnston, B. C. De Loach, and B. G. Cohen, "A Silicon Diode Microwave Oscillator," *Bell System Technical Journal*, vol. 44, no. 2, pp. 369–372, 1965.

[55] C. A. Burrus, "Gallium Arsenide Esaki Diodes for HighFrequency Applications," *Journal of Applied Physics*, vol. 32, no. 3, pp. 1031–1036, 1961.

[56] R. H. Pantell, G. Soncini, and H. E. Puthoff, "Stimulated photon-electron scattering," *Quantum Electronics, IEEE Journal of*, vol. 4, pp. 905–907, nov 1968.

[57] J. M. J. Madey, "Stimulated Emission of Bremsstrahlung in a Periodic Magnetic Field," *Journal of Applied Physics*, vol. 42, no. 5, 1971.

[58] E. H. Putley, "Impurity Photoconductivity in n-type InSb," *Proceedings of the Physical Society*, vol. 76, no. 5, p. 802, 1960.

[59] F. J. LOW, "Low-Temperature Germanium Bolometer," *J. Opt. Soc. Am.*, vol. 51, pp. 1300–1304, nov 1961.

[60] D. Renker and E. Lorenz, "Advances in solid state photon detectors," *Journal of Instrumentation*, vol. 4, no. 04, p. P04004, 2009.

[61] M. Brown and M. F. Kimmitt, "Far-infrared resonant photoconductivity in indium antimonide," *Infrared Physics*, vol. 5, no. 2, pp. 93–97, 1965.

[62] K. Shivanandan, J. R. Houck, and M. O. Harwit, "Preliminary Observations of the Far-Infrared Night-Sky Background Radiation," *Phys. Rev. Lett.*, vol. 21, pp. 1460–1462, nov 1968.

[63] M. Harwit, J. R. Houck, and K. Fuhrmann, "Rocket-Borne Liquid Helium Cooled Telescope," *Appl. Opt.*, vol. 8, pp. 473–477, feb 1969.

[64] F. Woody, J. Mather, N. Nishoka, and P. Richards, "Measurement of the Spectrum of the Submillimeter Cosmic Background," *Physical Review Letters*, vol. 34, no. 16, pp. 1036–1039, 1975.

[127] J. Bjorkholm, "Efficient Optical Parametric Oscillation Using Doubly and Singly Resonant Cavities," *Applied Physics Letters*, vol. 13, no. 2, pp. 53–56, 1968.

[128] R. G. Smith, J. E. Geusic, H. J. Levinstein, J. J. Rubin, S. Singh, and L. G. Van Uitert, "CONTINUOUS OPTICAL PARAMETRIC OSCILLATION in Ba2NaNb5O15," *Applied Physics Letters*, vol. 12, no. 9, pp. 308–310, 1968.

[129] R. Byer, M. Oshman, J. Young, and S. Harris, "Visible CW Parametric Oscillator," *Applied Physics Letters*, vol. 13, no. 3, pp. 109–111, 1968.

[130] C. Patel, "Parametric Amplification in the Far Infrared," *Applied Physics Letters*, vol. 9, no. 9, pp. 332–334, 1966.

[131] J. Yarborough, S. Sussman, H. Purhoff, R. Pantell, and B. Johnson, "Efficient Tunable Optical Emission From LiNbO3 Without A Resonator," *Applied Physics Letters*, vol. 15, no. 3, pp. 102–105, 1969.

[132] F. Zernike and P. Berman, "Generation of Far Infrared as a Difference Frequency," *Physical Review Letters*, vol. 15, no. 26, pp. 999–1001, 1965.

[133] T. Yajima and K. Inoue, "Submillimeter-wave generation by difference-frequency mixing of ruby laser lines in ZnTe," *IEEE Journal of Quantum Electronics*, vol. 5, pp. 140–146, mar 1969.

[134] J. Coffinet and F. De Martini, "COHERENT EXCITATION OF POLARITONS IN GALLIUM PHOSPHIDE," *Physical Review Letters*, vol. 22, no. 5, p. 71, 1969.

[135] D. Faries, K. Gehring, P. Richards, and S. Y.R., "Tunable Far-infrared Radiation Generated from the Difference Frequency between Two Ruby Lasers," *Physical Review*, vol. 180, no. 2, pp. 363–365, 1969.

[136] F. Zernike, "Temperature-Dependent Phase Matching for Far-Infrared Difference-Frequency Generation in InSb," *Physical Review Letters*, vol. 22, no. 18, pp. 932–933, 1969.

[137] M. a. Piestrup, R. N. Fleming, and R. H. Pantell, "Continuously tunable submillimeter wave source," *Applied Physics Letters*, vol. 26, no. 8, pp. 418–421, 1975.

[138] A. Bianchi and M. Musci, "4-12um tunable downconversion in GeSe from LiNO3 Parametric Oscillator," *Optics Communications*, vol. 25, no. 2, pp. 256–258, 1978.

[139] J. L. Oudar, P. Kupecek, and D. Chemla, "Medium Infrared Tunable Down Conversion of a YAG-Pumped Infrared Dye Laser in Gallium Selenide," *Optics Communications*, vol. 29, no. 1, pp. 119–122, 1979.

[140] C. Tang, W. Bosenberg, T. Ukachi, R. Lane, and L. Cheng, "Optical parametric oscillators," *Proceedings of the IEEE*, vol. 80, pp. 365–374, mar 1992.

[141] C. M. Armstrong, "1.1: The truth about terahertz," in *Vacuum Electronics Conference (IVEC), 2010 IEEE International*, p. 17, may 2010.

[142] Y.-J. Shen, B.-Q. Yao, Z. Cui, X.-M. Duan, Y.-L. Ju, and Y.-Z. Wang, "A ring ZnGeP2 optical parametric oscillator pumped by a Ho:LuAG laser," *Applied Physics B*, mar 2014.

[143] R. L. Sutherland, *Handbook of Nonlinear Optics*. Optical Science and Engineering, New York, Basel: Marcel Dekker, 2nd ed., 2003.

[144] M. Yamada, N. Nada, M. Saitoh, and K. Watanabe, "First-order quasi-phase matched LiNbO3 waveguide periodically poled by applying an external field for efficient blue second-harmonic generation," *Applied Physics Letters*, vol. 62, no. 5, p. 435, 1993.

[145] L. Myers, R. Eckardt, M. Fejer, R. Byer, W. Bosenberg, and J. Pierce, "Quasi-phase-matched optical parametric oscillators in bulk periodically poled LiNbO_3," *Journal of the Optical Society of America B*, vol. 12, p. 2102, nov 1995.

[146] Y. Sasaki, A. Yuri, K. Kawase, and H. Ito, "Terahertz-wave surface-emitted difference frequency generation in slant-stripe-type periodically poled LiNbO[sub 3] crystal," *Applied Physics Letters*, vol. 81, no. 18, p. 3323, 2002.

[147] L. Gordon, G. Woods, R. Eckardt, R. Route, R. Feigelson, M. Fejer, and R. Byer, "Diffusion-bonded stacked GaAs for quasiphase- matched second-harmonic generation of a carbon dioxide laser," *Electronics Letters*, vol. 29, no. 22, p. 1942, 1993.

[148] L. a. Eyres, P. J. Tourreau, T. J. Pinguet, C. B. Ebert, J. S. Harris, M. M. Fejer, L. Becouarn, B. Gerard, and E. Lallier, "All-epitaxial fabrication of thick, orientation-patterned GaAs films for nonlinear optical frequency conversion," *Applied Physics Letters*, vol. 79, no. 7, pp. 904–906, 2001.

[149] J. E. Schaar, K. L. Vodopyanov, and M. M. Fejer, "Intracavity terahertz-wave generation in a synchronously pumped optical parametric oscillator using quasi-phase-matched GaAs.," *Optics letters*, vol. 32, pp. 1284–6, may 2007.

[150] D. Zheng, L. A. Gordon, Y. S. Wu, R. S. Feigelson, M. M. Fejer, R. L. Byer, and K. L. Vodopyanov, "16-um infrared generation by difference-frequency mixing in diffusion-bonded-stacked GaAs.," *Optics letters*, vol. 23, pp. 1010–1012, jul 1998.

[151] G. Imeshev, M. E. Fermann, K. L. Vodopyanov, M. M. Fejer, X. Yu, J. S. Harris, D. Bliss, and C. Lynch, "High-power source of THz radiation based on orientation-patterned GaAs pumped by a fiber laser.," *Optics express*, vol. 14, pp. 4439–44, may 2006.

[152] K. L. Vodopyanov, J. Schaar, M. M. Fejer, X. Yu, J. S. Harris, Y.-S. Lee, V. G. Kozlov, G. Imeshev, M. E. Fermann, D. Bliss, and C. Lynch, "Tunable THz source based on frequency conversion in quasi-phase-matched GaAs," *Proceedings of SPIE*, vol. 6386, no. 2006, pp. 63860T–63860T–13, 2006.

[153] L. Bromley, A. Guy, and D. Hanna, "Sychronously Pumped Optical Parametric Oscillation in Beta-Barium Borate," *Optics Communications*, vol. 67, no. 4, pp. 316–320, 1988.

[154] K. Kawase, J. Shikata, H. Minamide, K. Imai, and H. Ito, "Arrayed silicon prism coupler for a terahertz-wave parametric oscillator.," *Applied optics*, vol. 40, pp. 1423–1426, mar 2001.

[155] H. Minamide, A. Sato, T. Ikari, and H. Ito, "All-in-one THz-wave parametric source driven by a compact LD-pumped Q-switched Nd:YAG laser," *2007 Conference on Lasers and Electro-Optics - Pacific Rim*, pp. 1–2, aug 2007.

[156] D. H. Wu and T. Ikari, "Enhancement of the output power of a terahertz parametric oscillator with recycled pump beam," *Applied Physics Letters*, vol. 95, no. 14, 2009.

[157] K. Kawase, M. Sato, T. Taniuchi, and H. Ito, "Coherent tunable THz-wave generation from LiNbO3 with monolithic grating coupler," *Applied Physics Letters*, vol. 68, no. 18, pp. 2483–2485, 1996.

[158] K. Kawase, M. Sato, K. Nakamura, T. Taniuchi, and H. Ito, "Unidirectional radiation of widely tunable THz wave using a prism coupler under noncollinear phase matching condition," *Applied Physics Letters*, vol. 71, no. 6, pp. 753–755, 1997.

[159] K. Imai, K. Kawase, H. Minamide, and H. Ito, "Achromatically injection-seeded terahertz-wave parametric generator.," *Optics letters*, vol. 27, pp. 2173–5, dec 2002.

[160] J. Kiessling, F. Fuchs, K. Buse, and I. Breunig, "Pump-enhanced optical parametric oscillator generating continuous wave tunable terahertz radiation," 2011.

[161] T. Liu, L. Liu, X. B. Wang, X. Li, and J. Hou, "Cascaded synchronous terahertz optical parametric oscillations in a single MgO:PPLN crystal," *Laser Physics*, vol. 22, pp. 678–683, mar 2012.

[162] T. Tanabe, K. Suto, J.-i. Nishizawa, and T. Sasaki, "Characteristics of terahertz-wave generation from GaSe crystals," *Journal of Physics D: Applied Physics*, vol. 37, pp. 155–158, jan 2004.

[163] Y. J. Ding and W. Shi, "Efficient THz generation and frequency upconversion in GaP crystals," *Solid-State Electronics*, vol. 50, pp. 1128–1136, jun 2006.

[164] J. Kiessling, R. Sowade, I. Breunig, K. Buse, and V. Dierolf, "Cascaded optical parametric oscillations generating tunable terahertz waves in periodically poled lithium niobate crystals.," *Optics express*, vol. 17, pp. 87–91, jan 2009.

[165] N. Leindecker, A. Marandi, R. L. Byer, K. L. Vodopyanov, J. Jiang, I. Hartl, M. Fermann, and P. G. Schunemann, "Octave-spanning ultrafast OPO with 26-61m instantaneous bandwidth pumped by femtosecond Tm-fiber laser," 2012.

[166] P. Zhao, S. Ragam, Y. J. Ding, and I. B. Zotova, "Intracavity Terahertz Generation in Laser Output Coupler Made from Stacked GaP Plates," *Conference on Lasers and Electro-Optics Technical Digest*, 2012.

[167] Y. J. Ding, P. Zhao, and D. Li, "Recent Progress on Compact and Portable Terahertz Source Based on Parametric Conversion from Dual-Frequency Solid-State Laser Pulses," *Journal of Physics: Conference Series*, vol. 414, p. 012003, feb 2013.

[168] W. Shi, Y. J. Ding, N. Fernelius, and K. L. Vodopyanov, "Efficient, tunable, and coherent 0.18-5.27 Thz source based on GaSe crystal," *Optics Letters*, vol. 27, no. 16, pp. 1454–1456, 2002.

[169] K. Finsterbusch, a. Bayer, and H. Zacharias, "Tunable, narrow-band picosecond radiation in the mid-infrared by difference frequency mixing in GaSe and CdSe," *Applied Physics B*, vol. 79, pp. 457–462, jul 2004.

[170] W. Shi and Y. J. Ding, "Tunable terahertz waves generated by mixing two copropagating infrared beams in GaP.," *Optics letters*, vol. 30, pp. 1030–2, may 2005.

[171] J. M. Fukumoto, "Three-Stage Optical Parametric Oscillator Conversion From 1 um to the 8-12 um Region," *Advanced Solid State Lasers*, vol. 68, pp. 558–562, 2002.

[172] G. Mennerat, "High-energy difference-frequency generation in the 5.8-22 m range," *Advanced Solid-State Lasers Congress*, p. MW3B.6, 2013.

[173] J. Huang, J. Tong, Z. Huang, and J. Chu, "Coherent CdTe terahertz source for high-resolutional imaging," *Proceedings of SPIE*, p. 914212, 2014.

[174] J. Huang, Z. Huang, J. Tong, C. Ouyang, J. Chu, Y. Andreev, K. Kokh, G. Lanskii, and A. Shaiduko, "Intensive terahertz emission from GaSe0.91S0.09 under collinear difference frequency generation," *Applied Physics Letters*, vol. 103, no. 8, p. 081104, 2013.

[175] Y. J. Ding and I. B. Zotova, "Second-order nonlinear optical materials for e cient generation and ampli ® cation of temporally-coherent and narrow-linewidth terahertz waves," *Optical and Quantum Electronics*, vol. 32, pp. 531–552, 2000.

[176] J. A. Giordmaine and R. C. Miller, "Tunable Coherent Parametric Oscillation in LinbO3 at Optical Frequencies," *Physical Review Letters*, vol. 14, no. 24, pp. 973–976, 1965.

[177] G. Malcolm, "New laser sources benefit terahertz and mid-infrared remote sensing," *SPIE Newsroom*, pp. 10–12, 2007.

[178] A. Ridah, P. Bourson, M. D. Fontana, and G. Malovichko, "The composition dependence of the Raman spectrum and new assignment of the phonons in LiNbO 3," *Journal of Physics: condensed Matter*, vol. 9, pp. 9687–9693, 1997.

[179] J. Shikata, K. Kawase, and H. Ito, "The generation and linewidth control of terahertz waves by parametric processes," *Electronics and Communications in Japan (Part II: Electronics)*, vol. 86, pp. 52–65, may 2003.

[180] M. H. Dunn, T. J. Edwards, D. J. M. Stothard, D. Walsh, P. G. Browne, and C. F. Rae, "Line-narrowed, compact and coherent source of widely tunable terahertz radiation," in *Infrared and Millimeter Waves, 2007 and the 2007 15th International Conference on Terahertz Electronics. IRMMW-THz. Joint 32nd International Conference on*, pp. 613–616, sep 2007.

[181] K. Suizu and K. Kawase, "Monochromatic-Tunable Terahertz-Wave Sources Based on Nonlinear Frequency Conversion Using," *IEEE Journal of Selected Topics in Quantum Electronics*, vol. 14, no. 2, pp. 295–306, 2008.

[182] C. L. Thomson and M. H. Dunn, "Observation of a cascaded process in intracavity terahertz optical parametric oscillators based on lithium niobate," *Optics Express*, vol. 21, no. 15, pp. 17647–17658, 2013.

[183] M. E. Klein, P. Gross, K. J. Boller, M. Auerbach, P. Wessels, and C. Fallnich, "Rapidly tunable continuous-wave optical parametric oscillator pumped by a fiber laser.," *Optics letters*, vol. 28, pp. 920–2, jun 2003.

[184] D. Stothard, I. Lindsay, and M. Dunn, "Continuous-wave pump-enhanced optical parametric oscillator with ring resonator for wide and continuous tuning of single-frequency radiation.," *Optics express*, vol. 12, no. 3, pp. 502–511, 2004.

[185] R. Sowade, I. Breunig, I. Cámara Mayorga, J. Kiessling, C. Tulea, V. Dierolf, and K. Buse, "Continuous-wave optical parametric terahertz source.," *Optics express*, vol. 17, pp. 22303–10, dec 2009.

[186] D. a. Walsh, P. G. Browne, M. H. Dunn, and C. F. Rae, "Intracavity parametric generation of nanosecond terahertz radiation using quasi-phase-matching.," *Optics express*, vol. 18, pp. 13951–63, jun 2010.

[187] J. E. Schaar, K. L. Vodopyanov, P. S. Kuo, M. M. Fejer, X. Yu, A. Lin, J. S. Harris, D. Bliss, C. Lynch, V. G. Kozlov, and W. Hurlbut, "Terahertz Sources Based on Intracavity Parametric Down-Conversion in Quasi-Phase-Matched

Gallium Arsenide," *IEEE Journal of Selected Topics in Quantum Electronics*, vol. 14, no. 2, pp. 354–362, 2008.

[188] K. L. Vodopyanov, I. Makasyuk, and P. G. Schunemann, "Grating tunable 4 - 14 m GaAs optical parametric oscillator pumped at 3 m," *Optics express*, vol. 22, no. 4, pp. 1413–1415, 2014.

[189] J. Waugh and G. Dolling, "Crystal Dynamics of Gallium Arsenide," *Physical Review*, vol. 123, no. 6, pp. 2410–2412, 1963.

[190] C. Kieleck, M. Eichhorn, A. Hirth, D. Faye, and E. Lallier, "High-efficiency 20-50 kHz mid-infrared orientation-patterned GaAs optical parametric oscillator pumped by a 2 m holmium laser," *Optics Letters*, vol. 34, no. 3, pp. 262–264, 2009.

[191] R. K. Feaver, R. D. Peterson, and P. E. Powers, "Longwave-IR optical parametric oscillator in orientation-patterned GaAs pumped by a 2 m Tm,Ho:YLF laser," *Optics express*, vol. 21, no. 13, p. 16104, 2013.

[192] G. L. Zhu, Y. L. Ju, P. B. Meng, B. Q. Yao, and Y. Z. Wang, "Effect of resonator length on ZnGeP2 doubly resonant optical parametric oscillator pumped by a Tm,Ho:GdVO4 laser," *Laser Physics*, vol. 20, pp. 1329–1330, may 2010.

[193] P. G. Schunemann, "New Nonlinear Optical Crystals for the Mid-Infrared," in *Advanced Solid-State Lasers*, p. 3061, 2015.

[194] G. Verozubova, a.O. Okunev, a.I. Gribenyukov, A. Trofimiv, E. Trukhanov, and a.V. Kolesnikov, "Growth and defect structure of ZnGeP2 crystals," *Journal of Crystal Growth*, vol. 312, pp. 1122–1126, apr 2010.

[195] K. L. Vodopyanov, F. Ganikhanov, J. P. Maffetone, I. Zwieback, and W. Ruderman, "ZnGeP2 optical parametric oscillator with 3.8-12.4-mum tunability.," *Optics letters*, vol. 25, pp. 841–3, jun 2000.

[196] Y. J. Ding and W. Shi, "Widely Tunable Monochromatic THz Sources Based on Phase-Matched Difference-Frequency Generation in Nonlinear-Optical Crystals : A Novel Approach," *Laser Physics*, vol. 16, no. 4, pp. 562–570, 2006.

[197] Y. M. Andreev, V. Apollonov, Y. Shakir, G. Verozubova, and A. Gribenyukov, "Submillimeter-Wave Generation with ZnGeP 2 Crystals," *Journal of Korean Physical Society*, vol. 33, no. 3, pp. 320–324, 1998.

[198] J. D. Rowley, D. A. Bas, K. T. Zawilski, P. G. Schunemann, and A. D. Bristow, "Terahertz emission from ZnGeP_2: phase-matching, intensity, and length scalability," *Journal of the Optical Society of America B*, vol. 30, no. 11, p. 2882, 2013.

[199] G. D. Boyd, H. M. Kasper, J. H. McFee, and F. G. Storz, "Linear and nonlinear optical properties of some ternary selenides," *IEEE Journal of Quantum Electronics*, vol. 8, pp. 900–908, dec 1972.

[200] A. BIANCHI and M. GARBI, "DOWN-CONVERSION IN THE 4-18 Itm RANGE WITH GaSe AND AgGaSe 2 NONLINEAR CRYSTALS," *Optical Communications*, vol. 30, no. 1, pp. 122–124, 1979.

[201] J. Van der Ziel, H. M. Meixner, Kasper, and J. Ditzenberger, "Lattice vibrations of AgGaS, AgGaSe and CuGaS," *Physical Review A*, vol. 9, no. 10, pp. 4286–4294, 1974.

[202] Q. Zhang, I. Chung, J. I. Jang, J. B. Ketterson, M. G. Kanatzidis, and J. D. I. Chem, "A Polar and Chiral Indium Telluride Featuring Supertetrahedral T2 Clusters and Nonlinear Optical Second Harmonic Generation," *Chemistry of Materials*, vol. 21, no. 8, pp. 12–14, 2009.

[203] R. a. Kaindl, M. Wurm, K. Reimann, P. Hamm, A. M. Weiner, and M. Woerner, "Generation, shaping, and characterization of intense femtosecond pulses tunable from 3 to 20 μm," *Journal of the Optical Society of America B*, vol. 17, no. 12, p. 2086, 2000.

[204] C.-w. Chen, T.-t. Tang, S.-h. Lin, J. Y. Huang, C.-s. Chang, P.-k. Chung, S.-t. Yen, and C.-l. Pan, "Optical properties and potential applications of ϵ-GaSe at terahertz frequencies," *Journal of the Optical Society of America B*, vol. 26, no. 9, pp. 58–65, 2009.

[205] W. Shi, Y. J. Ding, X. Mu, and N. Fernelius, "Tunable and coherent nanosecond radiation in the range of 2.728.7μm based on difference-frequency generation in gallium selenide," *Applied Physics Letters*, vol. 80, no. 21, p. 3889, 2002.

[206] K. C. Mandal, S. H. Kang, M. Choi, J. Chen, X.-c. Zhang, M. James, C. A. Schmuttenmaer, N. C. Fernelius, and S. Member, "III VI Chalcogenide Semiconductor Crystals for Broadband Tunable THz Sources and Sensors," *Quantum*, vol. 14, no. 2, pp. 284–288, 2008.

[207] Z.-S. Feng, Z.-H. Kang, F.-G. Wu, J.-Y. Gao, Y. Jiang, H.-Z. Zhang, Y. M. Andreev, G. V. Lanskii, V. V. Atuchin, and T. a. Gavrilova, "SHG in doped GaSe:In crystals.," *Optics express*, vol. 16, pp. 9978–85, jun 2008.

[208] N. Singh, D. Suhre, W. Rosch, R. Meyer, M. Marable, N. Fernelius, F. Hopkins, D. Zelmon, and R. Narayanan, "Modified GaSe crystals for mid-IR applications," *Journal of Crystal Growth*, vol. 198-199, pp. 588–592, mar 1999.

[209] S. Y. Tochitsky, C. Sung, S. E. Trubnick, C. Joshi, and K. L. Vodopyanov, "High-power tunable, 0.53 THz radiation source based on nonlinear difference frequency mixing of CO2 laser lines," *Journal of the Optical Society of America B*, vol. 24, no. 9, pp. 2509–2516, 2007.

[210] S. Das, C. Ghosh, S. Gangopadhyay, U. Chatterjee, G. C. Bhar, V. G. Voevodin, and O. G. Voevodina, "Tunable coherent infrared source from 5-16 m based on difference-frequency mixing in an indium-doped GaSe crystal," *Journal of the Optical Society of America B*, vol. 23, no. 2, p. 282, 2006.

[211] L.-M. Zhang, J. Guo, D.-J. Li, J.-J. Xie, Y. M. Andreev, V. A. Gorobets, V. V. Zuev, K. A. Kokh, G. V. Lanskii, V. O. Petukhov, V. A. Svetlichnyi,

and A. V. Shaiduko, "Dispersion properties of GaSe1-x S x in the terahertz range," *Journal of Applied Spectroscopy*, vol. 77, no. 6, pp. 850–856, 2011.

[212] V. V. Atuchin, Y. M. Andreev, K. a. Kokh, G. V. Lanskii, A. V. Shaiduko, T. I. Izaak, and V. a. Svetlichnyi, "Optimal doping of GaSe with isovalent elements," *Proc. SPIE*, vol. 8772, pp. 87721Q1–87721Q9, may 2013.

[213] Y.-K. Hsu, C.-W. Chen, J. Y. Huang, C.-L. Pan, J.-Y. Zhang, and C.-S. Chang, "Erbium doped GaSe crystal for mid-IR applications.," *Optics express*, vol. 14, pp. 5484–91, jun 2006.

[214] C.-W. Chen, Y.-K. Hsu, J. Y. Huang, C.-S. Chang, J.-Y. Zhang, and C.-L. Pan, "Generation properties of coherent infrared radiation in the optical absorption region of GaSe crystal.," *Optics express*, vol. 14, pp. 10636–44, oct 2006.

[215] Y. Jiang and Y. J. Ding, "Efficient terahertz generation from two collinearly propagating CO[sub 2] laser pulses," *Applied Physics Letters*, vol. 91, no. 9, p. 091108, 2007.

[216] Y. M. Andreev, K. a. Kokh, G. V. Lanskii, and a. N. Morozov, "Structural characterization of pure and doped GaSe by nonlinear optical method," *Journal of Crystal Growth*, vol. 318, no. 1, pp. 1164–1166, 2011.

[217] J. Guo, J.-J. Xie, D.-J. Li, G.-L. Yang, F. Chen, C.-R. Wang, L.-M. Zhang, Y. . Andreev, K. A. Kokh, G. V. Lanskii, and V. A. Svetlichnyi, "Doped GaSe crystals for laser frequency conversion," *Light*, vol. ?, no. ?, p. ?, 2015.

[218] J. Guo, D.-J. Li, J.-J. Xie, L.-M. Zhang, Z.-S. Feng, Y. M. Andreev, K. A. Kokh, G. V. Lanskii, A. I. Potekaev, A. V. Shaiduko, and V. A. Svetlichnyi, "Limiting pump intensity for sulfur-doped gallium selenide crystals," *Laser Physics Letters*, vol. 11, no. 5, p. 55401, 2014.

[219] Z.-S. Feng, Z.-H. Kang, X.-M. Li, Z.-B. Wang, J.-Y. Gao, Y. M. Andreev, V. V. Atuchin, K. A. Kokh, G. V. Lanskii, A. I. Potekaev, A. V. Shaiduko,

and V. A. Svetlichnyi, "Impact of fs and ns pulses on indium and sulfur doped gallium selenide crystals," *AIP Advances*, vol. 4, no. 3, 2014.

[220] V. Petrov, V. L. Panyutin, A. Tyazhev, G. Marchev, A. I. Zagumennyi, F. Rotermund, F. Noack, K. Miyata, L. D. Iskhakova, and A. F. Zerrouk, "GaS0.4Se0.6: Relevant properties and potential for 1064 nm pumped mid-IR OPOs and OPGs operating above 5 μm," *Laser Physics*, vol. 21, pp. 774–781, mar 2011.

[221] S. Y. Sarkisov, M. M. Nazarov, A. P. Shkurinov, and O. P. Tolbanov, "GaSe1-xSx and GaSe1-xTe x solid solutions for terahertz generation and detection," in *Infrared, Millimeter, and Terahertz Waves, 2009. IRMMW-THz 2009. 34th International Conference on*, pp. 1–2, sep 2009.

[222] A. G. Sitnikov, A. N. Panchenko, A. E. Tel'minov, D. E. Genin, S. Y. Sarkisov, S. A. Bereznaya, Z. V. Korotchenko, and A. V. Kazakov, "Single-pulse CO2 laser with frequency doubler based on GaSe and GaSe0. 7S0. 3 single crystals," in *16th SHCE. Proc. of 16th International Symposium on High Current Electronics. Tomsk, Russia*, pp. 586–588, 2010.

[223] S. Das, C. Ghosh, O. Voevodina, Y. Andreev, and S. Sarkisov, "Modified GaSe crystal as a parametric frequency converter," *Applied Physics B*, vol. 82, pp. 43–46, nov 2005.

[224] H.-Z. Zhang, Z.-H. Kang, Y. Jiang, J.-Y. Gao, F.-G. Wu, Z.-S. Feng, Y. M. Andreev, G. V. Lanskii, A. N. Morozov, E. I. Sachkova, and S. Y. Sarkisov, "SHG phase matching in GaSe and mixed GaSe1-xSx, x0.412, crystals at room temperature," *Optics express*, vol. 16, no. 13, pp. 9951–9957, 2008.

[225] S.-A. Ku, C.-W. Luo, H.-L. Lio, K.-H. Wu, J.-Y. Juang, A. I. Potekaev, O. P. Tolbanov, S. Y. Sarkisov, Y. . Andreev, and G. V. Lanskii, "Optical properties of nonlinear solid solution GaSe1-xSx (0x0.4) crystals," *Russian Physics Journal*, vol. 51, no. 10, pp. 1083–1089, 2009.

[226] S. A. Ku, W. C. Chu, C. W. Luo, Y. M. Andreev, G. V. Lanskii, A. V. Shaiduko, T. I. Izaak, V. A. Svetlichnyi, E. A. Vaitulevich, and V. V. Zuev, "Optical properties of Te-doped GaSe crystal," *Chinese Optics*, vol. 4, no. 6, pp. 660–666, 2011.

[227] Z. H. Kang, J. Guo, Z. S. Feng, J. Y. Gao, J. J. Xie, L. M. Zhang, V. Atuchin, Y. Andreev, G. Lanskii, and A. Shaiduko, "Tellurium and sulfur doped GaSe for mid-IR applications," *Applied Physics B: Lasers and Optics*, 2012.

[228] K. Miyata, G. Marchev, A. Tyazhev, V. Panyutin, and V. Petrov, "Picosecond mid-infrared optical parametric amplifier based on the wide-bandgap GaS(0.4)Se(0.6) pumped by a Nd:YAG laser system at 1064 nm.," *Optics letters*, vol. 36, pp. 1785–7, may 2011.

[229] E. Lippert, G. Rustad, G. Arisholm, and K. Stenersen, "High power and efficient long wave IR ZnGeP2 parametric oscillator.," *Optics express*, vol. 16, pp. 13878–84, sep 2008.

[230] B.-Q. Yao, G. Li, G.-L. Zhu, P.-B. Meng, Y.-L. Ju, and Y.-Z. Wang, "Comparative investigation of long-wave infrared generation based on ZnGeP 2 and CdSe optical parametric oscillators," *Chinese Physics B*, vol. 21, p. 034213, mar 2012.

[231] D. Creeden, J. C. McCarthy, P. a. Ketteridge, P. G. Schunemann, T. Southward, J. J. Komiak, and E. P. Chicklis, "Compact, high average power, fiber-pumped terahertz source for active real-time imaging of concealed objects.," *Optics express*, vol. 15, pp. 6478–83, may 2007.

[232] T. Taniuchi, S. Okada, and H. Nakanishi, "Widely-tunable THz-wave generation in 2 20 THz range from DAST crystal by nonlinear difference frequency mixing," *Electronics Letters*, vol. 40, no. 1, pp. 5–6, 2004.

[233] D.-w. Zhang and J.-m. Yuan, "Widely Tunable Terahertz-Wave Generation from Collinear Phase-matched GaSe," in *IRMMW-THz 2006 - 31th Interna-*

tional Conference on Infrared, Millimeter, and Terahertz Waves, Conference Guide, p. 112, 2006.

[234] K. Allakhverdiev, N. Fernelius, F. Gashimzade, J. Goldstein, E. Salaev, and Z. Salaeva, "Anisotropy of optical absorption in GaSe studied by midinfrared spectroscopy," *Journal of Applied Physics*, vol. 93, no. 6, p. 3336, 2003.

[235] Y. J. Ding, Y. Jiang, G. Xu, and I. B. Zotova, "<title>Recent progress on efficient generation of monochromatic THz pulses based on difference-frequency generation</title>," *Pro*, vol. 7600, pp. 76000G–76000G–10, feb 2010.

[236] B. L. Yu, F. Zeng, V. Kartazayev, R. R. Alfano, and K. C. Mandal, "Terahertz studies of the dielectric response and second-order phonons in a GaSe crystal," *Applied Physics Letters*, vol. 87, no. 18, p. 182104, 2005.

[237] K. A. Kokh, B. G. Nenashev, A. E. Kokh, and G. Shvedenkov, "Application of a rotating heat field in BridgmanStockbarger crystal growth," *Journal of Crystal Growth*, vol. 275, no. 12, pp. e2129 – e2134, 2005.

[238] K. A. Kokh, V. N. Popov, A. E. Kokh, B. A. Krasin, and A. I. Nepomnyaschikh, "Numerical modeling of melt flows in vertical Bridgman configuration affected by a rotating heat field," *Journal of Crystal Growth*, vol. 303, no. 1, pp. 253–257, 2007.

[239] C. P. Leon, L. Kador, K. R. Allakhverdiev, T. Baykara, and a. a. Kaya, "Comparison of the layered semiconductors GaSe, GaS, and GaSe[sub 1x]S[sub x] by Raman and photoluminescence spectroscopy," *Journal of Applied Physics*, vol. 98, no. 10, p. 103103, 2005.

[240] C. Ho, C. Wu, and Z. Cheng, "Crystal structure and electronic structure of GaSe1xSx series layered solids," *Journal of Crystal Growth*, vol. 279, pp. 321–328, jun 2005.

[241] M. Nuss and J. Orenstein, "Terahertz time-domain spectroscopy," *Millimeter and Submillimeter Wave Spectroscopy of Solids*, vol. 74, pp. 7–50, 1998.

[242] B. B. Hu and M. C. Nuss, "Imaging with terahertz waves.," *Optics letters*, vol. 20, p. 1716, aug 1995.

[243] D. M. Mittleman, M. Gupta, R. Neelamani, R. G. Baraniuk, J. V. Rudd, and M. Koch, "Recent advances in terahertz imaging," *Applied Physics B: Lasers and Optics*, vol. 68, pp. 1085–1094, 1999.

[244] B. Ferguson and X.-C. Zhang, "Materials for terahertz science and technology.," *Nature materials*, vol. 1, pp. 26–33, sep 2002.

[245] P. Smith, D. Auston, and M. Nuss, "Subpicosecond photoconducting dipole antennas," *IEEE Journal of Quantum Electronics*, vol. 24, pp. 255–260, feb 1988.

[246] C. Fattinger and D. Grischkowsky, "Point Source Terahertz Optics," *Applied Physics Letters*, vol. 53, no. 16, pp. 1480–1482, 1988.

[247] C. Fattinger and D. Grischkowski, "Terahertz Beams," *Applied Physics Letters*, vol. 55, no. 6, pp. 490–492, 1989.

[248] D. Grischkowsky, S. Keiding, M. van Exter, and C. Fattinger, "Far-infrared time-domain spectroscopy with terahertz beams of dielectrics and semiconductors," *Journal of the Optical Society of America B*, vol. 7, no. 10, pp. 2006–2015, 1990.

[249] Q. Wu and X. C. Zhang, "Free-space electro-optic sampling of terahertz beams," *Applied Physics Letters*, vol. 67, no. 1995, p. 3523, 1995.

[250] A. Nahata, D. H. Auston, C. Wu, and J. T. Yardley, "Generation of terahertz radiation from a poled polymer," *Applied Physics Letters*, vol. 67, no. 10, pp. 1358–1360, 1995.

[251] Q. Wu and X. C. Zhang, "Ultrafast electro-optic field sensors," *Applied Physics Letters*, vol. 68, no. 12, pp. 1604–1606, 1996.

[252] Q. Wu, T. D. Hewitt, and X. C. Zhang, "Two-dimensional electro-optic imaging of THz beams," *Applied Physics Letters*, vol. 69, no. 8, pp. 1026–1028, 1996.

[253] J. F. Ward, G. Weinreich, M. Bass, and P. A. Franken, "Optical Rectification," *Physical Review Letters*, vol. 9, no. 11, pp. 28–31, 1962.

[254] H. Hamster, a. Sullivan, S. Gordon, W. White, and R. W. Falcone, "Subpicosecond, electromagnetic pulses from intense laser-plasma interaction," *Physical Review Letters*, vol. 71, no. 17, pp. 2725–2728, 1993.

[255] H. Hamster, A. Sullivan, S. Gordon, and R. W. Falcone, "Short-Pulse Terahertz Radiation from high-intensity-laser-produced plasmas," *Physical Review E*, vol. 49, no. 1, pp. 671–677, 1994.

[256] M. Kress, T. Löffler, S. Eden, M. Thomson, and H. G. Roskos, "Terahertz-pulse generation by photoionization of air with laser pulses composed of both fundamental and second-harmonic waves.," *Optics letters*, vol. 29, no. 10, pp. 1120–1122, 2004.

[257] T. Bartel, P. Gaal, K. Reimann, M. Woerner, and T. Elsaesser, "Generation of single-cycle THz transients with high electric-field amplitudes.," *Optics letters*, vol. 30, no. 20, pp. 2805–2807, 2005.

[258] M. Naftaly and R. Dudley, "Linearity calibration of amplitude and power measurements in terahertz systems and detectors.," *Optics letters*, vol. 34, pp. 674–6, mar 2009.

[259] M. Naftaly and R. Dudley, "Methodologies for determining the dynamic ranges and signal-to-noise ratios of terahertz time-domain spectrometers.," *Optics letters*, vol. 34, pp. 1213–5, apr 2009.

[260] M. Naftaly, R. A. Dudley, and J. R. Fletcher, "An etalon-based method for frequency calibration of terahertz time-domain spectrometers (THz TDS)," *Optics Communications*, vol. 283, no. 9, pp. 1849–1853, 2010.

[261] W. Aenchbacher, M. Naftaly, and R. Dudley, "Line strengths and self-broadening of pure rotational lines of carbon monoxide measured by terahertz time-domain spectroscopy," *Appl. Opt.*, vol. 49, pp. 2490–2496, may 2010.

[262] J. F. Molloy, M. Naftaly, and R. A. Dudley, "Characterization of Terahertz Beam Profile and Propagation," *IEEE Journal of Selected Topics in Quantum Electronics*, vol. 19, p. 8401508, jan 2013.

[263] A. Steiger, M. Kehrt, C. Monte, and R. Müller, "Traceable terahertz power measurement from 1 THz to 5 THz," *Opt. Express*, vol. 21, pp. 14466–14473, jun 2013.

[264] J. F. Molloy and M. Naftaly, "Metrology for terahertz time-domain spectrometers," *Proceedings of SPIE*, vol. 9810, pp. 98101H–98101H–7, 2015.

[265] M. Naftaly and J. Molloy, "A multi-lab intercomparison study of THz time-domain spectrometers," in *Infrared, Millimeter, and Terahertz waves (IRMMW-THz), 2015 40th International Conference on*, pp. 1–2, aug 2015.

[266] M. Naftaly, *Terahertz Metrology:*. Artech House Publishers, 2015.

[267] M. Naftaly, "Metrology issues and solutions in THz time domain spectroscopy: noise, errors, calibration," 2013.

[268] K. a. Kokh, Y. M. Andreev, V. a. Svetlichnyi, G. V. Lanskii, and a. E. Kokh, "Growth of GaSe and GaS single crystals," *Crystal Research and Technology*, vol. 46, pp. 327–330, apr 2011.

[269] J. F. Molloy, M. Naftaly, Y. . Andreev, K. A. Kokh, G. V. Lanskii, and V. A. Svetlichnyi, "Absorption anisotropy in sulfur doped gallium selenide crystals studied by THz-TDS," *Optical Materials Express*, vol. 4, no. 11, pp. 2451–2459, 2014.

[270] K. Kokh, J. Molloy, M. Naftaly, Y. Andreev, V. Svetlichnyi, G. Lanskii, I. Lapin, T. Izaak, and A. Kokh, "Growth and optical properties of solid solu-

tion crystals GaSe1xSx," *Materials Chemistry and Physics*, vol. 154, pp. 152–157, 2015.

[271] J. F. Molloy, M. Naftaly, Y. M. Andreev, G. V. Lanskii, I. N. Lapin, a. I. Potekaev, K. a. Kokh, a. V. Shabalina, a. V. Shaiduko, and V. a. Svetlichnyi, "Dispersion properties of GaS studied by THz-TDS," *CrystEngComm*, vol. 16, no. 10, p. 1995, 2014.

[272] K. A. KOKH, V. V. ATUCHIN, T. A. GAVRILOVA, A. KOZHUKHOV, E. A. MAXIMOVSKIY, L. D. POKROVSKY, A. R. TSYGANKOVA, and A. I. SAPRYKIN, "Defects in GaSe grown by Bridgman method," *Journal of Microscopy*, vol. 256, no. 3, pp. 208–212, 2014.

[273] M. Naftaly, J. F. Molloy, Y. M. Andreev, K. A. Kokh, G. V. Lanskii, and V. A. Svetlichnyi, "Dispersion properties of sulfur doped gallium selenide crystals studied by THz TDS," *Optics Express*, vol. 23, no. 25, p. 32820, 2015.

[274] K. Allakhverdiev, T. Baykara, S. Joosten, E. Günay, a.a. Kaya, a. Kulibekov (Gulubayov), a. Seilmeier, and E. Salaev, "Anisotropy of two-photon absorption in gallium selenide at 1064nm," *Optics Communications*, vol. 261, pp. 60–64, may 2006.

[275] Y. Peng, C. Xia, H. Zhang, T. Wang, S. Wei, and Y. Jia, "1. Peng, Y. et al. Characteristics of p-type Mg-doped GaS and GaSe nanosheets. Phys. Chem. Chem. Phys. 16, 1879918804 (2014).Characteristics of p-type Mg-doped GaS and GaSe nanosheets," *Phys. Chem. Chem. Phys.*, vol. 16, no. 35, pp. 18799–18804, 2014.

[276] S. A. Ku, W.-c. Chu, C. W. Luo, Y. M. Andreev, G. Lanskii, A. Shaidukoi, T. Izaak, V. Svetlichnyi, K. H. Wu, and T. Kobayashi, "Optimal Te-doping in GaSe for non-linear applications.," *Optics express*, vol. 20, pp. 5029–37, feb 2012.

[277] S.-A. Ku, W.-C. Chu, C.-W. Luo, A. A. Angeluts, M. G. Evdokimov, M. M. Nazarov, A. P. Shkurinov, Y. M. Andreev, G. V. Lanskii, A. V. Shaiduko,

K. A. Kokh, and V. A. Svetlichnyi, "Optical properties and application of GaSe:AgGaSe2 crystal," *Chinese Optics*, 2012.

[278] P. U. Jepsen and B. M. Fischer, "Dynamic range in terahertz time-domain transmission and reflection spectroscopy," *Opt. Lett.*, vol. 30, pp. 29–31, jan 2005.

[279] R. Le Toullec, N. Piccioli, M. Mejatty, and M. Balkanski, "Optical constants of\varepsilon-GaSe," *Il Nuovo Cimento B Series 11*, vol. 38, no. 2, pp. 159–167, 1977.

[280] M. M. Nazarov, A. P. Shkurinov, A. A. Angeluts, and D. A. Sapozhnikov, "On the choice of nonlinear optical and semiconductor converters of femtosecond laser pulses into terahertz range," *Radiophysics and Quantum Electronics*, vol. 52, no. 8, pp. 536–545, 2009.

[281] S. a. Ku, C. W. Luo, Y. M. Andreev, and G. Lanskii, "Comment on GaSe1xSx and GaSe1xTex thick crystals for broadband terahertz pulses generation [Appl. Phys. Lett. 99, 081105 (2011)]," *Applied Physics Letters*, vol. 100, no. 13, p. 136103, 2012.

[282] J.-i. Nishizawa, T. Sasaki, Y. Oyama, and T. Tanabe, "Aspects of point defects in coherent terahertz-wave spectroscopy," *Physica B: Condensed Matter*, vol. 401-402, pp. 677–681, dec 2007.

[283] K. Zhong, J. Yao, D. Xu, Z. Wang, Z. Li, H. Zhang, and P. Wang, "Enhancement of terahertz wave difference frequency generation based on a compact walk-off compensated KTP OPO," *Optics Communications*, vol. 283, pp. 3520–3524, sep 2010.

[284] Y. G. X. Tan, X. L. J. Yao, Y. Geng, X. Tan, X. Li, and J. Yao, "Compact and widely tunable terahertz source based onadual-wavelength intracavity optical parametric oscillation," *Applied Physics B*, vol. 99, pp. 181–185, nov 2009.

[285] E. D. Palik, ed., *Handbook of optical constants of solids*, vol. 3, ch. Gallium Se, pp. 473–485. Academic press, 1998.

[286] Y. J. Ding and W. E. I. Shi, "Widely-tunable, monochromatic, and high-power terahertz sources and their applications," *Physics*, vol. 12, no. 4, pp. 557–585, 2003.

[287] W. Shi and Y. J. Ding, "Generation of backward terahertz waves in GaSe crystals.," *Optics letters*, vol. 30, pp. 1861–3, jul 2005.

[288] M. Naftaly and R. Miles, "A method for removing etalon oscillations from THz time-domain spectra," *Optics Communications*, vol. 280, pp. 291–295, dec 2007.

[289] D. Zhang, Z. Lv, L. Sun, Z. Shao, and J. Yuan, "Tunable terahertz wave generation in GaSe crystals," in *Proc. of SPIE Vol*, vol. 7277, pp. 727710–727711, 2009.

[290] K. Allakhverdiev, N. Ismailov, Z. Salaeva, F. Mikailov, A. Gulubayov, T. Mamedov, and S. Babaev, "Reflective light modulator based on epsilon-GaSe crystal.," *Applied optics*, vol. 41, pp. 148–53, jan 2002.

[291] K. R. Allakhverdiev, T. Baykara, a. K. Gulubayov, a. a. Kaya, J. Goldstein, N. Fernelius, S. Hanna, and Z. Salaeva, "Corrected infrared Sellmeier coefficients for gallium selenide," *Journal of Applied Physics*, vol. 98, no. 9, p. 093515, 2005.

[292] A. Kenmochi, T. Tanabe, Y. Oyama, K. Suto, and J.-i. Nishizawa, "Terahertz wave generation from GaSe crystals and effects of crystallinity," *Journal of Physics and Chemistry of Solids*, vol. 69, pp. 605–607, feb 2008.

[293] K. Allakhverdiev, T. Baykara, . Ellialtiolu, F. Hashimzade, D. Huseinova, K. Kawamura, a.a. Kaya, a.M. Kulibekov (Gulubayov), and S. Onari, "Lattice vibrations of pure and doped GaSe," *Materials Research Bulletin*, vol. 41, pp. 751–763, apr 2006.

[294] O. Madelung, U. Rössler, and M. Schulz, eds., *Non-Tetrahedrally Bonded Elements and Binary Compounds I*, ch. Gallium su, pp. 1–3. Berlin, Heidelberg: Springer Berlin Heidelberg, 1998.

[295] K. Vodopyanov and L. A. Kulevskii, "New dispersion relationships for GaSe in the 0.65-18 um spectral region," *Optics Communications*, vol. 118, no. July, pp. 375–378, 1995.

[296] G. G. Gurzadyan, V. G. Dmitriev, and D. N. Nikogosyan, *Handbook of nonlinear optical crystals*. Springer-Verlag, 1991.

[297] K. Kato and N. Umemura, "Sellmeier equations for GaS and GaSe and their applications to the nonlinear optics in GaSxSe(1-x).," *Optics letters*, vol. 36, pp. 746–7, mar 2011.

[298] T. A. McMath and J. C. Irwin, "Indices of refraction of GaS and GaSe," *physica status solidi (a)*, vol. 38, no. 2, pp. 731–738, 1976.

[299] G. B. Abdullaev, L. A. Kulevskii, A. M. Prokhorov, A. D. Savel'Ev, E. Y. Salaev, and V. V. Smirnov, "GaSe, a new effective material for nonlinear optics," *JETP Lett.*, vol. 16, no. 3, pp. 90–95, 1972.

[300] G. B. Abdullaev, K. R. Allakhverdiev, L. A. Kulevskii, A. M. Prokhorov, É. Y. Salaev, A. D. Savel'ev, and V. V. Smirnov, "Parametric conversion of infrared radiation in a GaSe crystal," *Soviet Journal of Quantum Electronics*, vol. 5, no. 6, p. 665, 1975.

[301] N. B. Singh, D. R. Suhre, V. Balakrishna, M. Marable, R. Meyer, and B. Road, "Far-infrared Conversiont Materials: Gallium Selenide For Far-Infrared Conversion Applications," *Progress in Crystal Growth and Characterization of Materials*, pp. 47–102, 1998.

[302] E. Takaoka and K. Kato, "Temperature phase-matching properties for harmonic generation in GaSe," *Japanese Journal of Applied Physics, Part 1: Regular Papers and Short Notes and Review Papers*, vol. 38, no. 5, pp. 2755–2759, 1999.

[303] W. Shi, Y. J.Ding, and N. Fernelius, "Improvement on tuning ranges and output powers of thz waves based difference-frequency generation in GaSe,"

in *Lasers and Electro-Optics, 2003. CLEO '03. Conference on*, pp. 340–341, jun 2003.

[304] E. Takaoka and K. Kato, "90 degrees phase-matched third-harmonic generation of CO(2) laser frequencies in AgGa(1-x)In(x)Se(2).," *Optics letters*, vol. 24, pp. 902–4, jul 1999.

[305] G. Ferraris, E. Makovicky, and S. Merlino, *Crystallography of modular materials*. Oxford University Press, 2004.

[306] V. I. G.P. Chuiko, N.L. Don, "Ordering and Polytypism in AIIBV crystals," *Functional Materials*, vol. 12, no. 3, pp. 455–460, 2005.

[307] L. U. O. Zhi-wei, G. U. Xin-an, Z. H. U. Wei-chen, T. Wei-cong, A. YURY, L. Grigory, M. Alexander, and Z. Vladimir, "Optical properties of GaSe S crystals in terahertz frequency range," *Optics and Precision Engineering*, vol. 2, p. 20, 2011.

[308] M. M. Nazarov, S. Yu. Sarkisov, a. P. Shkurinov, and O. P. Tolbanov, "GaSe1xSx and GaSe1xTex thick crystals for broadband terahertz pulses generation," *Applied Physics Letters*, vol. 99, no. 8, p. 081105, 2011.

[309] J.-J. Xie, J. Guo, L.-M. Zhang, D.-J. Li, G.-L. Yang, F. Chen, K. Jiang, M. Evdokimov, M. Nazarov, Y. Andreev, G. Lanskii, K. Kokh, a.E. Kokh, and V. Svetlichnyi, "Optical properties of non-linear crystal grown from the melt GaSeAgGaSe2," *Optics Communications*, vol. 287, pp. 145–149, jan 2013.

[310] R. L. Toullec, J. C. Chervin, N. Piccioli, and A. Chevy, "Anharmonic effects in phonon spectra of GaSe.," *Applied optics*, vol. 20, pp. 2566–73, jul 1981.

[311] K. Allakhverdiev, S. Hanna, a. Kulibekov (Gulubayov), S. Özbek, E. Gunay, and D. Huseinova, "Room-Temperature Mid-, and Far-Infrared Absorption and Electrical Properties of Intercalated GaSe and TlInS2 Crystals," *International Journal of Infrared and Millimeter Waves*, vol. 26, pp. 1741–1755, nov 2005.

[312] O. X. Crystals, V. V. Atuchin, Y. M. Andreev, and S. A. Bereznaya, "Structure , Defects , Mechanical and Optical Properties of Hexagonal Semiconductor Gase1lxsx Single," in *Siberian Conference on Control and Communications SIBCON-2007*, pp. 179–184, 2007.

[313] Y. Andreev, V. Atuchin, G. Lanskii, a.N. Morozov, L. Pokrovsky, S. Sarkisov, and O. Voevodina, "Growth, real structure and applications of GaSe1xSx crystals," *Materials Science and Engineering: B*, vol. 128, pp. 205–210, mar 2006.

[314] T. J. Wang, J. C. Gao, Y. M. Andreev, S. A. Bereznaya, T. N. Kopylova, Z. V. Korotchenko, G. V. Lanskii, T. D. Malinovskaya, A. N. Morozov, and S. Y. Sarkisov, "GaSe1-x S x solid solutions," *Russian Physics Journal*, vol. 50, no. 6, pp. 560–565, 2007.

[315] S. a. Ku, C. W. Luo, W. C. Chu, Y. M. Andreev, V. V. Atuchin, G. V. Lanskii, a. N. Morozov, a. V. Shaiduko, and V. V. Zuev, "Physical properties of electrooptical GaSe:Al," in *2010 IEEE Region 8 International Conference on Computational Technologies in Electrical and Electronics Engineering (SIBIRCON)*, pp. 581–583, Ieee, jul 2010.

[316] K. Allakhverdiev, J. Goldstein, N. Fernelius, D. Huseinova, E. Salaev, and a. Trker, "Low-Temperature Midinfrared Absorption in GaSe," *International Journal of Infrared and Millimeter Waves*, vol. 26, pp. 457–466, feb 2005.

[317] N. Piccioli, R. L. Toullec, M. Mejatty, and M. Balkanski, "Refractive index of GaSe between 0 . 45 um and 330 um," *Applied Optics*, vol. 16, no. 5, pp. 2–4, 1977.

[318] K. Allakhverdiev, N. Fernelius, F. Gashimzade, J. Goldstein, E. Salaev, and Z. Salaeva, "Anisotropy of optical absorption in GaSe studied by midinfrared spectroscopy," *Journal of Applied Physics*, vol. 93, no. 6, pp. 3336–3339, 2003.

[319] Moschetti G. Forbes A. Leach R.K. Jiang X. and O. D, "Phase and fringe order determination in wavelength scanning interferometry (Accepted).," *Opt. Express*, 2016.

[320] L. L. Deck and L. B. Road, "Absolute distance measurements using FTPSI with a widely tunable IR laser," *Proc. SPIE*, vol. 4778, pp. 218–226, 2002.

[321] P. C. Leung, G. Andermann, C. A. Meads, and L. Angeles, "Constants and Infrared Absorption of GaSe," *Journal of Physics and Chemistry of Solids*, vol. 27, pp. 849–855, 1966.

[322] N. C. Fernelius, "PROPERTIES OF GALLIUM SELENIDE SINGLE," tech. rep., Material Directorate, Wright Laboratory, Wright-Patterson AFB, OH 45433, USA, 1994.

[323] M. Hayek, O. Brafman, and R. Lieth, "Splitting and Coupling of Lattice Modes in the Layer Compounds Gase, GaS, and GaSe X S 1-X," *Physical Review B*, vol. 8, no. 6, p. 1973, 1973.

[324] N. S. Yoshida H. and A. Mitsuishi, "Phonon Raman spectra of layer compound GaSe," *Phys. Status Solidi B*, vol. 59, pp. 125–128, 1973.

[325] N. M. Gasanly, A. Aydnl, H. Özkan, and C. Kocaba, "Temperature-dependent Raman scattering spectra of ϵ-GaSe layered crystal," *Materials Research Bulletin*, vol. 37, pp. 169–176, 2002.

[326] J. L. Brebner, "The optical absorption edge in layer structures," *Journal of Physics and Chemistry of Solids*, vol. 25, no. 12, pp. 1427–1433, 1964.

[327] H. Serizawa, Y. Sasaki, and Y. Nishina, "Polytypes and Excitons in GaSe1-xSx Mixed Crystals," *Journal of the Physical Society of Japan*, vol. 48, no. 2, pp. 490–495, 1980.

[328] A. Gouskov, J. Camassel, and L. Gouskov, "Growth and characterization of IIIVI layered crystals like GaSe, GaTe, InSe, GaSe1-xTex and GaxIn1-xSe,"

Progress in Crystal Growth and Characterization, vol. 5, no. 4, pp. 323–413, 1982.

[329] N. M. Gasanly and A. Aydinli, "Low-Temperature Raman Scattering Spectra of GaSexS1-x Layered Mixed Crystals," *Crystal Research and Technology*, vol. 37, no. 9, pp. 1011–1017, 2002.

[330] N. M. Gasanly, "Compositional dependence of the Raman lineshapes in GaSxSe1x layered mixed crystals," *Journal of Raman Spectroscopy*, vol. 36, pp. 879–883, sep 2005.

[331] G. B. Abdullaev, K. R. Allakhverdiev, S. S. Babaev, E. Salaev, M. M. Tagyev, L. K. Vodopyanov, and L. V. Golubev, "Raman scattering from GaSe1xTex," *Solid State Communications*, vol. 34, no. 2, pp. 125–128, 1980.

[332] P. F. Bernath, *Spectra of Atoms and Molecules*. Oxford University Press, 2005.

[333] Y. Zhirko, V. Trachevsky, and Z. Kovalyuk, *On the Possibility of Layered Crystals Application for Solid*. InTech, 2012.

[334] M. Schlüter, J. Camassel, S. Kohn, J. Voitchovsky, Y. Shen, and M. Cohen, "Optical properties of GaSe and GaS_{x}Se_{1-x} mixed crystals," *Physical Review B*, vol. 13, pp. 3534–3547, 1976.

[335] K. Allakhverdiev, F. Ismailov, L. Kador, and M. Braun, "Second-Harmonic Generation in GaS Crystals," *Solid State Communications*, vol. 104, no. 1, pp. 1–3, 1997.

[336] G. B. Abdullaev, K. R. Allakhverdiev, R. K. Nani, E. Y. Salaev, and M. M. Tagyev, "Neutron diffraction, infrared, and raman scattering investigations of the layered GaSxSe1x system," *physica status solidi (a)*, vol. 53, no. 2, pp. 549–555, 1979.

[337] I. Shoji, T. Kondo, and R. Ito, "Tutorial review Second-order nonlinear susceptibilities of various dielectric and semiconductor materials," *Optical and Quantum Electronics*, vol. 34, pp. 797–833, 2002.

[338] D. J. Armstrong, W. J. Alford, T. D. Raymond, and a. V. Smith, "Absolute measurement of the effective nonlinearities of KTP and BBO crystals by optical parametric amplification.," *Applied optics*, vol. 35, no. 12, pp. 2032–40, 1996.

[339] I. B. Zotova and Y. J. Ding, "Optical parametric oscillators in the presence of strong two-photon absorption for extended applications of nonlinear optical materials," *Optical Communications*, vol. 198, no. November, pp. 453–458, 2001.

[340] K. Vodopyanov, S. Mirov, V. Voevodin, and P. Schunemann, "Two-photon absorption in GaSe and CdGeAs2," 1998.

[341] M. Yüksek, A. Elmali, M. Karabulut, and G. M. Mamedov, "Switching from negative to positive nonlinear absorption in p type 0.5 at% Sn doped GaSe semiconductor crystal," *Optical Materials*, vol. 31, no. 11, pp. 1663–1666, 2009.

[342] M. Yüksek, A. Elmali, M. Karabulut, and G. M. Mamedov, "Nonlinear absorption in undoped and Ge doped layered GaSe semiconductor crystals," *Applied Physics B: Lasers and Optics*, vol. 98, no. 1, pp. 77–81, 2010.

[343] V. Petrov, G. Marchev, P. G. Schunemann, A. Tyazhev, K. T. Zawilski, and T. M. Pollak, "Subnanosecond, 1 kHz, temperature-tuned, noncritical midinfrared optical parametric oscillator based on CdSiP(2) crystal pumped at 1064 nm.," *Optics letters*, vol. 35, no. 8, pp. 1230–1232, 2010.

[344] U. Kürüm, H. G. Yaglioglu, M. Yüksek, A. Elmali, A. Ate, M. Karabulut, G. M. Mamedov, and N. Gasanly, "The effect of thickness and doping on the nonlinear absorption behaviour of IIIA-VIA group amorphous semiconductor thin films," *International Conference on Transparent Optical Networks*, no. 1, pp. 10–12, 2011.

[345] C. Ferrer-Roca, J. Bouvier, A. Segura, M. V. Andres, and V. Munoz, "Light-induced transmission nonlinearities in gallium selenide," *Journal of Applied physics*, vol. 85, no. 7, pp. 1–6, 1999.

[346] C. Angermann, P. Karich, L. Kador, K. R. Allakhverdiev, T. Baykara, and E. Y. Salaev, "Resonance enhancement of nonlinear photoluminescence in gallium selenide and related compounds," *Quantum Electronics*, vol. 42, no. 5, pp. 457–461, 2012.

[347] R. C. Eckardt and R. L. Byer, "Measurement of nonlinear optical coefficients by phase-matched harmonic generation," *Spie*, vol. 1561, pp. 119–127, 1991.

[348] R. J. Gehr and a. V. Smith, "Separated-beam nonphase-matched second-harmonic method of characterizing nonlinear optical crystals," *Journal of the Optical Society of America B*, vol. 15, no. 8, p. 2298, 1998.

[349] D. J. Armstrong, M. V. Pack, and A. V. Smith, "Instrument and method for measuring second-order nonlinear optical tensors," *Review of Scientific Instruments*, vol. 74, no. 7, p. 3250, 2003.

[350] L. Kador, D. Haarer, K. R. Allakhverdiev, and E. Y. Salaev, "Phase-matched second-harmonic generation at 789.5 nm in a GaSe crystal," *Applied Physics Letters*, vol. 69, no. August, p. 731, 1996.

[351] G. B. Abdullaev, L. A. Kulevskit, A. M. Prokhorov, A. D. Savel'ev, E. Y. Salaev, and V. V. Smirnov, "GaSe, A New Effective mMaterial For Nonlinear Optics," *JETP Lett.*, vol. 16, no. 3, pp. 130–135, 1972.

[352] J. Jerphagnon and S. K. Kurtz, "Maker fringes: A detailed comparison of theory and experiment for isotropic and uniaxial crystals," *Journal of Applied Physics*, vol. 41, no. 4, pp. 1667–1681, 1970.

[353] W. N. Herman and L. M. Hayden, "Maker fringes revisited: second-harmonic generation from birefringent or absorbing materials," *Journal of the Optical Society of America B*, vol. 12, no. 3, p. 416, 1995.

[354] L. Kador, M. Braun, K. Allakhverdiev, and E. Salaev, "Second-harmonic generation in GaSe crystals investigated with the Maker fringe technique," 1997.

[355] E. W. Van Stryland and M. Sheik-Bahae, *Z-scan measurements of optical nonlinearities*, ch. 3, pp. 655–692. Marcel Dekker, 1998.

[356] I. B. Zotova and Y. J. Ding, "Spectral measurements of two-photon absorption coefficients for CdSe and GaSe crystals.," *Applied optics*, vol. 40, pp. 6654–8, dec 2001.

[357] B. Murdin and P. Weightman, "Advanced infraRed/Teraherz Facilities for Users of Lasers (ARTFUL)," tech. rep., EPSRC, London, 2015.

[358] K. Litvinenko, E. Bowyer, P. Greenland, N. Stavrias, J. Li, R. Gwilliam, B. Villis, G. Matmon, M. Pang, B. Redlich, A. van der Meer, C. Pidgeon, G. Aeppli, and B. Murdin, "Coherent creation and destruction of orbital wavepackets in Si:P with electrical and optical read-out," *Nature Communications*, vol. 6, p. 6549, 2015.

[359] K. L. Litvinenko, S. G. Pavlov, H. W. H??bers, N. V. Abrosimov, C. R. Pidgeon, and B. N. Murdin, "Photon assisted tunneling in pairs of silicon donors," *Physical Review B - Condensed Matter and Materials Physics*, vol. 89, no. 23, pp. 1–5, 2014.

[360] B. N. Murdin, J. Li, M. L. Y. Pang, E. T. Bowyer, K. L. Litvinenko, S. K. Clowes, H. Engelkamp, C. R. Pidgeon, I. Galbraith, N. V. Abrosimov, H. Riemann, S. G. Pavlov, H.-W. Hübers, and P. G. Murdin, "Si:P as a laboratory analogue for hydrogen on high magnetic field white dwarf stars.," *Nature communications*, vol. 4, p. 1469, 2013.